TECHNISCHE UNIVERSITÄT MÜNCHEN

Fakultät für Physik
Lehrstuhl für Experimentalphysik E21

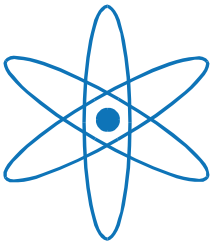

Implementation of neutron phase contrast imaging at FRM-II

Klaus Lorenz

Vollständiger Abdruck der von der Fakultät für Physik
der Technischen Universität München
zur Erlangung des akademischen Grades eines
Doktors der Naturwissenschaften (Dr. rer. nat.)
genehmigten Dissertation.

Vorsitzender:	Univ.-Prof. Dr. R. Netz
Prüfer der Dissertation:	1. Univ.-Prof. Dr. P. Böni
	2. Univ.-Prof. Dr. W. Petry

Die Dissertation wurde am 24.09.2008 bei der Technischen Universität München eingereicht und durch die Fakultät für Physik am 12.11.2008 angenommen.

Abstract

At ANTARES, the beam line for neutron imaging at the Forschungsneutronenquelle Heinz Maier-Leibnitz (FRM-II) in Garching, the option to do phase contrast imaging besides conventional absorption based neutron imaging was implemented and successfully used for the non-destructive testing of various types of objects.

The used propagation-based technique is based on the interference of neutron waves in the detector plane that were differently strong diffracted by the sample. A comparison with other phase-sensitive neutron imaging techniques highlights assets and drawbacks of the different methods. In preliminary measurements at ANTARES and the spallation source SINQ at PSI in Villigen, the influence of the beam geometry, the neutron spectrum and the detector on the quality of the phase contrast measurements were investigated systematically.

It was demonstrated that gamma radiation and epithermal neutrons in the beam contribute severely to background noise in measurements, which motivated the installation of a remotely controlled filter wheel for a quick and precise positioning of different crystal filters in the beam. By the installation of a similar aperture wheel, a quick change between eight different beam geometries was made possible. Besides pinhole and slit apertures, coded apertures based on non redundant arrays were investigated.

The possibilities, which arise by the exploitation of the real part of the refractive index in neutron imaging, were demonstrated in experiments with especially designed test samples and in measurements with ordinary, industrial components.

Zusammenfassung (German)

An der Tomographieanlage ANTARES der Forschungsneutronenquelle Heinz Maier-Leibnitz (FRM-II) in Garching wurde mit der Phasenkontrast-Radiographie eine neue Messmethode implementiert und erfolgreich für die zerstörungsfreie Prüfung verschiedenartigster Objekte verwendet.

Die verwendete Messtechnik basiert auf der Interferenz unterschiedlich stark am Probenort gebeugter Neutronenwellen in der Detektorebene. Beim Vergleich mit alternativen phasen-sensitiven Messverfahren wurden die Vor- und Nachteile der verschiedenen Methoden analysiert. In Vorversuchen an ANTARES und der Spallationsquelle SINQ des PSI in Villigen wurde der Einfluss der Strahlgeometrie, des Neutronenspektrums und des verwendeten Detektors auf die Qualität der Phasenkontrastmessungen systematisch untersucht.

Der erhebliche Beitrag zum Rauschen durch Gammastrahlung und epithermische Neutronen im Neutronenstrahl wurde nachgewiesen, woraufhin ein ferngesteuertes Filterrad für eine exakte Positionierung verschiedener Festkörperfilter im Strahl installiert wurde. Analog ermöglichte der Einbau eines Blendenrads den schnellen Wechsel zwischen acht verschiedenen Strahlgeometrien. Neben Loch- und Schlitzblenden wurden auch kodierte Masken hinsichtlich ihrer Verwendbarkeit für Phasenkontrastmessungen untersucht.

Die Möglichkeiten, welche sich durch die Nutzung des Realteils des Brechungsindex in der Neutronen-Radiographie und -Tomographie ergeben, wurden anhand von Messungen an selbst kreierten Testphantomen und an herkömmlichen, industriellen Bauteilen verdeutlicht.

Table of content

Introduction

Neutron phase contrast imaging – the consequential next step

Already in the Stone Age, the non-destructive testing of objects was vitally important for human beings. The hunter had to test his weapons before he tried to use them and the stability of a cave had to be judged carefully before a camp was set up inside. In this era, the reflected or transmitted light of the sun or from torches was detected by the human eye and the brain stored and analyzed the recorded data. By using mirrors or lenses in optical devices like telescopes or microscopes, scientists became able to investigate objects from microscopic to astronomic scales. The human eye remained however a big limitation, as it only responds to light with wavelengths in the range of approximately 400 to 700 nm. In 1724, Johann Heinrich Schultz discovered that a silver and chalk mixture darkens under exposure to light and the cornerstone for photography was laid. With a prism and a photographic paper, the invisible rays beyond the violet end of the visible spectrum were detected by Johann Wilhelm Ritter in 1801. Since the first permanent photograph by Joseph Nicéphore Niépce in 1826 scientists have been able to record images and to analyze them together with other scientists.

Photographic plates were also one of the first detectors for X-rays after their discovery in 1895 by Wilhelm Conrad Röntgen [Roe95]. Soon after the discovery, the great potential of X-rays for non-destructive testing of organic and inorganic objects was realized. The world famous X-ray image he recorded of his wife's hand can be considered as the first radiography.
In case of the neutron, the first radiography experiments by H. Kallman [Kal35] in 1935 were also carried out soon after the discovery of this new radiation by J. Chadwick in 1932 [Cha32]. Unlike X-rays, which interact mainly with the electrons in the atomic shell, the neutron attenuation coefficient of a material is determined by the neutron-nucleus interactions. For fast neutrons (E > 1 MeV) this interaction equals the collision of two hard spheres. The attenuation coefficient decreases accordingly with increasing atomic numbers, as the weight ratio of the neutron and the scattering nucleus differs more and more from one. This is exactly the opposite behavior than for X-rays. In case of thermal neutrons, the attenuation coefficients show no such simple dependence from the atomic number and can vary significantly also between neighboring elements. The contrast in conventional radiographs arises from the varying attenuation of the used radiation on different paths through the investigated object. Because of the different attenuation coefficients for

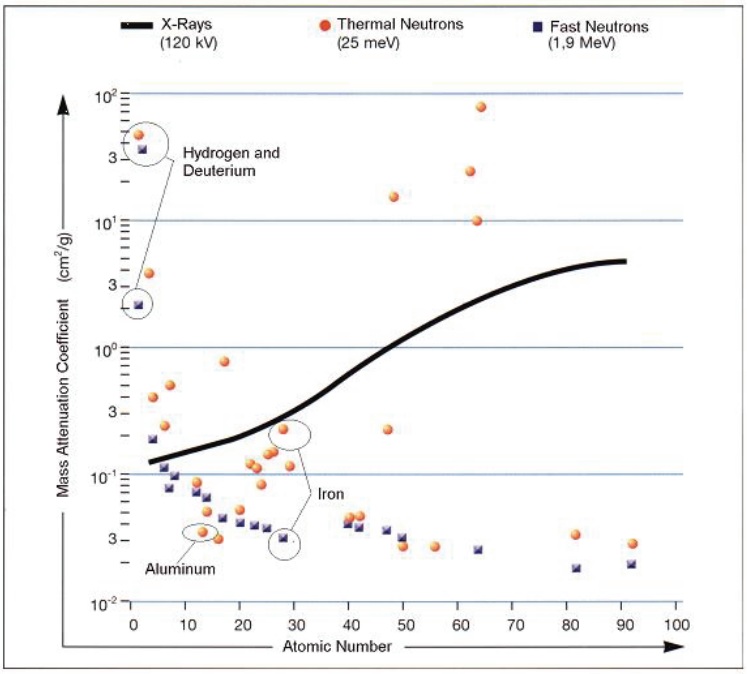

Fig. I.1: Comparison of the mass attenuation coefficient of the elements under standard conditions for X-rays, thermal and fast neutrons.

different types of radiation it is possible to use the complementary information from radiographic and tomographic measurements with X-rays and neutrons for an improved non-destructive testing of objects.

The invention of the phase contrast microscope in the early 1930s [Zer34], for which the Dutch physicist Frits Zernike received the Nobel prize for physics in 1953, opened up a new contrast mechanism for imaging with visible light, which allowed an improved delineation of the boundaries of transparent objects [Zer42]. This new measurement method was soon transferred to other types of radiation. In Transmission Electron Microscopy (TEM) and imaging with X-rays and synchrotron radiation, the phase contrast effect is used nowadays as a matter of routine for the investigation of weak absorbing objects and an improved visualization of edges and interfaces.

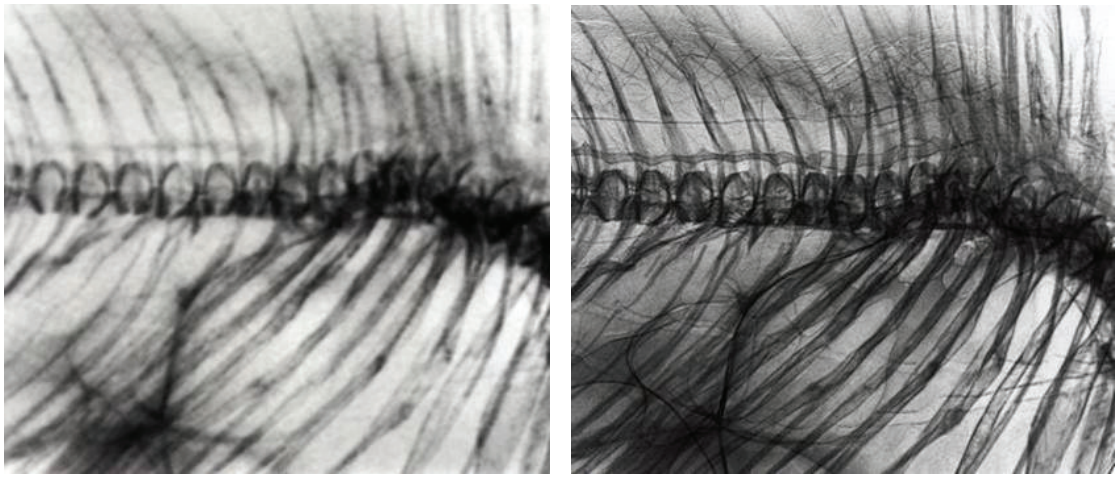

Fig. I.2: Comparison of a conventional, absorption based X-ray radiograph (left image) with an X-ray phase contrast radiograph (right image) of a goldfish. The increased delineation of the boundaries and edges of features can be used for an improved visualization of defects and allows the investigation of objects with poor absorption contrast [XRT08].

In 2000 propagation based phase contrast measurements were successfully carried out with a monochromatic neutron beam at NIST [All00]. The great potential of this new technique for the non-destructive testing with neutrons was evident and therefore an implementation of neutron phase contrast imaging at the new high flux neutron source Heinz Maier-Leibnitz (FRM-II) was soon aspired. This was the primary objective at the beginning of this PhD work.

In the beginning of chapter 1, the basic physics behind absorption based neutron imaging is overviewed. After this, different methods to use the phase information in the neutron beam for neutron imaging are presented and tomographic reconstruction is briefly explained.
The implementation of the experimental setup for propagation based phase contrast imaging at ANTARES, the beam line for neutron imaging at FRM-II, is described in the second chapter. This chapter is divided in three sections. The first section explains the adjustment of the beam geometry for phase contrast imaging. The second part records the development and implementation of a multi filter for the modification of the spectrum of the neutron beam, which was necessary for an improvement of the image quality. In the final section of this chapter the special demands on a detector system for neutron phase contrast imaging are explained and the assets and drawbacks of the used detectors are discussed.
The third chapter presents the analysis of the experimental measurements. This chapter is split into two parts as measurements were done at two different neutron sources, the spallation source SINQ at PSI in Switzerland and the research reactor FRM-II in Munich. At PSI experiments were carried out at the instruments NEUTRA, FUNSPIN and ICON. The results of these measurements are discussed in the first part of chapter. The remaining chapter describes the measurements at FRM-II and analyzes those results. At ANTARES,

the influence of the neutron spectrum, the detector and the used beam geometry on the quality of phase contrast images was systematically investigated.
The discussion of the results of the third chapter points out three major benefits of neutron phase contrast imaging compared to pure absorption based imaging, which are summed up in chapter 4. The improved spatial resolution due to the beam geometry, the enhanced contrast at edges and interfaces and the possibility to separate materials with similar attenuation coefficients allows an improved investigation of many objects of industrial and scientific interest.
The description of neutron phase contrast tomography at the end of chapter 4 shows in an impressive manner the great potential but also the experimental challenges of this measurement method. In the concluding outlook, prospects, challenges and the possible next steps are discussed.

Chapter 1

1 Theoretical considerations

1.1 Fundamental effects in neutron radiography

1.1.1 An idealized picture: The exponential attenuation law

The basic concept of neutron radiography is the investigation of the macroscopic structure of an object by position sensitive measurements of the transmitted neutron flux. For this purpose the object is put in a collimated neutron beam and a position sensitive detector behind the object registers the transmitted neutrons (Fig. 1.1).

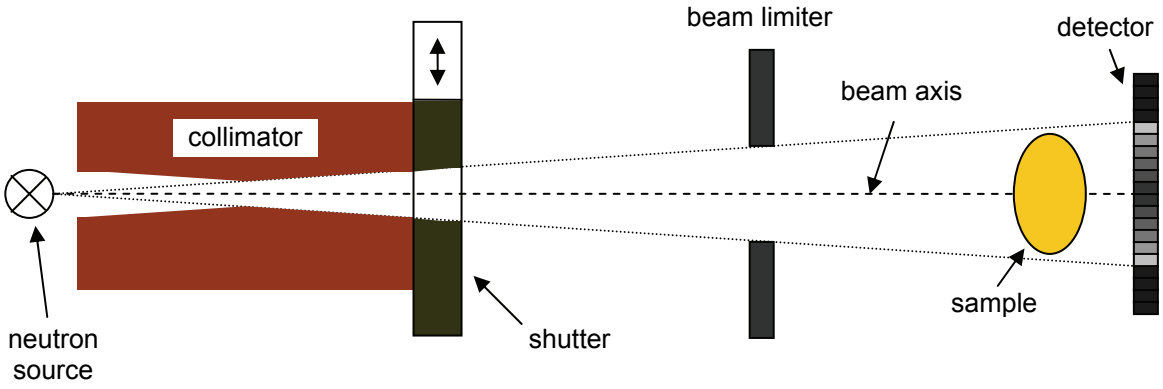

Fig. 1.1: Schematic diagram of an experimental setup for neutron imaging.

In general, the detector divides a certain field of view in the detector plane into an array of sections (pixels) with an equal surface area and measures the neutron flux in each section with the same sensitivity. In classical neutron radiography two fundamental assumptions are made that allow a simple interpretation of the measured data:

- neutrons move in straight lines through the object
- the interaction between the neutron beam and the object is fully described by the exponential attenuation law

The wave characteristics of neutrons are completely ignored in this simplified picture and it does not differentiate between scattering and absorption of neutrons. The cross sections for absorption σ_a and scattering σ_s are replaced by the total collision cross section

$$\sigma_t = \sigma_a + \sigma_s. \qquad (1.1)$$

The attenuation of the neutron beam by materials with a homogeneous atomic density n is described by the linear attenuation coefficient

$$\mu = n\,\sigma_t, \tag{1.2}$$

which has the dimension m^{-1}. The exponential attenuation law has the simple form

$$\phi(x,y) = \phi_0(x,y)e^{-\int_0^d \mu(x,y,z)dz}, \tag{1.3}$$

where ϕ_0 is the flux density of the incoming neutron beam and ϕ the flux density behind the sample with the thickness d. This is the neutron analogy of Lambert's law of absorption in ordinary optics. For a detector area of the size A, which is separated into N pixels of the same size, the neutron flux Φ_i on the pixel i that covers the region A_i is

$$\Phi_i = \iint_{A_i} \phi(x,y)dxdy\,. \tag{1.4}$$

After an exposure time t, a certain intensity I_i is registered in the pixel i with

$$I_i = \Phi_i t x\,, \tag{1.5}$$

where x is the sensitivity of the detector. In the course of the digital processing of the measured data, the intensity I_i is converted into a gray value for the pixel i. The arrangement of the gray values in the original array yields an image of the projection of the investigated object, the radiograph. The gray values indicate the attenuation of the neutron beam on different paths through the object. Their measurement uncertainty strongly depends on the exposure time t as they represent scaled statistical mean values averaged over the exposure time. In case of too short exposure times, the background is dominated by the neutron quantum noise. The different types of noise in neutron radiography are investigated in section 3.2.

1.1.2 A closer look on the interactions of the neutron beam with the sample

The simplified picture of the Lambert Beer law is not sufficient to explain phase contrast and other effects in neutron imaging. The interactions of the neutrons with the sample material have to be investigated in the atomic range and the wave characteristics of the neutron have to be considered. In contrast to X-rays, neutrons have a rest mass m_n. The momentum p of a neutron is related to a matter wave with a wavelength λ and a wave number k by the de Broglie relation

$$p = m_n v = h/\lambda = \hbar k. \tag{1.6}$$

1.1.2.1 The refractive index

The neutron interacts with its environment via all four forces of nature: gravitation, strong nuclear force, weak force and electromagnetism. The motion of a neutron is described by the Schrödinger equation

$$\left(-\frac{\hbar^2}{2m}\nabla^2 + V(\mathbf{r},t)\right)\Psi(\mathbf{r},t) = i\hbar\partial_t\Psi(\mathbf{r},t) \tag{1.7}$$

For an adiabatic motion in a spatially dependent potential $V(\mathbf{r})$, the wave function $\Psi(\mathbf{r},t)$ can be separated in a time-dependent and time–independent part $\Psi(\mathbf{r},t) = \psi(\mathbf{r})e^{-i\omega t}$, where $\psi(\mathbf{r})$ satisfies the time-independent Schrödinger equation

$$-\frac{\hbar^2}{2m}\nabla^2\psi(\mathbf{r})+V(\mathbf{r})\psi(\mathbf{r})=E\psi(\mathbf{r}), \tag{1.8}$$

where $E = \hbar\omega$ is the energy of the neutron. This is the well known Helmholtz equation

$$\nabla^2\psi(\mathbf{r})+\mathbf{K}^2(\mathbf{r})\psi(\mathbf{r})=0, \tag{1.9}$$

with the wave vector

$$\mathbf{K}^2(\mathbf{r})=\frac{2m}{\hbar^2}[E-V(\mathbf{r})]. \tag{1.10}$$

In free space this gives the simple isotropic dispersion relation

$$k^2=\frac{2mE}{\hbar^2} \tag{1.11}$$

The refractive index of a material is defined as the ratio of the spatially dependent wave vector **K**(**r**) to the free space wave vector **k**:

$$n(\mathbf{r})\equiv\frac{K(\mathbf{r})}{k}=\sqrt{1-\frac{V(\mathbf{r})}{E}} \tag{1.12}$$

1.1.2.2 Scattering and absorption

The interaction of neutrons with matter is dominated by the strong neutron-nucleus interaction. This interaction is characterized by the scattering amplitude $f(\theta)$, which gives the amplitude of the scattered wave relative to the incident wave with

$$f(\theta)=-\frac{4\pi^2 m}{\hbar^2}\langle\mathbf{k'}|\,T\,|\mathbf{k}\rangle \tag{1.13}$$

where θ is the angle between the incident and the scattered neutron wave vector **k** and **k'**, m the neutron mass and T the transition operator (T-matrix). Fermi found that for most practical purposes the scattering amplitude can be approximated by a single complex number, the scattering length b

$$f(\theta)=-b=-b'+ib''. \tag{1.14}$$

The corresponding potential

$$V_{nuc}(\mathbf{r})=\sum_j\frac{2\pi\hbar^2}{m}b\delta(\mathbf{r}-\mathbf{r}_j) \tag{1.15}$$

is called the Fermi pseudopotential and describes the effect of j hard nuclei at the positions $\mathbf{r}_j$. Averaged over a macroscopic volume, for a non-magnetic material with the atomic density N and the bound coherent scattering length b_c this gives the effective optical potential

$$V(\mathbf{r})=\frac{2\pi\hbar^2}{m}b_cN \tag{1.16}$$

If absorption and incoherent scattering are included, the scattering length and the refractive index is a complex value [Gol47]:

$$n = 1 - \frac{\lambda^2 N}{2\pi}\sqrt{b_c^2 - \left(\frac{\sigma_r}{2\lambda}\right)^2} + i\frac{\sigma_r N\lambda}{4\pi} = 1 - \delta + i\beta \qquad (1.17)$$

where $\sigma_r = \sigma_a + \sigma_i$ (1.22)(1.23) is the total reaction cross section.

The imaginary part of the scattering length is however in many cases very small and can be neglected, what simplifies the expression for the refractive index to

$$n = 1 - \frac{\lambda^2 N b_c}{2\pi} \qquad (1.18)$$

The fact that neutrons have a magnetic moment has been ignored up to this point. For a neutron with the spin **s** and a nucleus with the spin **I**, the scattering length b will in general (for I≠0) be spin dependent [Sea89]:

$$b = b_c + 2\left[I(I+1)\right]^{-1/2} b_i \mathbf{s}\cdot\mathbf{I} \qquad (1.19)$$

where b_i is the bound incoherent scattering length. Since s = ½, the total spin **J** = **I** + **s** has the eigenvalues J = I ± ½. For given values of J two bound scattering lengths can be distinguished:

$$b_+ = b_c + 2\left[I(I+1)\right]^{1/2} b_i \qquad (1.20)$$
$$b_- = b_c - 2\left[I(I+1)\right]^{1/2} b_i$$

The optical theorem

$$\sigma_t = \frac{\lambda}{2}\mathrm{Im}[f(0)] \qquad (1.21)$$

provides the simple relation between total collision cross section σ_t (1.1) and the imaginary part of the forward scattering amplitude (1.13).
The absolute value of the scattering length |b| determines the scattering cross section, where coherent and incoherent scattering can be distinguished [Sea89]:

$$\sigma_c = 4\pi|b_c|^2 \qquad (1.22)$$
$$\sigma_i = 4\pi|b_i|^2$$

The cross section for absorption is proportional to the imaginary part of the coherent scattering length

$$\sigma_a = \frac{\lambda}{2} b_c'' \qquad (1.23)$$

In contrary to the scattering cross section, the cross section for absorption depends on the neutron wavelength.

1.1.2.3 Total reflection

Over 95% of all isotopes have a positive coherent scattering length b_c and hence a positive, repulsive optical potential (1.16). If the kinetic energy of the neutron related to the momentum perpendicular to the surface of such a material is less than the optical potential, the neutron is reflected from the surface. All neutrons that hit the surface under an angle α (Fig. 1.2) less than the critical angle α_c given by

$$\alpha_c = \arcsin\left(\lambda\sqrt{\frac{Nb}{\pi}}\right) \tag{1.24}$$

are totally reflected.

This effect is today routinely used at neutron sources all over the world to transport neutrons with neutron guides to instruments far away from the neutron source. In state-of-the-art neutron guides, so called supermirrors are used, where multilayer structures are used to increase the angle for total reflection [Mez76].

The critical angle increases with the wavelength of the neutron and can reach 90° for ultra cold neutrons. Like this it is possible to confine ultra cold neutrons in magnetic bottles [Gol79] or traps [Pau78].

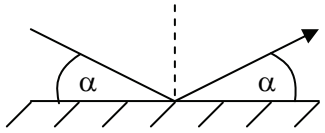

Fig. 1.2: Total reflection of a neutron beam hitting a surface under an angle $\alpha < \alpha_c$.

1.1.2.4 Phase shift and coherence

As the name implies, in neutron phase contrast imaging the shifting of the phase of the neutrons by the sample is used to obtain an additional image contrast besides attenuation based contrast. To explain the effect of phase shifting, the neutron is described as a coherent wave $\Psi(\mathbf{r},t)$ of the form

$$\Psi = Ae^{\frac{i}{\hbar}S}, \tag{1.25}$$

where A(**r**,t) and S(**r**,t) represent the amplitude and the phase of the coherent wave. The real scalar field S(**r**,t) is called the eikonal. If the spatial distribution of a constant value of S at a certain time t_0 S(**r**,t_0)=c describes a surface, this corresponds to a wave front in geometrical optics. The rays in geometrical optics that describe the beam direction are always perpendicular to those wave fronts and thus given by the gradient ∇S. To understand the physical meaning of this, the neutron number density ρ and current density **j** have to be expressed with A and S:

$$\rho = |\Psi|^2 = A^2 \tag{1.26}$$

$$\mathbf{j} = \mathrm{Re}\left(\Psi^* \mathbf{v} \Psi\right) = \frac{A^2}{m}\nabla S \tag{1.27}$$

where the operator **v** for the group velocity is given by **v** = **p**/m = (ħ/im)∇.

As **j** = ρ**v** and **p** = m**v**, the gradient field ∇S can be identified in Eq. (1.27) as the momentum field **p**.

The effect of δ, the departure from unity of the real part of the refractive index n = 1 – δ of a sample, on a neutron wave field that penetrates a sample on a certain path L is a phase shift

$$\varphi(L,\mathbf{k}) = \int_L (n-1)\mathbf{k}\cdot\mathbf{dl} \tag{1.28}$$

compared to propagation in free space, where **dl** is a vector element of displacement along the path of the neutron.

In facilities for neutron phase contrast imaging, which will be discussed in the following section 1.2, the incident neutron beam is in general well collimated, so that the neutrons move approximately parallel to the beam line direction and can be approximated by a plane wave that propagates in z-direction. A measure for how close the actual neutron beam is to a parallel beam at the sample position, is the transversal spatial coherence length L_c,

$$L_c = \frac{L}{D}\lambda\,, \tag{1.29}$$

where D is the lateral size of the source, L the distance between the source and the sample and λ the wavelength of the neutron beam. As we will never deal with a monochromatic neutron beam in the experiments concerned in this work, the L/D-ratio will be used to characterize the transversal coherence of the neutron beam.
For an almost parallel beam in z-direction (with a very high L/D-ratio), the phase shift φ caused by a sample of the thickness d in z-direction, can be expressed as a function of the (x,y)-position in a plane perpendicular to the beam direction and the wave number k of the neutron.

$$\varphi(x,y,k) = k\int_0^d (n(x,y,z')-1)dz \tag{1.30}$$

A homogeneous material with the refractive index $n = 1 - \delta$ and the thickness d causes the phase shift

$$\varphi = -k\delta d = -\frac{2\pi\delta d}{\lambda} \tag{1.31}$$

The introduction of a sample in a well collimated beam leads to a deformation of the wave fronts (Fig. 1.3). As the beam direction is always perpendicular to the wave fronts, those deformations represent deviations of the beam direction, which is the refraction of the beam. This effect, together with the ability of two waves to interfere with each other, give rise to several methods for experimental physicists, to exploit the phase shift of neutrons for measurements.

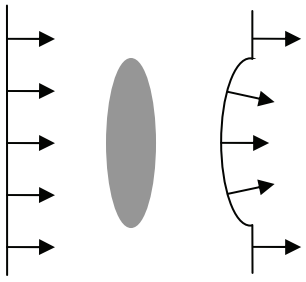

Fig. 1.3: Deformation of the wave front of an incident plane wave by an ellipsoid shaped sample.

1.2 Principles of neutron phase contrast imaging

For neutron imaging, basically three different types of phase sensitive measurement techniques can be distinguished and are discussed in the proceeding section. All three techniques have in common that they need an incident neutron beam with a high transverse spatial coherence to be able to convert lateral variations of the phase shift of the beam into measurable intensity variations in the detector plane. Besides the collimation, a monochromatization or at least a limitation of the bandwidth of the utilized neutron beam is required in many of the described techniques. This leads to a fundamental requirement to be able to perform neutron phase contrast imaging: a high flux neutron source.

1.2.1 Interferometry

The principle of interferometry is well known from classical experiments with visible light and can be transferred to neutrons. An incoming neutron beam is separated into two coherent neutron beams. One of them is used as a reference beam and propagates through free space, while the other beam is transmitted through the sample. The two beams meet each other again, interfere with each other and the intensity is measured in a detector. This intensity depends on the phase shift between the reference and the object beam.
The first attempts to construct a neutron interferometer with coherent beams were done by Heinz Maier-Leibnitz in 1962 [Lei62]. In this interferometer the two coherent beams were very close together (about 60μm) and the coherence properties were destroyed by samples introduced into the beam. A greater separation of the two beams became possible with the introduction of single crystal neutron interferometers, again a technique that was transferred from X-ray interferometry [Bon65].
The experimental setup of a single crystal neutron interferometer is shown in Fig. 1.4 [Rau74]. The heart of the interferometer consists of three crystal slices, which are cut out of one large, almost perfect monolithic silicon crystal. The first crystal slice acts as a beam splitter and separates the incoming monochromatic and well collimated beam in two coherent neutron beams. The second slice acts like a mirror and allows the recombination of the two beams in the third slice, the analyzer. A compensator is introduced in one of the coherent beams to compensate built-in phase patterns of the interferometer. The sample also is inserted in one of the two beams, normally between the mirror and the analyzer.

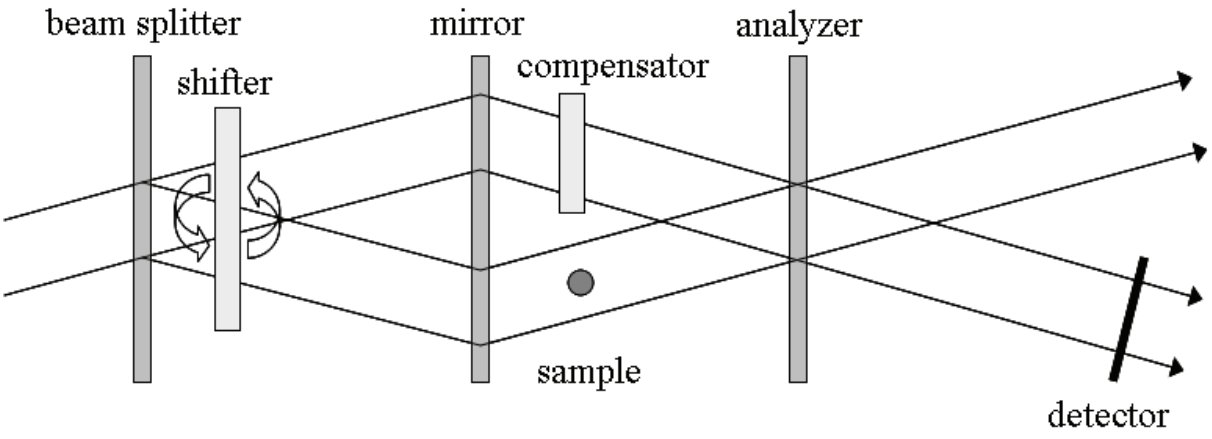

Fig. 1.4: Principle of neutron interferometry.

The measured intensity in the detector is a periodic and not a monotonous function of the path length in the sample. Therefore, in order to retrieve the phase from the interference pattern, it is necessary to measure at least three images. In general more than three images

are recorded to reconstruct a single phase map in order to avoid ambiguity on the sign of the phase, to eliminate the incoherent contributions to the intensity and to compensate static patterns. A phase shifter between the beam splitter and the mirror is used to vary the overall relative phase of the interfering beams by 2π over, in general, four or more steps. By this method, the phase is known except for a multiple of 2π.

At ILL in Grenoble, France it was shown in 2002 that it is possible to do tomographic measurements with a single crystal neutron interferometer and to reconstruct the local distribution of the refractive index decrement $\delta(x,y,z)$ [Dub02]. The complexity of the experimental setup for this kind of tomography is however a big disadvantage compared to the phase contrast imaging techniques presented in the following two sections. The neutron interferometer is very sensitive to thermal, mechanical and acoustic disturbances in the experimental environment. A neutron interferometer is even more sensitive to mechanical vibrations than a X-ray interferometer because of the low velocity of cold or thermal neutrons compared to the speed of light of X-rays.
For a successful operation of the interferometer, the three slices for beam splitter, mirror and analyzer are cut out of one single crystal block. Because of the limited available size of single crystal blocks, this leads to a drastic limitation of the available sample volume.
Another drawback of this method is the long exposure time to get a phase map with a sufficient signal-to-noise ratio. The incoming beam has to be monochromatized and collimated, which leads to a severely reduced incoming flux. As described earlier in this section, at least eight images have to be recorded for one phase map (one image with and one without sample at four different phase steps between 0 and 2π). To be able to record one hundred phase maps or more for a phase tomography in a reasonable time, a neutron source with a very high flux in the desired bandwidth is needed.

1.2.2 Differential phase contrast

As illustrated in Fig 1.3, the introduction of a sample in a neutron beam with a high transverse spatial coherence (well defined wave fronts) causes deformations of the wave fronts due to the position dependent phase shift φ (1.30). The propagation direction of waves is always perpendicular to their wave fronts and thus, those deformations of the wave fronts are equivalent to angular deviations of the neutron beam (neutron refraction). Because the refractive index for neutrons is very close to unity, the refraction angles in the sample are extremely small and can be approximated using the resulting phase gradient perpendicular to the neutron beam direction as

$$\alpha(x,y,k) = \frac{1}{k}\nabla_{\perp}\varphi(x,y,k) \tag{1.32}$$

Differential phase contrast methods are very sensitive to those angular deviations caused by refraction of the beam in the sample. A standard setup is a double crystal arrangement as shown in Fig 1.5. The first crystal acts as a monochromator or collimator depending on the type of the incoming beam. If the incoming beam is collimated but polychromatic, the crystal selects the used wavelength for the measurement, if the beam is monochromatic but not collimated, the crystal determines the used beam direction. The second crystal is an angular filter that allows only a narrow range of incident directions to reach the detector.

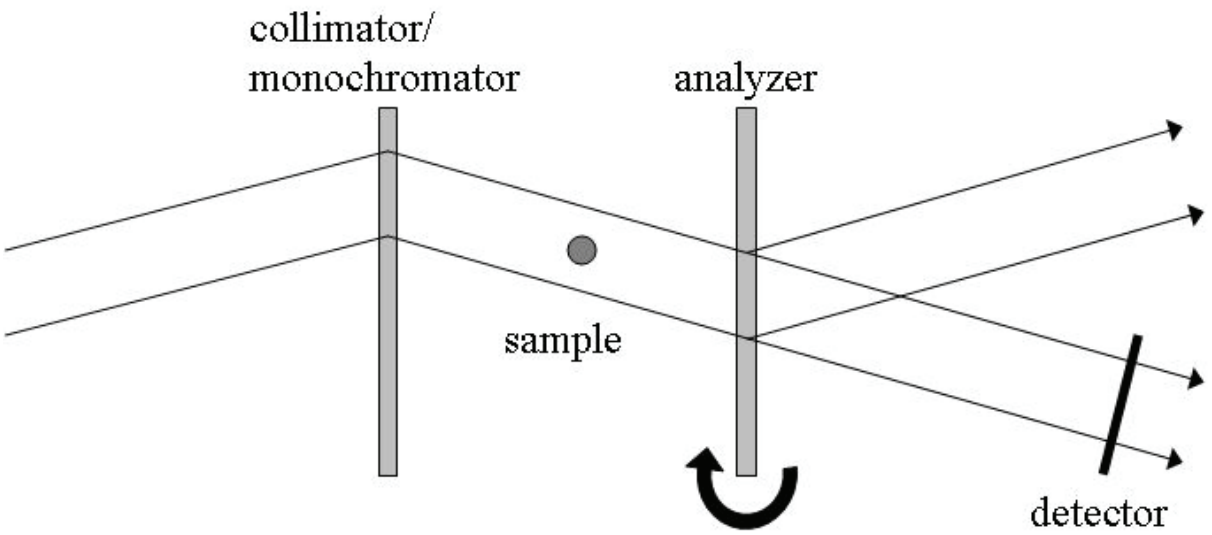

Fig. 1.5: Double crystal diffractometer as an example for differential phase contrast imaging.

This analyzer crystal is rotatable mounted to be able to vary the angle between the two crystals and thus measure a rocking curve. The measured intensity in the position sensitive detector behind the analyzer crystal changes in each point of the image as a function of the local angular deviation α (1.32) and the rocking curve. Without any further processing, the measured images already show contrast where strong phase gradients are present in the sample, which is mainly at edges and interfaces. The method is most sensitive to phase gradients in the sample which are perpendicular to the beam direction and perpendicular to the rotational axis of the analyzer crystal. Phase gradients parallel to this rotational axis are not visible in the raw data and must be reconstructed in further image processing. As the method is sensitive to the first derivative of the phase shift caused by the sample, the intensity variations caused by the phase gradient can be positive and negative. Like this, the left and the right edge of a perfectly symmetric cylinder show a completely different intensity (see Fig. 1.6b) in the raw data. The object phase shift φ can be retrieved by simple linear integration.

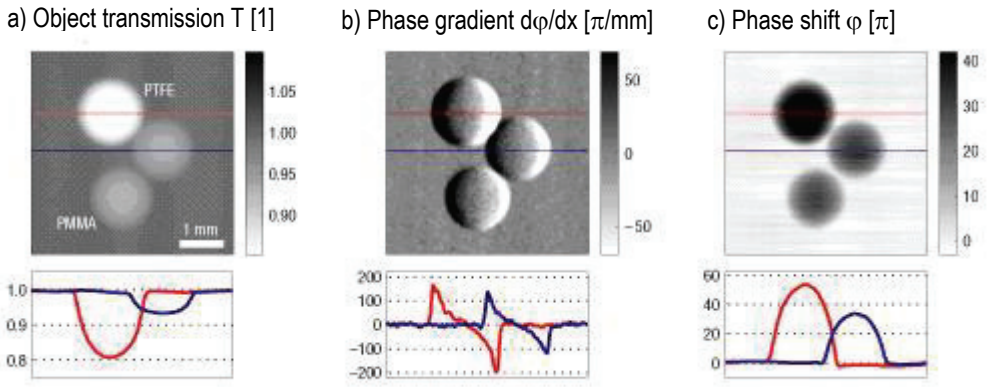

Fig. 1.6: Differential phase contrast image (b, image in the middle) of three plastic spheres with 40kV X-rays and the comparison with a conventional transmission image (a) and the object phase shift φ retrieved by integration of b) (c). Below the images, line profiles along the red and blue lines in the images are shown. The images are taken from the publication in Nature Physics [Pfe06a] with the kind permission of the author Franz Pfeiffer.

This measuring method corresponds to Schlieren imaging in classical optics [Hec07] and was enhanced to imaging with X-rays and neutrons. Besides its original name, Schlieren imaging, several different names are used for this technique like refraction contrast, phase

dispersive imaging or diffraction enhanced imaging. With neutron double crystal diffractometers three dimensional tomographic measurements with this technique were realized [Str04]. The stability requirements are much less stringent than in classical interferometry and the experimental setup is less complex. The collimator and analyzer crystal do not need to be monolithical, what allows the investigation of bigger samples. To have a well defined beam direction however, narrow slits with a width in the order of 1 mm have to be installed before and after the sample position. Like this, a scanning routine has to be executed for bigger samples. The measuring time for the first tomography of this kind was over 150 hours and the resulting quality was disappointing considering the huge effort. But it has to be kept in mind that this first tomography was a proof of principle and that there are still possibilities to reduce measurement time and improve image quality.

Beside this classical way to do Schlieren imaging with neutrons, a very promising new technique for differential neutron phase contrast imaging has been developed very recently at the Paul Scherrer Institute in Switzerland. In this method a grating-based shearing interferometer is used to retrieve quantitative differential phase contrast images with neutron sources of little spatial and chromatic coherence [Pfe06]. In the experimental setup, the two crystals of the double crystal interferometer are replaced by gratings as shown in Fig 1.7.

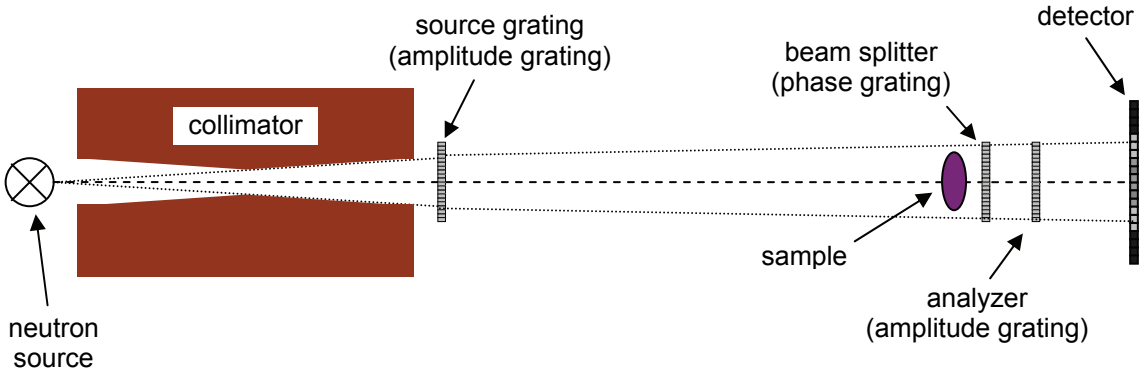

Figure 1.7: Experimental setup for a grating-based shearing interferometer.

The first grating, the source grating, is an absorbing mask with transmitting slits, which is typically placed as close as possible to the neutron source. It creates an array of line sources, where each line source fulfills the coherence requirements for the differential phase contrast image process [Pfe05]. The second grating is a phase grating and acts as a beam splitter that divides the beam into the two first diffraction orders. The diffracted beams interfere further downstream and form linear periodic fringe patterns in planes perpendicular to the optical axis. The fundamental idea of the method is to detect the local positions of the fringes and determine from these the phase shift introduced by the sample. Since the area detectors in neutron imaging do not have sufficient resolution to measure the exact position of the maxima of these fringes, another absorbing grating, the analyzer grating, with the same periodicity and orientation as the fringes is placed right in front of the detector. To separate the phase information, a phase stepping approach like in classical interferometry is used. The analyzer grating is scanned in the x-direction, perpendicular to the optical axis, the intensity I(x,y) in each pixel oscillates. The average signal for each pixel over an entire oscillation is identical to the radiography signal that would be measured without the interferometer. The phase $\phi(x,y)$ of those intensity oscillation in each pixel are related to the phase map $\varphi(x,y)$ by

$$\phi(x,y) = \frac{\lambda L_2}{d_2}\frac{\partial\varphi}{\partial x}, \tag{1.33}$$

where λ is the neutron wavelength, L_2 the distance between splitter and analyzer grating and d_2 the period of the analyzer grating. Like this, a single phase-stepping scan yields both the phase and the attenuation image.
The exposure time for one image is of the order of ten seconds. If ten images are taken in one phase stepping scan, one projection of the phase and the attenuation of the sample is recorded in about 2 minutes, including the readout time of the CCD detector. This is fast enough to allow high quality tomographic measurements. A drawback of this method is the complicate procedure to create the gratings and the demand for a complex experimental setup that has to work very precisely and reliably. The size of the sample is also restricted by the size of the gratings, which have up to now a maximum size of the order of 6-10 cm.

1.2.3 Propagation-based phase contrast

Already in 1979, K. Goetz and P. Zaumseil noticed, while using the X-ray Schlieren method for measurements of the parameters of shell targets for laser thermonuclear fusion, that an additional phase contrast can be recorded without an analyzer crystal between sample and detector [Goe79], if the sample is put in an highly collimated beam and the detector is positioned at a certain distance downstream of the sample. Hence, to get this phase contrast a simple experimental setup as described in Fig. 1.8 can be used.

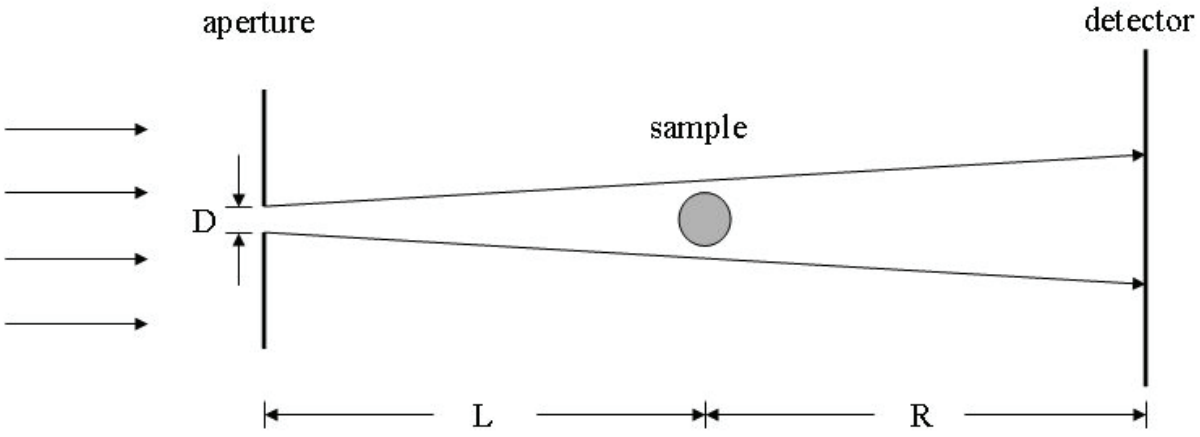

Fig. 1.8: Experimental setup for propagation-based phase contrast imaging.

The experimental setup is essentially the same as for conventional radiography except for the increased sample-to-detector distance R and additional apertures to create an incoming beam with a high transversal spatial coherence at the sample position. The phase contrast occurs due to interference between different parts of the wave front that have suffered slightly different angular deviations associated to different phase gradients in the sample. If the distance between sample and detector is too small, the different parts of the wave front cannot interfere with each other and only attenuation contrast is visible in the detector plane (Fig. 1.9). In theory, the distance between sample and detector can also be too big in terms that the detector plane is not any longer in the near field but in the Fresnel region or even in the Fraunhofer region. In the Fraunhofer region, not a projection of the sample is recorded any longer, but its Fourier transform. In practice, the maximum sample-to-detector distance is limited by the blurring of the image due to the divergence of the neutron beam (see 2.1.2.2.1).

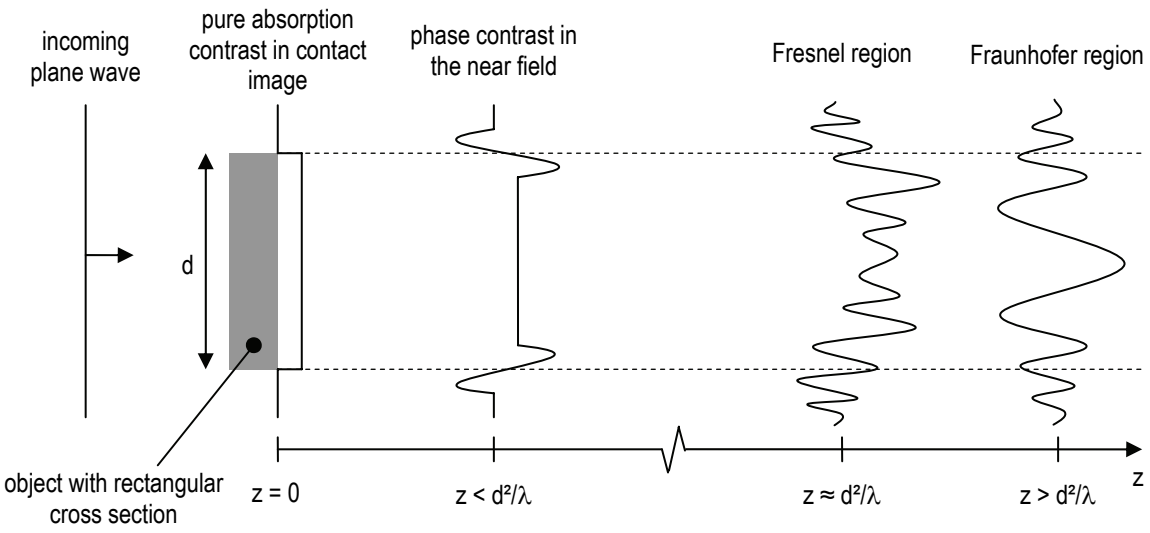

Fig. 1.9: Dependence of the measured signal on the sample-to-detector distance.

Compared to the first two methods for phase contrast imaging described in this chapter, propagation-based phase contrast imaging has three major benefits that make it very attractive for the experimental physicist:

1. The experimental setup is simple. No additional devices to a conventional neutron imaging setup are needed.
2. The exposure times are much shorter, compared to interferometric methods. Tomographic measurements can be done in a reasonable time.
3. The sample size is only limited by the beam diameter and the detector size (which can be circumvented by scanning the sample)

A drawback of this method is that it is not sensitive to linear phase gradients in the sample, because the second derivative of the phase is recorded in the image plane (see 1.2.3.1). Another drawback is the complicated algorithm that has to be used to retrieve the phase map from the raw recorded data.

1.2.3.1 Image formation

In this subsection the effect of phase variations in the object plane on the intensity distribution in the detector plane in propagation-based neutron phase contrast imaging is investigated. The goal is to derive with Fresnel diffraction theory [Cow95] an analytical expression for the intensity distribution in dependence on the object's refractive index n(x,y,z) and experimental parameters. To keep it simple in the beginning, a monochromatic neutron beam from a perfect point source is considered. When a result is obtained under these simplified conditions, the consequences of a polychromatic beam and an extended source are discussed.

An idealized picture of the motion of a neutron in a neutron radiography beamline is shown in Fig. 1.10. The neutron propagates in a spatially dependent potential $V(\mathbf{r})$ and is thus represented by a wave function that satisfies the time-independent Schrödinger equation (see 1.1.2.1)

$$-\frac{\hbar^2}{2m}\nabla^2\psi(\mathbf{r}) + V(\mathbf{r})\psi(\mathbf{r}) = E\psi(\mathbf{r}). \qquad (1.34)$$

A possible solution of this wave equation is a spherical wave emitted by a point source at the origin

$$\psi = \psi_0 \frac{\exp(-ikr)}{r}, \tag{1.35}$$

with r = |**r**| and kr = **kr**, since the direction of propagation is always radial.

A fundamental property of the solutions of linear differential equations is that the sum of any two solutions is also a solution. This principle of superposition leads to another basic principle in wave optics, Huygens principle, which was later extended by Fresnel to the so-called Huygens-Fresnel principle. It says that every point of a wave-front may be considered as a center of a secondary disturbance that gives rise to spherical wavelets and that the wave-front at any later instant may be regarded as the envelope of these wavelets. Fresnel added the postulate that the secondary wavelets mutually interfere. Kirchhoff put those postulates on a sounder mathematical basis and showed that the Huygens-Fresnel principle is an approximate form of a certain integral theorem.

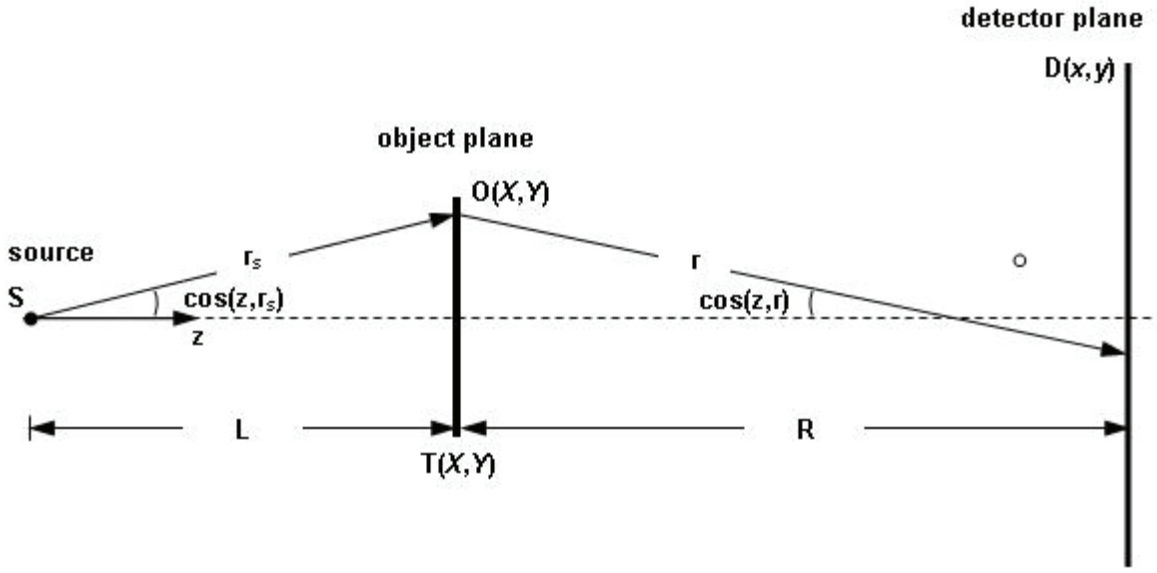

Fig. 1.10: Idealized picture of the wave propagation.

With the Kirchhoff formula, the disturbance at a point D in the detector plane due to any wave-field $\psi(\mathbf{r})$, created by the point source S, is given by integrating over any closed surface containing D as [Cow95]

$$\psi(x,y) = \frac{i}{2\lambda}\oint_S \frac{\exp(-ikr_s)}{r_s}\frac{\exp(-ikr)}{r}\left[\cos(\mathbf{z},\mathbf{r}) + \cos(\mathbf{z},\mathbf{r}_s)\right]dS, \tag{1.36}$$

where cos(**z**,**r**) and cos(**z**,$\mathbf{r}_s$) are the angles between the beam direction **z** and the vectors **r** and $\mathbf{r}_s$ as shown in Fig. 1.10. This was for the “open beam” case without an object. To be able to calculate the intensity I(x,y) = $\psi(x,y)\,\psi^*(x,y)$ in the detector plane, some simplifying assumptions have to be made.
As mentioned before, the refractive index for neutrons is very close to unity ($|n-1|\approx 10^{-6}$). Like this the angular deviation of the beam (see (1.32)) in the sample region can be ignored and the propagation inside the sample can be assumed as being straight. Like this it is possible to project the object onto a single plane perpendicular to the propagation direction and to describe the effect of the object by the two-dimensional transmission function T(X,Y).
Another characteristic of the setup described in Fig. 1.8 that gives opportunities for simplifications is the high transverse spatial coherence of the neutron beam at the sample

position. Like this, the incident neutron beam may be replaced by a plane wave of unity amplitude having zero phase in the object plane. With this the amplitude in the detector plane at a distance R behind the object is

$$\psi(x,y) = \frac{i}{2\lambda}\iint T(X,Y)\frac{\exp(-ikr)}{r}\left[\cos(\mathbf{z},\mathbf{r})+1\right]dXdY\,, \tag{1.37}$$

with $r = \sqrt{(X-x)^2+(Y-y)^2+R^2}$.

If the lateral dimensions of the object are much smaller than the object to detector distance, another small angle approximation can be made downstream the object with cos(**z**,**r**) ≈ 1 and r ≈ R. With this (1.37) can be further simplified to

$$\psi(x,y) = \frac{i\exp(-ikR)}{R\lambda}\iint T(X,Y)\exp\left(\frac{-ik[(X-x)^2+(Y-y)^2]}{2R}\right)dXdY\,. \tag{1.38}$$

If the transmission function varies only in one dimension, the integral over one dimension can be carried out

$$\int_{-\infty}^{+\infty}\exp\left(\frac{-ik(Y-y)^2}{2R}\right)dY = \sqrt{\frac{R\lambda}{i}} \tag{1.39}$$

and (1.38) becomes

$$\psi(x) = \sqrt{\frac{i}{R\lambda}}\exp(-ikR)\int_{-\infty}^{+\infty}T(X)\exp\left(\frac{-ik(X-x)^2}{2R}\right)dX \tag{1.40}$$

There are very few functions T(X) for which this integral can be evaluated analytically. Fortunately one of them is

$$q(x) = e^{i\varphi(x)}, \tag{1.41}$$

which represents the case of a pure phase object. It only changes the phase but not the amplitude of the incident wave. With this transmission function the integral in (1.40) can be evaluated [Cow95] and the amplitude in the detector plane becomes

$$\psi(x) = e^{i\varphi(x)}\left[1+\frac{R\lambda}{4\pi}\varphi''(x)+\frac{iR\lambda}{4\pi}(\varphi'(x))^2\right]. \tag{1.42}$$

The intensity distribution in the detector plane D is

$$I(x) = \Psi(x)\Psi^*(x) = 1+\frac{R\lambda}{4\pi}\varphi''(x) \tag{1.43}$$

The intensity variation in the detector plane due to the real part of the refractive index of the object is proportional to the sample-to-detector-distance *R*, the wavelength λ and the second derivative of the phase shift $\varphi(x)$.

1.2.3.2 Phase retrieval

Now that the nature of propagation-based phase contrast is clear, the next question that arises is whether it is possible to calculate the phase shift $\varphi(x,y)$ from the measured intensity distributions I(x,y) in the detector plane. This leads to the inverse problem of phase retrieval.

To solve this inverse problem, we first consider a monochromatic neutron beam with a wavelength λ propagating in the z-direction of an orthogonal coordinate system xyz. In paraxial approximation, the wave amplitude can be expressed by the real-valued quantities I_z and φ_z

$$u_z(\mathbf{r}_\perp) = \sqrt{I_z(\mathbf{r}_\perp)}e^{i\varphi_z(\mathbf{r}_\perp)} \quad , \tag{1.44}$$

where I_z is the irradiance, φ_z the phase and $\mathbf{r}_\perp$ a vector in a xy-plane at a distance z from the object plane. In paraxial approximation $u_z(\mathbf{r}_\perp)$ fulfills the parabolic equation [Pap68]

$$\left(i\frac{\partial}{\partial z} + \frac{\nabla^2}{2k} + k\right)u_z(\mathbf{r}_\perp) = 0 \, , \tag{1.45}$$

with $k=2\pi/\lambda$ and $\nabla^2=(\delta^2/\delta x^2)+ (\delta^2/\delta y^2)$. To eliminate the imaginary parts, Eq. (1.45) can be multiplied on the left-hand side by u_z^* and the complex conjugate of Eq. (1.45) can be multiplied on the left-hand side by u_z. The two resulting equations can be subtracted to get

$$\frac{2\pi}{\lambda}\frac{\partial}{\partial z}I_z = -\nabla \cdot I_z \nabla \varphi_z \, . \tag{1.46}$$

This is the so-called transport-of-intensity function (TIE), which relates the phase φ_z with the longitudinal intensity derivative $\delta I(\mathbf{r}_\perp)/\delta z$ [Tea83]. If the irradiance I_z is known by measurement, Eq. (1.46) becomes a two-dimensional Poisson equation, which can be solved to obtain the phase φ_z.

To solve Eq. (1.46), a connected bounded domain Ω (without holes) in the xy-plane with a boundary G is considered. If the intensity $I_z(x,y)$ is equal to zero at the boundary and outside W, Eq. (1.46) has a unique solution up to an arbitrary additive constant [Gur95]. For the following solution a rectangular region Ω_{ab} is considered, with an edge length of a in the x- and an edge length of b in the y-direction. On this region the Fourier harmonics W_{mn} and the standard scalar product <f,g> are defined as

$$W_{mn}(x,y) = \exp\left(i2\pi\frac{mx}{a}\right)\exp\left(i2\pi\frac{ny}{b}\right) \tag{1.47}$$

and

$$\langle f,g\rangle = \frac{1}{ab}\int_0^b\int_a^b f(x,y)g^*(x,y)dxdy \, . \tag{1.48}$$

The longitudinal intensity derivative can be approximated by a finite Fourier series

$$\frac{2\pi}{\lambda}\frac{\partial}{\partial z}I_z = \sum_{m,n} F_{mn}W_{mn} \, , \tag{1.49}$$

with $|m| \le M$ and $|n| \le N$.

The aim is to find a phase of similar form

$$\varphi = \sum_{m,n} F_{mn} W_{mn} \tag{1.50}$$

Taking the scalar product of Eq. (1.46) and a Fourier harmonic W_{pq}, and integrating by parts delivers

$$< I\nabla\varphi, \nabla W_{pq} >= F_{pq} \tag{1.51}$$

Substituting Eq. (1.50) in Eq. (1.51) delivers a system of algebraic equations for the unknown Fourier coefficients of the phase φ_{mn}:

$$\sum_{m,n} L_{pq}^{mn} \varphi_{mn} = abF_{pq} \tag{1.52}$$

with $$L_{pq}^{mn} = (2\pi)^2 \left(\frac{mpb}{a} + \frac{nqa}{b} \right) I_{(p-m)(q-n)} \tag{1.53}$$

where $I_{mn} = <I,W_{mn}>$ are the Fourier coefficients of the intensity distribution $I_z(x,y)$.
For the special case of a uniform illumination I_0=const. inside Ω_{ab} and I_0=0 outside Ω_{ab} and at the boundary Γ_{ab}, I_{mn} is only nonzero when p=m and q=n [Gur96] so that the Fourier coefficients of the phase reduce to

$$\varphi_{mn} = \frac{(ab)^2}{(2\pi)^2 (m^2 b^2 + n^2 a^2)} F_{mn} \tag{1.54}$$

To calculate the phase from the longitudinal derivative in this case, it is sufficient to perform the Fourier transform of kdI/dz, reweight its Fourier coefficients F_{mn} according to Eq. (1.54) and finally perform an inverse Fourier transform. This special case of uniform illumination is in practice approximately fulfilled for so called phase objects and very thin samples with negligible attenuation of the beam.

1.3 Edge detection

The detection of edges from gray-level images is one of the most intensively studied problems in digital image processing. A large number of different approaches have been developed to detect edges in images. The earliest schemes focused on the detection of points at which the gradient magnitude is high. For this cause, the images are convolved with certain operators such as Robert's cross operator [Rob65], the Sobel operator [Pin69] and the Prewitt operator [Pre70]. The Sobel operator represents a differentiation of the image in the x and y directions, whereas Robert's operator differentiates along the diagonal directions of the image. The corresponding Kernels are

Robert's operator:

$$\begin{pmatrix} -1 & 0 \\ 0 & 1 \end{pmatrix} \text{ and } \begin{pmatrix} 0 & -1 \\ 1 & 0 \end{pmatrix}$$

Sobel Operator:

$$\begin{pmatrix} -1 & 0 & 1 \\ -2 & 0 & 2 \\ -1 & 0 & 1 \end{pmatrix} \text{ and } \begin{pmatrix} -1 & 0 & 1 \\ -2 & 0 & 2 \\ -1 & 0 & 1 \end{pmatrix}$$

The Prewitt operator is also often called "compass operator" as it consists of eight kernels corresponding the eight direction of the compass. The kernels are therefore often named after these directions:
Prewitt Operator:

$$\begin{pmatrix} 1 & 1 & 1 \\ 0 & 0 & 0 \\ -1 & -1 & -1 \end{pmatrix}, \begin{pmatrix} 0 & 1 & 1 \\ -1 & 0 & 1 \\ -1 & -1 & 0 \end{pmatrix}, \begin{pmatrix} -1 & 0 & 1 \\ -1 & 0 & 1 \\ -1 & 0 & 1 \end{pmatrix}, \begin{pmatrix} -1 & -1 & 0 \\ -1 & 0 & 1 \\ 0 & 1 & 1 \end{pmatrix}, \text{ and so on...}$$

(N-filter) (NO-filter) (O-filter) (SO-filter)

In the same way as the first derivative is approximated by differences in these operators also the second derivative can be approximated by a Laplacian operator. By using the Laplacian, the position of an edge is no longer characterized by the maximal value of the first derivative, but by the zero crossing of the second derivative.

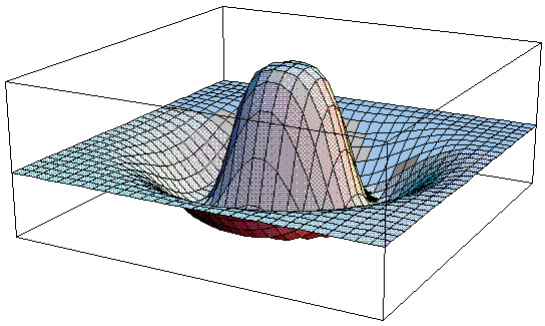

Fig. 1.11: Because of its shape, the LoG-Filter is also called Mexican-Hat-Filter.

A primary problem in edge detection is image noise as it represents sharp changes in the gray values of pixels, which is the typical indication for an edge. In 1980, Torre and Poggio motivated the need for linear filtering as a pre-processing step to differentiation [Tor80]. The Laplacian operator is because of the two differentiations especially sensitive to noise. The Marr-Hildreth operator [Mar80], also called Laplacian-of-Gaussian-Filter (LoG-Filter) or Mexican-Hat-Filter (Fig. 4.3), uses a Gaussian kernel to smoothen the image in combination with the Laplacian to detect the edges.

John F. Canny considered the problem of determining an optimal smoothing filter of finite support for detecting step edges in 1986. He showed that the resulting smoothing filter could be well approximated by the first-order derivative of a Gaussian kernel [Can86]. Deriche extended this approach to filters with infinite support, and proposed a computationally efficient implementation using recursive filters [Der87]. Canny also introduced in [Can86] the

notions of non-maximum suppression, edge following and hysteresis thresholding. Edge following identifies an edge as a connected chain of extrema. Non-maximum suppression describes the need to filter out local extrema that do not lie on an edge. For this cause, line profiles perpendicular to an edge are analyzed and side maxima are suppressed. Hysteresis thresholding reduces the number of detected edges by applying thresholds. The thresholds lead to broken edge curves. Hysteresis is a trick to “heal” these broken edge curves by using two thresholds. The larger threshold is used when starting an edge chain and the smaller while following it.

Hence, a typical procedure for the detection of edges in digital images consists of three steps:

1. Noise reduction and smoothing of the image.
2. Detection of sharp intensity variations in the image.
3. Non-maximum suppression, edge following and hysteresis thresholding

The choice of the algorithm for each step depends very much on the type of image, the structures on it and the image noise.

1.4 Tomographic reconstruction

In radiography, only the two-dimensional projection of a sample is recorded. To get more information about the three-dimensional inner structure of an object, multiple radiographs under different viewing angles have to be measured. In 1917, Radon showed theoretically how it is possible to reconstruct a three-dimensional structure from its projections [Rad17]. For such a tomographic measurement procedure, several projections of the sample under different viewing angles have to be recorded without changing any other parameter but the viewing angle. In neutron imaging this is possible by using a CCD detector system at a fixed position in the detector plane and by rotating the sample on a turntable, of which the rotational axis lies perpendicular to the beam direction, in the neutron beam (see Fig. 2.1).

For a successful tomographic reconstruction, the used type of radiation should be able to penetrate the sample under every measured viewing angle. If the recorded intensity in one or more projections drops below the background noise, artifacts will occur in the reconstructed data (this problem can be circumvented by applying discrete tomography methods as discussed in [Kub99]). For this reason, neutrons, which have for a lot of materials much higher penetration depths than X-rays, are for many thicker objects the only type of radiation that can be used for tomographic measurements. Another good characteristic of neutron beams is that they can be considered as being parallel for tomography. Thanks to this parallel beam geometry, it is not necessary to reconstruct the whole object in one step. Slices perpendicular to the rotational axis can be treated independently.

After the tomographic reconstruction, the investigated object is divided into cubic subvolumes, which can be visualized as volumetric pixels, so called voxels, with a certain gray value on a computer. The edge length of a voxel equals the size of a pixel in one of the radiographs (see 1.1.1).

In conventional neutron tomography as described in section 1.1.1, the attenuation of the neutron beam on different paths through the object is measured in the radiographs. Each radiograph corresponds to a projection of the 3D distribution of the attenuation coefficient $\mu(x,y,z)$ in the object. By performing a tomographic reconstruction with this data, it is possible to calculate the average attenuation of the neutron beam in every single one of those cubic subvolumes and to display the three dimensional distribution of the attenuation by voxels with different gray values.

As described earlier in this chapter, the complex refractive index of a material not only leads to attenuation, but also causes a phase shift of the penetrating matter waves. In section 1.2 different methods were described how this shifting of the phase by an object can be measured. All of the presented methods allow the recording of a 2D distribution of the phase, which corresponds to a projection $\varphi_\omega(x,y)$ of the 3D distribution of the real part of the refractive index n(x,y,z). These projections can be used for a tomographic reconstruction of the 3D distribution of $\delta(x,y,z) = 1 - n(x,y,z)$. This process is described now briefly (for more detailed information see [Her80]).
The measured quantity in one radiograph is the phase modulation

$$\varphi_\omega(x,y) = \int \delta(x_0, y, z_0)\,dz\,, \tag{1.55}$$

where $\delta(x_0,y,z_0)$ is the deviation from unity of the real part of the refractive index and x_0,y,z_0 are the coordinates attached to the rotating object (with the y-axis as the rotational axis).
A conversion of x_0 and z_0 in the fixed coordinate system of the lab yields

$$\varphi_\omega(x,y) = \int \delta(x\cos\omega - z\sin\omega, y, x\sin\omega + z\cos\omega)dz \qquad (1.56)$$

As mentioned above, for parallel beam geometry single slices perpendicular to the rotational axis can be considered and the problem is reduced to a two-dimensional one in the x-z-plane:

$$\varphi_\omega(x) = \int \delta(x\cos\omega - z\sin\omega, x\sin\omega + z\cos\omega)dz \qquad (1.57)$$

If the sampling rates in the x and ω dimension are sufficient, the analytical method of filtered backprojection can be used for the reconstruction of δ. The fundamental theorem behind this method is the Fourier-slice theorem [Her80], which links the Fourier transforms of the projections to the transform of the distribution. In practice, each value $\varphi_\omega(x)$ is distributed onto every point (x_0,z_0) in the sample that was projected onto the coordinate x on the detector and this is done for every projection angle ω.The result of this simple backprojection is just a very blurred version $\delta'(x_0,z_0)$ of the original distribution.

$$\delta'(x_0,y_0) = \int_0^\pi \varphi_\omega(x = x_0\cos\omega + z_0\sin\omega)d\omega \qquad (1.58)$$

To correct this blurring the projection have to be filtered before backprojection (see [Sla] for a more detailed description of filtered backprojection). The simplest mathematical expression that describes a complete filtered backprojection is given by the inverse Radon transform:

$$\delta(x_0,y_0) = \mathrm{RADON}(\varphi_\omega(x)) = \int_0^\pi \Im^{-1}\{\,|f|\cdot\Im[\varphi_\omega(x)]\}d\omega \qquad (1.59)$$

In this function, the used filter is the simple absolute value function |f| in the frequency domain, which compensates the lower sampling rate far from the origin of the spectrum. The filter function is multiplied with the Fourier transformed of the measured projection $\varphi_\omega(x)$. This product is transformed back in real space with the inverse Fourier transform $\Im^{-1}$ and then projected back. In practice many more filters are used to improve the result [Schil99], [Kak99].

Chapter 2

2 Experimental setup at ANTARES

The successful neutron phase contrast measurements of Allman et al [All00] in 2000 motivated the group for neutron tomography at Garching to investigate this new technique further [Kar03]. As the FRM-I had already been shut down and the FRM-II had not yet been in operation, the first phase contrast experiments were carried out at PSI in Villigen, Switzerland. The good results of those experiments in Switzerland convinced Burkhard Schillinger, the responsible scientist for the design of the new beamline for neutron imaging at FRM-II to further investigate phase contrast imaging and to use this new technique at the emerging ANTARES (Advanced Neutron Tomography and Radiography Experimental System) beamline at FRM-II.
At that time the design of the shielding, the flight tube and many other components of the new beamline ANTARES was already finished and optimized for neutron radiography with an L/D ratio of 400 or 800 [Grü05]. The task was now to implement in the existing layout of the ANTARES beamline the necessary components for propagation-based neutron phase contrast imaging.

The ANTARES facility for neutron radiography and tomography is situated in the experimental hall and looks through the beam tube SR4B (Strahlrohr 4B) onto the cold source of FRM-II. This cold source is a small vessel within the moderator tank filled with liquid deuterium with a temperature of 25 K. The moderator tank itself is filled with heavy water (D_2O) at room temperature. The effect of the cold source is to further cool down the already thermalized neutrons in the moderator tank. The term “thermalized” means that the neutrons in the D_2O moderator are in thermal equilibrium with their environment and their spectrum is a Maxwell distribution with a maximum at $E=k_BT$, where E is the neutron energy, and T the temperature of the environment.
Because of the limited volume of the cold source, the neutrons that are scattered in SR4B are not fully thermalized and their spectrum differs from a Maxwell distribution. This has consequences for the design of the apertures in 2.1, the choice of the detector in 2.3 and will lead to the implementation of a multi filter system in 2.2. A detailed experimental investigation of the different components of the experimental setup is done in section 3.2.

2.1 Adjustment of the beam geometry

2.1.1 The basic conditions at SR4B

The ANTARES facility was designed for neutron radiography and tomography with an L/D ratio of 400 or 800. To be able to switch quickly between the two L/D ratios, two different apertures were installed in the secondary shutter (Fig. 2.1).

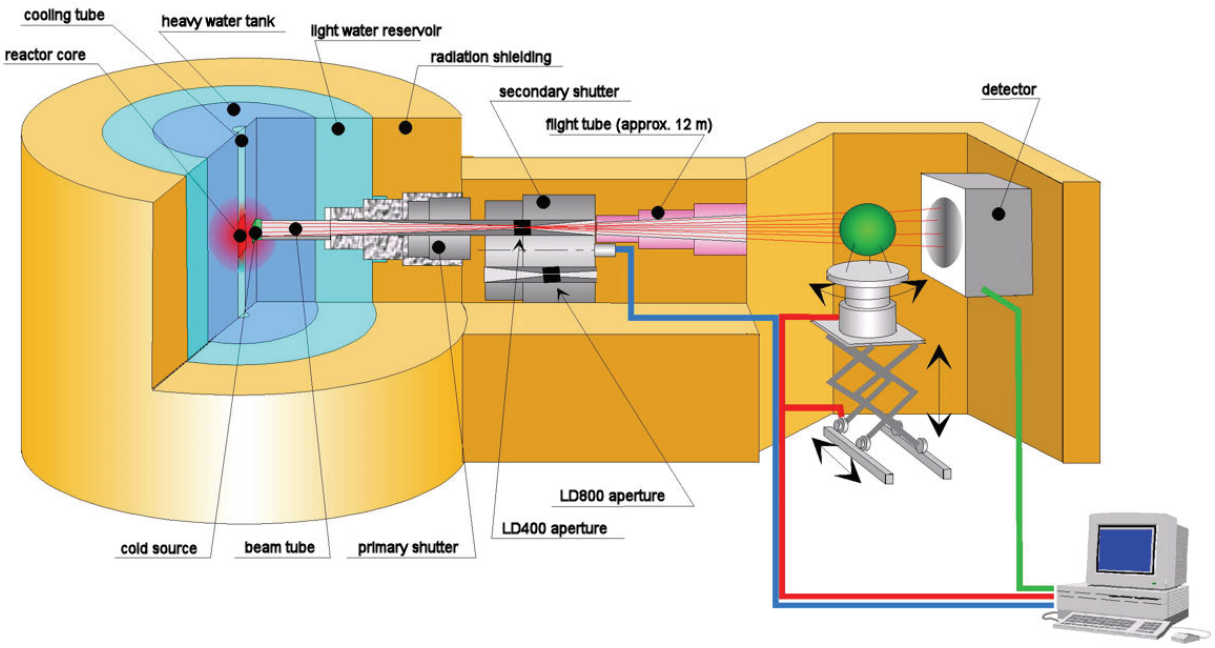

Fig. 2.1: Schematic of ANTARES

The entrance window of the beam tube SR4 next to the cold source has a surface of 18 cm x 12 cm (height x width). The channel in the biological shielding for SR4B has a diameter of 12 cm x 12 cm. The apertures were designed to use an area of 12 cm x 12 cm of the entrance window of the beam tube (the effective secondary neutron source for SR4B) to homogenously illuminate a region of at least 30 cm x 30 cm in the detector plane. The aperture for L/D=800 (LD800 aperture) was installed at a distance of 4.3 m from the cold source and has a diameter of 2.09 cm. The fully illuminated area in the detector plane with this aperture is 36.4 cm x 36.4 cm. The aperture for L/D=400 (LD400 aperture) was installed at a distance of 3.7 m (inside the biological shielding) and has a diameter of 4.33 cm. With this big aperture, the fully illuminated region in the detector plane is 31.5 cm x 31.5 cm.

An L/D ratio of 800 is still too small for phase contrast measurements. Using a beam with such a divergence and a sample-to-detector distance of 80 cm for instance (which is quite small for propagation-based phase contrast with neutrons), a point in the object is smeared out on a circle with a diameter of 1 mm in the detector plane (for a detailed explanation see Fig. 2.14 in subsection 2.1.2.2.1). For propagation-based phase contrast imaging, an additional aperture had to be installed to increase the transversal spatial coherence of the beam.

2.1.2 Implementation of an aperture changer at ANTARES

A suitable space for the additional aperture was right behind the secondary and the fast shutter at a distance of 560 cm from the cold source. At this position, there was enough space in the shielding of the beamline for a remotely controlled aperture changer (Fig. 2.2).

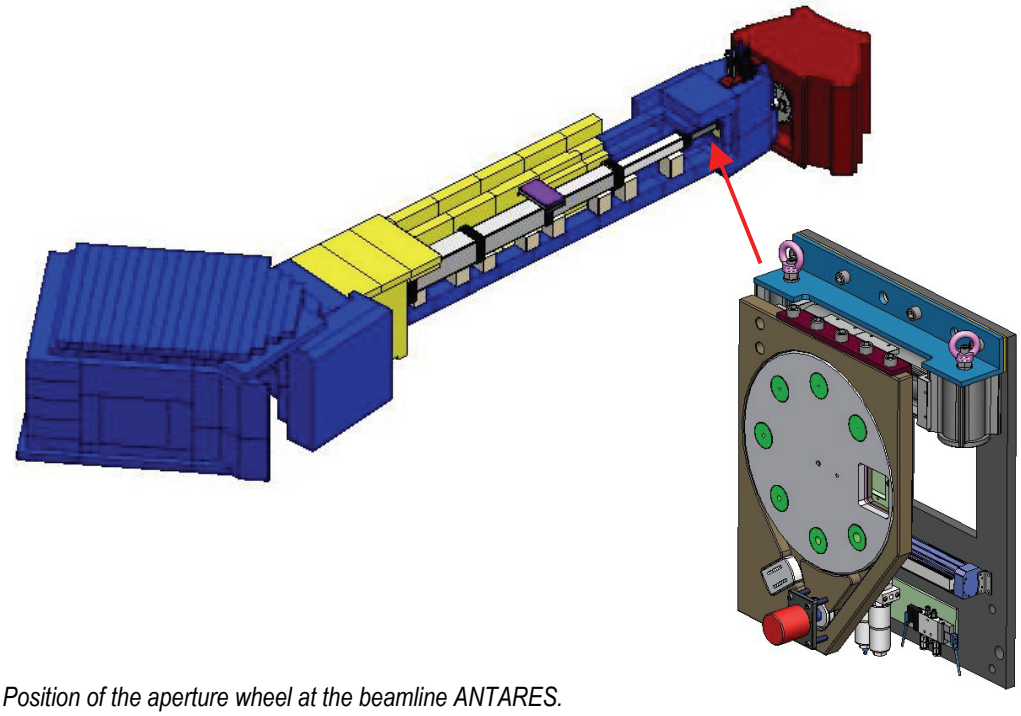

Fig. 2.2: Position of the aperture wheel at the beamline ANTARES.

For the following considerations on the beam geometry, a pinhole aperture with a negligible thickness is assumed at z_{ph} = 5,6 m. The sample position is about 14 meters away in the measurement chamber of ANTARES and the detector plane is at z_D = 21 m. As the following schematic (Fig. 2.3) illustrates, two different regions can be distinguished in the detector plane. The central region is homogeneously illuminated by the neutron beam (for infinitesimal thin aperture; see section 2.1.2.2.1 for thick aperture effects) and will be referred to as fully illuminated region from now on. The outer penumbra region in the detector plane is illuminated by a smaller source area.

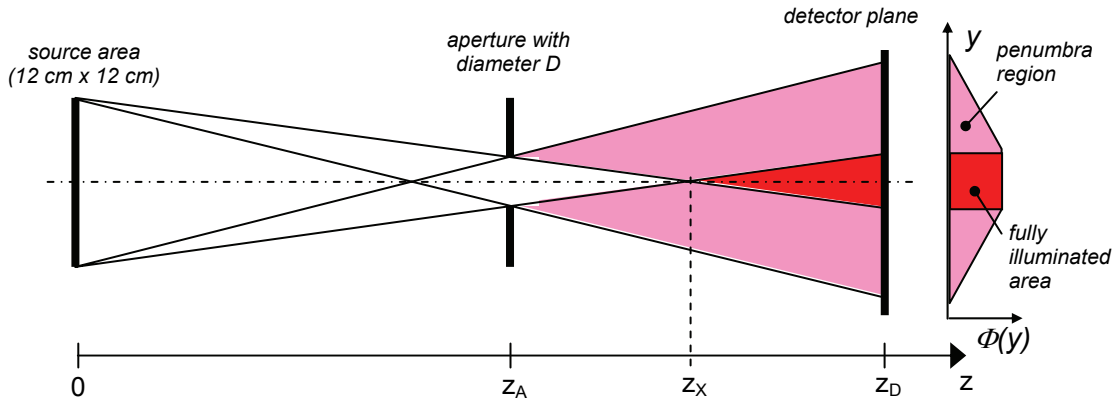

Fig. 2.3: Idealized beam geometry with only one big aperture in the beam. In the penumbra region the intensity of the neutron beam drops as the source area is only partially visible there.

A closer look at the beam geometry shows two different cases for the positioning of the pinhole on the beam axis. In the white area to the left of the cross-over point z_X, the whole

source area can be seen through the pinhole. In the red region to the right of z_X, a part of the source area is covered by the aperture in the secondary shutter. A calculation of z_X for the two installed apertures at ANTARES yields a value of 579 cm for the LD400 aperture and a value of 521 cm for the LD800 aperture. The aperture wheel at z = 560 cm is for one aperture behind the cross-over point z_X and for the other in front of this point. Schematics of the resulting two different beam geometries are shown in Fig. 2.4. Open beam measurements at ANTARES with the two different apertures are displayed in Fig. 2.5.

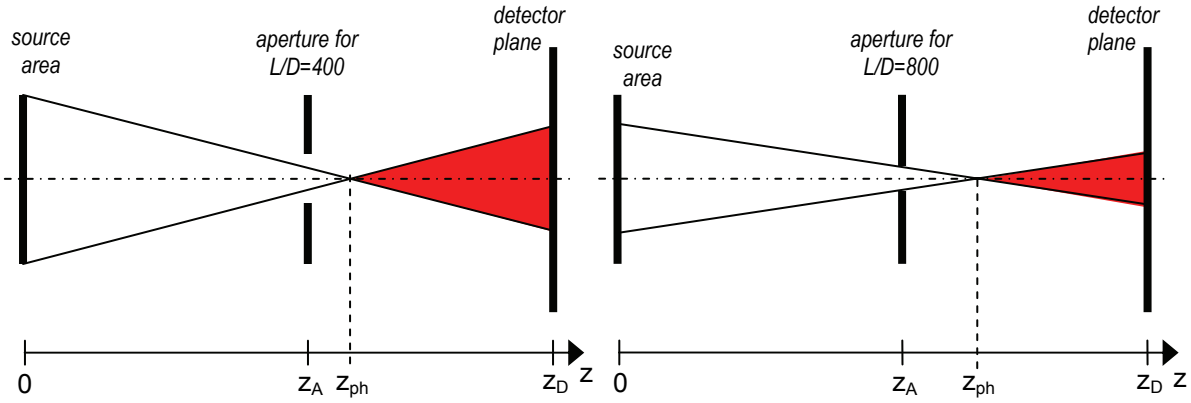

Fig. 2.4: Comparison of the beam geometries with a pinhole in combination with the LD400 (left image) and LD800 (right image) aperture. With the LD800 aperture, the source area is only partially used and the circular shape of the LD800 aperture borders the illuminated area in the detector plane.

If the pinhole is used in combination with the LD800 aperture (Fig. 2.4b, 2.5b), only the central region of the source area is mapped to the detector plane. In open beam pictures with this configuration, the circular shape of the LD800 collimator is clearly visible. The diameter d_{LD800} of this circular shape in the detector plane is

$$d_{LD800} = D_{LD800}*(z_D-z_{ph})/(z_{ph}-z_A) = 24.8 \text{ cm}.$$

The open beam picture shows a gray border around the circular, fully illuminated region. This is the penumbra region due to the non-zero diameter of the pinhole aperture. A pinhole with a diameter D_{ph} of 1 mm causes a penumbra border with the thickness

$$d_{penumbra} = D_{ph}*(z_D-z_{ph})/(z_{ph}-z_A) = 1.2 \text{ cm}.$$

In combination with the LD400 aperture (Fig. 2.4a, 2.5a), the whole source area is mapped to the detector plane and causes a homogenously illuminated, square region with an edge length l_{hom} = 12 cm * $(z_D-z_{ph})/z_{ph}$ = 33.0 cm.

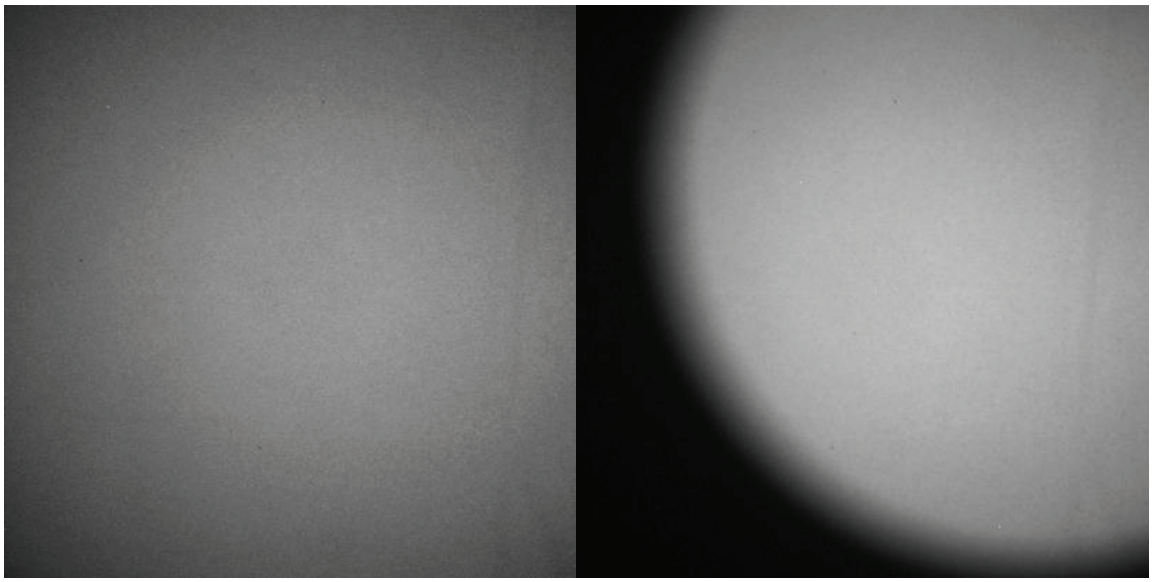

Fig. 2.5: Open beam measurement with the pinhole in combination with the LD400 (left) and LD800 (right) aperture (CCD; FOV = 20,3 cm).

2.1.2.1 The aperture wheel

The installation of the aperture wheel right behind the fast shutter inflicts three fundamental requirements on its design: The components must be very reliable (close to failsafe), they must not contain materials with a long half-life for neutron activation and the whole device must be remotely controlled.
The first and the last requirement arise from the difficult accessibility of this location. To be able to open the shielding of ANTARES at this position, the neighboring instrument NEPOMUC has to be shut down and partially disassembled and several blocks of heavy concrete with a weight of up to 10 t have to be moved by a crane. If this routine has to be performed when the neutron source is operational, a special permission by the radiation protection is required.
The second requirement arises from the high neutron flux at this position. The components of the aperture wheel must not be activated over certain limit values in order to uninstall the device for maintenance work or modifications. Therefore most parts were made of aluminum alloys and materials with a long half life like cobalt (which is contained in a lot of steel alloys) were avoided wherever possible.
Fig. 2.6 shows the aperture wheel before its installation at ANTARES. The finally installed device is displayed in Fig. 2.7 with the 320 keV X-ray tube in front of it.
The wheel with its eight different apertures is mounted on an aluminum base plate with a thickness of 4 cm. The positioning of the wheel is done with a stepping motor, which drives the wheel over a transmission belt. Eight aluminum blocks with notches between the apertures tell the control box the actual position of the wheel by pressing four micro switches. The uppermost switch detects whether an aperture is in the beam or not. The lower three switches tell the control box which aperture is in the beam (table 2.1).

Pin 1	Pin 2	Pin 3	Abbr.	aperture
0	0	0	b0	no aperture
1	0	0	b1	7 mm hole
0	1	0	b2	2 mm hole
1	1	0	b3	1 mm hole
0	0	1	b4	10 hole mask
1	0	1	b5	6 hole mask
0	1	1	b6	1 mm slit
1	1	1	b7	Cd-filter

Table 2.1: Coding of the aperture wheel.

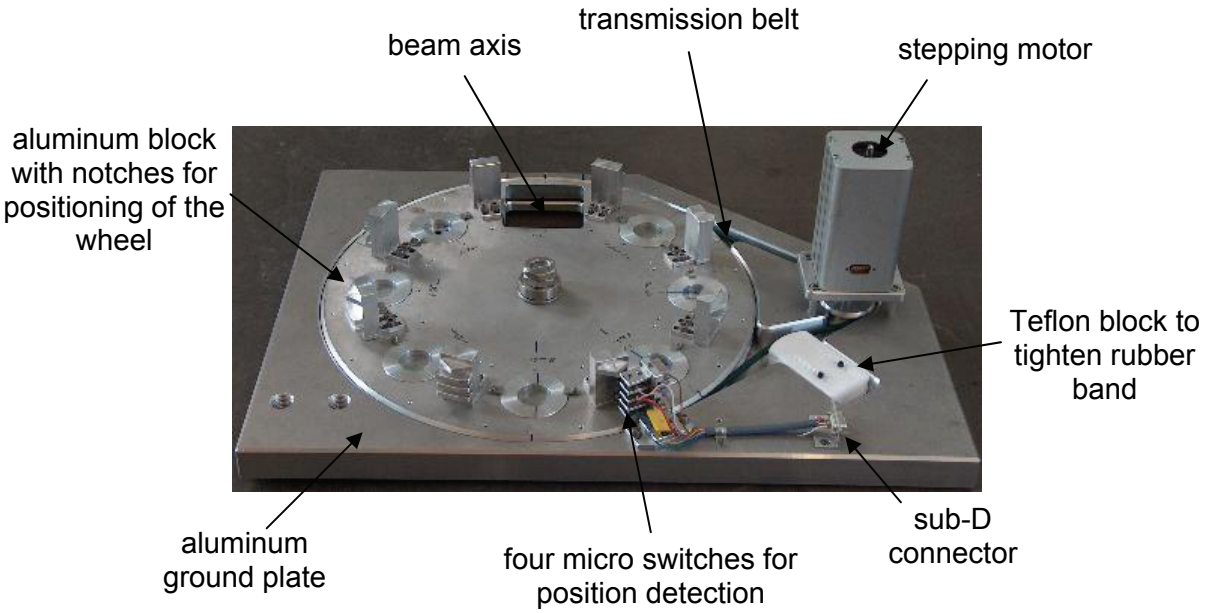

Fig. 2.6: Description of the components of the aperture wheel.

At the beam line the aperture wheel was mounted on the same base plate as the fast shutter, right behind the secondary shutter. Fig. 2.7 shows the limited space at this position. The blue wall at both sides and on top of the picture is the heavy concrete shielding of ANTARES. The direction of the neutron beam in this picture is top down. In the lower part of the picture, the 320 keV X-ray tube is visible. It is mounted on a guide rail and can be moved remotely controlled between two positions. In Fig. 2.7 the X-ray tube is on the right end of the guide rail and the neutron beam would go directly through the focal spot of the X-ray tube. An installed safety mechanism prevents the opening of the secondary shutter, if the X-ray tube is not out of the beam on the left end of the guide rail. The distance between the ground plate of the aperture wheel and the cooling pipes of the X-ray tube is only 20 cm and sets strict limits for the size of the aperture wheel in beam direction.

Fig. 2.7: The installed aperture wheel with the 320keV X-ray tube right downstream of it.

Another critical issue at the installation of the device was the precise adjustment of the aperture wheel. The sensitivity of the beam geometry with respect to the adjustment of a pinhole is illustrated in Fig. 2.8. The center of the pinhole and the LD800 aperture must sit perfectly on the beam axis in order to map the central region of the source onto the center region of the detector plane. A misalignment of the pinhole of 1 cm perpendicular to the beam direction causes a displacement of the used source area of 3.30 cm and a displacement of the image in the detector plane of 12.8 cm. If the used source area moves out of the 12 cm x 12 cm region described in section 2.1.1, the neutron beam becomes inhomogeneous. On the other end of the beam line, the entire cross section of the neutron beam has to hit the 40 cm x 40 cm wide window of the measurement chamber.

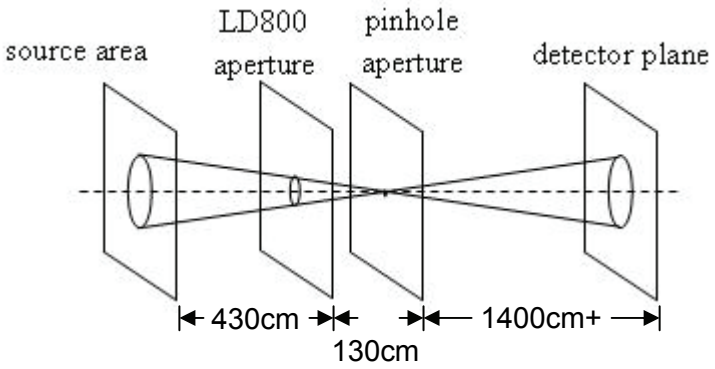

Fig. 2.8: Sensitivity of the beam geometry on misalignments of the aperture wheel.

2.1.2.2 The apertures

The aperture wheel works like a revolving cylinder and places eight different apertures into the neutron beam. One of them (b0) is a square shaped window which does not influence the beam at all. The other seven slots are loaded with different apertures. In the first version of the aperture wheel (see Fig. 2.6), these apertures where made from pure cadmium. In a 1 mm thick cadmium sheet, the actual pattern of the aperture was drilled. In another 1 mm thick foil the same pattern was drilled with a little bit bigger holes. The two sheets where glued together and formed a 2 mm thick cadmium aperture. In one slot (b7) a 2 mm thick cadmium sheet without holes was installed to serve as a filter that is only penetrable for epithermal and faster neutrons (E > 0.4 eV). The apertures in the remaining six slots (b1-b6) and their functions are described in the following subsections.
This first version of the apertures had two major shortcomings:

1. epithermal neutrons are able to penetrate the cadmium easily and contribute to background noise
2. high neutron flux on cadmium generates a lot of high energy gamma radiation (1.2 MeV)

The solution for both problems was the replacement of the simple cadmium apertures by composite apertures. Fig. 2.9 shows the sandwich structure of the new apertures. The neutron beam hits first a 5 mm thick layer of boron epoxy. The secondary gammas produced by the irradiation of boron have low energies compared to cadmium and gadolinium and are easily stopped by the shielding of the beam line.

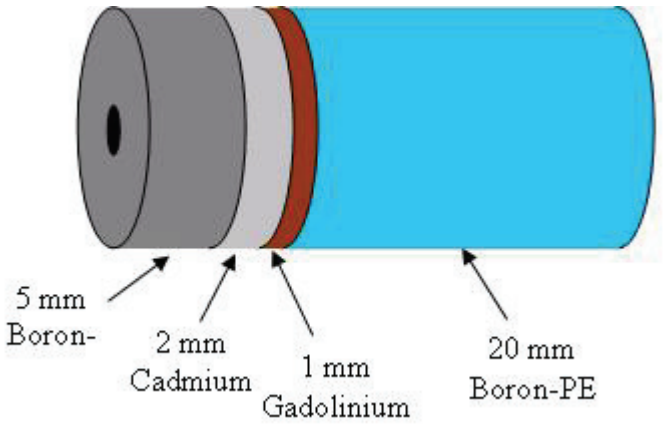

Fig. 2.9: Sandwich structure of the improved composite apertures.

The second layer is the old 2 mm thick cadmium aperture with the difference that the size of the holes in both sheets is now the same. The size of the holes is slightly bigger than in the

following gadolinium layer which contains the actual apertures. The cadmium layer serves now as a pre-collimator for the gadolinium aperture. The last layer is a 20 mm thick block of boronized polyethylene. With the intention not to waste anything of the remaining free space between aperture wheel and the X-ray tube, another 50 mm thick brick of boronized polyethylene was attached to the sandwich (see Fig. 2.10). But the effect of these polyethylene bricks was negligible (see sect. 3.2.2) and the additional weight was only causing mechanical problems, so they where removed again.
With these composite apertures the gamma and neutron dose on top and on the side of the shielding where the same as without an aperture and the noise due to epithermal neutrons was drastically reduced.

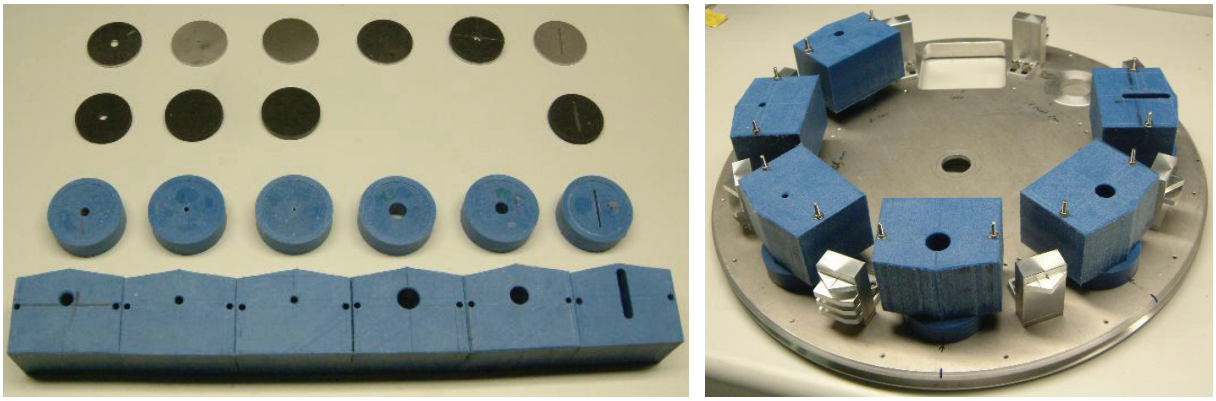

Fig. 2.10: The layers of the composite apertures and the fully equipped aperture wheel

The increased thickness of the new composite apertures caused a new problem concerning the beam geometry. For long pinholes, the homogeneously illuminated area in the detector plane is reduced to the diameter of the pinhole (Fig. 2.11). For very long pinholes it is even possible that the outer region of the detector is not illuminated at all anymore. This happens if the position of the cross-over point z_X (see Fig. 2.3) is in the first half of the pinhole. In case of the 1 mm pinhole b3 this happens if its length exceeds a value of 13 mm. But already at shorter lengths, a reduction of the neutron flux outside the 1 mm circle in the middle of the detector plane would occur. This was the reason to take gadolinium, the metal with the highest attenuation coefficient available, to make the aperture masks as thin as possible.

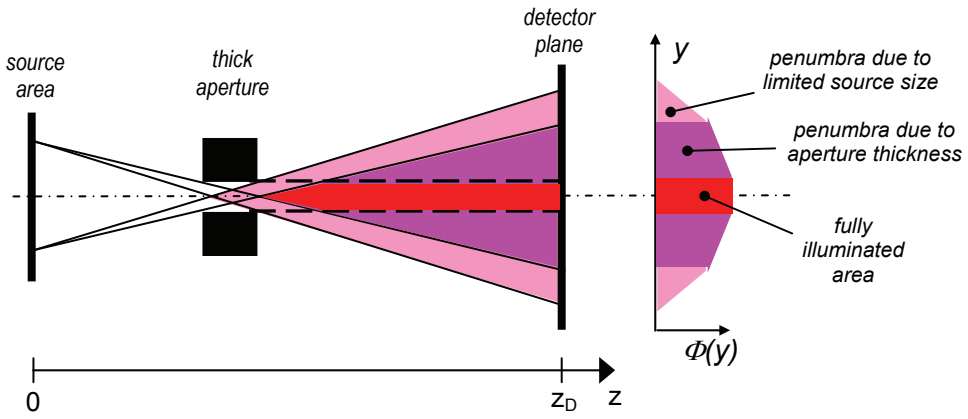

Fig. 2.11: Inhomogeneities in the detector plane caused by long apertures.

2.1.2.2.1 Single hole apertures

The aperture wheel contains three different pinhole apertures with diameters of 1 mm, 2 mm and 7 mm and one slit aperture with a 2.5 cm long and 1 mm wide slit. The function of these apertures is to create a neutron beam with a high transversal coherence at the sample position. A measure of the transversal coherence of the beam is the L/D ratio, where L is the distance between aperture and sample and D the diameter of the pinhole. As the neutron flux is proportional to $(D/L)^2$, an enhancement of the transversal coherence by pinhole apertures always causes a reduction of the neutron flux (table 2.2). Two possibilities to circumvent this problem are the utilization of coded apertures or neutron lenses, which are described in section 2.1.2.2.2 and 2.1.3. If a high transversal coherence is only needed in one dimension, the neutron flux can be increased by using a slit aperture instead of a pinhole. At first a slit was installed in slot b6 horizontally, but later it was rotated by 90 degree for the utilization as a source for the shearing interferometer of Christian David's group from PSI. With the now installed slit the L/D ratio is horizontally 14000 and vertically 400 or 800, depending on the aperture in the secondary shutter.
The required transversal coherence for a neutron radiography depends on the desired spatial resolution for a given sample-to-detector distance. For long sample-to-detector distances as they are common in propagation-based phase contrast imaging, high L/D ratios are needed to avoid too much blurring. The reason for this blurring is the non-zero diameter of the aperture, which is the effective source for the radiography setup. Due to this expanded area of the source, a single point in the sample is mapped to a certain area in the detector plane (for circular apertures; see Fig. 2.12).

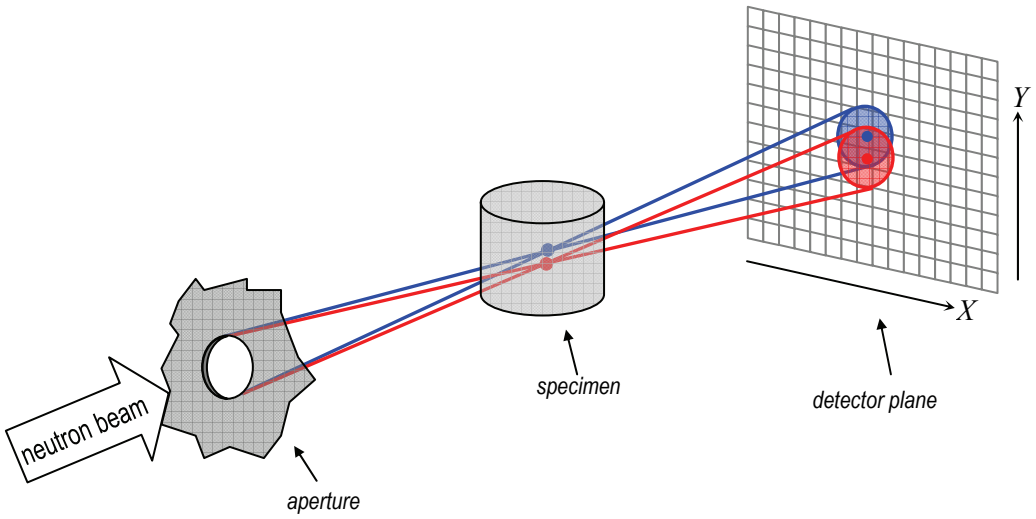

Fig. 2.12: Blurring of the image due to extended source size.

How one point is mapped exactly to the detector plane is described by the point spread function (*PSF*). With the PSF it is possible to calculate the intensity distribution $I_{blurred}$ of an image in the detector plane for a known 'ideal' image I_{ideal}, obtained with a point source. The blurred image is the folding of I_{ideal} with the PSF [Ros82]:

$$I_{blurred}(X,Y) = I_{ideal} \otimes PSF = \int_{-\infty}^{\infty}\int_{-\infty}^{\infty} I_{ideal}(x,y)\cdot PSF(X+x,Y+y)dxdy \qquad (2.1)$$

Equation 2.1 implies a shift invariant PSF. This is in good approximation fulfilled in the fully illuminated area. For a perfectly opaque circular pinhole aperture, the PSF is mathematically a pill-box function taking the value 1 in a circular area around the origin and the value 0 elsewhere. With the 1 mm pinhole and a sample-to-detector distance of 140 cm for example, a point in the sample is mapped on a circle in the detector plane with a diameter of 100 μm.

Besides the blurring of the image due to the beam geometry, the detector system also degrades the spatial resolution of the image. To keep exposure times reasonable in phase contrast imaging, the diameter of the pinhole and the sample-to-detector distance is chosen in such a way that the blurring due to geometry effects is similar to the blurring due to the detector system. A more detailed description of the image formation and a definition of spatial resolution are given in section 2.3.

Aperture	Diameter	L/D ratio	hole area	neutron flux at sample position	homog. illuminated area at sample position
b1	7 mm	2000	38.48 mm^2	$4.5x10^6$ $cm^{-2}s^{-1}$	27.6cm x 27.6cm
b2	2 mm	7000	3.14 mm^2	$3.7x10^5$ $cm^{-2}s^{-1}$	29.3cm x 29.3cm
b3	1 mm	14000	0.79 mm^2	$9.2x10^4$ $cm^{-2}s^{-1}$	29.7cm x 29.7cm
b4	10 x 0.8mm	20000	5.03 mm^2	$5.9x10^5$ $cm^{-2}s^{-1}$	19.5cm (see Fig. 2.16)
b5	6 x 1.2mm	11667	6.79 mm^2	$7.9x10^5$ $cm^{-2}s^{-1}$	21,1cm (see Fig. 2.16)
b6	1 mm slit	14000	25 mm^2	$2.9x10^6$ $cm^{-2}s^{-1}$	29.7cm x 31.5cm

Table 2.2: Comparison of the beam parameters with different pinhole apertures and the slit aperture in combination with the LD400 aperture in the secondary shutter.

2.1.2.2.2 Coded apertures

Compared to single hole apertures, apertures with multiple holes with the same diameter have two benefits:

1. Enhanced neutron flux at the sample position
2. Improved ratio of useful neutrons to background radiation

The first benefit is obvious, because n holes mean n times the area of only one hole and deliver n times the neutron flux. The second benefit arises because the composite apertures can still be penetrated by gamma radiation and epithermal neutrons (see section 3.2.1).
When a multiple hole aperture is used, the measured image is blurred without further image processing. The n holes in the aperture behave like n sources and create n overlapping images in the detector plane. Mathematically, the blurred image can be calculated again as a convolution of the ideal image with a special PSF that is defined by the coded aperture (Eq. 2.1). The ideal image can be reconstructed by inverse filtering:

$$I_{ideal} = \Im^{-1}\left\{\frac{\Im(I_{blurred})}{\Im(PSF)}\right\} = \Im^{-1}\left\{\frac{\Im(I_{blurred})}{MTF}\right\}, \tag{2.2}$$

where $\Im$ denotes the Fourier transform

$$\Im I(u,v) = \int_{-\infty}^{\infty}\int_{-\infty}^{\infty} I(x,y)e^{-i\cdot 2\pi(ux+vy)}dxdy\,, \tag{2.3}$$

$\Im^{-1}$ the Fourier back transform

$$\Im^{-1}\{\Im I(u,v)\} = \int_{-\infty}^{\infty}\int_{-\infty}^{\infty} \Im I(u,v)e^{i\cdot 2\pi(ux+vy)}dudv = I(x,y)\,, \tag{2.4}$$

and MTF the modular transfer function

$$MTF = \Im(PSF)\,. \tag{2.5}$$

The inverse filtering yields a very noisy image because the noise in the blurred image gets amplified by for near zero denominators. A method to avoid this problem is the addition of a real constant c in the denominator, which dominates the denominator at frequencies where the MTF becomes close to zero:

$$I_{wiener} = \Im^{-1}\left\{\frac{\Im\{I_{blurred}\}}{\Im\{PSF\}} \cdot \frac{MTF^2}{MTF^2 + c}\right\} \tag{2.6}$$

This improved version of the simple inverse filter is called wiener filter [Wie49] and is used nowadays as a standard routine in image processing.
When a coded aperture is used however, a very elegant alternative to the Wiener filter can be used to reconstruct the ideal image. Coded apertures create a PSF for which a certain decoding pattern DP exists [Ski84] with

$$PSF \otimes DP \approx \delta\,. \tag{2.7}$$

This means that the cross correlation of the PSF with the DP must be a good approximation of the delta function [Wou73]. The projected image in the detector plane $I_{blurred}$ is the correlation of the ideal image I_{ideal} with the PSF:

$$I_{blurred} = I_{ideal} \otimes PSF \tag{2.8}$$

If a decoding pattern exists that fulfills condition (2.7), equation (2.8) can be transformed to

$$I_{blurred} \otimes DP \approx I_{ideal}\,. \tag{2.9}$$

The ideal image can be reconstructed without the need for deconvolution routines with divisions like in inverse filtering, where near zero denominators lead to uncontrollable amplification of noise. With coded masks the image can be reconstructed by a simple cross correlation of the blurred image with the decoding pattern, without the need for divisions.
A lot of applications of coded masks can be found in X-ray and gamma-ray astronomy, where for example Fresnel zone plates [Mer61], random arrays or uniformly redundant arrays (URA) [Fen73] were used as mask patterns. At FRM-II numerous Monte Carlo simulations with MCNP were done with the different types of coded apertures [Grü05]. For neutron phase contrast imaging, non redundant arrays (NRA) [Wou73] were found to be the best pattern for coded apertures. The main advantages of NRA masks are:

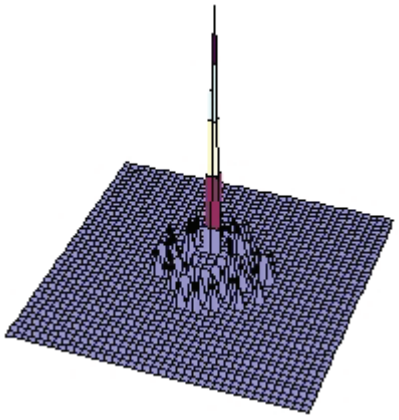

Fig. 2.13: The autocorrelation function for the installed 10-hole NRA coded aperture has almost the shape of a delta function.

- The mesh size of the NRA mask does not have to be adjusted exactly on the pixel mesh of the detector system like for URA or random array masks. Like this the distances between mask, sample and detector can be chosen freely.
- Random arrays are not suitable because they fulfill Eq. (2.7) only for an infinite pattern size. The diameter of the neutron beam is at the aperture position very limited and thus the correlation of the PSF with the DP would depart greatly from a delta function.
- In URA masks a periodic correlation is used for reconstruction. Hence only structures of the dimension of the basic mask pattern can be reconstructed.

The fundamental characteristic of a NRA mask is that if all connections between two holes in the aperture are expressed as vectors, no identical vectors exist. The autocorrelation function of a NRA has a strong central peak and minimal side lopes (Fig. 2.13). Like this, the pattern itself can be used for the decoding. Two NRA masks were installed in the aperture wheel, a 6-hole aperture in slot b4 and a 10-hole aperture in slot b5. The diameter of one hole is 1.2 mm in the 6-hole aperture and 0.8 mm in the 10-hole aperture. The patterns, pictures of the finally installed cadmium apertures and a calculation of the homogeneous illuminated area for each mask are displayed in Fig. 2.14.

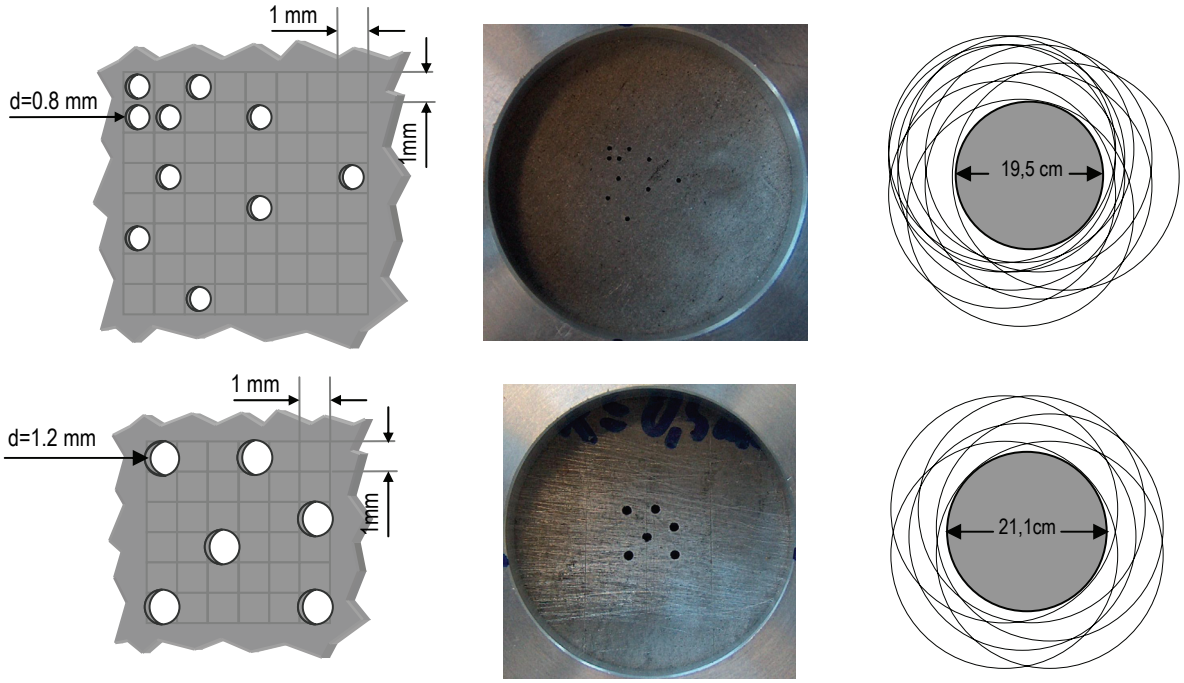

Fig. 2.14: Patterns (left) and pictures (middle) of the installed 10-hole (top) and 6-hole (bottom) coded apertures. On the right hand side, the homogeneously illuminated area in the sample plane was simulated (true to scale 10:1).

2.1.2.2.3 Cadmium filter

In slot b7 of the aperture wheel a plain 2 mm thick cadmium sheet was inserted. Cadmium strongly attenuates cold and thermal neutrons but is very transparent for epithermal and high energy neutrons. The total neutron cross section of cadmium drops by three orders of magnitude in the energy range between 0.2 eV and 2 eV.
In the introduction of chapter 2 it was already mentioned that the limited volume of the cold source causes the energy spectrum of the neutron beam at ANTARES to differ from a Maxwellian distribution and leads to an enhancement in the high energetic tail. A good measure for the ratio of high energy neutrons in the beam is the cadmium ratio. This value is determined by measuring the neutron flux with and without a cadmium filter in the beam. At ANTARES the measurements were done with gold foils and showed a Cd ratio (neutron flux without Cd filter divided by the flux with filter) of 12.8 ± 32% [Grü05].
The low value denotes a high ratio of epithermal neutrons in the beam and suggests the application of a cadmium filter. This filter has two positive effects for neutron radiography:

+ with epithermal neutrons it is possible to penetrate thicker samples
+ by filtering out the lower energetic neutrons, activation of the sample is reduced

Beside those benefits it also brings some disadvantages with it:

- the greatly reduced flux causes long exposure times, which is made even worse by the reduced sensitivity of neutron detectors for epithermal neutrons
- the attenuation coefficients of materials for epithermal neutrons are less varying which leads to smaller contrasts in the radiographs.

2.1.3 Application of neutron optical devices

Besides coded apertures there is another way to increase the neutron flux and maintain the high transverse coherence. The basic idea is not to throw away 99% of the neutron beam by blocking it with a pinhole aperture, but to feed the neutron beam in the pinhole with neutron lenses or mirrors as described in Fig. 2.15.

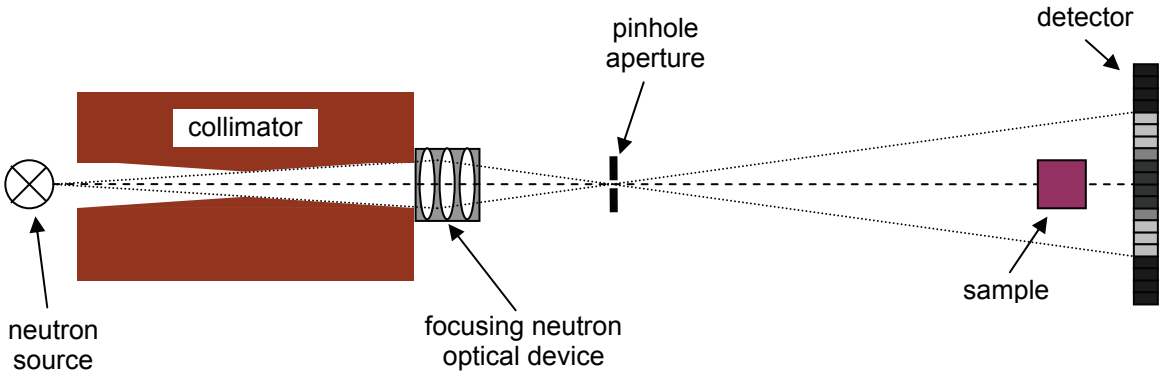

Fig. 2.15: Application of neutron optical devices to increase neutron flux in phase contrast imaging. As the proceeding section will demonstrate, neutron lenses cannot be used in this way.

Just like for synchrotron radiation the refractive index of materials for neutrons is very close to 1. This has the effect that the focal length f of a single lens is very long and that lens systems of up to some hundreds of lenses have to be used to achieve a focal length in the order of several meters. A compound refractive lens, containing N spherical lenses with a radius R and a refractive index $n = 1 + \delta$ has the total focal length

$$f = \frac{R}{2N\delta} \qquad (2.10)$$

Introducing a stack of several hundred lenses in a neutron beam goes along with a severe reduction of the neutron flux because of the additional material that has to be penetrated by the neutron beam. Hence the lens material has to fulfill two basic requirements:

- small linear attenuation coefficient
- big value for the decrement from unity δ of the real part of the refractive index

An element that satisfies these requirements very well is aluminum. For 25 meV neutrons its linear attenuation coefficient is 0.10 cm^{-1} and its δ-value is 2.14×10^{-6}. A compound lens made out of 400 aluminum lenses with a radius of 10 mm would have a focal length of 5.8 m. The attenuation caused by this compound lens however would reduce the neutron flux through the pinhole aperture to zero. A reduction of the radius of the lenses reduces the diameter of the used incoming neutron beam too much and a reduction of the lens number leads to too big focal lengths and thus too small beam diameters at the sample position. Therefore neutron lenses are not applicable in this manner and focusing lenses should be used instead. Diverging neutron lenses however can be used to increase the magnification factor in neutron imaging with large sample-to-detector distances. For this cause a compound lens made out of convex neutron lenses is positioned right behind the sample as displayed in Fig.

2.16. Like this a small area in the sample plane can be mapped magnified on the detector plane. The interest to circumvent limitations in spatial resolution will become clearer after the description of the neutron detection processes in section 2.3. In section 3.2.3 the application of magnification in neutron imaging will be demonstrated in measurements.

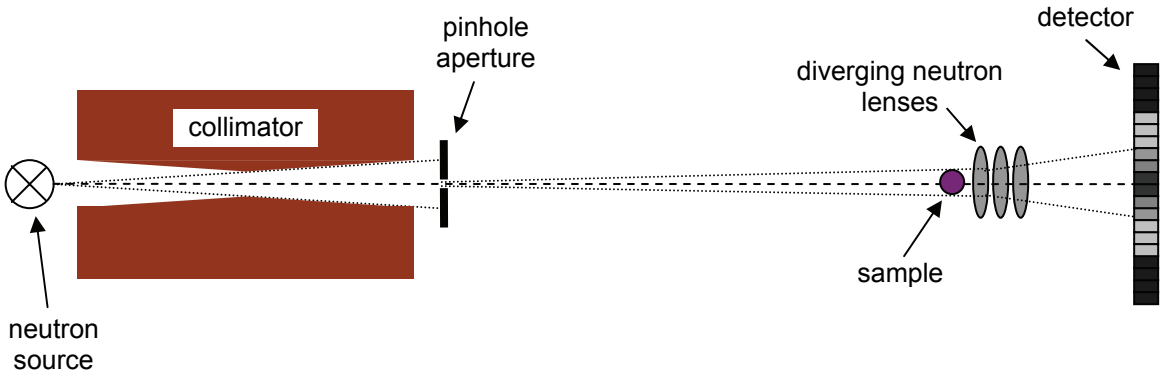

Fig. 2.16: Improvement of the spatial resolution by application of a diverging neutron lenses downstream the sample.

2.2 Modification of the neutron spectrum with filters

The possibility to manipulate the spectrum of the neutron beam by the introduction of a cadmium filter was already described in the preceding section. For phase contrast imaging unfortunately, the cadmium filter turns things for the worse as it is opaque to the useful cold neutrons and quite transparent for epithermal neutrons. There are other filter materials, however, which can improve the conditions for phase contrast imaging.

2.2.1 Implementation of a multi filter at ANTARES

The most simple way to install crystal filters at ANTARES would have been to place them in the entrance window of the measurement chamber, right behind the beam limiter. This location is well accessible and there is a lot of space for the mounting of the filters. Actually it would have been possible to change filters manually. But this position has some disadvantages

1. Activation of the filters leads to an increase of the gamma background in the measurement chamber
2. Additionally scattered neutrons cause background noise
3. Big beam diameter requires big filters
4. Inhomogeneities in the filter destroy the coherence of the neutron beam

To solve all four problems, the perfect location for crystal filters would be in front of the aperture wheel. A short look at Fig. 2.2 and 2.7 shows that there is only very few free space left between the fast shutter and the aperture wheel. The solution to overcome the problem of limited space is shown in Fig. 2.17. Four different filters are mounted in a 5 cm high cylinder of boronized polyethylene with a diameter of 30 cm. This filter wheel as a whole can be moved in and out of the beam by a pneumatic translation stage. Besides the filter wheel, a 10 mm lead plate was mounted on a separate translation stage to be able to use the lead in combination with sapphire or beryllium.

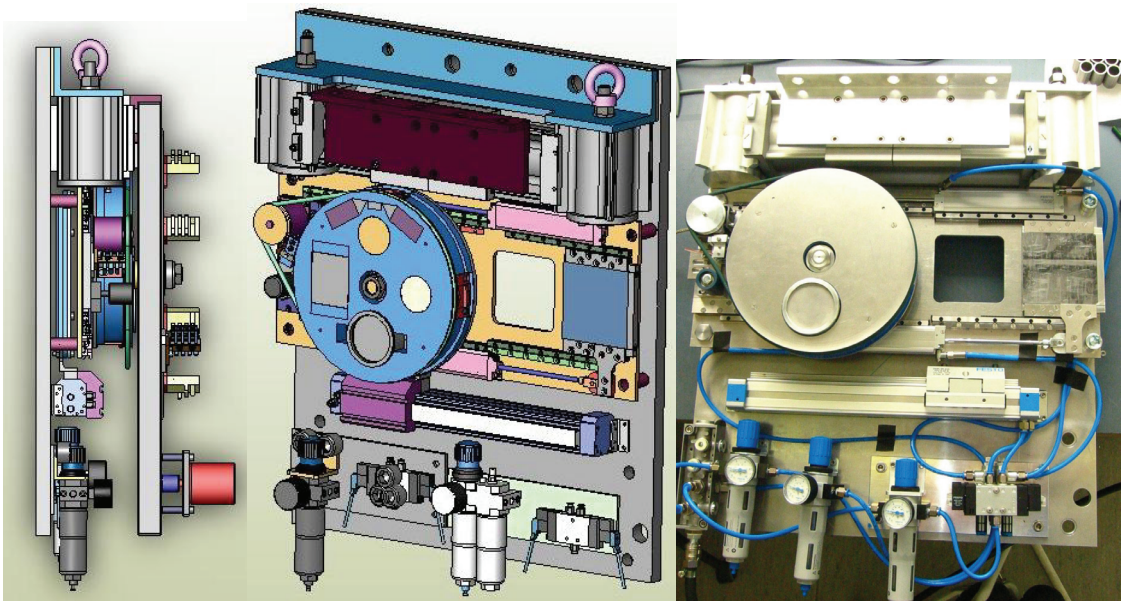

Fig. 2.17: On the left side is shown a side view of the whole package (fast shutter left, multi filter middle, aperture wheel right) and a schematic of the package without the wheel for the apertures. The right hand side shows a photograph of the completed construction.

2.2.2 Single crystal sapphire filter

Especially in phase contrast imaging, where a high lateral coherence of the neutron beam is achieved with small pinhole apertures, epithermal neutrons penetrating the diaphragm material cause a major contribution to the background signal. The ability of sapphire crystals to suppress epithermal neutrons, while being very transparent for cold and thermal neutrons has been pointed out in many publications [Bor87, Sta00, Adi05] and is often used at beam lines to purify a cold neutron spectrum. In the multi filter, a sapphire single crystal filter with a thickness of 5 cm was installed to reduce the ratio of epithermal neutrons to thermal and cold neutrons in the beam.

2.2.3 Polycrystalline and single crystal Bismuth filter

Besides epithermal neutrons, gamma rays are a cause for background signal and artifacts in neutron radiography. Although the ZnS scintillation screen is rather insensitive to gamma radiation, the contribution becomes significant when pinhole apertures are put into a neutron beam of several centimeters diameter where the diaphragm material is opaque for neutrons, but transparent for gamma radiation. Scattered gamma rays may in addition hit the employed CCD camera chip directly, causing bright spot artifacts. To minimize this problem, bismuth and lead are the filter materials of choice [Kam96, Kob96]. The dependence of the transmission of thermal neutrons and gamma radiation of different energy on the thickness of the Bismuth filter is displayed in Fig. 2.18. The installed 5 cm

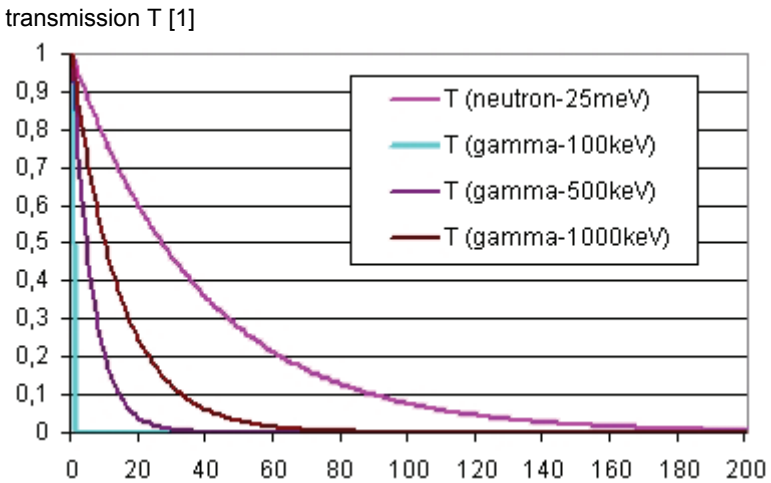

Fig. 2.18: Calculated transmission T of gamma radiation and thermal neutrons through Bi with thickness d.

thick filter effectively suppresses gamma radiation with energies up to 1000 keV and reduces the thermal neutron flux to 28%.

2.2.4 Beryllium filter

Beryllium very effectively blocks neutrons with a wavelength shorter than 3.96 Å and thus provides a “purified” cold neutron spectrum [Web69]. The transparency of beryllium for cold neutrons can be further increased by cooling, but due to limited space and time for the installation at ANTARES the beryllium filter is only used at room temperature. A cooling of the beryllium filter from room temperature down to a temperature of 100K reduces the total neutron cross section by approx. 1 order of magnitude [Hug58].

2.2.5 Lead filter

Beryllium and Sapphire are very good filters to suppress epithermal neutrons but both are very transparent for high energy X-rays. To be able to reduce the gamma background when using one of these two filters, a lead filter was mounted separately on the ground plate of the multi filter. Because of the limited space, the thickness of this lead filter is only 10 mm, which is enough to suppress X-rays up to energies of 300 keV.

2.3 Neutron detectors

A detector for neutrons has to be able to produce a measureable signal of an incident neutron that enters a certain detector volume. For a quantitative evaluation of the measured signal and further processing in a computer it is necessary to convert it into a number. This way, the experimentalist obtains a certain signal in one volume element of a neutron detector. In most cases, neutron detectors are placed in neutron beams with a well defined beam direction. In this case, the spatial information in beam direction is of minor interest and only the coordinates in the plane perpendicular to the beam direction are recorded along with the counting rate.
(As neutrons carry no electric charge but an electronic signal is needed for the further processing on the computer, the detection process in neutron detectors consists of two basic steps. The incoming neutrons are first converted into electrons or electromagnetic waves, which are detected by a detector for this type of radiation. Those two steps can be executed in one combined device as it is done in image plates or they can be done spatially and temporally separated as in CCD detector systems. The benefits and disadvantages of those two types of detectors, which are the most common in neutron imaging and which were exclusively used for measurements at ANTARES, will be discussed in the proceeding section. Before proceeding, a brief overview over the demands on a detector system for neutron phase contrast imaging is presented.)

2.3.1 Demands on detector systems for neutron phase contrast imaging

For propagation-based phase contrast measurements as described in section 1.2.3 pinhole apertures are used to create a neutron beam with a high transversal spatial coherence. Due to the drastically reduced neutron flux, exposure times in phase contrast measurements are much longer than for conventional neutron radiography, which makes this method much more sensitive to background noise. Main causes for noise are epithermal neutrons and gamma radiation in the beam, secondary radiation due to activation and inherent noise of the detector system. The different types of radiation-based noise will be investigated thoroughly in section 3.2.1.1.

2.3.1.1 High sensitivity for cold and thermal neutrons

It is always desirable to keep the exposure times in radiography or tomography as short as possible. This is on the one hand because of the fact that beam time at neutron beam lines is precious, on the other hand a reduction of the exposure time directly reduces the noise due to activation in the sample area. On this account, the detector should have a high neutron sensitivity, which describes the ability of the detector to convert the incoming neutron flux into a measureable signal. In this process the used converter material plays the major role. It has to have a high cross section for neutron absorption and the secondary radiation that is created in this absorption reaction has to be measureable by a position sensitive detector.

2.3.1.2 Low sensitivity for epithermal neutrons and gamma radiation

The pinhole apertures described in section 2.1.2.2 are apart from the pinhole in the center opaque for cold and thermal neutrons. Epithermal neutrons however can penetrate the cadmium and the gadolinium layer in the aperture quite easily. For gamma radiation the whole aperture sandwich is very transparent. Because of this, the ratio of useful cold/thermal neutrons to unwanted background radiation like gammas becomes worse by the introduction of a pinhole aperture. It is therefore important that the used neutron detector is very insensitive to those types of unwanted background radiation.

2.3.1.3 Low inherent noise

The background created by the inherent noise of a detector system can be classified in two categories: Noise that does depend on the exposure time and noise that does not. Both types are unwanted in neutron imaging, but the first type, which was perhaps never even

realized in conventional radiographs, can become a serious problem in phase contrast imaging.

2.3.1.4 High spatial resolution

The spatial resolution of neutron detectors is not as good as the resolution of detectors for X-ray and synchrotron radiation, which can already achieve sub-micrometer resolution. This is because of the need for a conversion reaction in neutron detectors that leads to a blurring of the image. Despite this fact the results in neutron imaging will be always compared with those achieved with X-rays. This demands for a steady effort to improve the spatial resolution of neutron detectors. A detector for neutron phase contrast imaging has to have the best possible spatial resolution to be able to answer current problems of industrial interest. The magnification effect in propagation-based phase contrast images leads to an improvement of the spatial resolution in the object plane at a given detector resolution by a factor of up to 1.5. This gain in spatial resolution alone can justify the application of the phase contrast setup. Therefore it makes sense to use the detector with the highest spatial resolution available for phase contrast measurements.
The negative effect of small pixel sizes is low counting rates and thus the need for long exposure times to obtain a sufficient quantum statistic. If not the best possible resolution is needed for a measurement this problem can be solved easily by binning. In the binning procedure, two or more adjacent pixels are combined to one bigger pixel with a gray value equal to the sum of the gray values of the replaced pixels.

2.3.2 CCD detector

A schematic drawing of the CCD-detector system at ANTARES is displayed in Fig. 2.19. In this drawing the beam direction is from left to right. Behind the sample the neutrons hit in a certain sample-to-detector distance the scintillator screen. A scintillator based on a mixture of ZnS and LiF is used at ANTARES, as this type shows the highest light production compared to other commercially available scintillators like ZnS+B and Gd_2O_2S scintillators [Fuj04]. In this screen the neutrons are converted to visible light through a Li(n,α)T detection reaction and the consecutive ionization of ZnS by the α and T particles. A CCD camera, which is installed in a light-tight detector casing, looks through a 45° mirror on the scintillator screen and measures position sensitive the lights intensity on the scintillator screen.

The field of view on the scintillator screen is defined by the objective and the distance from the mirror. The 45° mirror is used to keep the CCD camera away from the neutron beam in order to reduce the radiation damage to it. The recorded data is read out by a computer. Besides the connection cables to the computer a power supply for the camera and the cooling for the CCD chip has to be fed through the light tight casing.

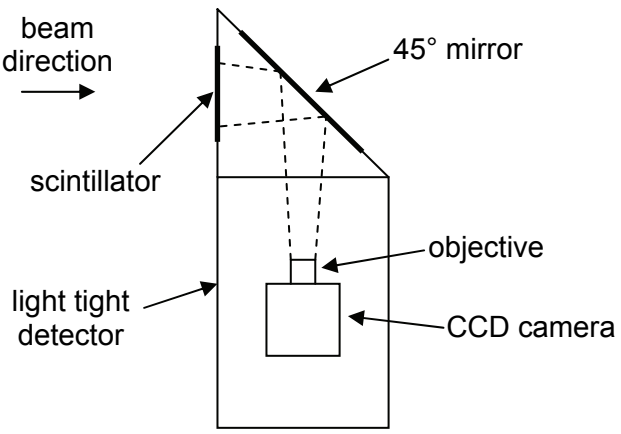

Fig. 2.19: Schematic of the CCD-detector system at ANTARES.

The standard CCD camera at ANTARES is an Andor DW436 with 2048x2048 pixels and a dynamic range of 16-bit. The CCD chip has a pixel size of 13.5μm x 13.5μm and can be kept by Peltier cooling without water cooling at constant temperatures down to -70°C. It is controlled and read out by a purpose-built camera software provided by Andor. The measured intensity distributions are saved as 16-bit images of different file types.
The quickest readout time for one pixel is 1μs, which leads to a total readout time of slightly more than 4s for the complete CCD chip. This is very fast. When the data is read out, a new measurement can be started under very similar conditions with identical beam geometries.

This is the reason why CCD detector systems are the detectors of choice for dynamic radiography with a good time resolution and for quantitative measurements in general. It is possible to normalize images by dividing them with an open beam image (without sample) and to do tomographic measurements, where several projections of one sample under different viewing angles, but besides this under similar conditions, have to be measured.
Another benefit of the CCD detector system is the possibility to choose the field of view of the camera on the scintillator screen and thus to adjust the spatial resolution and the exposure time to the investigated sample.

For phase contrast measurements the CCD detector system shows benefits and disadvantages compared to an image plate detector.
A big advantage of the CCD-detector compared to the image plates is the separation of the converter and the actual detector. This allows a systematic investigation of the influence of the converter material on the background noise. Using the standard LiF-scintillator, the detector has a high sensitivity for cold and thermal neutrons, but also for epithermal neutrons and to a certain degree even for gamma radiation. The LiF can be replaced for example by a scintillator based on Gd_2O_3 as converter material to reduce the sensitivity for epithermal neutrons.
Besides the benefit of flexibility the spatial separation of the converter and the detector leads to additional material in the neutron beam (45° mirror, mounting of mirror and scintillator, light tight casing) that is activated during measurements and causes background.
Concerning the inherent noise, CCD detectors have the disadvantage that the CCD chip produces thermal noise, which accumulates with the duration of the measurement. The thermal noise is suppressed by cooling the CCD chip, but cannot be prevented completely. For long time measurements the readout noise is negligible compared to the thermal noise (see section 3.2.2).
The spatial resolution of a CCD depends on the chosen field of view and the installed scintillator. The field of view defines the pixel size, but the effective resolution in one image is always worse than the pixel size because of the blurring of the image due to imperfect optical devices (mirror, objective) and, what dominates in neutron detectors, because of the conversion reaction. The optimization of scintillators for high spatial resolution or high sensitivity is a recent topic of research in neutron imaging [Bae02]. At present, with common neutron scintillators a spatial resolution better than 100 μm is hardly to achieve.

2.3.3 Image Plates

Originally developed as an erasable X-ray imaging plate for medical radiography [Son83], image plates were soon applied as two dimensional position sensitive detectors in many fields of research with X-rays [Miy86] and neutrons [Rau92]. The reason for this success was the wide dynamic range, the high spatial resolution, the high detective quantum efficiency and the large active area.
Neutron image plates are based on image plates for X-rays that store information in the form of locally trapped electron-hole pairs. All image plates used within this work are based on $BaFBr:Eu^{2+}$ as storage material. It contains Br^- anion vacancies, which are able to store electrons created by ionizing radiation, thereby forming Br^- based F-centers [Tho91]. The holes also created by the radiation are bound at Eu^{2+}-ions forming Eu^{2+}-hole-complexes [Han90]. By optical stimulation using a focused laser beam, the information can be position sensitively read out. The electrons in the F-centers are hereby exited from their ground state to their first exited state, which relaxes due to an altered charge distribution to the so called relaxed exited state [Seg89]. From this state, the electrons can either tunnel to a neighboring Eu^{2+}-hole-complex or escape into the conduction band where they drift until captured by an Eu^{2+}-hole-complex. After the recombination, the captured electron and the Eu^{2+}-hole-complex form a bound exciton. The released energy upon the decay of the exciton is transferred to the Eu^{2+}-ion, which subsequently deexcites by emitting characteristic blue Eu^{2+} photons. The hereby emitted photons are detected by a photomultiplier with color filter. The number of photons is proportional to the neutron fluence.

After the read out process, the image plate can be erased by irradiation with intense light and then reused. To become sensitive for neutrons, gadolinium is added as a converter material to the image plate. In this image plate incoming neutrons are absorbed by gadolinium atoms and create exited Gd-isotopes, which emit high energetic gamma rays and conversion electrons. The gamma radiation in general leaves the image plate without any further interactions, whereas the conversion electrons produce electron-hole pairs. Pure gadolinium is opaque for visible light, which makes it unsuitable as converter material. Transparent Gd compounds like Gd_2O_3, GdF_3 or $GdBr_3$ are therefore used instead.
At ANTARES only neutron image plates produced by Fujifilm are used with Gd_2O_3 as converter material. Three different image plate detectors were used which can be separated in two different types: The Fujifilm BAS-2500/5000 and the Duerr NDT CR35 are image plate scanners that are used to read out thin image plates that can be handled independently from the scanner. The third detector is a MAR345 detector, which is an image plate detector where the image plate is non-detachably integrated in the scanner. The technical specifications of the different devices are listed in table 2.3.
Image plates are very suitable for neutron imaging measurements with long exposure times because there is no inherent noise that accumulates with the exposure time like the thermal noise in CCD detectors. In case of the free image plates for the BAS scanners, no material but the 1 mm thin image plate itself has to be put in the neutron beam for detection. This helps to reduce the activation in the sample environment to a minimum. Another benefit for phase contrast is the application of gadolinium as the converter material, as it provides a high sensitivity for cold and thermal neutrons but shows a rapid decrease in the absorption coefficient for neutron energies over 0.7 eV. This reduces the influence of unwanted epithermal neutrons in the beam. Like this, it is to be expected, that image plates are the detector of choice concerning background noise for neutron phase contrast imaging.
But besides those positive characteristics image plates have also some disadvantages compared to a CCD detector. The cycle time for one radiography, that is the time between the start of one radiography and the start of the next one, is much longer. In case of the thin image plates for the BAS reader this loss of time is due to the manual exchange of the image plate, the transport to the scanner and the execution of the scanning process. In case of the MAR345 detector, the image plate has to be erased after each radiography (more than once if the irradiation was very high). The long cycle times and the fact that it is very difficult to do two radiographies under same conditions make image plates not suitable for tomographic measurements.

	BAS-2500	BAS-5000	Duerr NDT CR35	MAR345
detector area [cm]	20x40	20x25	up to 35x43	Ø 34,5
pixel size [μm]	50 - 250	25 - 250	12,5 - 250	100 or 150
dynamic range	16bit	16bit	16bit	16bit

Table 2.3: Comparison of the technical specifications of the different image plate scanners.

Chapter 3

3 Experimental results

In 2003 the new neutron source FRM-II and the tomography station ANTARES were still under construction. The old neutron source FRM-I was shut down in 2001, which forced scientists to travel to be able to do measurements with neutrons. With the neutron tomography group at PSI in Switzerland, which was also interested to use the phase contrast effect in neutron imaging, a very close, friendly cooperation existed. This cooperation helped a lot to get access to beam time at PSI in the time before the first neutrons were produced at FRM-II in March 2004. Also after the inauguration of FRM-II the constant exchange of knowledge and scientists between the two neutron sources continued.
In the first part of this chapter the results of the measurements at three different beam lines at the neutron source SINQ at PSI are presented. The main objective of these measurements was to find the best possible beam geometry for phase contrast imaging at the emerging imaging beam line ANTARES at FRM-II. The second part covers experiments which were done at the tomography station ANTARES at FRM-II. In this second part, the influence of the neutron spectrum and the detector type on the image quality is investigated in detail and results with the experimental setup at ANTARES are compared with those obtained at PSI. Already at an early stage, these measurements were not only done on especially designed test sample but also on regular industrial components.

3.1 Preliminary experiments at SINQ

SINQ at PSI is in contrast to FRM-II no reactor based neutron source but a spallation source. In this a high frequency pulsed current of accelerated protons hits a heavy metal target (e. g. Pb), which leads to a continuous production of free neutrons. Around the heavy metal target is a moderator tank with water, where the free neutrons are slowed down by collisions. Beside the thermal neutrons in the moderator tank also neutrons with a cold spectrum are produced in a cold source. Like at FRM-II beam tubes are introduced in the moderator tank to transport the neutrons to the different instruments, which are positioned all around the neutron source in a horizontal plane. Three of those instruments were used for phase contrast measurements during the course of this PhD work: NEUTRA, FUNSPIN and ICON.

3.1.1 Measurements at NEUTRA

NEUTRA was the first beam line at SINQ that was primarily dedicated for neutron imaging. The layout of the facility is sketched in Fig. 3.1. The nozzle of the beam tube of NEUTRA guides a neutron beam with a predominant thermal spectrum to the instrument. Like at ANTARES, three different shutters control, whether the neutrons can enter the instrument or not. In the experimental chamber, several moveable, evacuated flight tubes can be inserted in the beam to reduce losses due to attenuation in air. The experimentalist can choose between basically three different sample positions for measurements which are marked in Fig. 3.1. The beam characteristics at position 3 are summed up in table 3.1 and compared to those at ANTARES.

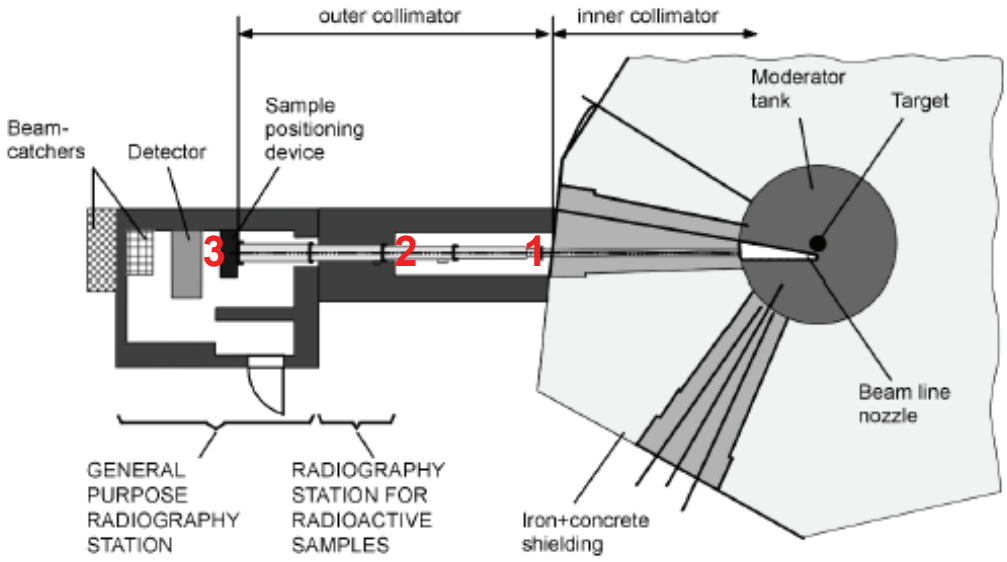

Fig. 3.1: Layout of the tomography station NEUTRA at PSI.

For the propagation-based phase contrast measurements a 0.5 mm thick gadolinium foil with a pinhole was introduced in the neutron beam at position 1. The sample was placed in position 3, which is 6.7 m behind position 1 and the image plate was placed in variable sample-to-detector distances up to 165 cm, which was the maximum distance at the beam dump. The detector for all phase contrast measurements at NEUTRA were Fujifilm image plates of the type ND2040, which were read out with a BAS-2500 scanner (see table 2.3 for specifications).

	NEUTRA Pos. 3	ANTARES
Energy of the neutrons	thermal neutrons	cold neutrons
Distance from the pinhole position [mm]	6675	13600
Neutron flux without pinhole [$cm^{-2}s^{-1}$]	3.60E+06	1.0E+08
Neutron flux with 1 mm pinhole [$cm^{-2}s^{-1}$]	1.45E+04	9.2E+04
Beam diameter with 1 mm pinhole [mm]	36.3	290
L/D-ratio without pinhole	550	400
L/D-ratio with 1 mm pinhole	6675	14000

Table 3.1: Beam characteristics at position 3 at NEUTRA compared to ANTARES.

3.1.1.1 Basic investigation on the phase contrast effect

The first samples to investigate the phase contrast mechanism systematically were three aluminum rods with different cross sections as shown in Fig. 3.2. The rod in the middle (B) had a circular profile with a diameter of 3 mm. The outer rods had a square profile with an edge length of 5 mm, where the side of one rod (C) was aligned to be perpendicular to the neutron beam and the sides of the other rod (A) were aligned in a 45 degree angle to the beam. The two dark spots marked by the green circles in the radiograph in Fig. 3.2 are caused by dirt or damages on the surface of the image plate. This kind of noise has to be taken into account in the further image processing and has to be avoided or corrected to allow a quantitative analysis of the data. The occurrence of the dark border (penumbra region) on the fringe of the circular beam cross section was already explained in sec. 2.1.2 (see Fig. 2.5).

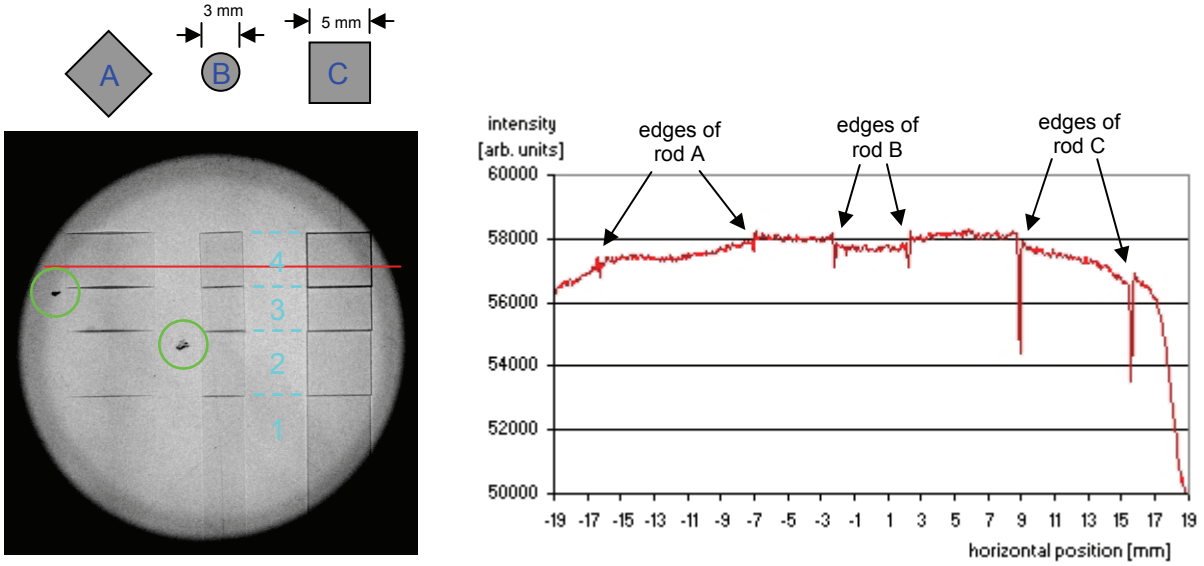

Fig. 3.2: Radiograph of three aluminum rods with different cross sections as shown above. The red line marks the position of the line profile displayed on the right side of the radiograph.

For the quantitative analysis, the recorded images are further processed with the image processing software IDL. A useful method to visualize the phase contrast effect at certain edges in an image are line profiles. In line profiles the gray values along a horizontal line in an image are plotted versus their positions. In order to compensate noise, the thickness of the horizontal line is typically more than one pixel to be able to use filter algorithms to calculate the grey value for one position. In Fig. 3.2 the line profile along the red line in the radiograph is displayed. The line profile crosses the uppermost part of the three rods, which is marked with the turquoise number four. The vertical width of this line profile was 5 pixels and the final grey value was determined with a median filter.

In the four regions marked with the turquoise numbers, the aluminum rods were coated with layers of nickel with different thicknesses. The lowest part, marked with the number one, is not coated with nickel at all. The thickness of the nickel layer in region two is 5 μm, in region three 20 μm and in region four 50 μm. The dark lines between the layers in the radiograph are due to the adhesive that was used to glue the separately coated parts together.

Five phase contrast radiographs were measured using five different sample-to-detector distances: 5 cm, 50 cm, 80 cm, 100 cm and 165 cm. The exposure time for every distance was 3 hours with a ND2040 image plate. At first the influence of the sample-to-detector distance on the phase contrast is investigated. For this only the uncoated lowest part of the rods is considered. In Fig. 3.3 the line profiles through region one of the radiographs in the five different distances are displayed. To be able to compare the line profiles easily, all five profiles were plotted in one diagram and separated by adding a constant value to each graph.
As expected no phase contrast occurs in the radiograph taken in 5 cm distance from the sample. But already in a distance of 50 cm phase contrast can be clearly seen at the edges of rod C and in 80 cm also at rod B with the circular shape. Only the edges of the diamond shaped profile are at all distances not clearly visible and can only be guessed due to the high noise level. If the intensity of the phase contrast at rod C for the different distances is compared, an increase can only be recognized from 50 cm to 80 cm. At higher distances it stays approximately the same, which is not conform to Eq. (1.43). At this point, it has to be remembered that this equation was derived for the special case of a pure phase object and that the intensity was measured only in some few, discrete positions.

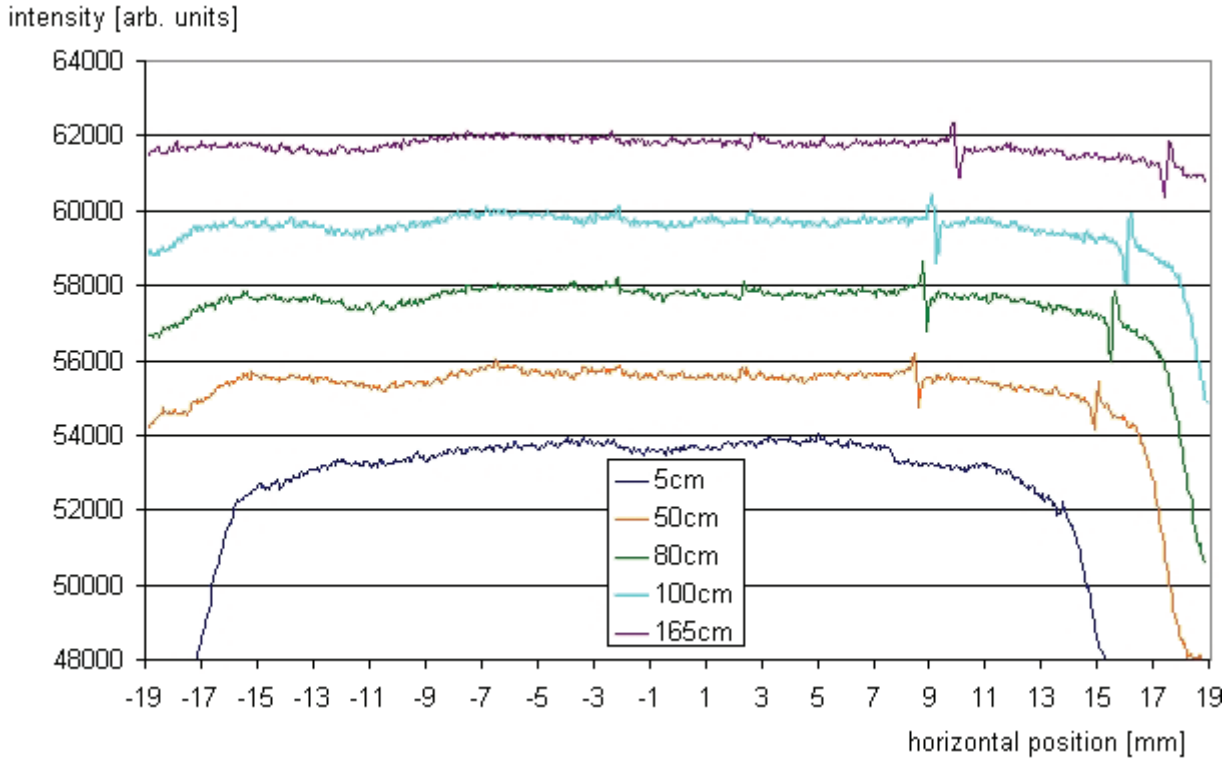

Fig. 3.3: Line profiles through radiographs of the aluminum rods without nickel coating for various sample-to-detector distances.

Another effect that is visible in this illustration is the magnification of the image due to the beam divergence. In Fig. 3.4 the beam diameter at the detector plane is plotted versus the sample-to-detector distance. It can be approximated. by a linear function that crosses the ordinate at 36,3 mm (beam diameter at sample position) and has a gradient of 0.054. This beam divergence corresponds very well the expected beam divergence for a point source at the position of the pinhole aperture.

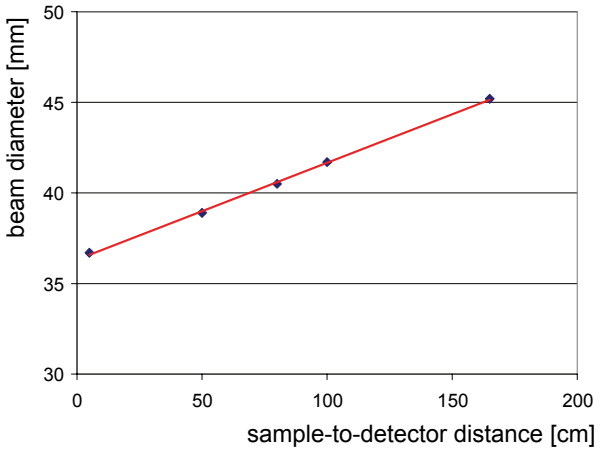

Fig. 3.4: Measurement of the beam divergence at NEUTRA.

By coating the aluminum rods with a nickel layer of varying thickness, the possibility to use nickel as a contrast medium in neutron phase contrast was investigated. Nickel shows the second greatest deviation from unity in the real part of the refractive index of all elements behind Beryllium (see Fig. 4.9). In Fig. 3.5 four line profiles through the four different thick coated regions of the rods are displayed. All four are taken from the phase contrast image measured in 165 cm distance from the sample. Again the four graphs were separated from each other in the diagram by summation with a constant value.
A notable increase in contrast with the thickness of the coating at the edges of the rods is observable. But especially at rod C it is clearly to see that this gain in contrast is not due to the greater δ-value of nickel but a result of its bigger attenuation coefficient. It is not an increase in phase contrast but in absorption contrast. In case of phase contrast, the intensity gain is proportional to the second derivative of the phase, which always leads to a gain and a loss peak at edges. In the line profiles at rod C the gain peak vanishes with the nickel coating and only an increase in the loss peak occurs. At this point it has to be kept in mind that

phase contrast occurs two times at each edge at two different interfaces: the air-nickel interface and the nickel-aluminum interface. The gradient of the Ni-Al interface has the opposite sign than the gradient of the Air-Ni interface. And as the two interfaces are separated by a distance less than the pixel size of the detector, gain and loss peaks of the two phase contrast signals extinguish each other. What is left is only the additional attenuation by the nickel layer which is 20 times higher than for aluminum.

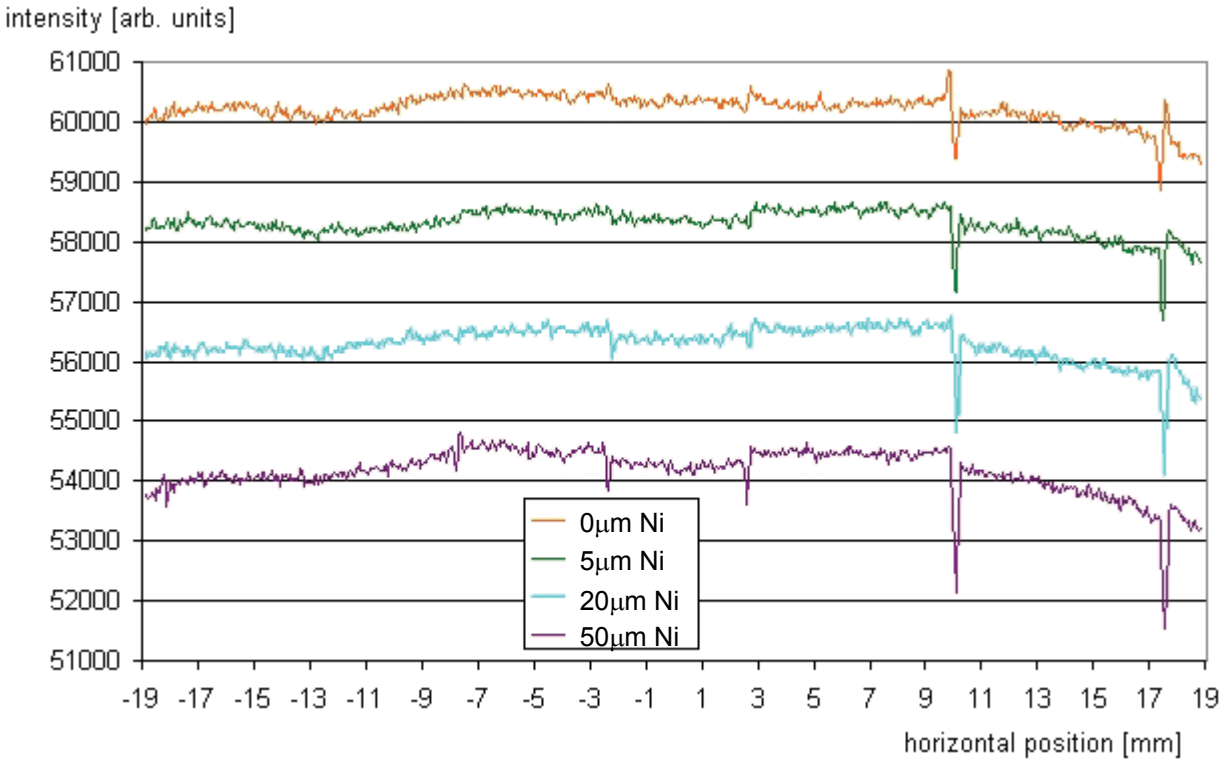

Fig. 3.5: Line profiles for varying thicknesses of nickel coating.

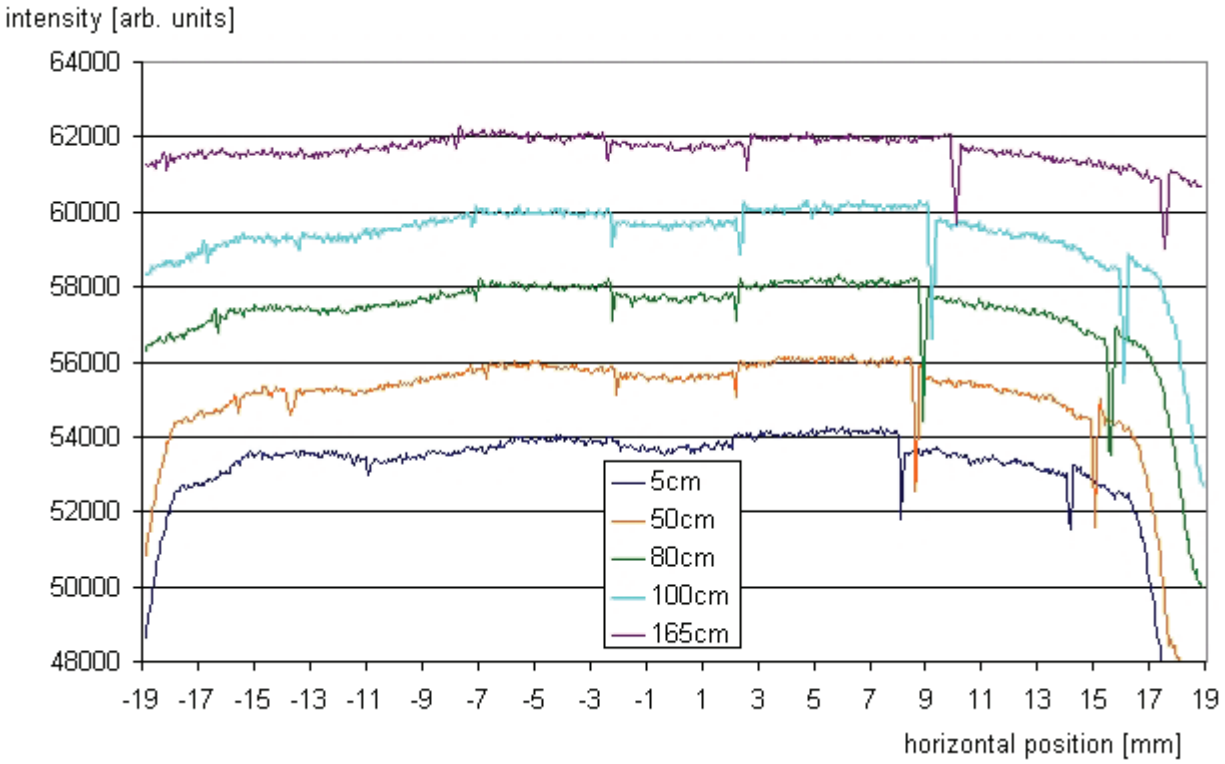

Fig. 3.6: Line profiles for various sample-to-detector distances with 50μm Ni coating.

Nevertheless, with increasing thickness of the nickel layer, the edges of rod B and even the edges of rod A become visible. To check if this is also only due to attenuation the line profiles through region 4 of the radiographs in different sample-to-detector distances are displayed in Fig. 3.6. The absorption contrast at the edges of rod C is clearly visible for all sample-to-detector distances. The edges of the other two rods are not visible in the contact image with R = 5 cm, they appear at distances over 50 cm, what is an indication for phase contrast. In contrast to the edge in rod C, which is a flat surface perpendicular to the beam direction, the phase contrast peaks of the two interfaces at the round and 90° tilted edges do not fully extinguish each other.
Another test sample for the use of nickel as a contrast medium for neutron phase contrast imaging was an aluminum frame with aluminum wires with various thicknesses wound on it. The two uppermost wires had a round cross section with a diameter of 1mm, where the lower one was coated with a 50 μm thick plastic layer. The four 3 mm broad aluminum bands below had a thickness of 0.5 mm in beam direction and were coated with a 0 μm (band 1), 5 μm (band 2), 20 μm (band 3) and 50 μm (band 4) thick nickel layer. A phase contrast radiograph of the different wires is compared with a pure absorption-based radiograph in Fig. 3.7. Both radiographs were measured with Fuji image plates and read out with a BAS2500 scanner with a pixel size of 50 μm. Unfortunately the image quality suffers from a lot of scratches and other damages on the surface of the IP, but the phase contrast effect is nevertheless clearly visible. The strong attenuation at the connections between the wires and the frame is causes by the used adhesive. The first two aluminum bands with no nickel layer and a 5 μm thick layer are not visible in the conventional radiograph. With a 20 mm and 50 mm thick nickel layer, the aluminum band becomes visible because of the additional attenuation caused by the nickel. The exact positions of the edges are only visible in case of wire 2 and band 4. With phase contrast, the edges of all wires become clearly visible and the width of all wires can be measured very precisely. The contrast enhancement at edges and interfaces is beneficial for distance measurements in neutron radiographs. Measurement of distances between sharp boundaries is a first straight forward application for neutron phase contrast imaging.

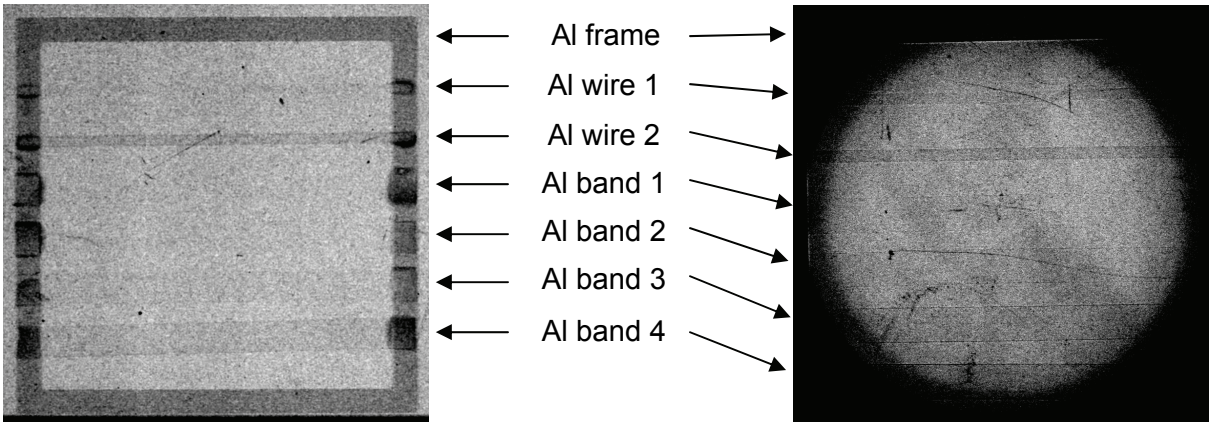

Fig. 3.7: Comparison of a conventional and a phase contrast radiograph with image plates of different aluminum wires. The uppermost two wires had a round cross section with a diameter of 1mm, where the lower one was coated with a 50 μm thick plastic layer. The four 3 mm broad aluminum bands below had a thickness of 0.5 mm in beam direction and were coated with a 0 μm (band 1), 5 μm (band 2), 20 μm (band 3) and 50 μm (band 4) thick nickel layer.

3.1.1.2 Application of the technique on industrial samples

After the proof of principle, more applications for neutron phase contrast imaging were searched. In this subsection, no more especially designed test samples, but regular industrial objects are investigated to determine the strengths and limitations of propagation-based neutron phase contrast imaging.

The first object to be considered is a cast aluminum component with shrink holes. Shrink holes occur after the casting process of a component, when it cools down from a temperature above the melting point to room temperature. As the volume of most materials decreases with the temperature, hollow spaces can occur inside the cast object, which are called shrink holes. Shrink holes reduce the mechanical stability of cast components and modify other physical characteristics like the heat conductivity. It is therefore of great industrial interest to detect this material defect as early as possible during the production process.

To determine the exact positions of the shrink holes in the test object, it was non-destructively tested with neutron tomography (Fig. 3.8). The gray values of the hollow spaces differ considerably from the gray values of the bulk material (aluminum alloy). Like this, the volumes of the shrink holes could be separated easily in the reconstructed 3D image and were marked with an orange color.

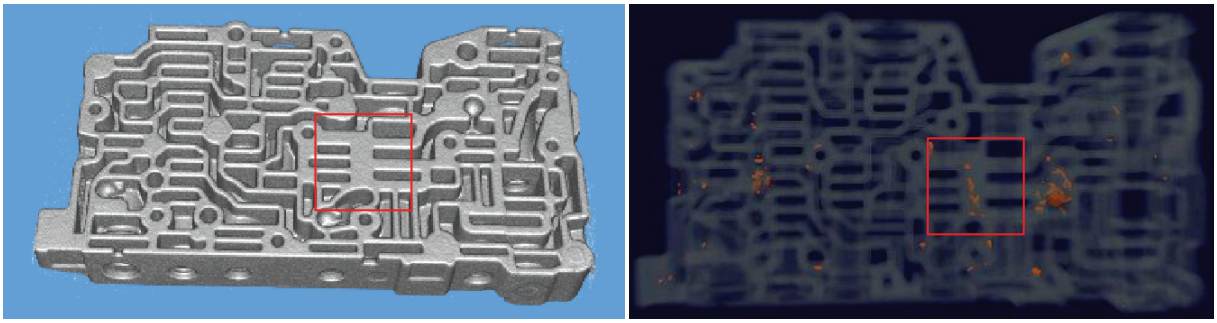

Fig. 3.8: 3D visualization of a tomographic measurement with neutrons of a cast aluminum object. In the left image, the surface of the reconstructed object is displayed, in the right image, the bulk material is made transparent and the shrink holes inside are marked with an orange color. The red outlined area was further investigated with phase contrast imaging (Fig. 3.9).

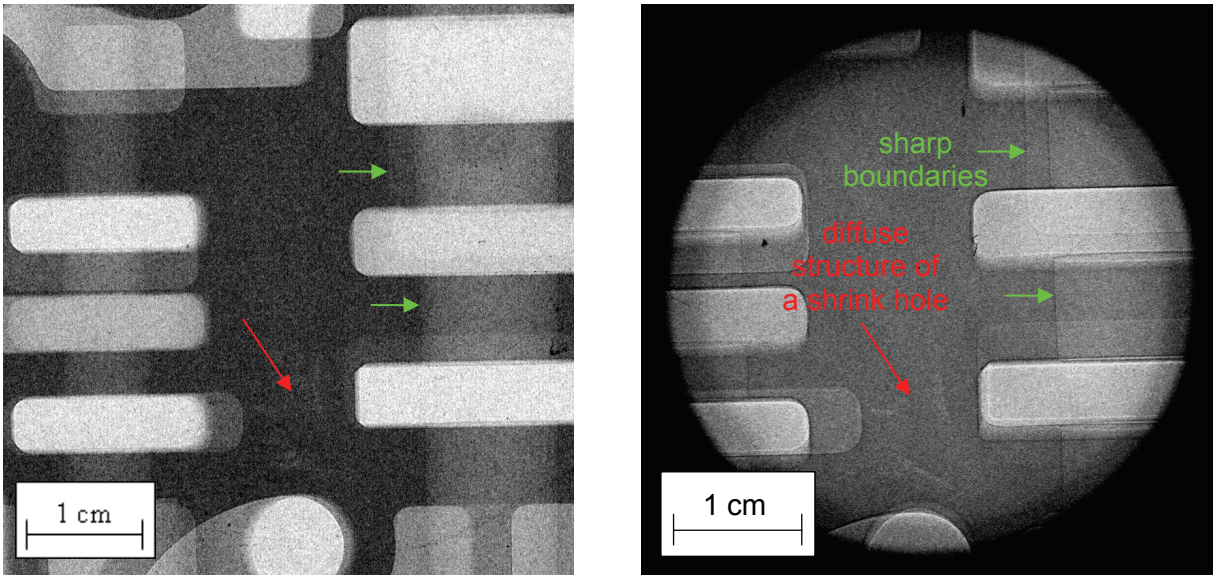

Fig. 3.9: Conventional (left) and phase contrast (right) radiography of a cast aluminum sample with shrink holes. Both radiographs were measured with an image plate that was read out with a pixel size of 50 μm. The exposure time for the absorption based radiograph was 30 s and for the phase contrast image 180 min. The position of sharp edges is much better visible with phase contrast (green arrows) but the visibility of shrink holes is not improved (red arrow).

A small area of 4.3 cm x 4.3 cm with well visible shrink holes in it (red outlined area in Fig. 3.8) was investigated in more detail with absorption-based and phase contrast radiographs. These radiographs were done with Fuji image plates, which were read out with the BAS2500 scanner with a pixel size of 50 μm. The exposure time for the phase contrast radiograph was 180 min, whereas the conventional radiograph was measured in 30 s. With these exposure times, the dynamic range of the image plates was fully used in both radiographs.
At first glance, the enhanced contrast at the sharp edges of the object is visible in the phase contrast image (green arrows in Fig. 3.9). This contrast enhancement recommends again the use of phase contrast imaging for distance measurements. The increased spatial resolution in phase contrast images caused by the magnification of the object due to the large distance between object and detector plane, leads to an additional gain in precision in distance measurements (see section 4.1).
The visibility of the shrink holes however is not noticeably improved by phase contrast (red arrow in Fig. 3.9). The reason for this is the diffuse structure of the shrink holes that does not create steep gradients in the phase shift, which is the prerequisite for a clearly visible phase contrast. In aluminum foams for example, where each bubble has a well defined, clean surface, the phase contrast contours occur wherever the neutron beam hits the surface of a bubble tangentially (Fig. 3.10). The use of phase contrast imaging for the non-destructive testing of metal foams will be discussed in detail in chapter 4, where the most beneficial applications of propagation-based neutron phase contrast imaging are summarized.

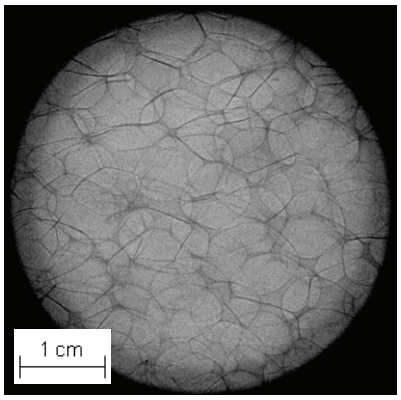

Fig. 3.10: Phase contrast radiograph of aluminum foam (exposure time: 180min; sample-to-detector distance 80cm).

Prof. Mollenhauer from the University of Jena provided us with another sample with a foam structure. It was a broken hip implant out of a titanium alloy (Ti_6Al_4V) with remains of bone on it. The trabecular bone tissue represents an open cell foam structure. In Fig. 3.11 an absorption-based radiograph is compared with a phase contrast radiograph. The organic material attenuates the neutron beam much stronger than the metal alloy. The visibility of the trabecular meshwork of the bone tissue is in both radiographs similar, phase contrast imaging is not advantageous in this case. The reason for this is the more diffuse structure of the organic foam on the one hand and its high attenuation coefficient on the other hand. In section 3.2.3.1 it will be demonstrated with an iron step wedge that no phase contrast can occur at an edge, if the neutron beam is attenuated much more on one side of the edge than on the other.

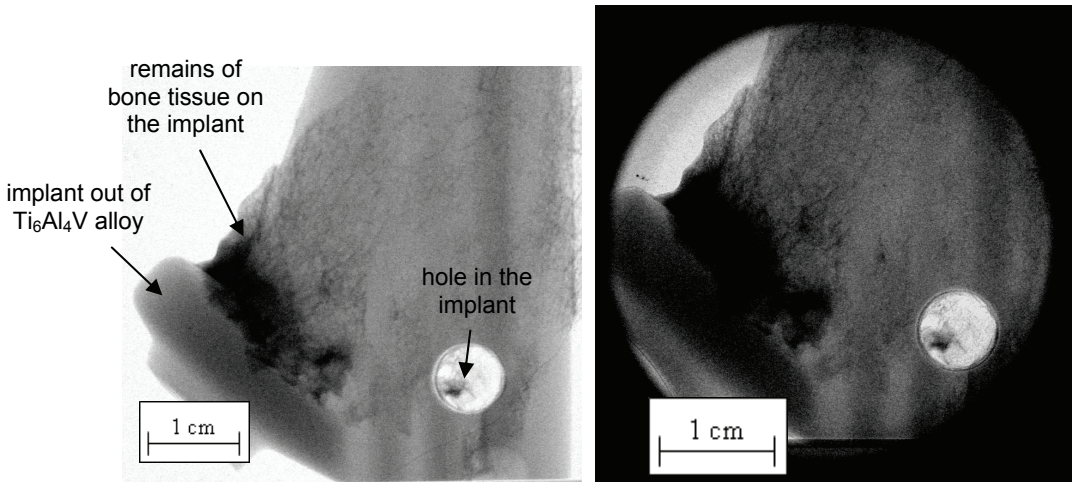

Fig. 3.11: Neutron phase contrast imaging delivers no additional information on the trabecular meshwork of bone tissue on a broken hip implant.

In the radiographs of the severed head of the hip implant, the benefits of phase contrast are clearly visible. The contrast enhancement at the interface between the titanium alloy and the ceramic head allows a precise separation of the two materials (Fig. 3.12). This improved indication of the boundary layer can also be used for the separations of volumes in phase contrast tomography, which will be demonstrated in section 4.4.

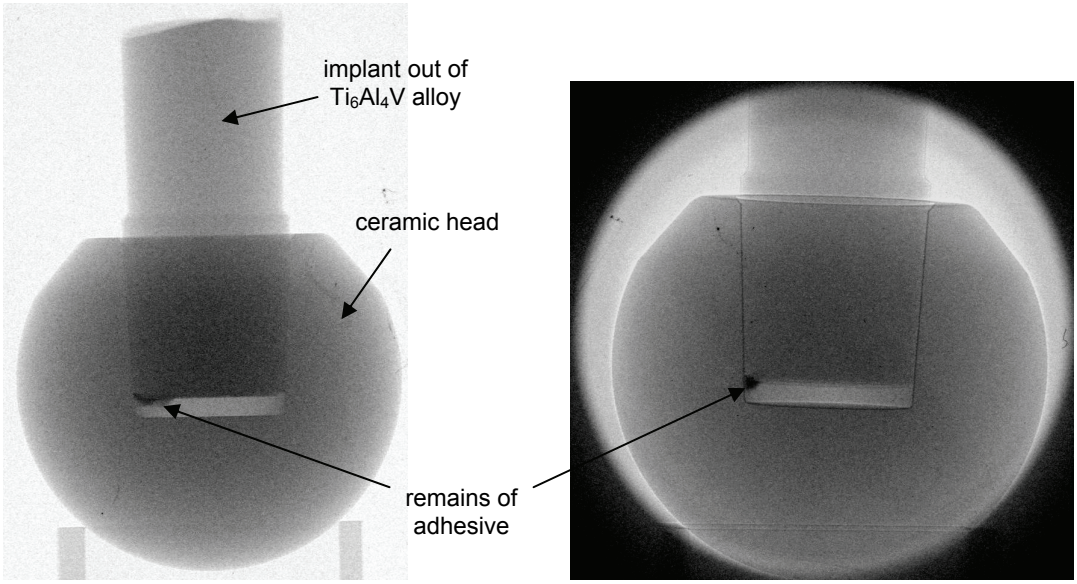

Fig. 3.12: Comparison of conventional and phase contrast radiographs of the ceramic head of the broken hip implant. The interface between the titanium alloy of the shaft and the ceramic head is much better visible in the phase contrast image. Beside this contrast enhancement, the magnifying beam geometry improves the spatial resolution of the phase contrast image (see chapter 4.1)

.

3.1.2 Measurements at FUNSPIN

FUNSPIN is a facility for experiments with a polarized cold neutron beam at SINQ. As illustrated in Fig. 3.13 downstream the beam shutter (labeled with a 2) an approximately 7m long neutron optic system follows. It consists of a multi-slit supermirror polarizer bender and a focusing beam guide that tapers the diameter of the neutron beam in the horizontal dimension from 8 cm down to 4cm. The whole facility is contained in a massive, concrete shielding.
For phase contrast measurements a gadolinium foil with a 0.5 mm pinhole was attached to the boron/lithium-collimator. All other instruments and devices in the experimental chamber were removed to provide space for a sample and detector at various distances from the pinhole aperture. But already in the first open beam image, shown in Fig. 3.14, taken with a ND2040 image plate, which was attached to the beam dump on the right concrete wall in Fig. 3.12, a fundamental problem of this experimental setup for phase contrast imaging became clear. The gadolinium aperture together with the experimental chamber formed a pinhole camera that delivered pictures of high quality of the beam structure at the exit of the polarizer.

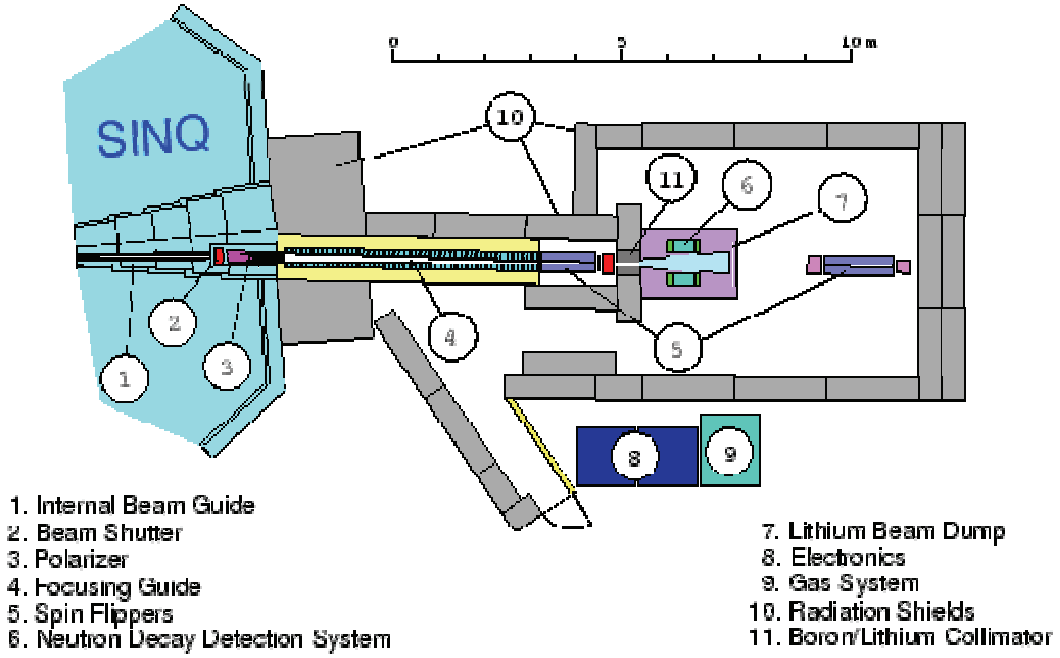

Fig. 3.13: Layout of the polarized cold neutron facility FUNSPIN.

Attempts to remove the structure from images by normalizing them with open beam images failed due to the high contrast of the structures and the limited accuracy of the positioning of image plates in the beam compared to the high resolution of the scanner. But even if the normalization process could be done perfectly, the strong intensity variations in the open beam are visible in the normalized image as variations in the SNR due to the varying counting statistics.
To solve this problem, materials with high scattering cross sections like polyethylene were introduced in the beam to destroy the structure in the beam. However the results were not satisfying and as the available beam time at FUNSPIN was very short, the experiment ended without a useful result. An answer to this problem was found in a paper by McMahon et al. [McM03] some time after the measurements at FUNSPIN. According to this paper, the best method to remove artifacts in the beam generated by the upstream beam guides, polarizer or other devices is powdered activated carbon just upstream of the pinhole to diffuse the beam.

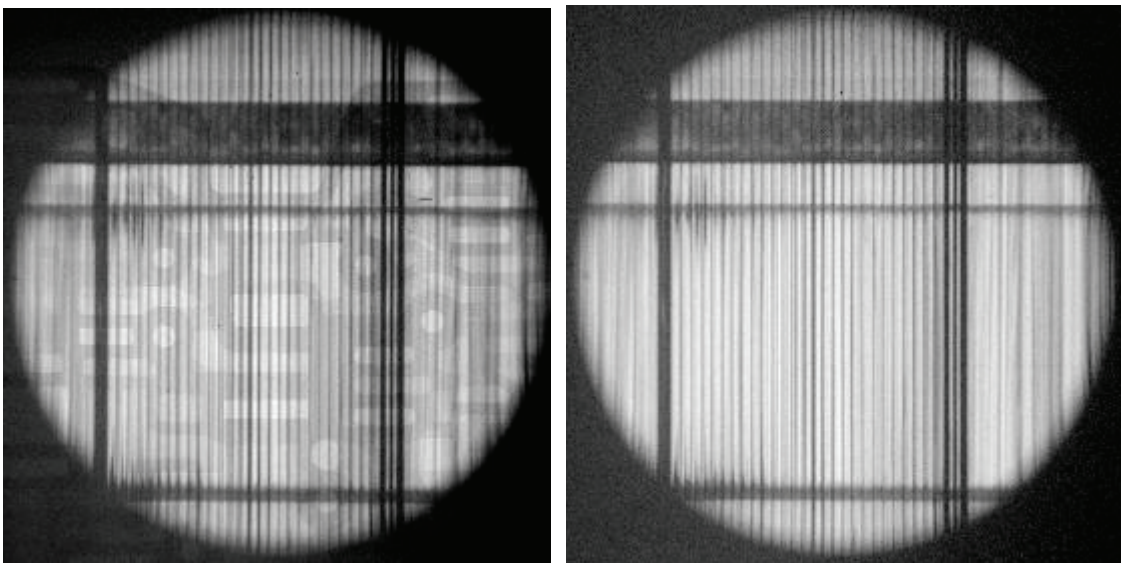

Fig. 3.14: Phase contrast image with and without an aluminum sample (see Fig. 3.8) at FUNSPIN.

3.1.3 Measurements at ICON

ICON stands for **I**maging with **CO**ld **N**eutrons and is a new neutron imaging facility at PSI that started its operation in 2005. As the name implies, ICON uses a neutron beam with a cold spectrum like ANTARES at FRM-II. In May 2007 some measurements with metal step wedges were done at ICON, which were already executed in a similar way at ANTARES (see 3.2.1.4). At ICON a beryllium filter with a thickness of 9 cm in beam direction can be introduced in the beam to suppress thermal and epithermal neutrons in the cold neutron beam (see 3.2.1.2).

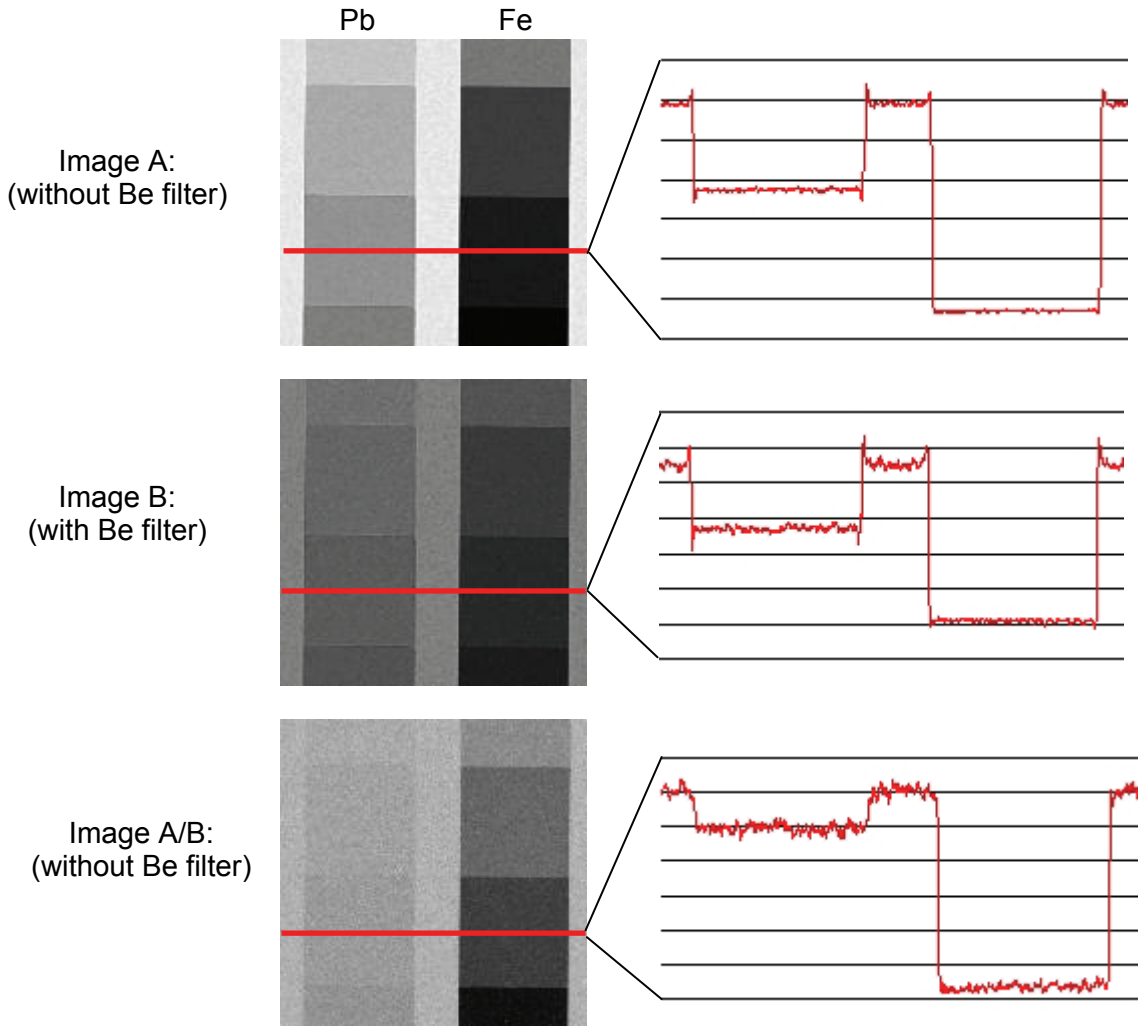

Fig. 3.15: Change of the contrast between a lead and an iron step wedge by a beryllium filter.

The basic idea behind the experiment is, to amplify the contrast in radiographs between certain elements, by doing one radiograph with and one without the beryllium filter and calculating the quotient of the two afterwards. The single radiographs are displayed in Fig. 3.15 (image A and image B were normalized). The improvement in contrast between the iron and the lead step wedge is clearly visible, but compared with the result at ANTARES (see Fig. 3.25) the contrast gain is much smaller. The attenuation of the beam by the two elements in general seems to be completely different than in the corresponding measurement at ANTARES. This was a strange result at first glance, as the two step wedges at both measurements were exactly the same.
The explanation for this discrepancy lies in the used detector systems. In both measurements a CCD detector was used, but the scintillator at ANTARES used lithium and the one at ICON gadolinium as converter material. The gadolinium-based scintillator at ICON is very insensitive to epithermal neutrons, which are strongly affected by the introduction of the beryllium filter and thus cause the great contrast gain at ANTARES.

The CCD-based neutron detector at ICON is most probably currently the neutron detector with the highest spatial resolution for quantitative neutron imaging. To achieve the highest possible spatial resolution, the field of view of the camera on the scintillator screen is reduced to 27 mm, which leads with the 2048x2048 pixels of the CCD chip to a pixel size of less than 13.5 μm. At these dimensions, the microscopic structure of the scintillator screen becomes clearly visible and is a major contribution to noise in the picture (Fig. 3.16).

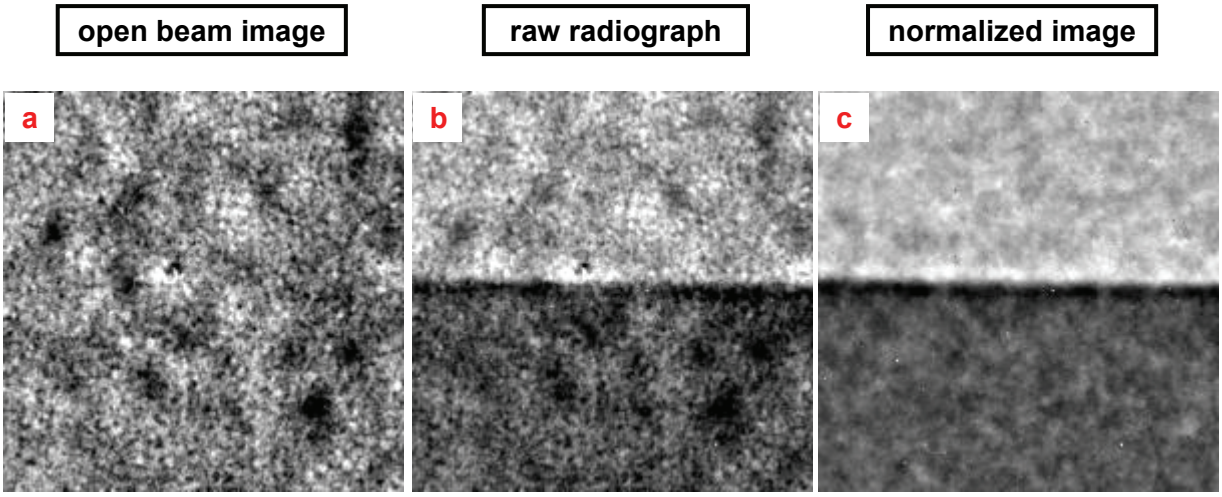

Fig. 3.16: Comparison of a 200x200 pixels (corresponding 2,7 mm x 2,7 mm) large ROI at the same position in a) the open beam image, b) the sample image and c)the normalized images. The scintillator structure is clearly visible in the first two and is greatly reduced in the normalized picture.

To eliminate the fixed structures caused by the scintillator, an open beam normalization of the measured images is indispensable. As the sample has to be removed from or driven in the neutron beam between the two necessary measurements, the sample holder has to be decoupled from the very stable detector system, because the slightest shift causes the normalization procedure to fail.

3.2 Measurements at FRM-II

When the FRM-II reached criticality for the first time in March 2004, the main parts of the assembly of the tomography station ANTARES were already successfully installed and the facility was ready to use the first neutrons. The first measurements at the new beam line were the open beam measurements displayed in Fig. 3.17. They show a very homogenous neutron beam in the field of view of the CCD detector and marked the start for neutron imaging at FRM-II.

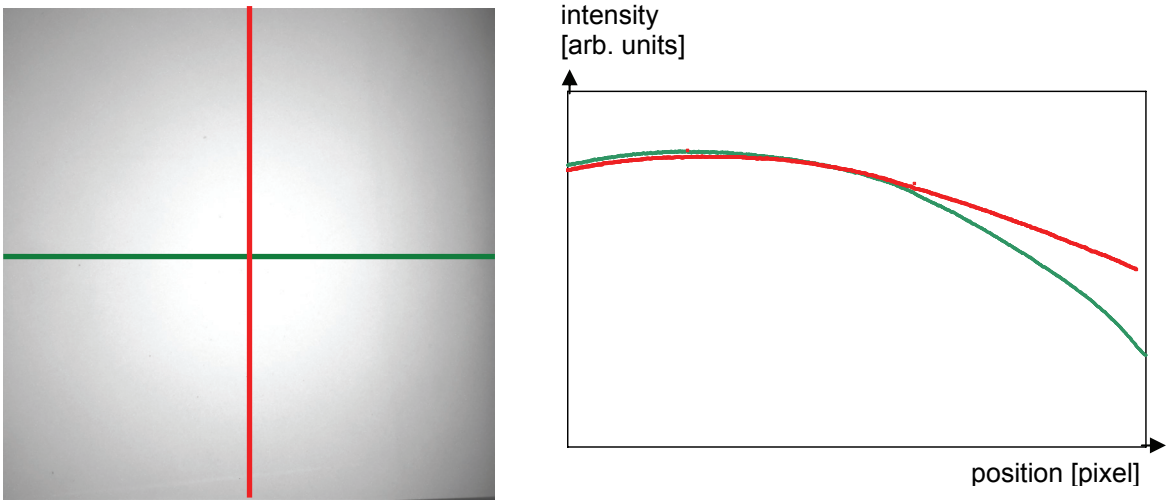

Fig. 3.17: Horizontal and vertical beam profile at ANTARES (taken with CCD detector; Field of view: 26x26 cm²). The intensity loss towards the corners is mainly due to the optical imaging of the scintillator screen on the CCD chip (see 3.2.2.1)

Approximately one year later, on the 8th of April in 2005, the installation of the aperture wheel (see 2.1.2) allowed neutron phase contrast imaging at ANTARES. Again the first measurements were open beam images with the new apertures in the beam. One of the first phase contrast radiographs at ANTARES of metal step wedges are displayed in Fig. 3.18 with the corresponding open beam image.

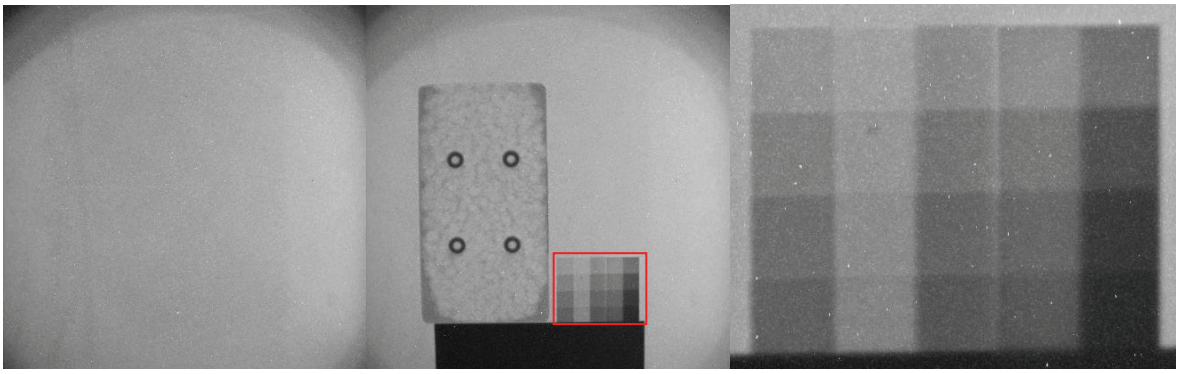

Fig. 3.18: First phase contrast image at ANTARES (1 m sample-to-detector distance; 40 min exposure time with CCD detector).

No phase contrast at all is visible in these images due to a large background noise. The bad SNR was not unexpected as phase contrast images with a CCD detector at NEUTRA showed even worse results. Before the phase contrast itself could be further analyzed, the origins of the noise in the images had to be found and reduced. For the analyzing of the recorded data different types of image processing software was used. At ANTARES the most important software for the further image processing is IDL (Interactive Data Language), a program designed by David Stern especially for image analysis and data visualization.

3.2.1 Investigations on radiation-based noise and counter measures

3.2.1.1 Types of radiation-based noise

Since the image quality of conventional neutron radiographs at ANTARES was excellent, the reason for the bad SNR had to emanate from the peculiarity of the phase contrast measurement method, i. e. that the neutron flux is greatly reduced due to the introduction of a pinhole aperture in the beam. Because of this the ratio of two sources of radiation-based noise is amplified:

1. Radiation in the beam that is not blocked by the aperture.
2. Noise due to activation of the sample and the detector area.

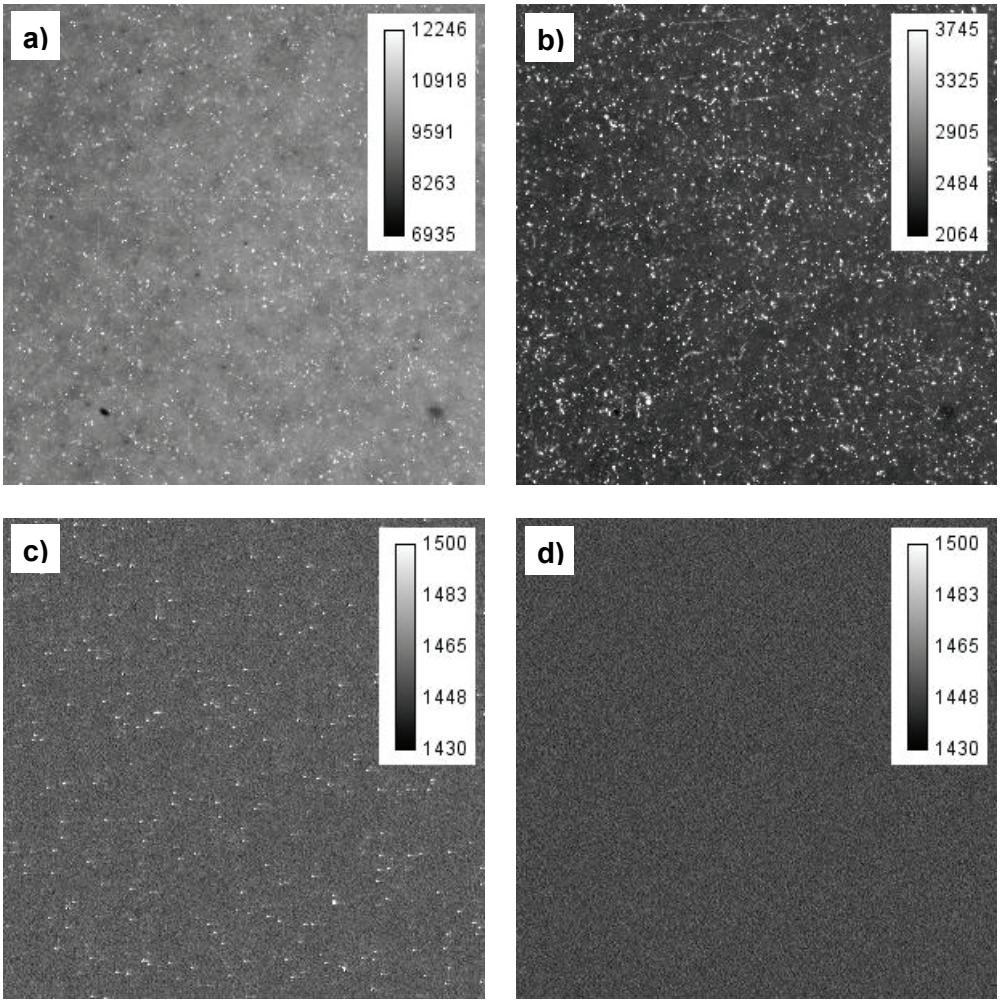

Fig. 3.19: "Open beam" images with a)Cd-filter, b)fast shutter and c)fast and secondary shutter in the beam. The three images were measured with a CCD detector using a LiF scintillator and the exposure time was 180 s in each case. Image d) in the lower right corner is a dark current image with an exposure time of only 0.1 s that gives a measure for the readout noise of the CCD detector.

The different types of radiation-based noise are visible in the open beam images displayed in Fig. 3.19. Each open beam image (a – c) was measured with a CCD detector using a LiF scintillator and an exposure time of 180 s. The first image was measured with a 2 mm thick cadmium filter in the beam and shows the background in the images due to epithermal neutrons and gammas. The second image was recorded while the fast shutter was closed and thus is a measure for the gamma background in the beam. During the measurement of the image 3.19c, the primary and secondary shutters at ANTARES were closed. Before they were closed, a tomographic measurement was done at the facility, which led to activation in the experimental chamber. Fig. 3.19c is thus a measure for the background due to activation,

but it does not represent this background thoroughly, because the contribution of elements with a short half-life is only partially detected. The last displayed image is the result of a dark current measurement with closed camera shutter and an exposure time of only 0.1s. It represents the readout noise of the CCD detector.
The solution to minimize the background due to activation is the reduction of material in the beam and close to it and the optimization of the shielding of the detector. The other type of noise can be reduced by filtering unwanted radiation out of the beam. For this cause the multi filter described in section 2.2 was installed.

3.2.1.2 TOF measurements

To investigate the effect of the multi filter on the spectrum of the neutron beam, time-of-flight measurements were carried out at the sample position of the ANTARES facility. A schematic representation and a photo of the experimental setup of the TOF spectrometer are shown in Fig. 3.20. The 2 mm cadmium sheet with the 1 mm pinhole at the entrance of the TOF spectrometer creates a needle beam, which is chopped into short pulses by the following chopper wheel. At a distance of 1 meter to this chopper, a ^{3}He tube counts the incoming neutrons with a time resolution of 1 µs.

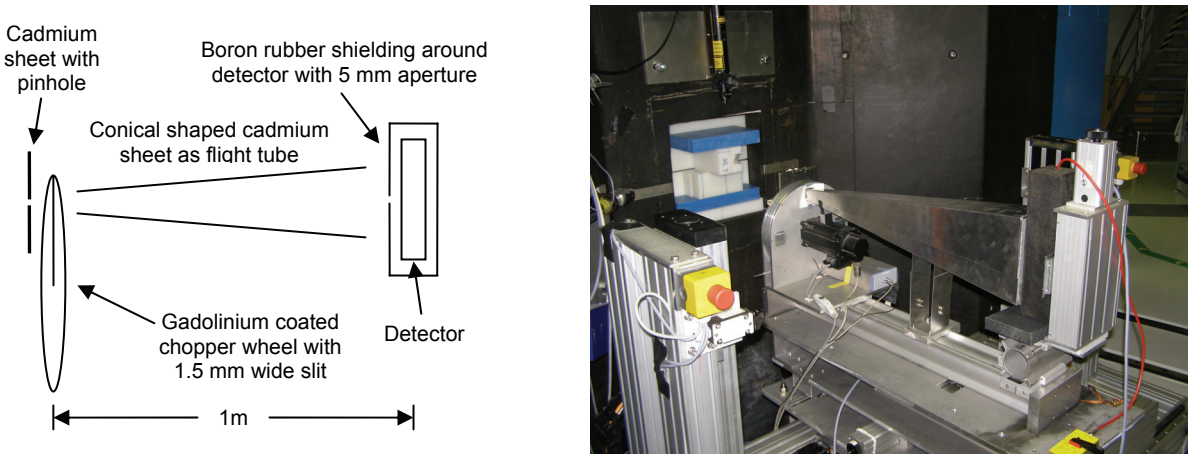

Fig. 3.20: Schematic representation and photograph of the experimental setup of the time of flight spectrometer used to measure the neutron spectrum at ANTARES.

The detector system receives a trigger signal whenever the 1.5 mm wide slit of the chopper passes the 1 mm pinhole in the cadmium sheet. This way the time a neutron needs to pass the distance from the chopper to the detector can be measured very precisely. The time resolution is mainly determined by the chopper (width of the slit and rotation speed; contributions of detector and the electronics are negligible) and is better than 40 µs for the setup described above.
Running the chopper with a rotation frequency of 70 Hz, neutrons with a velocity down to 70 m/s (≈ 60 Å) can be detected before the next pulse starts at the chopper.
The low energy part of the neutron spectrum can be measured well with this spectrometer. At higher energies of the neutron spectrum the chopper setup faces some problems. The main problem is the transparency of the Cadmium sheet and the Gadolinium coating of the chopper wheel for epithermal neutrons. To minimize this problem, the cross section of the neutron beam was reduced to 2 x 2 mm^2 by blocking the rest of the beam with borated polyethylene bricks. Still the epithermal neutrons in this reduced beam caused a background in the TOF measurements that demanded very long accumulation times to obtain a satisfying signal-to-noise ratio.

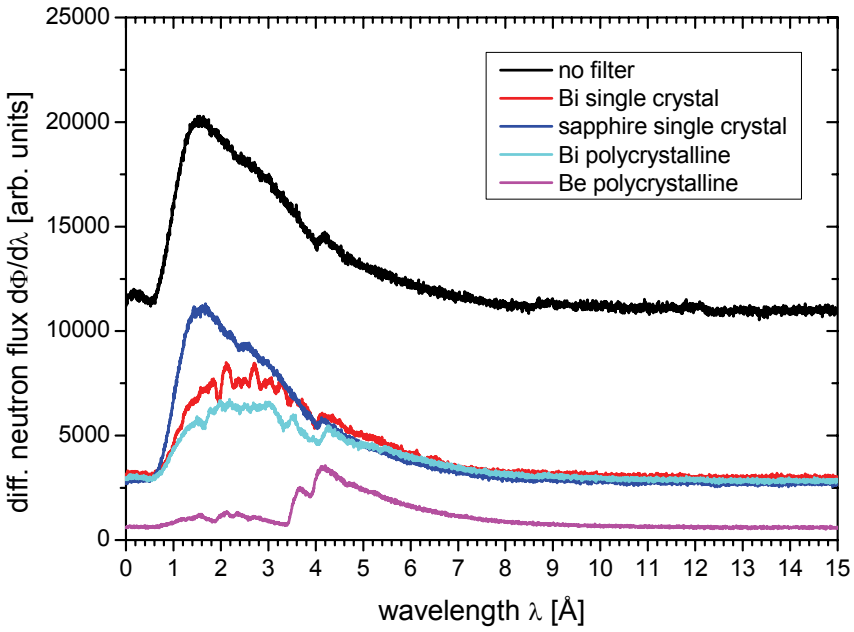

Fig. 3.21: Raw data of the TOF measurements with the different filters. The huge offset especially in the spectrum without a filter is caused by neutrons that are not blocked by the gadolinium coating of the chopper wheel.

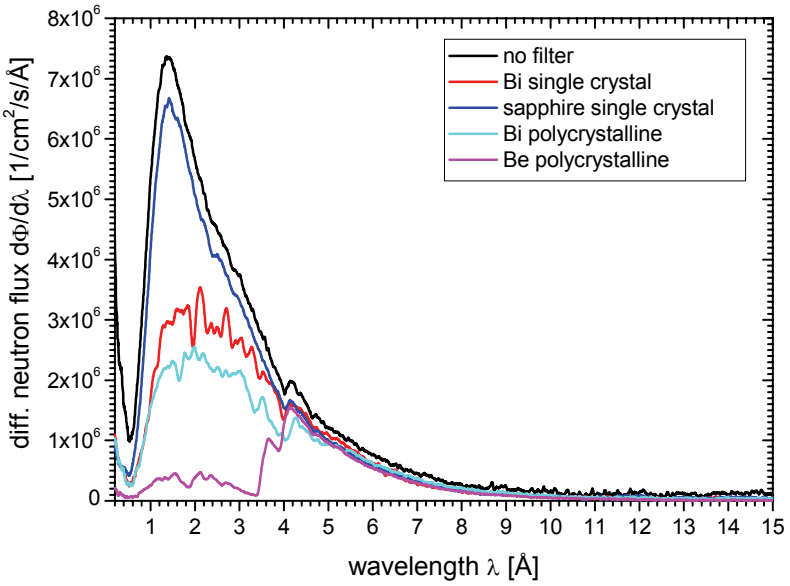

Fig. 3.22: Background corrected data of the TOF measurements. Because the neutron flux for wavelengths above 15Å is negligible at ANTARES, the measured value for 15Å was taken as offset and subtracted.

Fig. 3.21 displays the raw data of the TOF measurements. For each filter the spectrum was accumulated in a 10 hour measurement. The huge offset, especially in the measurement without filter, is mainly caused by epithermal neutrons that penetrate the Gadolinium covered chopper wheel and are counted by the detector uncorrelated to the trigger signal. All filters reduce this background. The fact that beryllium reduces it best although the thickness of the beryllium filter is 1 cm less compared to the other filters demonstrates how strong thermal and epithermal neutrons are attenuated by it.
Also remarkable at the first glance is the measured spectrum with the sapphire filter. It effectively blocks the epithermal neutrons without modifying the thermal and cold part of the neutron spectrum. This result becomes even more evident when the epithermal background in the measurements is subtracted and the corrected data is plotted as shown in Fig. 3.22

and 3.23. The small dip in all five spectra at 4 Å is caused by the aluminum windows of the evacuated flight tubes between the cold source and the sample position.

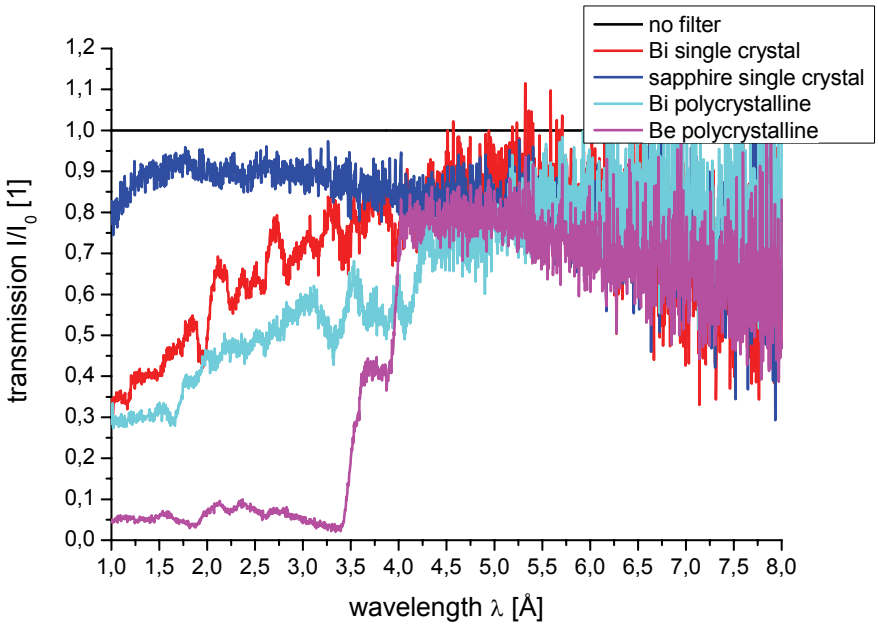

Fig. 3.23: Wavelength dependent transmittance of the filters (normalized on spectrum without filter)

3.2.1.3 CCD measurements

To investigate the effect of the filters on measurements with the standard CCD detector system, radiographies of step wedges were recorded with the different filters. The CCD camera system detects visible light generated in a ZnS + ^{6}LiF scintillation screen by the reaction ^{6}Li(n,α)^{3}H. While the detection efficiency of the ^{3}He counter tube for the TOF setup is close to one for a wide spectrum, this is not the case for the thin scintillation screen, where the energy dependent cross section for the ^{6}Li(n,α)^{3}H reaction, which is proportional to the square root of the wavelength for cold and thermal neutrons, affects the resulting intensity in the CCD detector. Beside this, the influence of the filters on the signal to noise ratio in radiographies can be investigated.

With the sapphire filter the intensity of the signal drops to 83 % of the intensity without a filter. In spite of this loss of intensity, the signal-to-noise ratio is improved. This proves that epithermal neutrons are a major contribution to noise in radiographic measurements at the ANTARES facility.

As a gamma filter, the bismuth single crystal is better than the polycrystalline bismuth because its transmittance for cold and thermal neutrons is higher.

With the beryllium filter the intensity drops down to

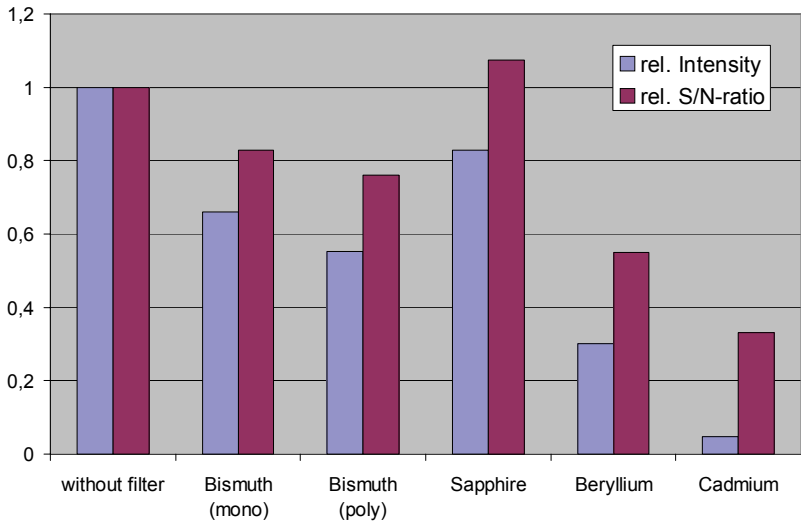

Fig. 3.24: Intensity and signal-to-noise-ratio of neutron radiographies with our standard CCD-detector-setup (8s exposure time; LiF-scintillator) as measured for various filters.

30%, which may be expected when the corresponding neutron spectrum in Fig. 3.23 is considered. The great suppression of thermal neutrons offers several possibilities in neutron radiography. A first direct application of this filter is presented in section 3.2.1.4.

3.2.1.4 A direct application of the Beryllium filter

Neutron radiographies of step wedges of different materials were done without a filter and with a beryllium filter. In the radiograph without a filter there is nearly no contrast between the lead and the iron step wedge. The attenuation of the neutron beam by iron is only slightly higher than by lead. In the radiography with the beryllium filter, the effective spectrum lies below the Bragg cutoff of iron at 4 Angstrom, and the transmission through iron increases. Now the lead attenuates the beam more than the iron. The contrast is still not high, but if the radiography without filter is divided by the radiography with beryllium filter, the contrast becomes clearly visible. This method is an simple way to increase the contrast for certain materials in neutron radiographies.

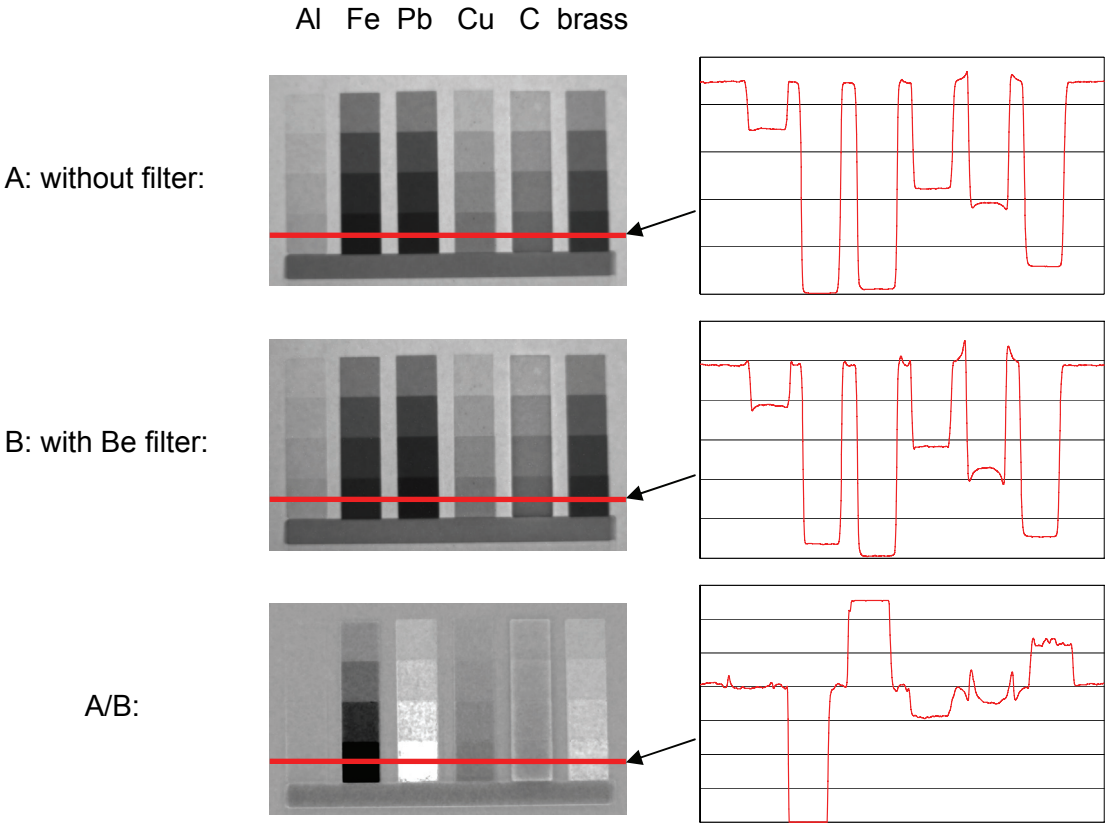

Fig. 3.25: Simple method to increase the contrast in neutron radiographies with a beryllium filter. Neutron radiographs of the metal step wedges were done with and without the beryllium filter and the results were divided by each other. The contrast between the iron and the lead step wedge is greatly increased in the quotient image.

3.2.2 Influence of the detector on image quality

Besides the beam quality, which was considered in the last subsection, the detector has the most significant influence on the signal-to-noise ratio of a neutron radiograph. Therefore this component of the experimental setup was systematically investigated with a series of measurements.
To evaluate different neutron detectors how suitable they are for phase contrast imaging, open beam images and images of step wedges were measured under similar conditions. The quality of an image was characterized by measurements of the intensity and the signal-to-noise ratio. Besides those two parameters, the homogeneity of the sensitivity and optical deformations were measured and the reproducibility of measurements was checked.

3.2.2.1 CCD detector

In the first two years of operation, only a CCD-based detector system was available at ANTARES. All phase contrast measurements at PSI were done with image plates up to then. The disadvantages of the CCD detector compared to the image plate detector were the thermal noise that accumulates for long exposure times, the higher sensitivity for epithermal neutrons due to the LiF scintillator and the worse resolution for similar pixel sizes. Apart from that, CCD detectors have two major benefits compared to image plates: They can be read out more quickly and measurements are very well reproducible, which allows for the application of several image processing techniques to improve image quality like normalization and median filtering.
For one radiography with a CCD detector usually three types of images are measured: a dark current image DI (aka background image or black image), an open beam image OB (also known as flat field image or white image) and one image with the sample in the beam. All three images are measured with identical experimental setups and exposure times.
For the measurement of the dark image, the shutter of the optical system of the CCD camera remains closed. Hence the measured intensity in the dark current image mainly derives from the inherent noise of the CCD detector (read-out noise and thermal noise) and very rarely from radiation that directly hits the CCD chip. In case of the open beam image, the shutter is opened during the exposure time, but the sample is removed from the sample position. The recorded image is a measure for the homogeneity of the beam and the optical system.
The normalization of a recorded neutron radiograph is done by subtracting the dark current image from both, the neutron radiograph and the according open beam image, followed by a division of the two as stated in Eq. (3.1).

$$I_{norm} = \frac{NR - DI}{OB - DI} \tag{3.1}$$

3.2.2.1.1 Inherent noise

The thermal noise of a CCD chip is suppressed by cooling. In Fig. 3.26 the dependence of the gray values in dark images on the temperature of the CCD chip is investigated. The used Andor CCD camera has a dynamic range of 16bit and can thus devide the recorded intensity into 65536 gray values, where in Fig. 3.26 a gray value of 0 corresponds to no intensity and 65535 to maximum intensity. The mean gray value in the DI decreases exponentially with temperature in the region from 20 °C to -20 °C. At lower temperatures the mean gray value approaches asymptotically a lower limit. It never drops below a value of 330, which seems to be the readout noise of the CCD chip. The camera can be cooled down to a temperature of -70 °C without water cooling. As in rare cases the temperature started to rise uncontrolled in long time measurements at very low temperature, the standard setting for phase contrast measurements was -60 °C, where no such temperature drifts occurred and the additional noise compared to -70 °C was marginal.

At this point it has to be mentioned that the noise level in dark current images has continuously increased over the three years of intensive measuring at ANTARES. This degradation of the CCD chip is most probably caused by scattered neutrons and secondary gamma radiation due to activation in the measurement chamber.

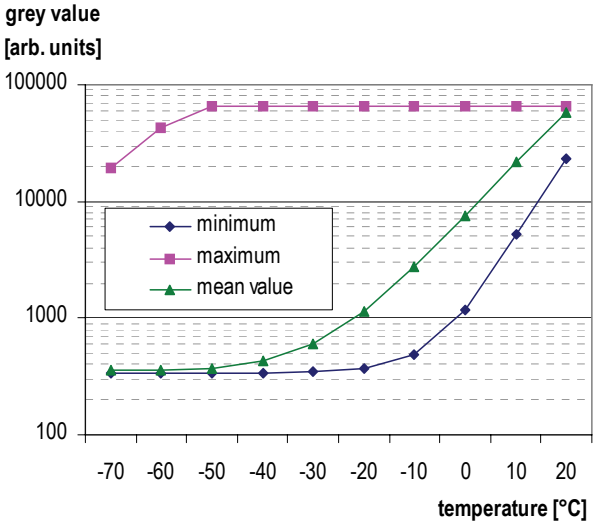

Fig. 3.26: Minimum, mean and maximum gray value in dark images in dependence of the temperature of the CCD chip (5min exposure time).

3.2.2.1.2 Radiation-based noise

In section 3.2.1, gamma radiation and epithermal neutrons in the used beam were found to be the major cause for noise in phase contrast images. Gd- and Li- based scintillators show similar sensitivity for gamma radiation [Kar99]. Concerning epithermal neutrons the energy dependent cross section for Gd-based scintillators shows a steep drop at energies above 50 meV opposite to Li-based scintillators. As the introduction of apertures for phase contrast imaging increase the ratio of epithermal neutrons in the beam, Gd-based scintillators are preferable for these kinds of measurements, although the neutron sensitivity is approximately eight times lower than with standard ^{6}LiF/ZnS:Ag scintillators [Bae02].

Most of the high energetic gamma rays in the neutron beam pass the scintillator screen without any interaction, but the cross section is not zero and thus the gamma radiation also contributes to the background noise. Beside the background noise in the scintillator, gamma radiation that directly hits the CCD chip can produce free charge clouds which are the cause for the so called white spots in CCD images (Fig. 3.19c). To minimize this problem, activation has to be prevented in the measurement chamber and the CCD camera has to be shielded against gamma radiation. If still white spots occur in CCD measurements, software filters can be used to eliminate them, which is described in the following paragraph.

In a single image, gamma filtering is done by comparison of the gray values in small groups of 3x3, 5x5 or more adjacent pixels. If the gray value of a single pixel in such a small array exceeds a certain limit, defined by the mean values of the other pixels plus-minus a certain value, it is replaced by the mean or median gray value in this pixel array. This mathematical operation can lead to severe falsifications of the information in an image, if it is done carelessly and the limits are set too high. Especially in long time measurements, the number of white spots in one image can become very high, even too high for this type of single image gamma filter.
At this point the great advantage of good reproducibility of CCD measurements can be used. One measurement with a long exposure time is replaced by several identically short duration measurements that create a stack of images which differ from each other only because of noise. If this image stack is considered now, the image number can be used as a third dimension for filter algorithms. The gray values of all pixels at the same x-y-coordinate in the different images are compared and replaced by the minimum, median, mean value or another value in the filtered image. In Fig. 3.27 two phase contrast images are compared, which were collected under exactly the same conditions, but one image was recorded in one continuous 40 min exposure time and the other is the result of eight 5 min radiographs.

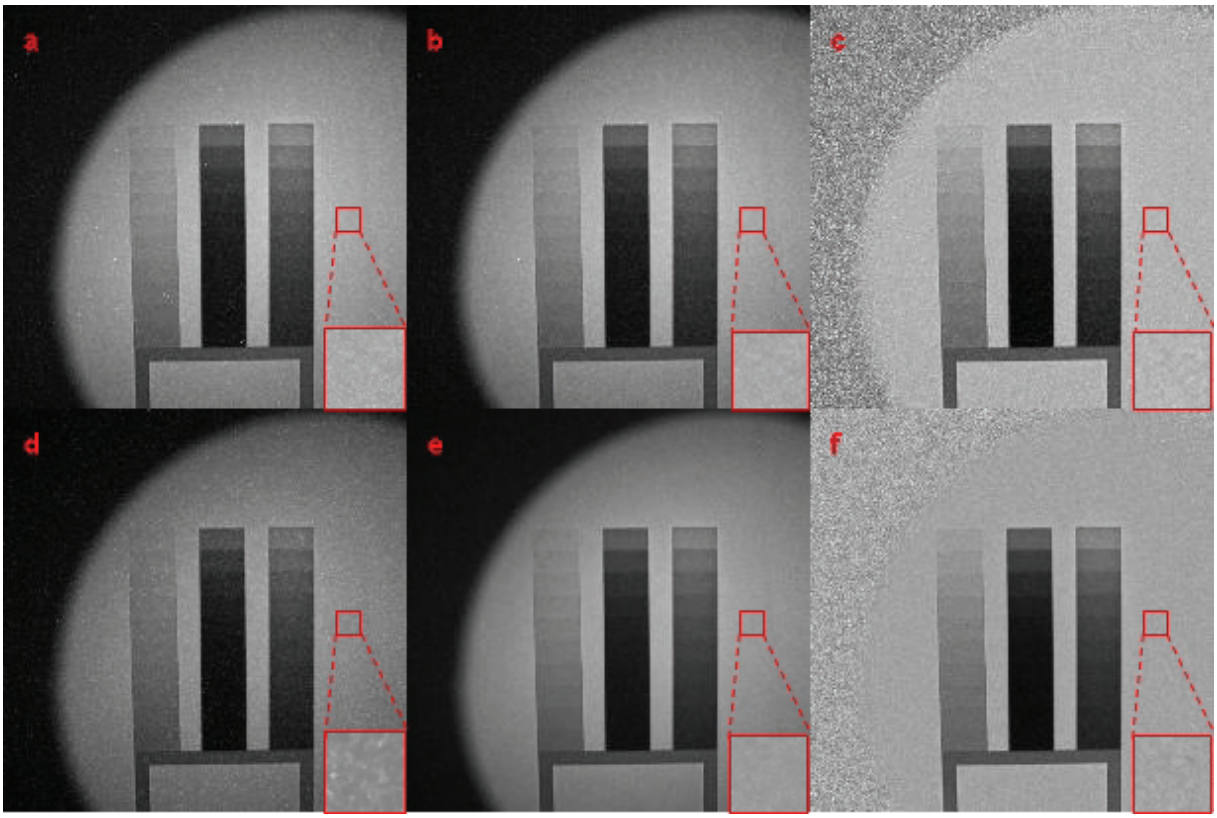

Fig. 3.27: Comparison of phase contrast images of three step wedges (from left to right: Al, Fe and Pb) with a CCD detector: a) 40min without filter, b) 40min with single image gamma filter, c) image b normalized with identically processed open beam image, d) 5min without filter, e) 8 5min images summed up and treated with median filter, f) image e normalized with identically processed open beam image.
In the lower right corner of each image a magnification of the small red outlined area above is displayed.

A first glance at the two normalized images c and f in Fig. 3.27 reveals that the latter has a higher SNR. At a closer look even some white spots are visible in 3.27c, which derive from big white spots that span over several pixels and are thus too large for the used single image gamma filter to correct them. A quantitative measurement of the SNR in the marked and magnified red squares yields a numerical value of 22.14 in 3.27c and 35.14 in 3.27f. On this account, phase contrast radiographies with CCD detectors at ANTARES with exposure times over 15 minutes were always split up in three or more equally long radiographies with exposure times between 5 and 10 minutes. The recorded image stack is first treated cautiously with single image gamma filters and afterwards with a filter that uses the third dimension of the image stack.

3.2.2.1.3 Linearity and homogeneity

Over the whole dynamic range the CCD detector showed a very good linearity. For a constant neutron flux, the dependence of the measured intensity on the exposure time is in good accordance with a linear function with an offset corresponding to the dark current and the DC offset.
Considering the uniformity of the response, the CCD detector shows a greater departure from the optimum. This is mainly caused by two effects: Inhomogeneities in the scintillator (see 3.1.3) and optical effects due to the mapping of the scintillator screen on the CCD chip.
The inhomogeneities caused by the scintillator structure or impurities are usually of small dimension and thus perceived as additional noise in the images. The main optical effect that affects homogeneity is the intensity loss in CCD images towards the edges and especially the corners of the image. This occurs due to the mapping of the flat scintillator screen on the CCD chip with the lens system of the camera (see Fig. 3.17). Both effects can be corrected by open beam normalization (see Fig. 3.16).

3.2.2.1.4 Spatial resolution

The optimization of the scintillator in CCD-based detectors for neutron imaging is a very active field of research today. As the requirements on the detector system for different measurement techniques in neutron imaging can vary a lot, the development of scintillators, which are especially designed for certain types of applications is reasonable. Beside the fundamental decision if lithium or gadolinium is used as converter material, the thickness of the scintillator plate and the mixing ratios of the ingredients are the main parameters for optimization.
The choice of the scintillator thickness is in the first instance an optimization of the neutron sensitivity of the CCD detector. On the one hand, the thicker the scintillator is in beam direction, the higher is the chance to detect a neutron. On the other hand, the scintillator material is opaque for its own light and thus a too thick scintillator decreases the number of photons reaching the CCD chip. In case of a thermal neutron beam and ^{6}LiF/ZnS:Ag as scintillator material, a thickness of 0.42 mm has been found [Bae02] to be a good compromise between self-shielding effects and interaction probabilities. A common way to further improve the spatial resolution is the reduction of the scintillator thickness below this value for optimized sensitivity. At this point the choice of the scintillator thickness becomes a decision between high spatial resolution and high sensitivity.

In 2.1.2.2.1 the point spread function (PSF) was introduced to characterize the spatial resolution Δx of a detector. More precisely, the normalized Fourier transform of the PSF, which is called modular transfer function (MTF) is used for the definition of the spatial resolution. The MTF is normalized to one for frequencies close to zero and drops to zero for higher frequencies. The most common way to express the system resolution is to quote the frequency where the MTF is reduced to either 3%, 5% or 10%. In this work, the MTF10% definition was used in all measurements of the spatial resolutions.
In practice, an edge spread function (ESF) is measured to determine the MTF as it is easier to measure than the PSF. The ESF is the line profile perpendicular to a projection of the edge of an absorber plate in the beam. The derivation of the ESF is a cut through the PSF. The disadvantage of this method is that only one dimension of the PSF is obtained. This is not bothering if the PSF is rotational symmetric, which is the case for circular pinholes. The derivation of the ESF is finally Fourier transformed and normalized to obtain the MTF.

If the blurring of the image is mainly caused by the finite diameter of a circular pinhole aperture, the PSF has a Gaussian shape according to Eq. (3.2) and the ESF, which is the integration of the PSF over one dimension, can be fitted by an error function (Eq. 3.3; Fig. 3.28). If the image blurring comes predominantly from the conversion reaction in the scintillator, the PSF has a Lorentzian shape [Kob90]. In phase contrast imaging, the blurring is usually determined by the beam geometry and thus the ESF can be fitted by the error function.

$$\text{Fit function for PSF:} \quad f(x) = a \cdot e^{-\frac{(x-b)^2}{2\sigma^2}} + c \tag{3.2}$$

$$\text{Fit function for ESF:} \quad g(x) = \frac{a}{2} \cdot \left(\mathrm{ERF}\left(\frac{x-b}{\sigma\sqrt{2}} \right) + 1 \right) + c \text{, with } \mathrm{ERF}(x) = \frac{2}{\sqrt{\pi}} \int_0^x e^{-t^2} dt \tag{3.3}$$

In these functions a, b, c and σ are the fit parameters. For the determination of the spatial resolution in an image, a line profile is taken perpendicular to a sharp edge in the image. The mean values in the constant regions on both sides of the edge determine the parameters a and c. The parameter b, which defines the actual position of the edge, is given by the equation

$$g(b) = \frac{a}{2} + c, \tag{3.4}$$

which marks the position where the intensity has dropped to the arithmetic half of the values left and right of the edge. Finally, the parameter σ, which determines the spatial resolution, is the only remaining parameter to be fit. As the PSF can be expressed by a Gaussian function, its Fourier transform, the MTF, can also be fitted by a Gaussian function with $\sigma' = 1/\sigma$.

Sometimes the spatial resolution is directly measured in real space by fitting the PSF with a 2D Gaussian curve and taking the full width at half maximum (FWHM) or by taking the distance of the 90%-10%-drop in the ESF (Fig. 3.28). The conversion factors between the different spatial resolutions are

$$\Delta x_{MTF10\%} = 0.36\Delta x_{PSF} = 0{,}33\Delta x_{ESF} \tag{3.5}$$

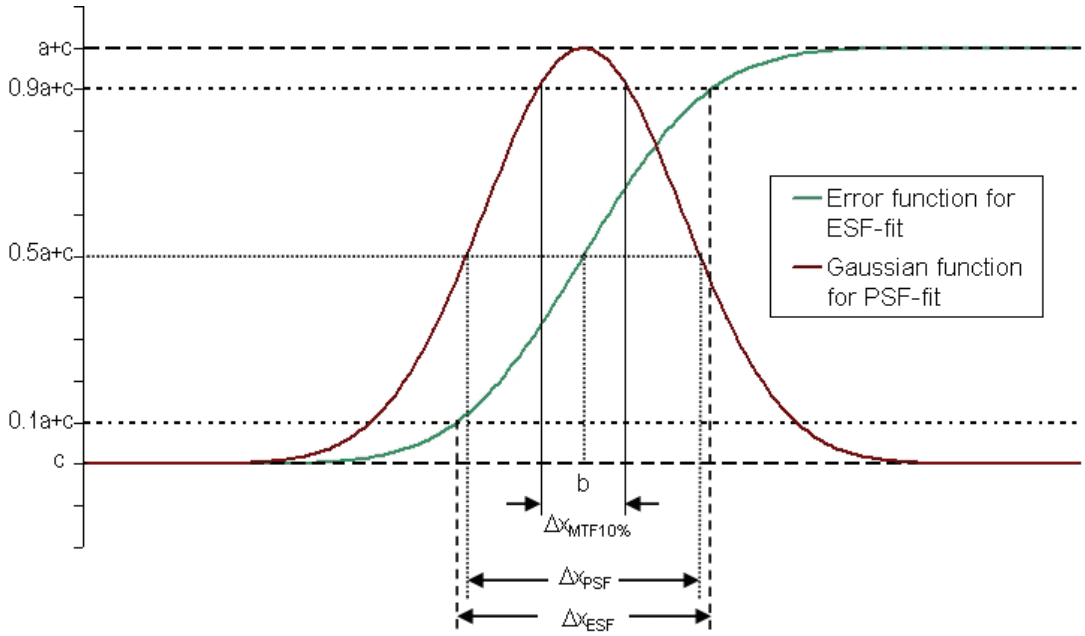

Fig. 3.28: Alternative methods for the determination of the spatial resolution Δx by measurement of the FWHM in the Gaussian fit of the PSF yields a 9% better resolution than the measurement of the 90%-10% intensity drop in the fitted error function in the ESF.

For the calibration of the CCD detector for highest achievable spatial resolution an optical test pattern displayed in Fig. 3.29a is used. After the calibration of the detector the optical test pattern is replaced by the scintillator in the detector plane. In Fig. 3.29 three line profiles are displayed. The first was taken at an edge in an image of the test pattern, the ESF in the middle stems from a radiograph of a gadolinium edge in contact with the scintillator and the last one represents the ESF of a gadolinium edge in 230 cm distance from the scintillator with the LD800 aperture in the beam. In the first ESF, blurring is only caused by the detector system, in the second the scintillator additionally blurs the edge and in the last ESF the beam geometry is the predominant reason for blurring. All three line profiles were fitted with an error function as described above and showed a very good agreement with it. The determination of the spatial resolution $\Delta x_{MTF10\%}$ gave 53 ± 3 μm in the case of the optical test pattern (Fig. 3.19c), 172 ± 5 μm in case of the contact image (Fig. 3.29b) and 1200 ± 10 μm in case of the blurred image of the gadolinium edge in 230 cm distance of the scintillator (Fig. 3.29a). The uncertainties were determined statistically by repetition of the measurement procedure.

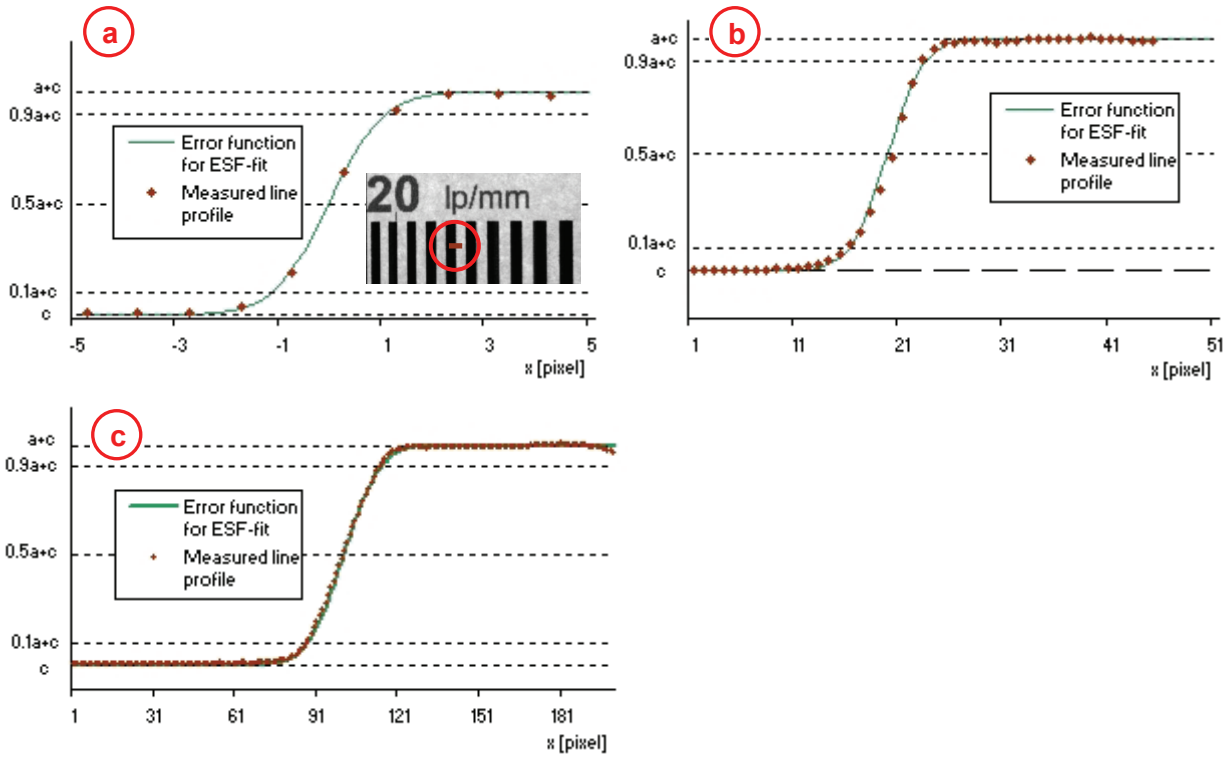

Fig. 3.29: Investigation of the line profiles perpendicular to edges in a) an optical test pattern, b) an image of a Gd edge in contact with the scintillator and c) an image of a Gd edge in 230 cm distance from the scintillator. The size of one pixel was 75 x 75 μm^2.

3.2.2.2 Image Plates

After the good results with image plates at PSI and the first measurements with the CCD detector at ANTARES, which delivered already images of considerably better quality than the CCD measurements at PSI, the expectations on the first phase contrast measurements with image plates at ANTARES were very high. In September 2005 ANTARES borrowed a MAR345 image plate detector from the team of the neighboring powder diffractometer SPODI and soon after that ANTARES obtained a Duerr CR35 and a BAS5000 image plate scanner, what allowed a high flexibility in neutron imaging with image plates.

In all three image plate detectors only image plates of the Fuji ND type were used, which contain a mixture of Gd_2O_3 and $BaFBr:Eu^{2+}$ to convert neutron fluence in a measureable signal (see section 2.3.3 for details). The measured signal primarily depends on three settings of the image plate reader: pixel size, laser intensity and voltage of the photo multiplier.

The chosen pixel size determines the maximal achievable spatial resolution and the intensity per pixel for a given exposure time. Most measurements were done with a pixel size of 50 μm, which corresponds to CCD measurements with a field of view of 10 cm (with a 2000 x 2000 pixels CCD chip). The standard setting for the laser intensity is the maximal possible for a continuous operation of the laser at a given laser diameter. The Duerr CR35 is the only scanner that allows a direct reduction of the laser strength by software settings, which can avoid cross talk between adjacent pixels for very small pixel sizes but leads to a significant reduction of the intensity of the measured signal. The last parameter mentioned, the setting of the high voltage supply of the photo multiplier, controls the amplification of the measured signal by the photo multiplier.

3.2.2.2.1 Effect of the photo multiplier voltage (PMV)

In case of the MAR345 and the Duerr CR35 detector, the voltage of the photo multiplier can be directly set to a certain value up to 1200 V via software (Duerr CR35) or by manual adjustment in the hardware (MAR345). The effect of this parameter on the signal intensity and the SNR in neutron images was investigated in a series of measurements and the results are displayed in Fig. 3.30. Four images were measured under exactly the same conditions, only with different settings for the photo multiplier voltage. The exposure time was 30 seconds and the neutron flux was $4x10^5$ $cm^{-2}s^{-1}$ with the 2 mm pinhole in the beam.

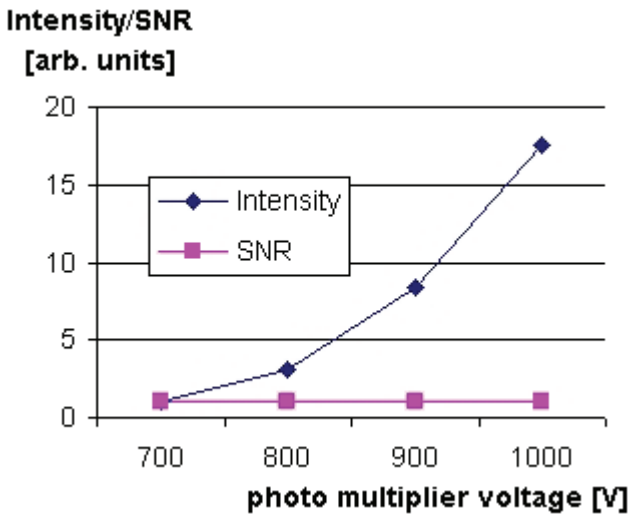

Fig. 3.30: Effect of the photo multiplier voltage on the intensity and the SNR in an image (values for PMV=700V set to 1)

As Fig. 3.30 shows, the intensity of the measured signal increases exponentially with the photo multiplier voltage. An increase of the PMV does however not help to increase the SNR in the image, which is comprehensible as the noise is amplified in the same way as the signal. This result has consequences for a very important characteristic for the Image Plate as a neutron detector: Its detective quantum efficiency (DQE). The DQE is defined by the ratio of the square of the SNR of the measured signal to the square of the SNR of the incoming signal:

$$DQE = \frac{SNR^2_{measured}}{SNR^2_{incoming}} \tag{3.6}$$

The PMV in the range between 700 V and 1000 V, which covers the range of common usage, has no effect on the DQE. Of course a change of the PMV to values far above or below this common range can reduce the DQE.

3.2.2.2.2 Inherent noise

Beside the inevitable readout noise of the image plate detector (IP), three other sources of inherent noise in image plate measurements were found, which depend on the execution of the measurement and can be, at least partially, avoided by the scientist. These are

1. stray light that hits the photo multiplier during the readout process
2. instability of the stored information on the image plate
3. artifacts on the image plate due to an insufficient erasure of the IP

The first two sources of noise are mainly a problem of image plate detectors like the Duerr CR35, where the image plate is separated from the scanner and has to be inserted manually for the readout process. The effect of stray light can be directly investigated with the driver software of the Duerr CR35, where the background due to stray light is dynamically displayed with a time resolution of 1 s. The photo multiplier is already well shielded against stray light by the design of the scanner, but at voltages above 900 V the additional noise due to the stray light in a commonly illuminated room becomes clearly visible and an additional shielding against visible light is advisable.
The decrease of stored information on an IP with time is most severe if the IP is stored in a not perfectly light tight place. The manual process of inserting the IP in the scanner usually additionally exposes the IP to visible light. To reduce the loss of information during this process, the installation of the scanner in a dark room is advisable, which also prevents the

previously described type of noise. Even if the loss of stored information occurs homogeneously, this effect corrupts the reproducibility of measurements and can impede the quantitative analysis of a series of measurement.

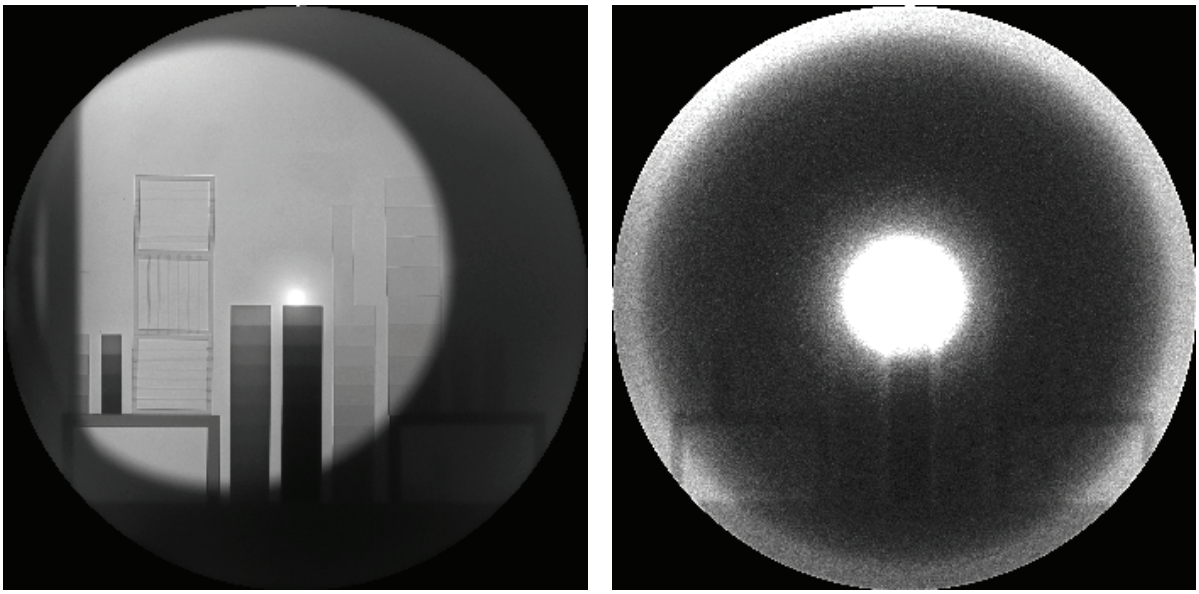

Fig. 3.31: The left image shows a neutron radiograph with a MAR345 detector. On the right hand side, the detector was read out again after three erasure cycles. Many structures of the recorded image are still well visible.

The necessary erasure time for an image plate depends on the intensity and spectrum of the used erasure light and on the intensity of the stored signal. The build-in erasure unit in the MAR345 scanner has a standard erasure time of 3 minutes, which was in many cases insufficient. Even after three erasure cycles artifacts of the last measurement were sometimes visible as displayed in Fig. 3.31. As the MAR345 detector is the sole scanner of the three with a permanently attached image plate that can be programmed to perform automated exposure-readout-erasure-cycles while standing at a fixed position in the beam, it was the only image plate scanner able to perform a tomographic measurement with 200+ projections with reasonable effort. But due to the long time of over 12 minutes per projection for erasure and readout this plan was discarded.

3.2.2.2.3 Radiation-based noise

Only image plates based on the Fuji ND type, which use Gd_2O_3 as converter material, were used for measurements. As gadolinium shows a rapid decrease in the absorption coefficient for neutron energies over 0.7 eV, the contribution of epithermal neutrons to the background noise in image plate measurements is small compared to measurements with LiF as converter material. The sensitivity to X-rays and gamma radiation up to 300 keV is, however, considerable [Kar99] as the measurements displayed in Fig. 3.32 show.

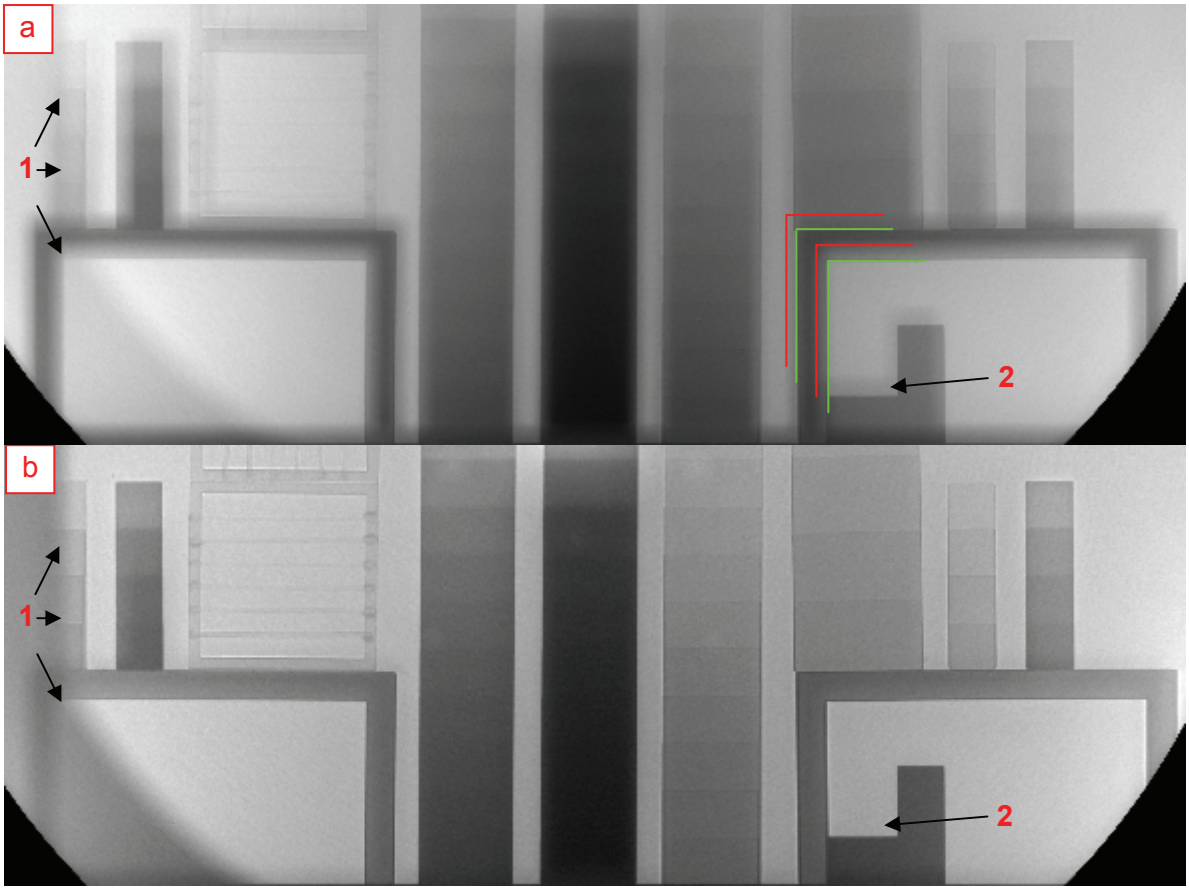

Fig. 3.32: Effect of gamma radiation in the neutron beam in phase contrast radiographs with the MAR345 image plate detector. The upper image (a) was measured without and lower (b) with a 10 mm thick lead filter. The red marked edges are due to gamma radiation, the green due to neutrons (see Fig. 3.33 for explanation).

The images displayed in Fig. 3.32 were measured under phase contrast settings. A closer look on Fig. 3.32a reveals that the image is an overlap of two radiographs, one with neutrons and one with gamma radiation. The radiation which causes the blurred, red outlined shapes can be clearly identified as gamma radiation at the two positions marked in the image as “1” and “2”. At position 1 in image b, the gray shade of a thin plastic frame becomes visible, that was close to invisible in image a. The L-shaped cadmium edge at position 2 creates only a very weak contrast in the gamma image.

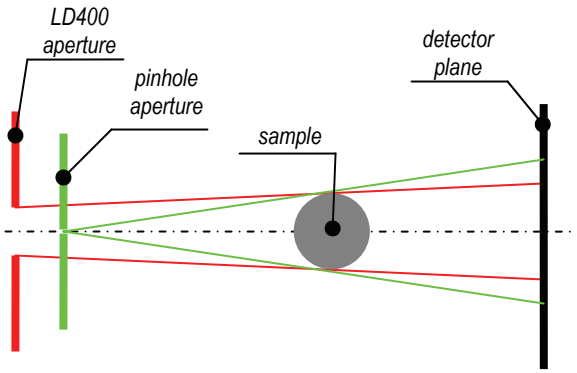

Fig. 3.33: Explanation of the different position of edges in Fig. 3.32a. The pinhole aperture is (apart from the pinhole) opaque to neutrons but almost transparent for gamma radiation.

The overlapping of neutron and gamma images happens in all neutron radiographies, but in this special case, the two images can be separated as the beam geometries for the two types of radiations differ (Fig. 3.33). To get phase contrast, a 2 mm pinhole aperture was introduced a little bit downstream of the LD400-aperture and the sample was placed in 230 cm distance from the detector plane. The pinhole aperture (Fig. 2.9) blocks cold and thermal neutrons very effectively outside the diameter of the pinhole, but is almost transparent for gamma radiation. This has two visible effects: The ratio of gamma radiation in the beam is increased considerably (table 2.2) and

the geometry of the neutron beam differs from the beam geometry of the gamma radiation. The neutron beam, defined by the pinhole aperture, creates the expected phase contrast image, but the gamma radiation, only shaped by the LD400-aperture in the secondary shutter, produces a second, blurred image, which is less magnified.
This gamma background is virtually removed by the introduction of one of the bismuth filters described in 2.23 and 3.2.1.2. If those filters cannot be used as another filter in the wheel is needed in a measurement, the introduction of a 10 mm thick plate of lead is also sufficient to remove gamma background effectively, as Fig. 3.32b shows.

Beside the gamma radiation in the beam, X-rays and gammas due to activation of parts of the image plate detector cause background noise. This problem is most severe in case of the MAR345 detector, where the scanner is directly exposed to the neutron beam. Especially if the detector has not been used for several days, the image plate has to be erased thoroughly before the next measurement, as it has been irradiated meanwhile by the activated inner parts. Also the image plates themselves get activated, what causes background also in case of the BAS5000 and Duerr CR35 detector. This effect however, which was investigated with neutron activation analysis by Thomas Bücherl et al [Büc93], is small even in case of the low signal intensities in phase contrast imaging and can normally be neglected.

3.2.2.2.4 Homogeneity and reproducibility

The used Fuji ND image plates showed a very high uniformity of response. Unfortunately the surface of the image plates can easily be damaged or become dirty, which deteriorates this uniformity and often cannot be repaired. Examples for this kind of defect are the two dark spots marked with a green circle in Fig. 3.2. In case of both scanners, the BAS5000 and the Duerr CR35, where the thin, separate image plates are inserted through an automated transport mechanism, small straight scratches in the transport direction became visible on the IP surface.
In case of the MAR345 detector, a strong radial symmetric inhomogeneity is observed in the dark field image, as displayed in Fig. 3.34. This is caused by the automated readout process, where the circular image plate is rotated, while a read-out laser moves linearly from the edge of the plate to its center. The laser that is used to read out the data should stimulate every position of the image plate for a similar time period, which requires that the rotational frequency of the spinning image plate increases as the laser gets closer to the center of the plate. Close to the center of the plate, the needed angular speed cannot be achieved any more, which leads to an increase of the signal (see Fig. 3.34).

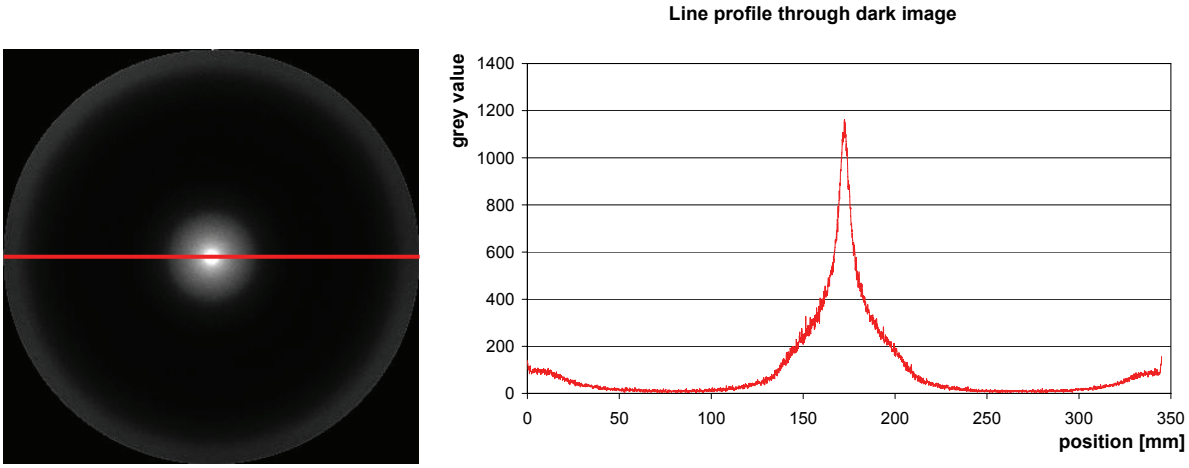

Fig. 3.34: Inhomogeneity in images with the MAR345 detector caused by the readout process.

But this automated readout process of the inseparable, integrated IP is also a great advantage of this detector, as it allows to do multiple measurements under similar conditions, without the need to remove the IP in between for the scanning process. This allows

normalization procedures, which again can be used to correct the inhomogeneities. Only in a small 'dead' region in the center of the detector area, the occurring errors are so big, that it cannot be used for measurements at all and has to be avoided.
This reproducibility of measurements cannot be achieved with the other two scanners. Even with a very precise mounting for the thin, flexible IP in the neutron beam, the automated transport mechanism in the BAS5000 and Duerr CR35 scanner causes tilting and shifting of the images of different measurements. To a certain degree it is possible to use image processing software to correct these misalignments, but the interpolation of gray values especially in rotations of images cause visible artifacts in normalization procedures. Beside these mechanical problems the sources of inherent noise described in 3.2.2.2.2 make the reproducibility of image plate radiographs very difficult and thus the possibility of quantitative neutron imaging.

3.2.2.2.5 Spatial resolution

For the determination of the maximal spatial resolution in image plate measurements, a radiograph of the edge of a 1 mm thick gadolinium sheet in contact with the image plate was analyzed. This measurement was done with all three image plate scanners and in each case with the smallest possible pixel size, which is 12,5 μm for the CR35, 25 μm for the BAS5000 and 100 μm in case of the MAR345. The result of the analysis of the three edge spread functions was, that the value for MTF10% is in all three cases almost the same, namely 127 ± 6 μm for the CR35, 122 ± 6 μm for the BAS5000 and 137 ± 23 μm in case of the MAR345.
This surprising result was further investigated with measurements of the gadolinium edge with the Duerr CR35 image plate scanner with pixel sizes from 12.5 μm to 250 μm. The results are displayed in fig. 3.35 and show a very constant value of the MTF10% value up to a pixel size of 100 μm, although the uncertainty of the measured value increases considerably with the pixel size.

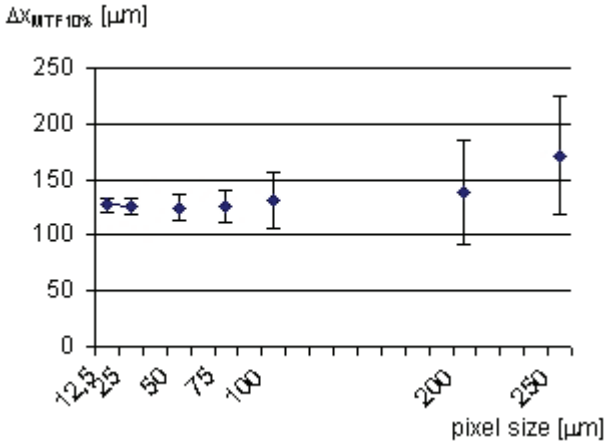

Fig. 3.35: Dependence of the spatial resolution on the pixel size in image plate measurements.

Compared with the CCD detector, which delivered a spatial resolution of 172 μm for similar measurement (Fig. 3.29b), the image plates show a significantly better spatial resolution.

3.2.3 Phase contrast radiography with different apertures

Phase contrast imaging became possible at ANTARES with the installation of the aperture wheel described in section 2.1.2. Six apertures in this wheel were intended for phase contrast imaging and can be divided in three groups: three single hole apertures, two coded apertures and one slit aperture.
The apertures in the wheel can be used either in combination with the LD400 or the LD800 aperture in the secondary shutter. In the following subsections, measurements with the different apertures are analyzed systematically on their image quality and their usefulness for phase contrast imaging.

3.2.3.1 Single hole apertures

By introduction of the single hole apertures, the L/D ratio of the neutron beam at the sample position is increased to 2000 with the 7mm pinhole, 7000 with the 2mm pinhole and 14000 with the 1mm pinhole. The increase of the L/D-ratio reduces the blurring in radiographs due to the beam geometry and allows measurements with increased sample-to-detector distances.
The spatial resolution $\Delta x_{MTF10\%}$ was measured at a cadmium edge in radiographs with the different single hole apertures and with different sample-to-detector distances. The results of these measurements are displayed in Fig. 3.36. The uncertainties in this measurements are between 5 and 10 μm and thus too small to be displayed as error bars in this diagram.

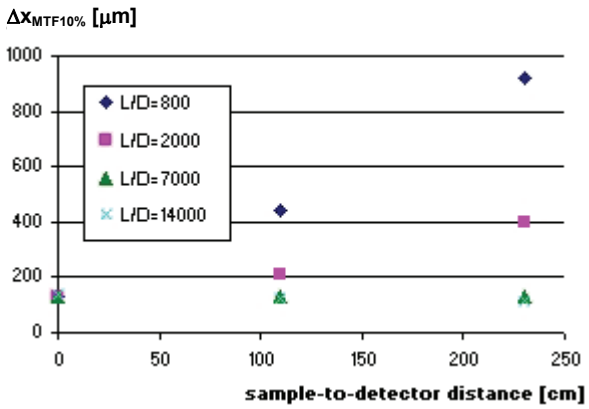

Fig. 3.36: Dependency of the spatial resolution on the aperture and sample-to-detector distance.

Fig. 3.37: Comparison of the contrast at the edges of an iron and an aluminum step wedge in a phase contrast radiograph. The colored lines represent the positions of the line profiles displayed in Fig. 3.38/39.

In case of the radiographs of the sample in contact with the detector plane, the spatial resolution does not depend on the L/D-ratio and is identical for all four aperture sizes. For larger sample-to-detector distances, the blurring of the image due to the beam geometry is clearly visible in case of the two bigger apertures with an L/D-ratio of 800 and 2000. With the 1mm and 2 mm pinholes in the beam, which produce an L/D-ratio of 14000 and 7000 respectively, the spatial resolution stays constant even at a sample-to-detector distance of 230 cm.
The analysis of the measurements with the gadolinium edge delivers an on the first look surprising observation concerning phase contrast. Even with the 1mm pinhole and a sample-to-detector distance of 230 cm no phase contrast at all is visible at the gadolinium edge. Still, the line profiles perpendicular to the edge correspond perfectly to an error function.
The reason for this observation is simply understood, if the contrast mechanism described in section 1.2.3 is remembered. The contrast enhancement at edges occurs as the matter waves that propagate through the medium on one side of the edge interfere in the detector plane with the waves that propagate through the medium on the other side. If the attenuation of the neutrons in one of the two media is much higher than in the other, no phase contrast is visible. And this is definitively the case for the interface between gadolinium and air.

This effect was investigated more systematically with two step wedges made of aluminum and iron. The attenuation coefficient of iron is more than 10 times higher than that of aluminum. In Fig. 3.37, a phase contrast radiograph of the two step wedges with a 2 mm pinhole and a sample-to-detector distance of 230 cm is shown. In case of the aluminum step wedge phase contrast is clearly visible as a black line as the minimum peak on the aluminum side of the edge and a white line as the maximum peak on the air side of the edge. The thickness of the aluminum step wedge in beam direction increases from 5 mm in the uppermost step to 50 mm in the step at the bottom.

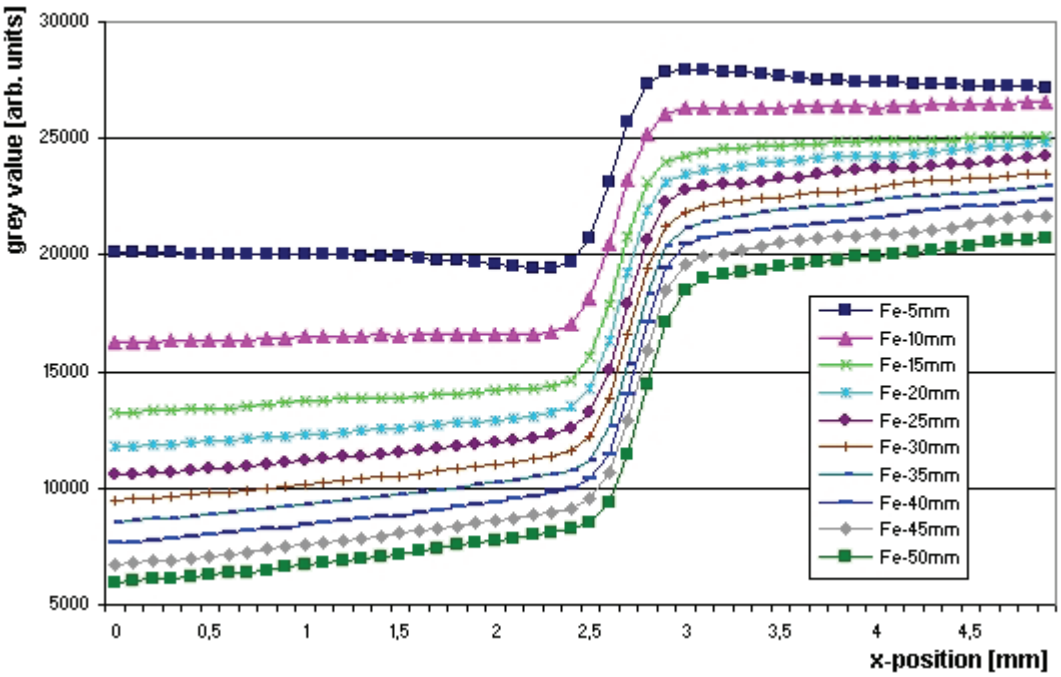

Fig. 3.38: Line profiles through the edges of the iron step wedge as marked in Fig. 3.37. The line profiles were vertically separated from each other by addition of the constant value 500. Except the ESF at the 5mm thick iron step all line profiles can be fitted very well by an error function.

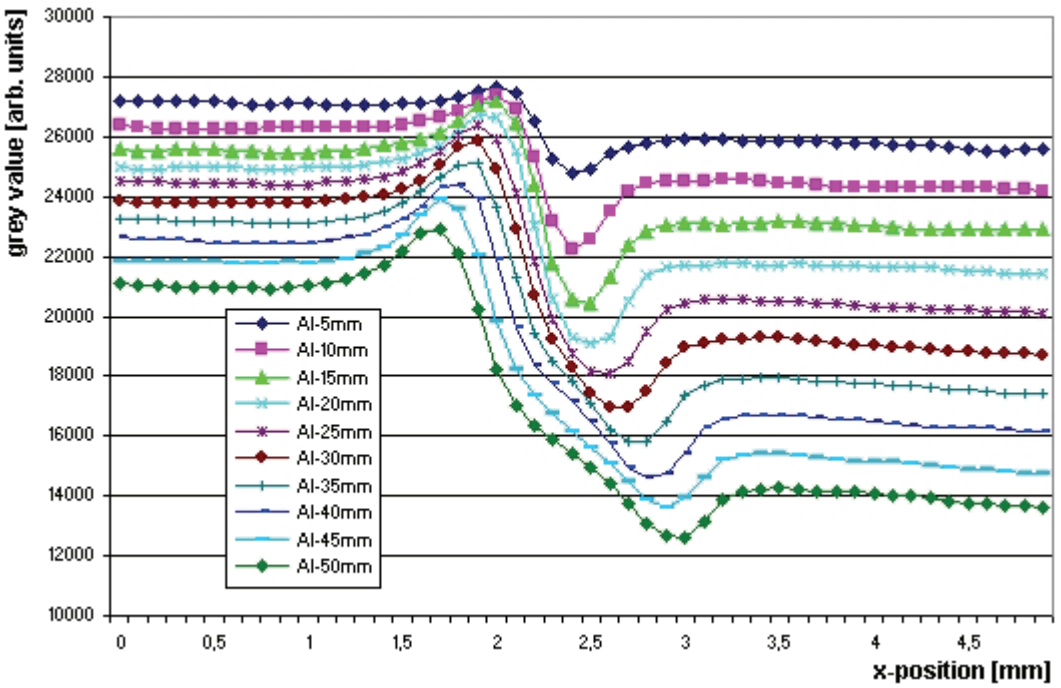

Fig. 3.39: Line profiles through the edges of the aluminum step wedge as marked in Fig. 3.37. The line profiles were vertically separated from each other by addition of the constant value 500. The distance between minimum and maximum peak increases with the thickness of the edge.

In Fig. 3.38 line profiles perpendicular to the edges of the two step wedges are displayed. The positions of the different line profiles are marked in Fig. 3.37 with a line of the corresponding color.
At the edges of the iron steps with thicknesses over 10 mm only absorption contrast can be observed. The shape of the edge spread functions corresponds very well to an error function. Only for the thinnest iron step with a thickness of 5 mm the line profile deviates strongly from an error function and even shows flat peaks. This measurement clearly demonstrates that phase contrast imaging is only applicable for weakly attenuating samples.
A very common, weakly attenuating material of technical interest is aluminum. The line profiles at the edges of the aluminum steps show clearly the typical phase contrast peaks. With the thickness of the steps in beam direction also the distance between the minimum peak and the maximum peak increases. This derives from the dependence of the angular deviation of the propagation direction from the gradient of the phase shift (Eq. 1.32). The complicated structure of the line profiles at the thick aluminum steps arises from the superposition of the phase contrast signal with the absorption contrast. For distance measurements, the actual position of the edge is needed, which is not directly visible any more in phase contrast images. It can be calculated easily as the arithmetic mean of the positions of the two peaks.

A closer look on the measured data in Fig. 3.36 reveals that in case of the 1 mm and 2 mm pinholes the spatial resolution improves with the sample-to-detector distance. The reason for this is the magnification of the image. The magnification factor m at ANTARES with pinholes is

$$m = 1 + \frac{R}{1400\text{cm}}, \tag{3.7}$$

where R is the sample-to-detector distance in cm. The magnification at ANTARES in phase contrast imaging is relatively small because of the large distance of 14 meters between pinhole aperture and sample position. This distance could not be reduced as the neutron beam is not accessible in these 14 meters because of the shielding and the flight tube. At the projected new imaging beam line at FRM-II the neutron beam will be accessible at every distance downstream the secondary shutter, which shall allow a very flexible choice for the position of the sample and detector plane.
Even if no phase contrast is needed, neutron imaging with large sample-to-detector distances can bring great advantages, as it is a possibility to circumvent the limited spatial resolution of neutron detectors. As described in section 2.3 these limitations are caused by the conversion reactions used to detect the uncharged neutron. A magnification factor of 2 and higher is without great efforts feasible and improves the resolution in the sample plane for a given spatial resolution of the detector by a similar factor. Even higher magnification factors can be achieved by application of diverging neutron lenses as described in section 2.1.3 and displayed in Fig. 3.16. Neutron optical devices can be also used to compensate the intensity loss due to the pinhole (Fig. 2.15).

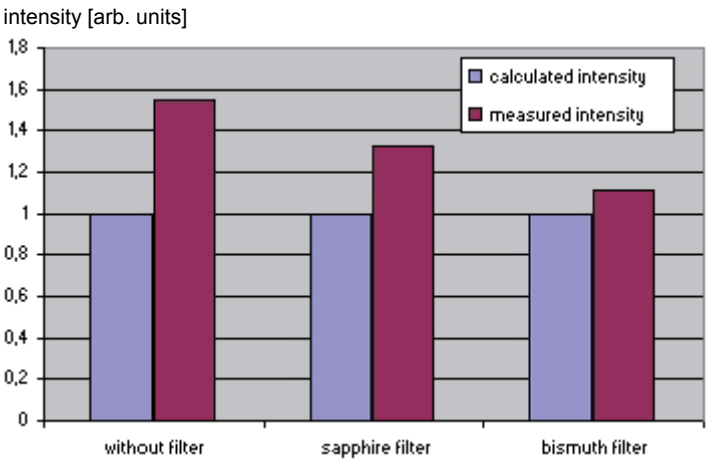

Fig. 3.40: Deviation of the measured from the calculated intensity with the 1mm (b3) pinhole aperture and different filters in the beam (the calculated intensity is always set to 1).

With the introduction of apertures the ratio of gamma radiation and epithermal neutrons in the beam is

increased. Especially in the first version of the apertures, where only a 2 mm thick cadmium sheet was used as aperture material, gamma radiation and epithermal neutrons were practically not blocked by the aperture at all. By upgrading the apertures to the sandwich structure described in section 2.1.2.2 and in Fig. 2.9, the noise in images due to epithermal neutrons was greatly reduced. The gamma radiation however was still able to penetrate this sandwich structure easily and caused gamma background in images as displayed in Fig. 3.32a. In table 2.2 the neutron flux at the sample position was calculated for the different apertures. This calculation was done on condition that the neutron flux is proportional to the opening area of the aperture. In fig. 3.40, the expected intensity of a CCD measurement with the 1mm pinhole aperture was calculated in the same way from the measured intensity with the LD800 aperture and is then compared with the measured intensity. This comparison was done with no filter, the sapphire filter and the bismuth filter in the beam. Without a filter in the beam, the measured intensity is over 50% higher than the calculated. With the introduction of filters this deviation is reduced significantly, which clearly proofs that there are types of radiation in the beam which are not blocked by the sandwich aperture.

The fact that the bismuth filter reduces this deviation more efficiently than the sapphire filter shows that more gamma radiation penetrates the aperture than epithermal neutrons. This result was expected as the apertures were especially upgraded to reduce the epithermal neutron background. In fig. 3.41 the reduction of the intensity by a sapphire filter and a bismuth filter are displayed for all single hole apertures and the 2 mm cadmium sheet. The smaller the opening of the aperture is, the bigger is the reduction of the intensity by the filters. In the special case of the 2 mm cadmium sheet (which was the aperture material of the first apertures), the intensity loss is huge and the intensity loss with the bismuth filter is higher than with the sapphire filter. This result already shows that the upgrade of the aperture structure reduced the epithermal background effectively. This improvement becomes even more evident, if the intensity with the cadmium sheet is directly compared to the intensities with the new sandwich apertures as done in fig. 3.42. The measured intensity in the detector plane with the 2 mm thick sheet without a pinhole (b7) is ten times higher than with the new sandwich aperture with a 1 mm pinhole aperture (b3). The sapphire filter reduces the intensity to 17% in case of the cadmium sheet and to 74% in case of the 1 mm pinhole.

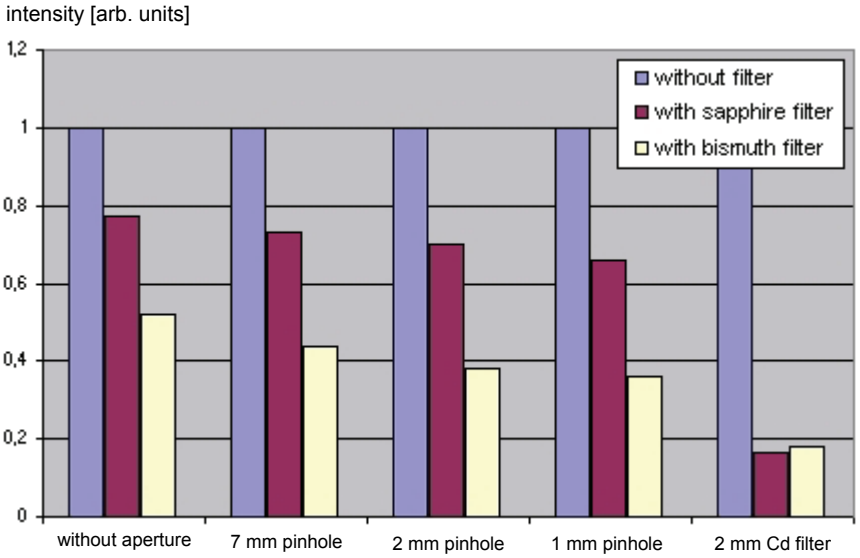

Fig. 3.41: Effect of the sapphire and bismuth filter on the measured intensity, with different apertures in the beam (intensity without filter is always set to 1).

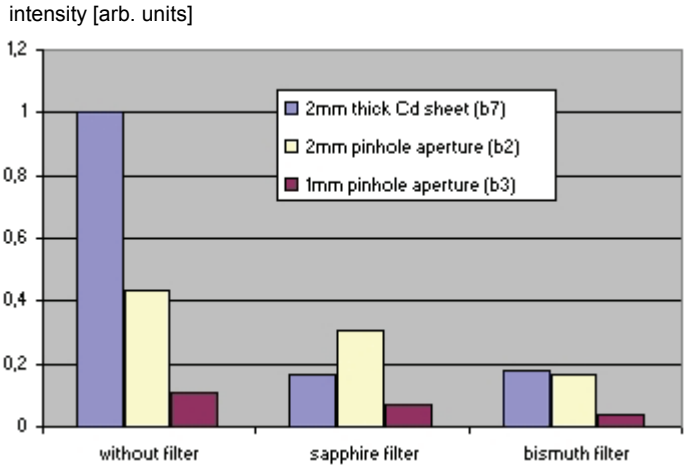

Fig. 3.42: Comparison of the measured intensities with the 2 mm thick cadmium sheet and the new pinhole apertures with sandwich structure (intensity with Cd sheet and without filter was set to 1).

Hence the ratio of radiation, which is attenuated by the sapphire filter, is 3.2 times higher with b7 than with b3.
With the bismuth filter the intensity drops to 19% with b7 and to 43% with b3. This difference in the intensity loss with a gamma filter was not expected, as the ratio of gamma radiation in the beam should be similar for both types of apertures. But it has to be kept in mind that the 5 cm thick bismuth filter does not only have an effect on gamma radiation, but also alters the neutron spectrum (see fig. 3.21).
Before the installation of the multi filter, a simple method to reduce the epithermal and gamma background was to use the pinhole apertures in combination with the LD800 aperture instead of the LD400 aperture. With the pinhole apertures in the beam, the intensity in the homogeneously illuminated area in the detector plane should be independent of the aperture size in the secondary shutter. This is not the case as the measured intensities displayed in fig. 3.43 show. The additional intensity with the LD400 aperture in combination with b1, b2 and b3 is only due to the increased flux of gamma radiation and epithermal neutrons that hit the pinhole apertures. In case of the 7 mm aperture (b1) the intensities with the LD400 and the LD800 aperture is almost the same. This is because the 7 mm pinhole perfectly matches the diameter of the direct neutron beam at this position (see fig. 3.44). The neutron flux outside these 7mm is very small as the neutron beam is shaped very precisely by long collimators [Grü05]. Pinhole apertures with a smaller diameter have to block parts of the direct beam, which works properly only for cold and thermal neutrons. The smaller the diameter of the pinhole, the bigger is the surface of the aperture that is hit by the full beam and the higher is the ratio of gamma radiation and epithermal neutrons in the beam. This increasing difference in intensity between decreasing diameter of the pinhole aperture is clearly visible in figure 3.43.

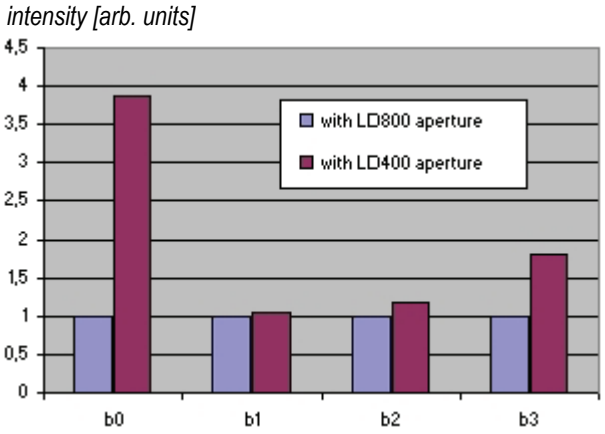

Fig. 3.43: Effect of the aperture in the secondary shutter on the intensity in measurements with pinhole apertures.

3.2.3.2 Coded apertures

The results of the measurements in the previous subsection have shown that the ratio of unwanted, noise producing radiation in the neutron beam increases with the ratio of the beam that is blocked by the apertures in the aperture wheel. This is because of the incapability of the aperture materials to block gamma radiation and epithermal neutrons. As described in section 2.1.2, coded apertures are a possibility to increase the opening area of a pinhole aperture without lowering the L/D ratio. The trick is to create multiple neutron beams with a high lateral coherence that create multiple overlapping images of the sample in the detector plane. To be able to deconvolve the measured image, the intensities of the created neutron beams should be equal. Therefore the area with the different holes of the aperture has to be illuminated homogeneously with neutrons. This is only fulfilled for one of the two apertures in the secondary shutter as the sketch of the two beam geometries in Fig. 3.44 shows.

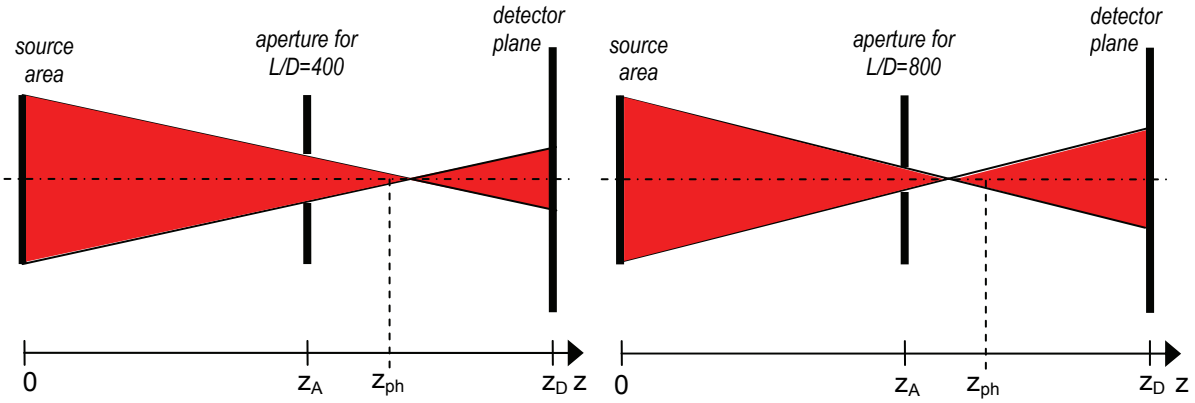

Fig. 3.44: The homogeneously illuminated area (red color) in the plane of the aperture wheel has a diameter of 4 mm with the LD400 aperture (left image) and 9 mm with the LD800 aperture (right image).

The shadow of the LD800 aperture (Fig. 3.45) can be used to determine the orientation of the installed coded aperture. With the coded aperture, the diameter of the homogeneously illuminated area in the sample plane is greatly reduced. The diameter of the biggest possible homogeneously illuminated circular area is 21.1 cm with the 6-hole aperture (b5) and 19.5 cm with the 10-hole aperture (b4). Within this fully illuminated area, the intensity is n times higher than the intensity with one single hole, where n is the number of holes in the aperture.

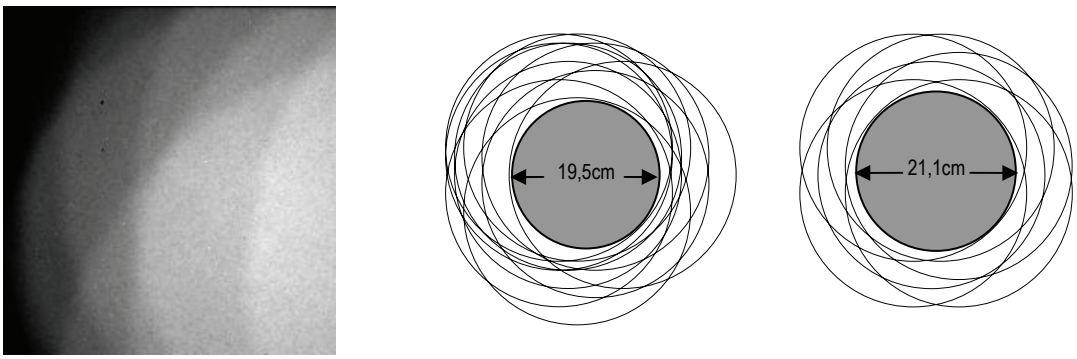

Fig. 3.45: Overlapping fringes of the collimator shadows of the single pinholes of a coded aperture. Measured image (left) and true-to-scale (1:10) simulations of the fringes for the 10-hole aperture (middle) and the 6-hole aperture (right). The structure of the overlapping fringes can be used to determine the exact orientation of the installed aperture.

For a comparison with the 1 mm and 2 mm single hole apertures, radiography under phase contrast conditions of the aluminum step wedge shown in Fig. 3.37 was done with the 10-hole coded aperture b4 (Fig. 2.16). The CCD detector system described in section 2.3.2 was used and the sample-to-detector distance in this measurement was again 230 cm. The raw, unprocessed images with the apertures b1, b2, b3 and b4 are displayed in Fig. 3.46.

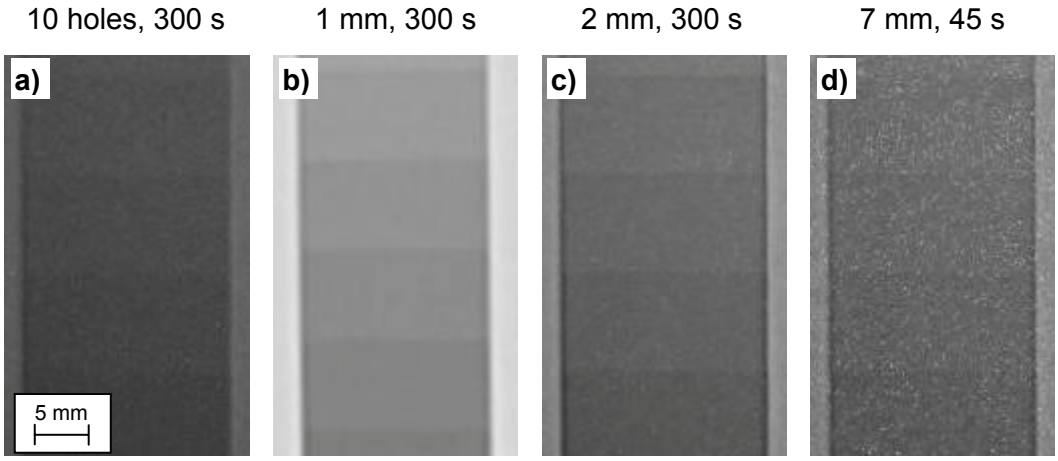

Fig. 3.46: Unprocessed radiographs of an aluminum step wedge at a distance of 230cm from the detector plane with different apertures. From left to right: a)10-hole coded aperture (b4), b)1mm (b3), c)2mm (b2) and d)7mm (b1) pinhole aperture.

The exposure time for the radiographs with aperture b2, b3 and b4 was 300 seconds. With the 7 mm aperture, the dynamic range (16bit) of the CCD camera was already fully used with an exposure time of 45 seconds. The mean gray values are higher in the radiograph with the coded aperture than with the pinhole apertures b2 and b3, which confirms the higher neutron flux at the sample position with the multi-hole aperture. Phase contrast is visible in all four radiographs, but with the coded aperture, the blurring is very severe and comparable to the blurring with the 7mm pinhole. For the reconstruction of the image with the coded aperture, the PSF with it had to be calculated for the given beam geometry. Calculations of the resulting PSF and its Fourier transform, the modular transfer function MTF, with this coded aperture are displayed in Fig. 3.48. To the right of the MTF is a 2D-plot of the autocorrelation function of the PSF. In section 2.1.2.2.2 coded apertures with NRA patterns were proposed for neutron imaging as the pattern itself can be used as the decoding pattern. The autocorrelation function of the PSF with a NRA pattern has a very strong central peak and flat side lopes. But this is only the case for the idealized, theoretical PSF, which was simulated in the top row of Fig. 3.48. In practice, the PSF with the NRA pattern is not a set of ten perfect pillow box functions, but a landscape of ten connected hills that is created by a convolution of the idealized PSF with a Gaussian function.

A three-dimensional visualization of the calculated blurred PSF of the 10-hole coded aperture is displayed in Fig. 3.47. The FWHM of the resulting autocorrelation function is comparable to the FWHM of the PSF with a single hole aperture with a diameter of 6.8 mm, but its shape differs considerably from a Gaussian function as shown in the image in the lower right corner of Fig. 3.48.

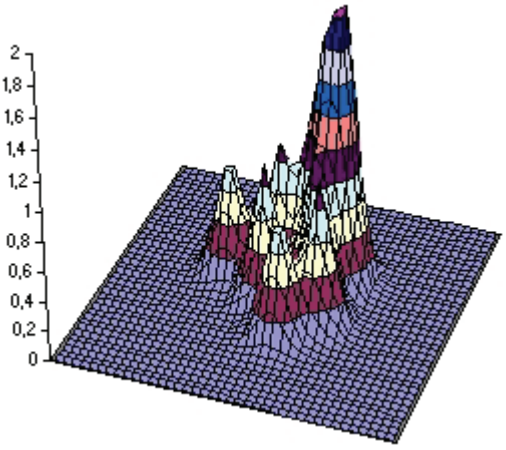

Fig. 3.47: 3D Visualization of the blurred PSF with the 10-hole coded aperture.

The effect of this blurring on the MTF and the autocorrelation function is severe and is displayed in the second and third row of images in Fig. 3.48. The autocorrelation function transforms from an almost perfect delta function to a broad mountain. The images in the bottom row represent the situation in the measurements. The blurring of the PSF was determined by the analysis of blurring in images with the 1mm single pinhole.

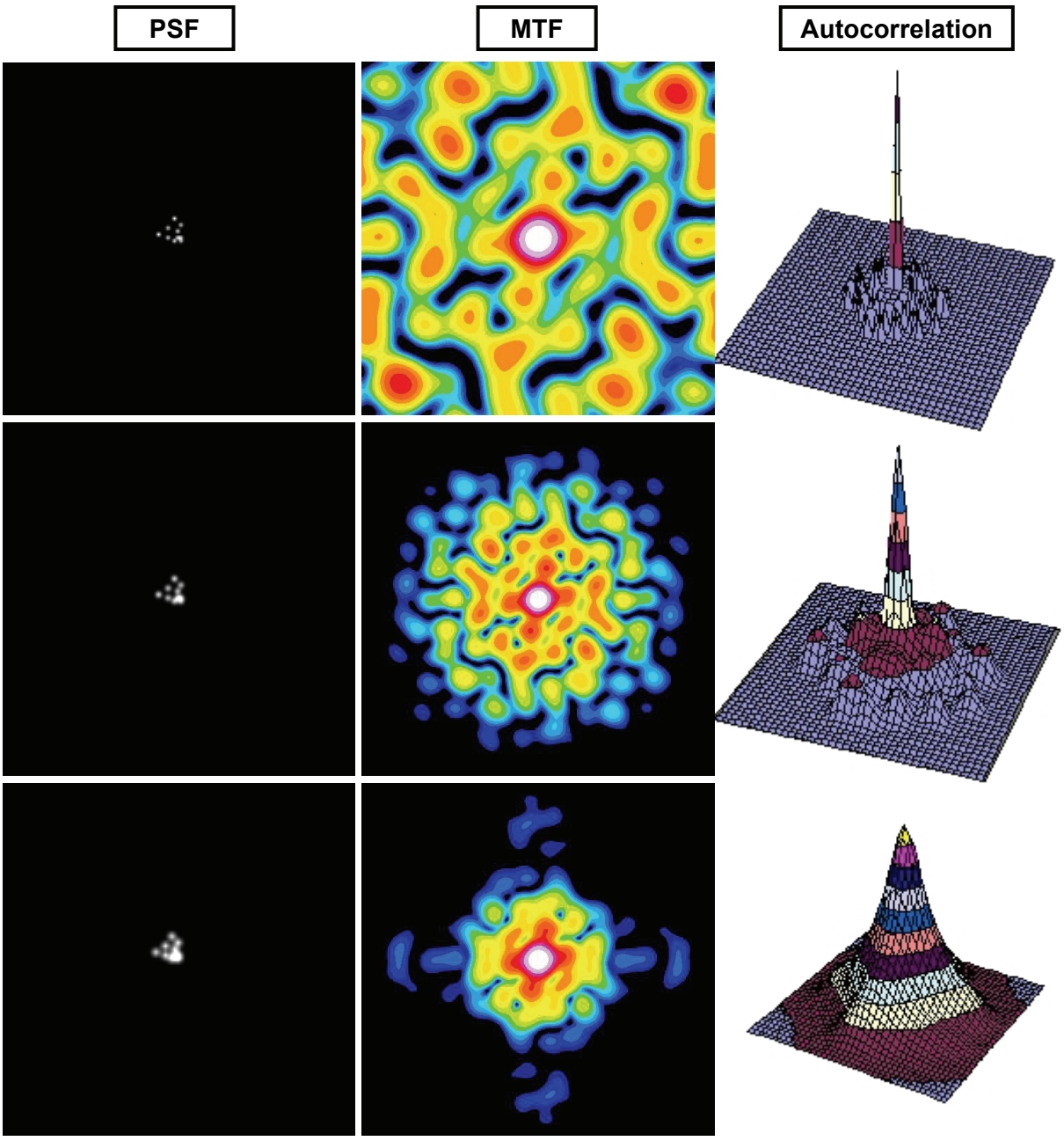

Fig. 3.48: Calculations of the PSF (left), MTF (middle) and autocorrelation function (right) for measurements with the 10-hole coded aperture (b4) with a sample-to-detector distance of 230 cm. The calculations in the top row were done for the idealized case that the PSF is a set of ten perfect pillow box functions. In this case, the MTF fills the complete frequency domain and the autocorrelation function is very close to a 2D delta function. In the two rows below, the effect of the blurring by the scintillator is considered, which causes the autocorrelation function to depart more and more from a delta function.

The reconstructed image by deconvolution with the PSF is displayed in Fig. 3.49a. The broad side lopes of the autocorrelation function create a dim shade over the whole image. In an attempt to further improve the image quality, the calculated autocorrelation function was used as the kernel to deconvolve the reconstructed image. The deconvolution was done as an iterative deconvolution based on the DAMAS algorithm [Dou05] and the result is displayed right next to the reconstructed image as Fig. 3.49b.

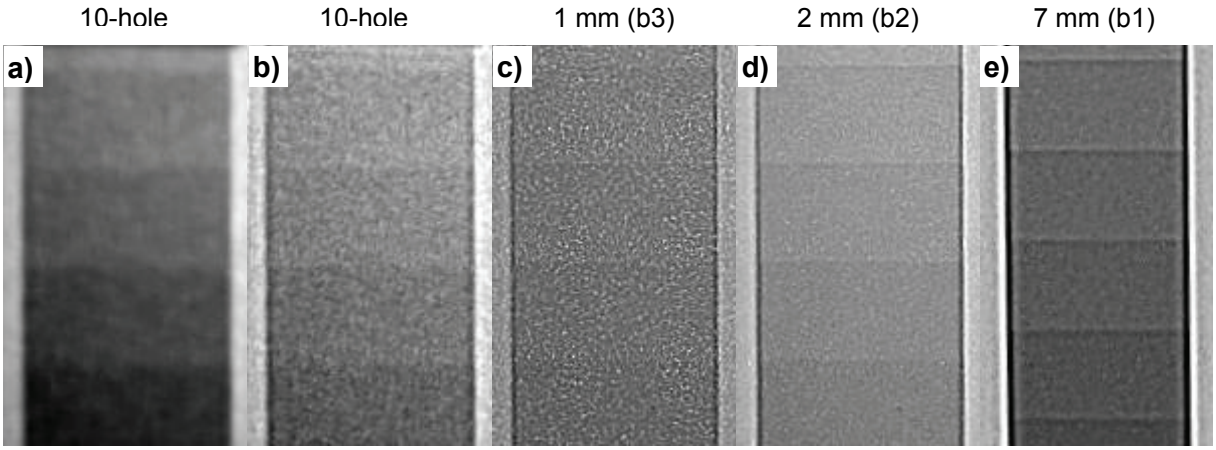

Fig. 3.49: Comparison of the reconstructed images: a) correlation of image with 10-hole aperture with its PSF, b) iterative deconvolution of image a with the autocorrelation function as kernel and the iterative deconvolution of the images with 1mm (c), 2mm (d) and 7mm (e) single-hole apertures with the corresponding Gaussian PSF as kernel.

With the same algorithm for iterative deconvolution, the raw phase contrast images with single-hole apertures displayed in Fig. 3.49b-d were processed. The kernels for the deconvolution algorithm were the corresponding bell-shaped Gaussian PSF. A strong contrast enhancement at the edges is visible for all four apertures. A closer look on the SNR in the images reveals the advantages of the correlation technique compared to deconvolution algorithms. The SNR in the deconvolved images is approximately halved on average, whereas the SNR in the correlated image is significantly increased compared to the unprocessed image. It is comparable with the SNR in the unprocessed image with the 7 mm pinhole.

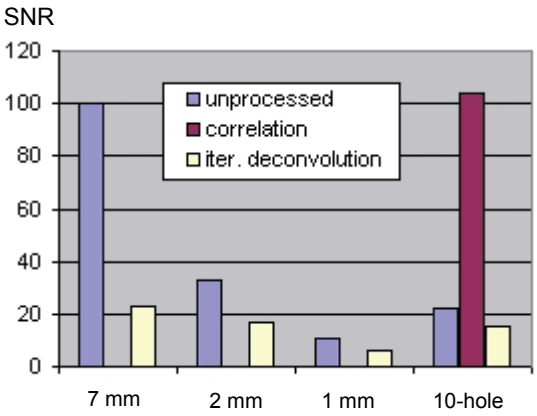

Fig. 3.50: Effect of correlation and deconvolution algorithms on the signal-to-noise ratio in phase contrast images with single hole apertures and coded apertures.

For an exposure time of 300 s, phase contrast images with the pinhole apertures b2 and b3 produce a much better phase contrast signal and deliver much more information on the inner structure of a sample than the investigated coded aperture. Concerning the spatial resolution, they are superior to coded aperture with holes of a similar diameter. The application of coded aperture can be beneficial however, if a high time resolution is needed in phase contrast imaging or the exposure times have to be short for any other reason. In those cases, the increased neutron flux with the multi hole aperture can help to achieve a sufficiently high SNR for a further analysis of the data. An example for this kind of measurement would be the dynamic phase contrast radiography of aluminum foam under stress.

3.2.3.3 Slit aperture

If a high lateral coherence in just one dimension is sufficient, it is reasonable to avoid unnecessary intensity losses and to switch from a pinhole aperture to an aperture with a narrow slit. At ANTARES a 1 mm thin vertical slit was installed for this reason. The L/D ratio with this slit is 14000 in the horizontal direction and 400 or 800 in the vertical direction, depending on the chosen collimator in the secondary shutter. A phase contrast radiograph of the already well known aluminum step wedge with this slit aperture is shown in Fig. 3.51. The sample-to-detector distance was 230 cm. The thickness of the steps decreases from the left to the right from 25 mm to 5 mm. The horizontal edges of the step wedge are extremely

blurred, the vertical edges show the characteristic contrast enhancement of propagation-based phase contrast images (Fig.3.52a). The maximum peak and the minimum peak along the horizontal edge are caused by total reflection. It can be clearly distinguished from a phase contrast signal, as the position of the peak is independent of the thickness of the step (which decreases from 25 mm to 5 mm from left to right). The thickness of the step only affects the intensity of the peak as the ratio of totally reflected neutrons increases with the increasing surface parallel to the beam direction. All neutrons that hit the surface in an angle smaller than the critical angle (Eq. 1.24) α_c(Al, 1.8Å) = 0.084° are totally reflected. For the given sample-to-detector distance of 230 cm this causes a severe modification of the measured intensity in an area of 3.4 mm (37 pixel in this radiograph) above and below the horizontal edge in the image. The resulting beam profile perpendicular to the horizontal edge (blue line in Fig. 3.51) is displayed in Fig. 3.52b and is produced by the superposition of the blurred ESF and the intensity shift caused by total reflection.

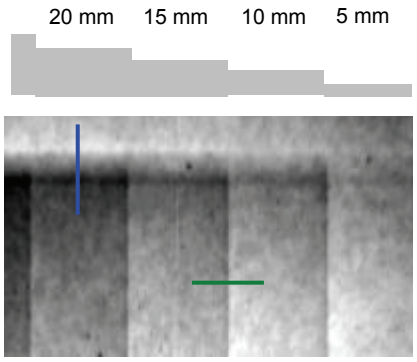

Fig. 3.51: Phase contrast radiograph of an aluminum step wedge with the vertical 1 mm slit aperture and a sample-to-detector distance of 230 cm. The line profiles along the blue and green line are displayed in Fig. 3.52.

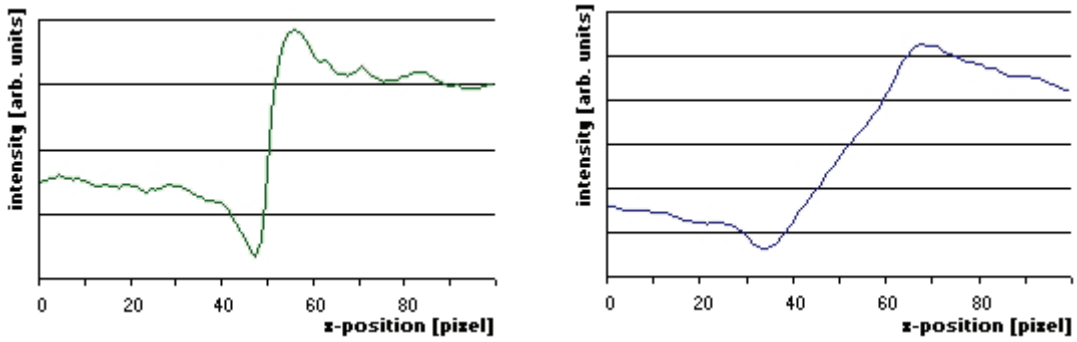

Fig. 3.52: Line profiles along a vertical edge (green line) and a horizontal edge (blue line) in Fig. 3.51. The peaks in the green line profile are characteristic for propagation-based phase contrast, whereas the peaks in the blue line profile are mainly caused by the superposition of a blurred ESF and the intensity transport due to total reflection.

A very important application of the slit aperture and the main reason for its installation at ANTARES was its ability to serve as a source for a grating-based neutron shearing interferometer as described in section 1.2.2. A schematic of the experimental setup is shown in Fig. 3.53.

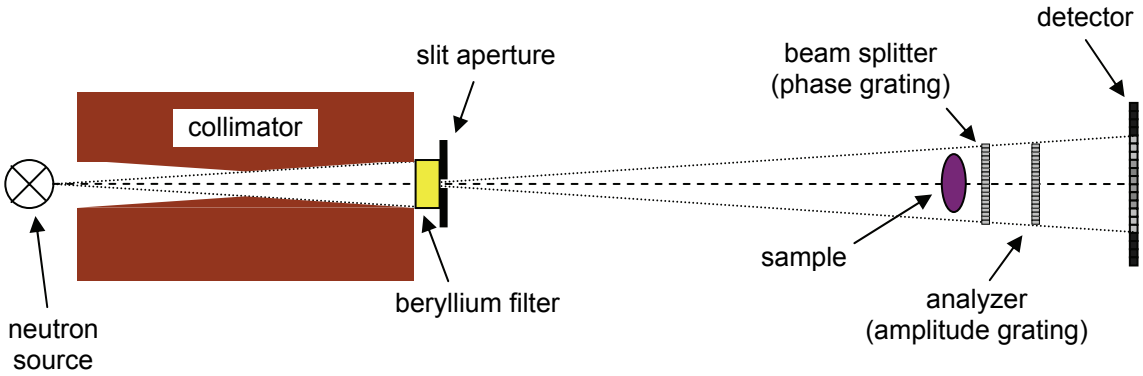

Fig. 3.53: Schematic of the experimental setup of the grating-based shearing interferometer at ANTARES.

The two gratings were manufactured by Christian Grünzweig at PSI for the special beam conditions at ANTARES. The neutron beam does not have to be monochromatic for the

interferometer to work, but a very broad band width decreases its efficiency [Pfe06]. Therefore the beryllium filter of the multi filter was used to reduce the band width.
In Fig. 3.54 the results of an open beam measurement with the setup described above are displayed. It shows a quadratic image of 400x400 pixels with several, slightly tilted horizontal fringes on it. This is the moiré image caused by the gratings. They are orientated horizontally as the slit aperture was installed horizontally in the aperture wheel at that time. This moiré pattern is a good measure for the efficiency of the gratings. Ideally, the beam splitter grating should induce a phase shift of π and have a duty cycle of 0.5, and the analyzer grating should absorb 100% of the beam with the same duty cycle of 0.5. For a quantitative analysis of this moiré pattern, a vertical line profile through the center of the image is shown next to it. The peak-to-peak amplitudes of the oscillations in this line profile do not exceed a value of 0.08, which is very disappointing as a similar measurement at ICON (PSI) yielded a value of more than 0.4. One reason for this low contrast in the moiré pattern was obviously the high ratio of gamma radiation and epithermal neutrons in the beam. For both types of radiation the two gratings do not work, so that they only contribute to noise. Beside this, the used beryllium filter had only a thickness of 4 cm (9 cm at ICON, PSI) and thus was not able to fully suppress neutrons with wavelengths under 4 Å (see Fig. 3.23). With this very low efficiency of the two gratings, no reasonable phase contrast measurements were possible at ANTARES with the grating-based interferometer. The results of these first test measurements helped however to reveal deficiencies in the experimental setup for grating-based interferometry at FRM-II concerning the filtering of the neutron beam and radiation shielding. Modifications of the experimental setup at ANTARES and new experiments in cooperation with the PSI are already planned to make this measurement technique available at FRM-II.

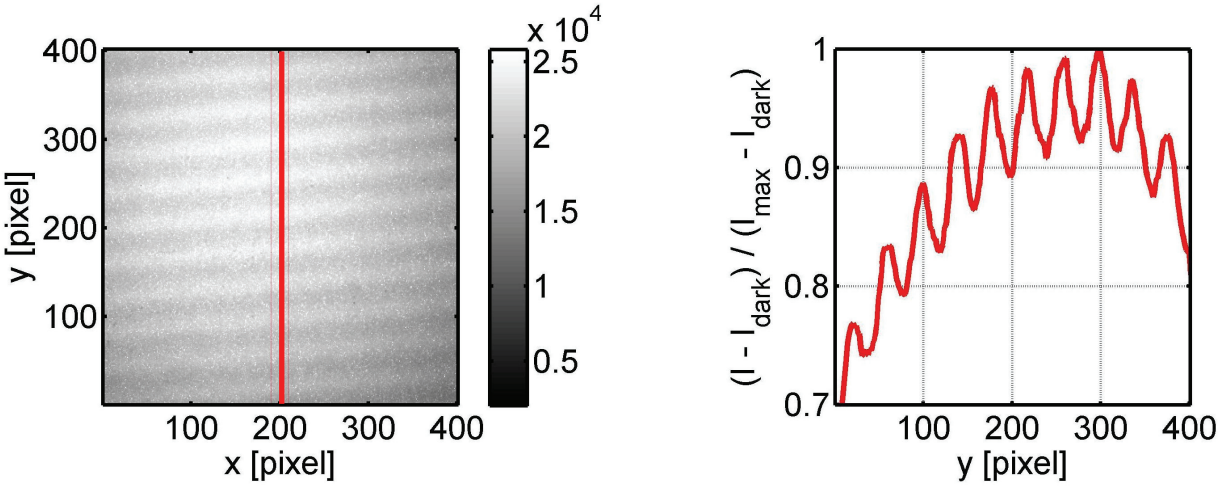

Fig. 3.54: Open beam image with a grating-based shearing interferometer and a vertical line profile through it. The amplitude of the oscillations is a benchmark for the efficiency of the two gratings of the interferometer. The amplitudes achieved at ANTARES were very low, because of a high ratio of gamma radiation in the neutron beam and an insufficient reduction of the bandwidth of the neutron spectrum by the beryllium filter.

Chapter 4

4 Applications

The systematic, experimental investigation of propagation-based phase contrast in the preceding chapter revealed some major benefits of this measurement method compared to pure absorption-based neutron imaging. This chapter summarizes these benefits and shows the opportunities they offer in neutron imaging.

4.1 Improved spatial resolution

In the beginning of this chapter an application of propagation-based phase contrast imaging is described, where the phase contrast itself is not used at all, but only the modification of the beam geometry in this imaging technique. The spatial resolution in neutron imaging is considerably worse than in comparable imaging techniques with X-rays or synchrotron radiation. The reason for this is the blurring of the image due to the conversion reaction in the detector that is needed to convert the neutron flux into a measureable signal. This blurring constitutes a very stringent limitation of the spatial resolution of nowadays neutron detectors.

The modification of the beam geometry in propagation-based phase contrast imaging offers a simple way to circumvent this limitation, as the sample is mapped magnified onto the detector plane. The spatial resolution in the object plane is thus improved for a given detector resolution. For a pinhole with a negligible diameter D, the degree of magnification m is only defined by the distance L between pinhole and object and the distance R between object and detector:

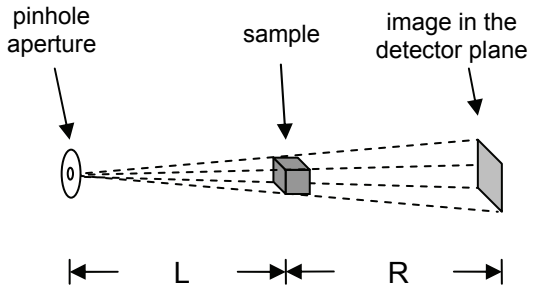

Fig. 4.1: Magnification of the image in propagation based phase contrast imaging.

$$m = \frac{L+R}{L} = 1+\frac{R}{L} \tag{4.1}$$

At ANTARES, the distance L is always around 14 m and cannot be varied very much. The distance between sample and detector was varied between 0 and 2.8 meters. Because of the long distance L between pinhole and sample, the maximum magnification at ANTARES was 20%. At this point it has to be kept in mind that an increase of R also leads to a blurring.

$$x_b = R \cdot \frac{D}{L} \tag{4.2}$$

Because of this blurring, the magnification factor is not equal to the gain in spatial resolution. To be able to improve the spatial resolution, the quotient x_b/m must be smaller than the

spatial resolution of the detector system Δx_s. This demand results in an upper limit for the diameter D of the used pinhole:

$$\frac{x_b}{m} = \frac{R \cdot D}{L + R} < \Delta x_s \Leftrightarrow D < \frac{R + L}{R} \Delta x_s \tag{4.3}$$

The upper limit for the pinhole diameter in dependency of the sample-to-detector distance R is displayed in Fig. 4.2 for two different spatial resolutions of the detector. This calculation is based on the pinhole-to-detector distance L at ANTARES. As the calculation for a detector with a spatial resolution of 200 μm shows, a pinhole aperture with a diameter of 1mm can be used up to a sample-to-detector distance of 300 cm to increase the spatial resolution.
In the end, the choice of the diameter of the pinhole is a decision between high spatial resolution and short exposure times. The price for the gain of spatial resolution is very high, as the neutron flux decreases quadratically with the diameter of the pinhole. But as there still exist no competing alternatives to increase the spatial resolution in neutron imaging for a given detector resolution, every means to do so have to be used and carefully investigated.

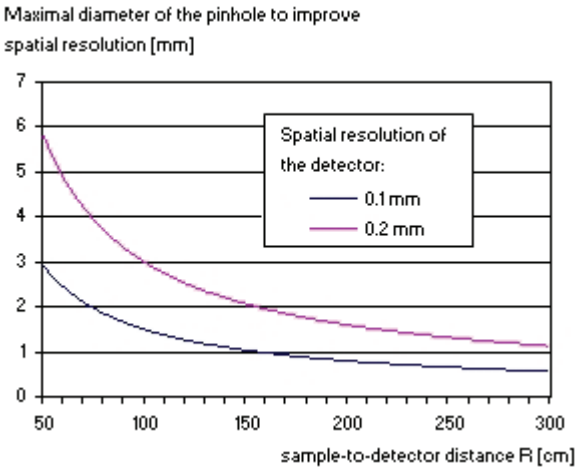

Fig. 4.2: Calculation of the necessary pinhole diameter to be able to improve the spatial resolution in neutron images for a given spatial resolution of the detector.

4.2 Enhanced contrast at edges and interfaces

4.2.1 Edge detection with propagation-based phase contrast imaging

In propagation-based phase contrast imaging, strong gradients in the refractive index perpendicular to the beam direction cause intensity peaks in the detector plane. These kinds of sudden changes in the refractive index of an object appear at its edges and at interfaces between two materials with different refractive indices.
Edges and interfaces are often of special interest in the non-destructive testing of objects and a precise determination of their positions is needed when distances are measured. Apart from the direct measurement of distances in digital images, the edge information is also of great importance for many image processing techniques like segmentation, where the connected interfaces between different segments in an image have to be found in an array of discrete gray values. For this cause, lines have to be fitted to a set of points that represent an edge in a 2D image and surfaces that represent interfaces have to be found in 3D pixel arrays.
In section 1.3 some basic algorithms for edge detection were introduced. Of course strong gradients at edges and interfaces are always beneficial for edge detection procedures and thus it is reasonable to use them on propagation-based phase contrast images as the following images show.

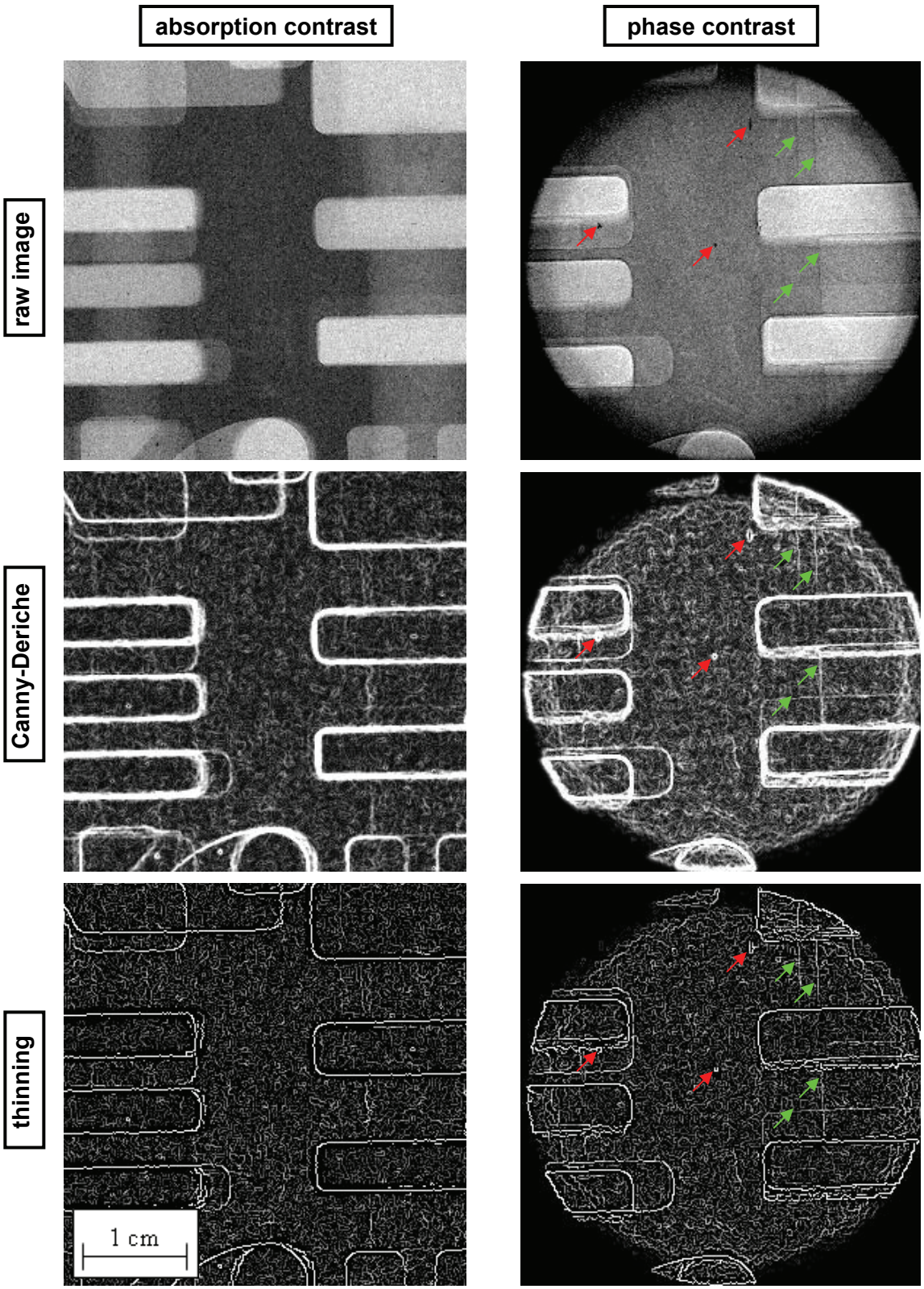

Fig. 4.3: Comparison of the results of an edge detection procedure with a Canny-Deriche detector on a conventional neutron radiograph (left side) and a phase contrast radiograph (right side). The images in the top row show the raw data, in the middle row the results of the edge filtering is displayed and the images at the bottom show the effect of non-maximum suppression ("thinning"). The final result with the phase contrast image shows several edges which could not be detected in the absorption-based radiograph.

The radiographs in the first row of Fig. 4.3 show the raw data obtained in a conventional and a phase contrast neutron radiography of an aluminum sample with several sharp edges. The

enhanced contrast at the edges caused by the propagation-based phase contrast is well visible and allows the precise measurement of the position of edges, which are only vaguely visible in the absorption-based radiograph (e. g. the edges marked with the green arrow). In the row below, the raw images were filtered with a Canny-Deriche edge detector. The noise in the raw images leads to a strong background structure after the edge detection procedure as the noise represents sharp intensity fluctuations, which are amplified by the derivation-based edge detection algorithm. Especially spurious are small black spots caused by impurities on the surface of the image plate (marked with red arrows in image).
Still the Canny-Deriche edge detector is able to clearly bring out the edge structure of the object in both images. The edge detection filter leads to a strong broadening of the edges and has to be followed by a non-maximum suppression procedure as suggested by Canny [Can86]. This procedure reduces the thickness of the detected edges to one pixel and allows clear position measurements. The thinning however often leads to broken edges and can also result in multiple lines from only one edge in the radiograph. Especially in phase contrast images, where every edge creates a maximum and a minimum peak, the parameters and thresholds in the non-maximum suppression algorithm have to be adjusted carefully.

4.2.2 Example: Non destructive testing of aluminum foams

The enhanced contrast at strong density gradients offers new opportunities for the non-destructive testing of foams. Foams can be classified into two types based on their internal structure [Wea99]. Closed cell structured foams are built up of many densely packed bubbles, which are not connected to each other. Each bubble is separated from its neighbor by a thin film, which is in general not a flat surface. Where three bubbles meet, the films meet in plateau borders and at interconnections of more than three bubbles the plateau borders meet in vertices. If the bubbles are not separated by cell walls, the foam only consists of a network of plateau borders and is called open cell structured foam.

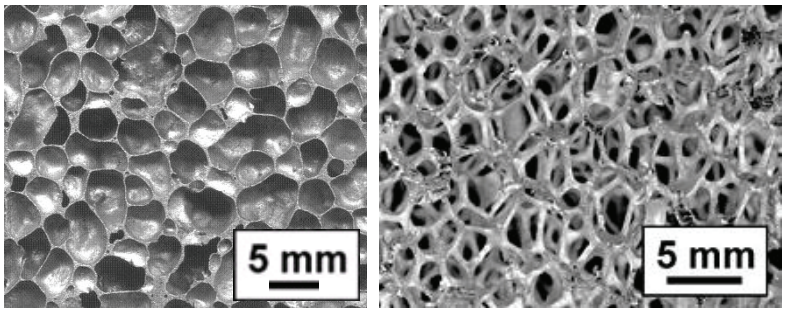

Fig. 4.4: Internal structure of an aluminum foam with a closed cell structure (left picture) and an open cell structure (right picture)

Contrary to other structures used for lightweight construction like honey comb structures, where the structure is machine made and represents simple geometries, the foam structure is not easily reproducible and every technical component containing a metal foam is unique. As great deviations in the planned bubble size can lead to a severe reduction of the mechanical stability of the component, the quality control in industrial processes of these types of components is of great importance.
Neutron phase contrast imaging is a very good method for the non-destructive testing of aluminum foams as aluminum is on the one hand very transparent for neutrons and on the other hand the foam structure shows sharp edges, which leads to phase contrast in the detector plane. A propagation-based phase contrast radiograph of an aluminum foam with a closed cell structure is displayed in Fig. 4.5. The thickness of the sample in beam direction was 2 cm, and the average diameter of the bubbles was in the range of 5 mm to 10 mm. Like this, the number of overlapping layers of bubbles in the radiograph was small enough to be able to distinguish the borders of the single bubbles.

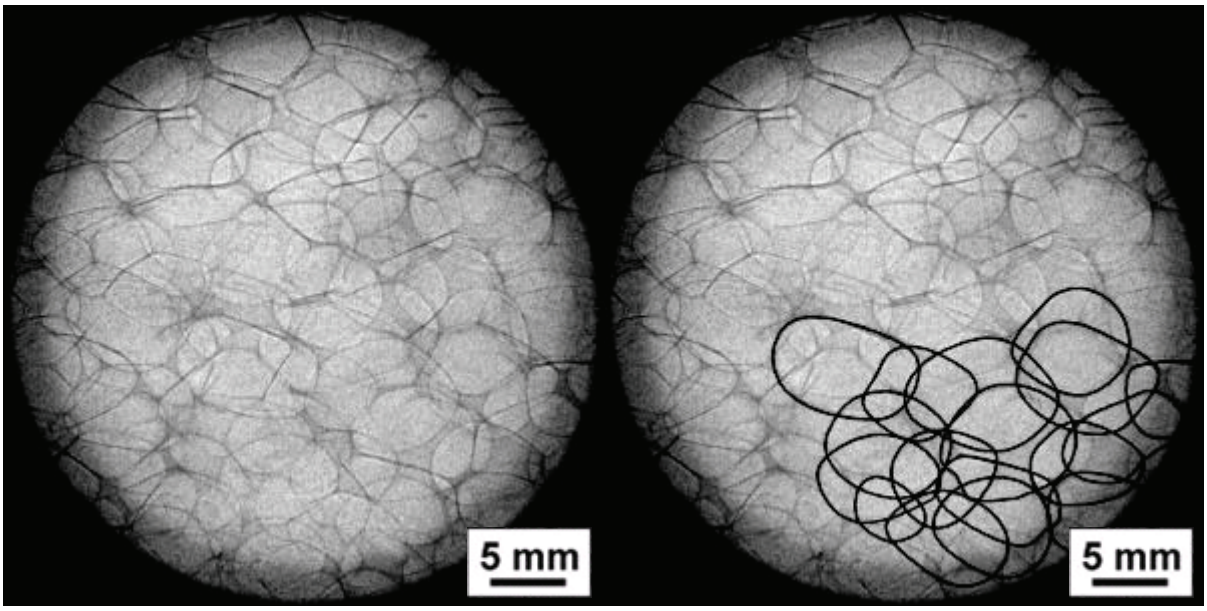

Fig. 4.5: Phase contrast radiograph of an aluminum foam and the detection of bubble sizes in it. If the thickness of the object in beam direction is not much bigger than the average diameter of the bubbles, each bubble creates one closed line in the radiograph, which represents the surface of one bubble that is hit tangentially by the neutron beam. This allows a quick measurement of the average bubble size, the standard deviation from it and the homogeneity of the bubble distribution.

In the right image of Fig. 4.5, the projected borders of some of the bubbles were marked by hand. The result is an overlapping set of closed lines with shapes that deviate clearly from symmetric circles. With this set of closed lines, it is possible to determine the average bubble size, the standard deviation from it and the homogeneity of the distribution of the bubbles in the foam.

To be able to analyze the radiograph automatically with an edge detection algorithm, the software has to be able to recognize the single bubbles. This computer vision problem shows again in an impressive way the abilities of human perception, as it is in most cases for the human eye no problem to decide at crossings, which line belongs to which bubble. For the image processing software this is a not so easy task.

The curvature of the border of one bubble has certain characteristics that can be used for the detection procedure: It is smooth and when one follows the border of one bubble until the starting point is reached again, the direction must have changed by 360°. Close to the surface of metal foams and at interfaces to other materials, the automation of the detection process becomes even more difficult. Fig. 4.6 shows the phase contrast radiograph of aluminum foam with four steel thread inlays. The programming of software that is able to automatically determine the mechanical stability of the steel inlays in the aluminum foam by analyzing two of three phase contrast radiographs is a challenging task that requires a team with profound knowledge in computer vision and mechanical engineering.

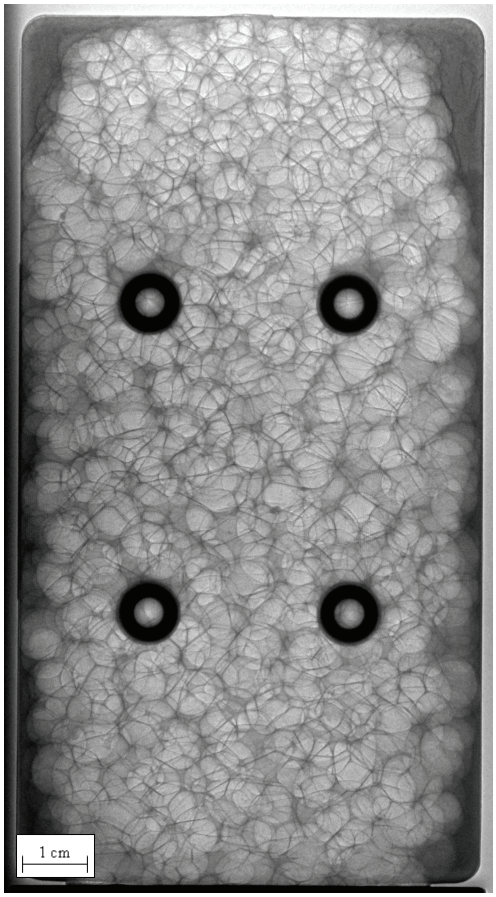

Fig. 4.6: Aluminum foam with four steel thread inlays.

Another type of material that was investigated in the same way as the metal foams were sintered hollow sphere structures. This special structure is manufactured in a two step procedure. In the first step, plastic spheres with a specified diameter are coated with a metal alloy of a certain thickness. In a second step, the coated plastic spheres are filled in a form and heated up to temperatures, at which the coating of neighboring spheres coalesce (sintering process) and the plastic core of the spheres evaporates. The result of this process is a very stable sintered component that is made up of thin-walled hollow spheres with a similar diameter.

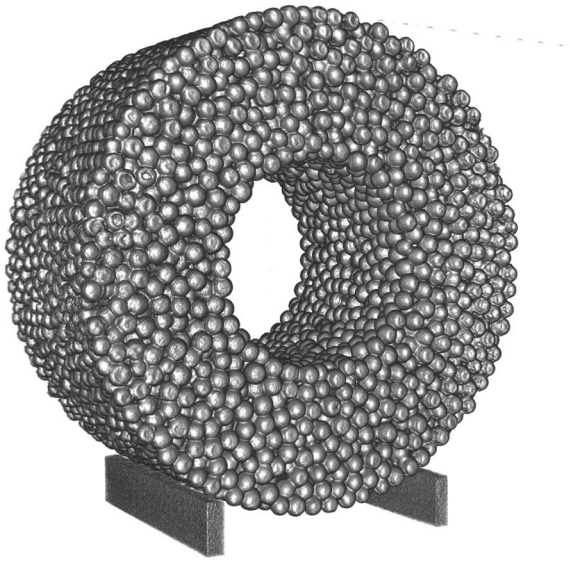

Fig. 4.7: Absorption-based tomography of a soot filter made of sintered hollow spheres (outer diameter of 24 cm).

In Fig. 4.7 the result of a conventional, absorption-based neutron tomography of a soot filter made out of sintered steel hollow spheres is displayed. The filter has a cylindrical shape with a diameter of 24 cm and a height of 6 cm. Each hollow sphere has a diameter of 6 mm. In a phase contrast radiograph of a perfectly structured component of this material type, each hollow sphere creates a perfect circle, which makes automated non-destructive testing very simple. The tomography shows however that the shape of many hollow spheres departs significantly from a perfect sphere. An additional problem was the high ratio between the sample thickness in beam direction and the diameter of one hollow sphere. Because of the many overlapping layers of spheres, the exact shape of most of the single spheres could not be distinguished any more. A good rule of thumb for an upper limit for the number of bubble layers n in beam direction up to which the shape of a single bubble can be distinguished is

$$n < \frac{d_{sphere}}{2\Delta x_{10\%MTF}}, \tag{4.1}$$

where d_{bubble} is the average diameter of the bubbles/spheres in the material and $\Delta x_{10\%MTF}$ is the spatial resolution. The factor of 2 in the denominator derives from the necessity that two edges have to be separated by background.

In Fig. 4.8 two radiographs, one with phase contrast and one without, of a cylindrical hollow sphere structure with a diameter of 3 cm are displayed. The diameter of one sphere is 3 mm. The additional contrast in the phase contrast radiograph allows an improved detection of the spheres, but especially in the center of the cylinder where up to ten spheres are overlapping the borders of one single sphere cannot be determined.

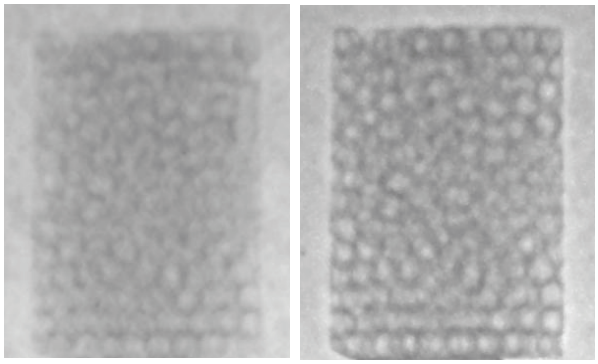

Fig. 4.8: Comparison of an absorption based radiograph (left image) and a phase contrast radiograph (right image) of a cylindrical hollow sphere structure (3 cm diameter).

4.3 Separation of materials with similar attenuation coefficients

4.3.1 Comparison of the complex refractive indices of the elements

Neutron phase contrast imaging allows the utilization of the deviation from unity δ of the real part of the refractive index for NDT purposes. This opens a new dimension in neutron imaging, which is illustrated in Fig. 4.9, where the attenuation coefficient of the elements is plotted against the δ-value. Remarkable is the occurrence of negative δ-values for the elements manganese, titanium, lithium and vanadium. In Fig. 4.10, where the δ-value is divided by the particle density under standard conditions and is plotted against the mass attenuation coefficient, it is revealed that hydrogen is a fifth element with a negative δ-value. It has also the highest mass attenuation coefficient beside gadolinium and boron. Elements that lie on one horizontal line cannot be separated in conventional, absorption-based neutron imaging. This limitation can be overcome with phase contrast.
The opposite sign of the δ-value of the two elements manganese and copper (which are marked with a red circle in Fig. 4.9) will be used in the following subsection to obtain contrast at the interface of two aluminum alloys with very similar attenuation coefficients.

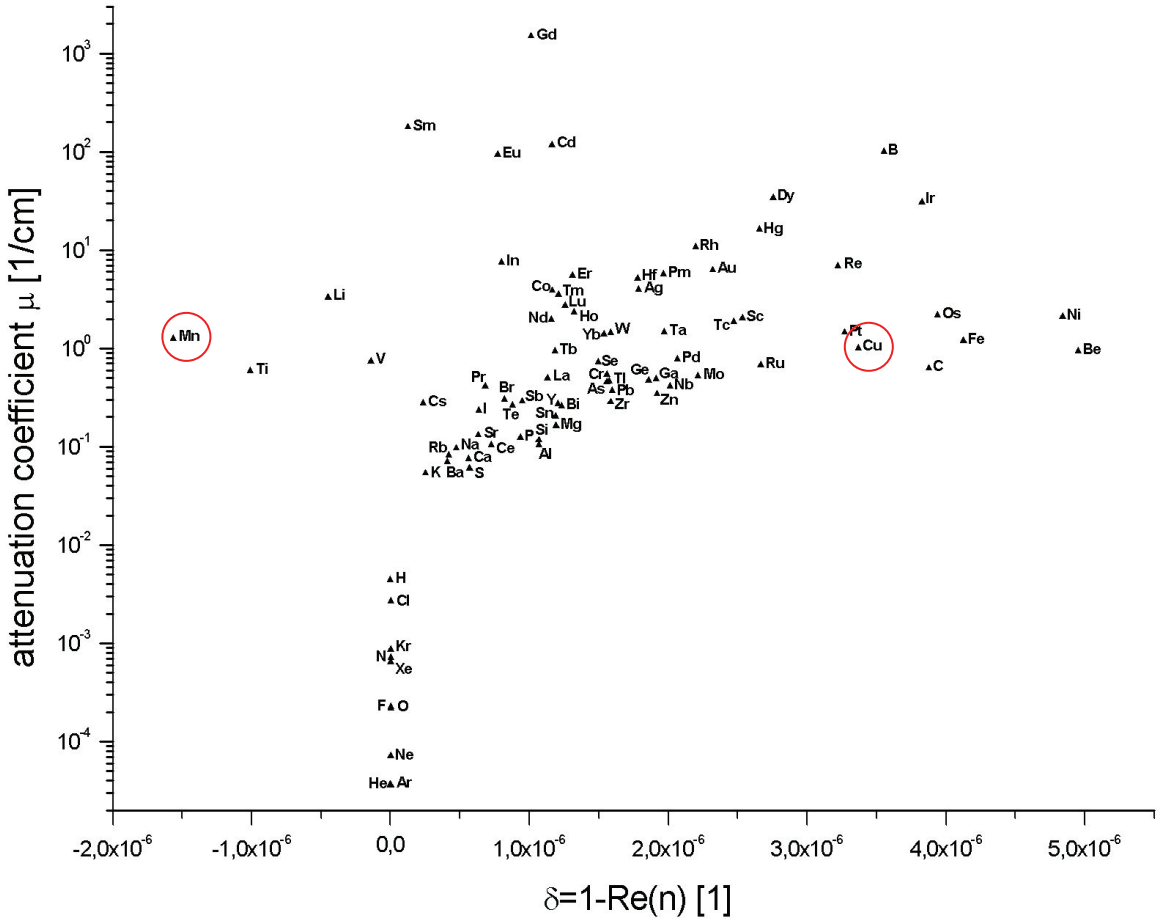

Fig. 4.9: Plot of the attenuation coefficient against the deviation from unity δ of the real part of the refractive index of the elements under standard conditions for thermal neutrons (25 meV). All data was taken from [Neu92].

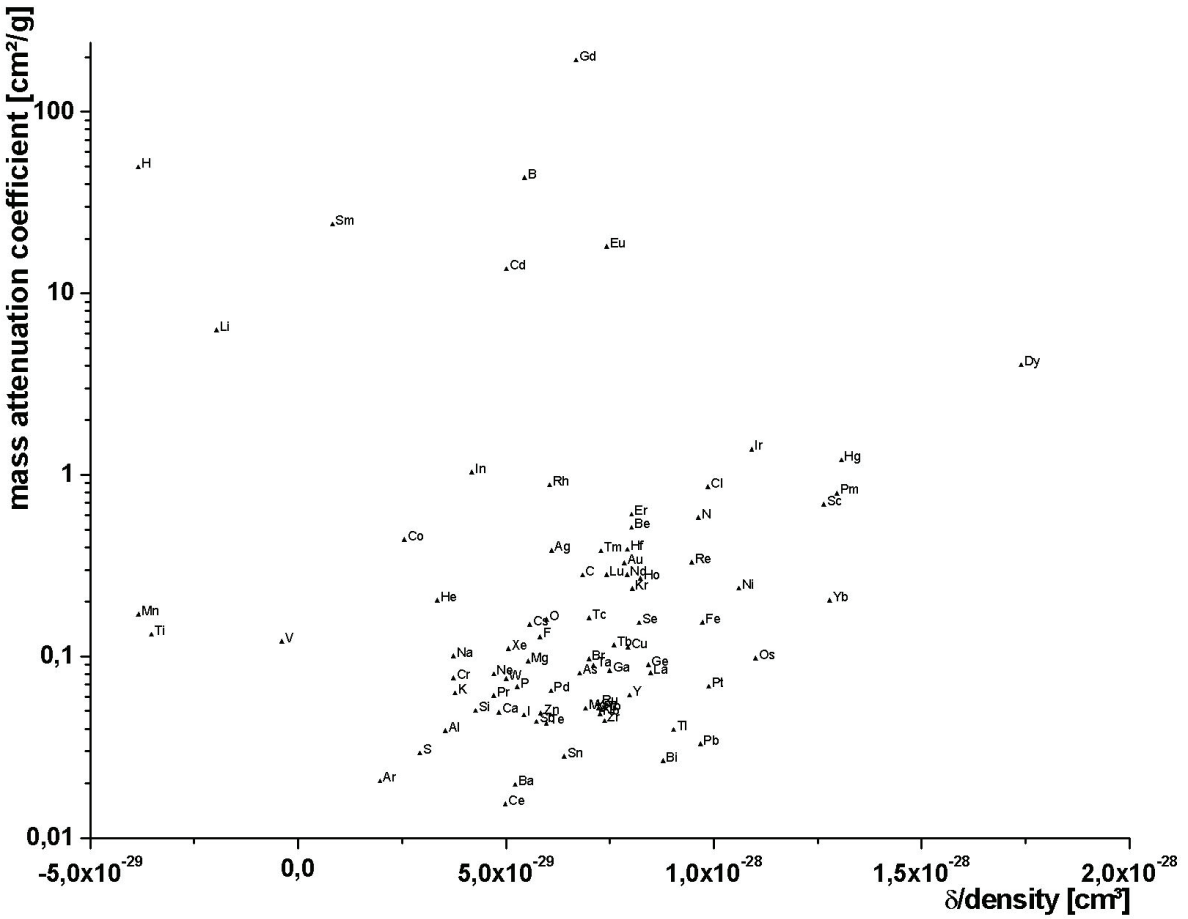

Fig. 4.10: Plot of the mass attenuation coefficient against the δ-value divided by the particle density of the elements under standard conditions for thermal neutrons (25 meV). All data was taken from [Neu92].

4.3.2 Example: Separation of two aluminum alloys ($AlMg_{4,5}Mn/AlSi_9Cu_4$)

To be able to systematically investigate the phase contrast effect at interfaces between two materials with similar attenuation coefficients, but different δ-values, special test samples were designed. In Fig. 4.11 a gedankenexperiment is described with an idealized test sample. This imaginary test sample is made up of two different materials A and B with refractive indices n_A and n_B that have an identical imaginary part ($\beta_A = \beta_B$), but differ in the real part, the δ-value ($\delta_A << \delta_B$). The geometry of the test sample resembles a simple cuboid shape, which is made up of two step wedges that were put together antipodally. The cuboid is positioned in the neutron beam in such a way that it has a constant thickness in beam direction. The inner step structure causes a variation of the thicknesses of the two materials in x-direction. Because of this geometry, the attenuation of the neutron beam does not vary in the x-direction, but the phase shift does. Like this, conventional, absorption-based neutron radiography delivers no contrast in x-direction, but phase contrast imaging does. At this point it has to be distinguished again between qualitative and quantitative phase contrast imaging. The results of the different measurement methods are displayed on the right side of Fig. 4.11. Absorption-based radiographs show a constant intensity in x-direction (black line), whereas with phase contrast techniques the interfaces parallel to the beam direction become visible. The red lines represent the characteristic intensity peaks in propagation-based phase contrast imaging. If phase retrieval algorithms are used to calculate the actual phase shift (sec. 1.2.3.2) or interferometric measurements are carried out to measure it directly (sec. 1.2.1 and 1.2.2), the inner step structure of the test sample becomes perfectly visible (green line).

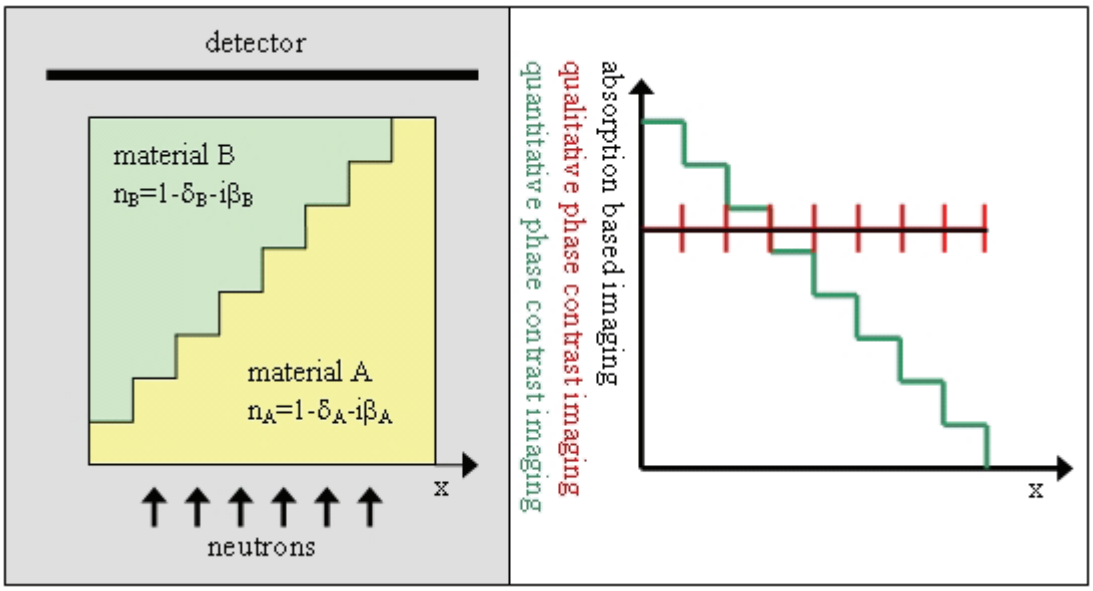

Fig. 4.11: Design of a test sample for systematic investigations on quantitative and qualitative phase contrast imaging. The refractive indices of material A and B are equal in the imaginary part but differ considerably in their real parts ($\beta_A \approx \beta_B$, $\delta_A << \delta_B$).

In cooperation with the utg, the institute of metal forming and casting of the Technical University of Munich, test samples were manufactured with a geometry very similar to the one described above. A detailed drawing of the geometry of the test samples and the edge lengths are shown in Fig. 4.12. Around a step wedge made of an aluminum forging alloy ($AlMg_{4.5}Mn$), an aluminum casting alloy ($AlSi_9Cu_4$) was cast. Both alloys have very similar attenuation coefficients, but due to the great difference in the real part of the refractive index of manganese and copper, phase contrast occurs at the interfaces between those two materials. The sample is positioned in the neutron beam in such a way that it has a constant thickness of 26 mm in beam direction. The height of the steps in beam direction varies between 0.25 mm and 5 mm.

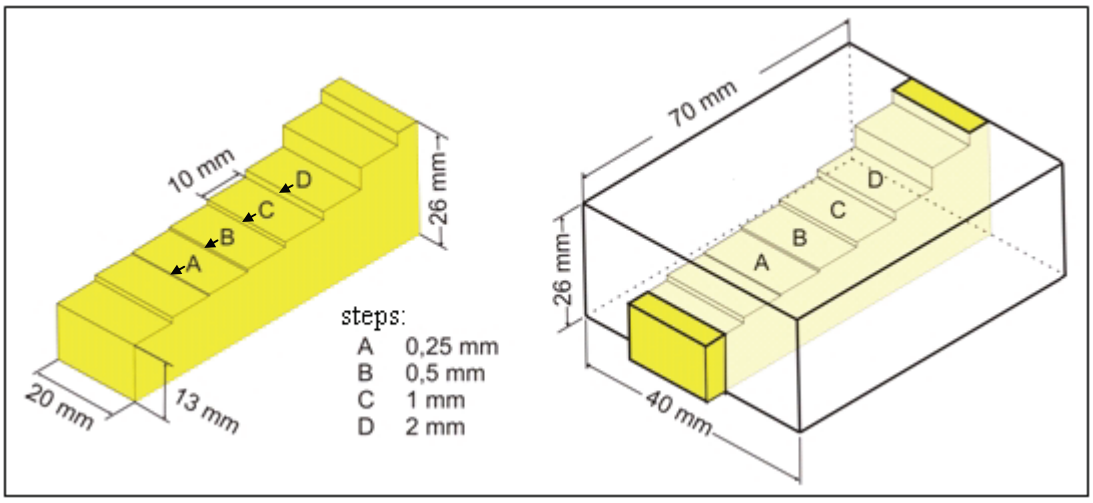

Fig. 4.12: Schematics of the test sample that were manufactured in cooperation with utg: The material A is cast around an step wedge out of material B to get a sample geometry as shown in Fig. 4.11.

4.3.3 Phase contrast tomography

With the test sample described in Fig. 4.12, not only conventional and phase contrast radiographs were investigated, but also complete tomographic measurements were carried out and analyzed with both techniques. For this purpose, a set of radiographs under different viewing angles had to be recorded as described in sec. 1.3. Two projections respectively with and without phase contrast, under a viewing angle that differs by 90° degree are displayed in Fig. 4.13. In one projection the direction of the neutron beam is perpendicular to the steps and in the other it is parallel.

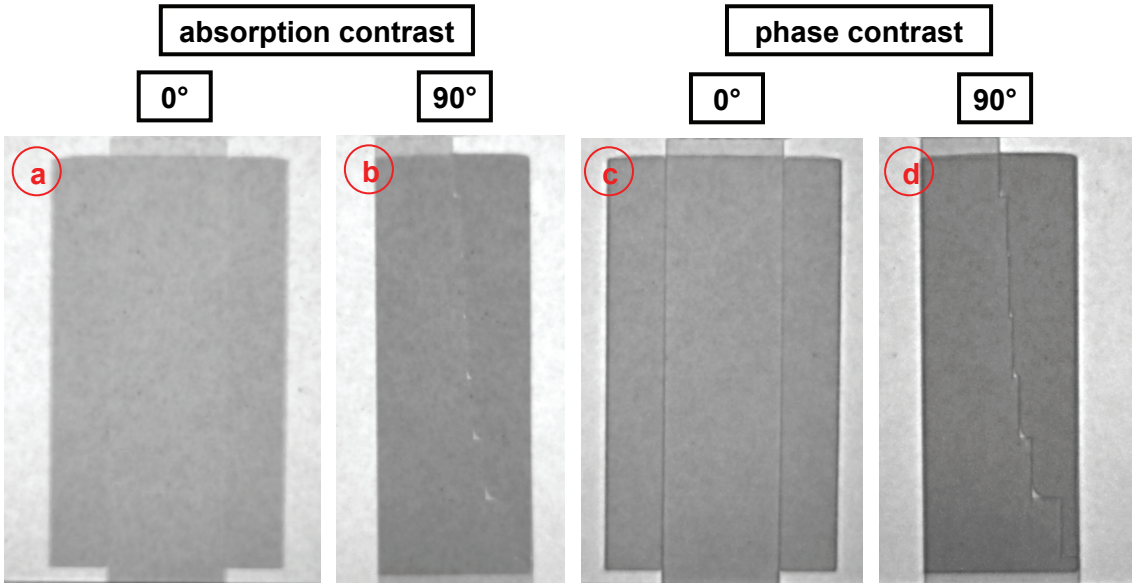

Fig. 4.13: Comparison of single projections perpendicular and parallel to the steps (left: conventional radiographs, right: phase contrast radiographs). The exposure time for a conventional radiograph was 7 seconds. In case of the phase contrast images, the exposure time was 8 minutes.

The contrast enhancement at the edges and interfaces is clearly visible in the radiographs obtained with propagation-based phase contrast imaging (Fig. 4.13cd). In the projections perpendicular to steps (Fig. 4.13ac), the inner structure is only visible with phase contrast. Failures in the casting process in form of trapped air in the corners of the steps are visible in the projections parallel to the steps. Nevertheless, the additional information obtained in the single projections by the use of phase contrast imaging could be well demonstrated with this sample. The important question is, if this additional contrast at the interfaces remains after a further processing of the data for a tomographic reconstruction.

The reconstruction of the data set was done with a conventional filtered back projection algorithm. The exposure time for one single phase contrast radiograph was 8 minutes. To be able to filter out gamma spots that are accumulated on the CCD detector, three images are recorded per projection angle and processed with median and sigma filters. Including the readout time of the CCD detector, the cycle time for one projection was approximately 25 minutes. The complete phase contrast tomography was done with 200 projections over 180 degrees resulting in an overall measurement time of 83 hours.
Due to the parallel beam geometry the reconstruction of the data could be done slice by slice. One slice represents the distribution of the attenuation coefficient in a plane perpendicular to the rotation axis of the sample. In Fig. 4.14 a reconstructed slice of the conventional tomography is compared with one of the phase contrast tomography. Also after the reconstruction, the contrast enhancement at the edges and interfaces is clearly visible. This is especially useful to find the borders of volumes in the reconstructed data and to separate those volumes. A negative effect of the strong phase contrast on the reconstruction is the occurrence of additional artifacts in the form of extensions of the phase contrast edges (red arrows).

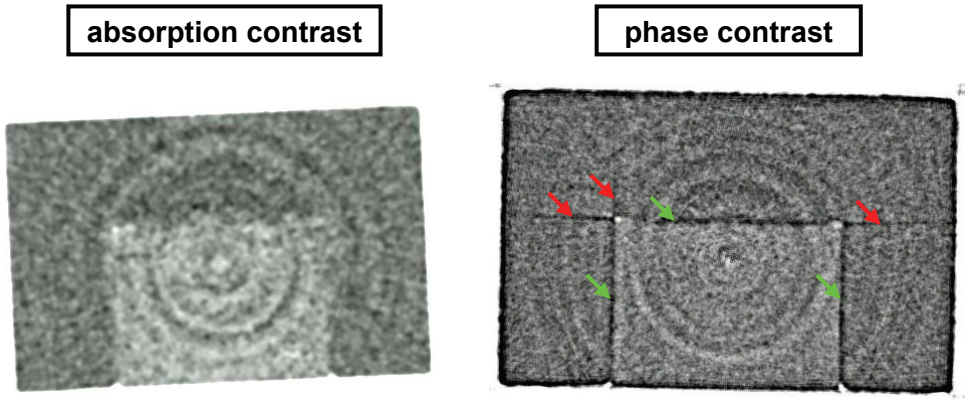

Fig. 4.14: Comparison of reconstructed slices with and without phase contrast. Beside the desired contrast enhancement at interfaces (green arrows), artifacts in the form of extensions beyond the endings of the interfaces are created.

The benefit of the additional contrast at the interfaces is shown in Fig. 4.15, where three steps in the visualization process are displayed. For the three dimensional visualization of the data, the software VGStudio Max from Volume Graphics was used. In the first image, the reconstructed slices were simply stacked, voxels with gray values above and below certain thresholds were rendered invisible and a linear look-up table was applied on the gray values in between the two thresholds. In the second image, the phase contrast peaks at the interface between the inner aluminum wrought alloy and the outer aluminum cast alloy were used to find the surface of the cast-in step wedge. The voxels inside this surface were colored cyan. In the last image, the aluminum cast alloy was rendered transparent to be able to see the detailed shape of the cast-in step wedge.

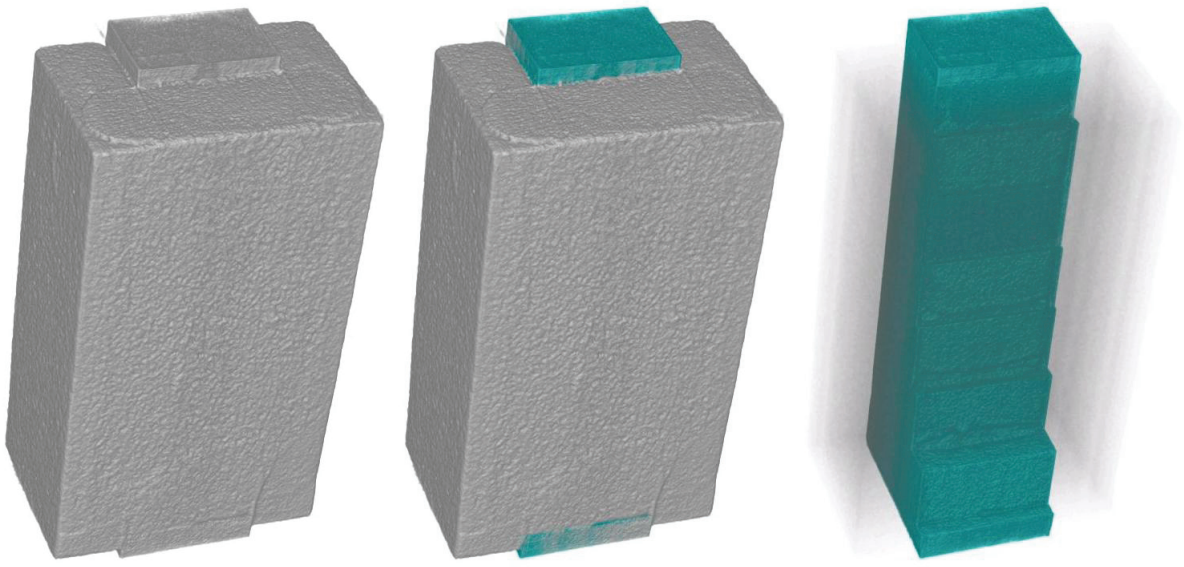

Fig. 4.15: The improved visibility of interfaces in reconstructed volumes allows better segmentation of the virtual objects. The 3D image was generated and analyzed with VGStudio Max.

The separation of these two aluminum alloys would not be possible in a conventional neutron tomography without phase contrast. This clear separation of different materials allows precise measurements of volumes inside the investigated specimen.
With the help of the tables shown in Fig. 4.9 and 4.10 many other material combinations can be found, where the application of a phase contrast setup can improve the visibility of interfaces in neutron tomography.

Chapter 5

5 Conclusion and outlook

Propagation-based neutron phase contrast imaging is able to deliver structural information of objects that create no absorption contrast in conventional neutron imaging. The exploitation of the real part of the refractive index of a material extends considerably the applicability of neutron radiography and tomography for non-destructive testing purposes. In theory, the experimental effort to upgrade a conventional neutron imaging beam line with the option to do propagation-based phase contrast imaging is small compared to the experimental setups needed for interferometric measurements.

Without a further processing of the measured data, the contrast enhancement at edges and interfaces can be used for the non-destructive testing of objects and the visualization of data. This straight forward application of the phase contrast effect for neutron imaging is generally referred to as qualitative phase contrast imaging. Quantitative phase contrast imaging demands a spatially resolved measurement of the phase shift, which was before the year 2000 [All00] exclusively done by neutron interferometry. The step from qualitative to quantitative neutron phase contrast imaging is possible with the propagation-based imaging technique investigated in this work by the application of the transport-of-intensity equation (TIE) [Tea83]. With this phase retrieval method, good results were however only achieved with a monochromatized neutron beam, which leads to greatly increased exposure times. As the measurement time for a qualitative phase contrast tomography with only 200 projections over 180 degrees as described in section 4.4 is already of the order of 4 days, quantitative neutron phase contrast tomography seems to be not feasible with propagation-based phase contrast imaging. But this has to be the next step as it opens up a new dimension in neutron imaging. Therefore alternative methods for phase imaging have to be investigated to achieve this goal. With the grating-based neutron interferometer presented in section 1.2.2 quantitative phase contrast tomography is already successfully done today.

Grating-based neutron interferometry as proposed by Franz Pfeiffer and his group at PSI [Pfe06] allows the quick tomographic measurement of both, the real and imaginary part of a material's refractive index. Like this, two values can be assigned to every voxel of the reconstructed tomographic data set, where one value represents the attenuation of the neutron beam at this position and the other the introduced phase shift. As the tables in Fig. 4.9 and 4.10 illustrate, this additional information allows the separation of a multitude of additional material combinations compared to conventional, pure absorption-based neutron tomography. The combination of phase contrast tomography with neutrons and X-rays results in four characteristic parameters that can be used for the separation of materials. Again the grating-based method is perfectly suitable for this extension on multiple types of radiation as it was already successfully used with X-rays from synchrotron sources and conventional X-ray tubes. The technical challenges in the manufacturing process of the gratings for this measurement method are however considerable and slow down the distribution process of this new technique.

At this point a big advantage of propagation-based phase contrast imaging has to be remembered: The simplicity of the experimental setup. In case of propagation-based phase

contrast imaging, no additional components compared to conventional, absorption-based neutron imaging are needed. The only prerequisites for the implementation in an existing imaging beamline are the possibility to achieve a sufficient high L/D ratio at the sample position and adequate space behind it to position the detector far away enough. These two simple modifications in the experimental setup improve the spatial resolution in measurements by the magnified projection of the sample on the detector plane and produce the contrast enhancement at edges and interfaces. It is therefore for every imaging beamline with enough free space and neutron flux reasonable to implement this technique.

A. Appendix

A.1 Neutron scattering lengths of isotopes

In the columns of the following table various material constants of isotopes are listed that make up their complex refractive indices. All this data was taken from [Neu92]. The first row contains the symbol of the chemical element and eventually a number in front of it that represents the mass number of a certain isotope. In the second row, the concentration of an isotope in the naturally occurring element is displayed or its half-life time for unstable isotopes. The following rows contain the coherent and incoherent scattering lengths and cross sections and the resulting scattering and absorption cross section. The next three rows contain the atomic weight, the density ρ and the atomic density n, which are needed for the calculation of the δ-value (Eq. 1.18) and (mass) attenuation coefficient $\mu(/\rho)$.
In A.2, these material constants are displayed again in a more concise overview for the natural elements.

	conc	Coh b	Inc b	Coh xs	Inc xs	Scatt xs	Abs xs	At. Wght	ρ	N	δ	μ	μ/ρ
	[%]	[fm]	[fm]	[barn]	[barn]	[barn]	[barn]	[amu]	[g/cm³]	[1/m³]	[1]	[1/cm]	[cm²/g]
H	---	-3,739	---	1,7568	80,26	82,02	3,33E-01	1,01	8,99E-05	5,37E+25	-2,07E-09	4,42E-03	4,92E+01
1H	99,985	-3,7406	25,274	1,7583	80,27	82,03	3,33E-01						
2H	0,015	6,671	4,04	5,592	2,05	7,64	5,19E-04						
3H	(12.32 a)	4,792	-1,04	2,89	0,14	3,03	0,00E+00						
He	---	3,26	---	1,34	0	1,34	7,47E-03	4,00	1,79E-04	2,68E+25	9,01E-10	3,62E-05	2,03E-01
3He	0,00014	5,74-1,483i	-2,5+2,568i	4,42	1,6	6	5,33E+03						
4He	99,99986	3,26	0	1,34	0	1,34	0,00E+00						
Li	---	-1,9	---	0,454	0,92	1,37	7,05E+01	6,94	5,30E-01	4,60E+28	-8,99E-07	3,31E+00	6,24E+00
6Li	7,5	2-0,261i	-1,89+0,26i	0,51	0,46	0,97	9,40E+02						
7Li	92,5	-2,22	-2,49	0,619	0,78	1,4	4,54E-02						
Be	100	7,79	0,12	7,63	0,0018	7,63	7,60E-03	9,01	1,85E+00	1,24E+29	9,91E-06	9,44E-01	5,10E-01
B	---	5,3-0,213i	---	3,54	1,7	5,24	7,67E+02	10,81	2,34E+00	1,30E+29	7,11E-06	1,01E+02	4,30E+01
10B	20	-0,1-1,066i	-4,7+1,231i	0,144	3	3,1	3,84E+03						
11B	80	6,65	-1,3	5,56	0,21	5,77	5,50E-03						
C	---	6,646	---	5,551	0,001	5,551	3,50E-03	12,01	2,26E+00	1,13E+29	7,75E-06	6,30E-01	2,79E-01
12C	98,9	6,6511	0	5,559	0	5,559	3,53E-03						
13C	1,1	6,19	-0,52	4,81	0,034	4,84	1,37E-03						
N	---	9,36	---	11,01	0,5	11,51	1,90E+00	14,01	1,25E-03	5,37E+25	5,18E-09	7,21E-04	5,77E-01
14N	99,63	9,37	2	11,03	0,5	11,53	1,91E+00						
15N	0,37	6,44	-0,02	5,21	0,00005	5,21	2,40E-05						
O	---	5,803	---	4,232	0,0008	4,232	1,90E-04	16,00	1,43E-03	5,38E+25	3,21E-09	2,28E-04	1,59E-01
16O	99,762	5,803	0	4,232	0	4,232	1,00E-04						
17O	0,038	5,78	0,18	4,2	0,004	4,2	2,36E-01						
18O	0,2	5,84	0	4,29	0	4,29	1,60E-04						
F	100	5,654	-0,082	4,017	0,0008	4,018	9,60E-03	19,00	1,70E-03	5,39E+25	3,14E-09	2,17E-04	1,28E-01
Ne	---	4,566	---	2,62	0,008	2,628	3,90E-02	20,18	9,00E-04	2,69E+25	1,26E-09	7,16E-05	7,96E-02
20Ne	90,51	4,631	0	2,695	0	2,695	3,60E-02						
21Ne	0,27	6,66	0,6	5,6	0,05	5,7	6,70E-01						
22Ne	9,22	3,87	0	1,88	0	1,88	4,60E-02						
Na	100	3,63	3,59	1,66	1,62	3,28	5,30E-01	22,99	9,70E-01	2,54E+28	9,49E-07	9,68E-02	9,98E-02
Mg	---	5,375	---	3,631	0,08	3,71	6,30E-02	24,31	1,74E+00	4,31E+28	2,38E-06	1,63E-01	9,35E-02
24Mg	78,99	5,66	0	4,03	0	4,03	5,00E-02						
25Mg	10	3,62	1,48	1,65	0,28	1,93	1,90E-01						
26Mg	11,01	4,89	0	3	0	3	3,82E-02						
Al	100	3,449	0,256	1,495	0,0082	1,503	2,31E-01	26,98	2,70E+00	6,02E+28	2,14E-06	1,05E-01	3,87E-02
Si	---	4,1491	---	2,163	0,004	2,167	1,71E-01	28,09	2,33E+00	4,99E+28	2,13E-06	1,17E-01	5,01E-02
28Si	92,23	4,107	0	2,12	0	2,12	1,77E-01						
29Si	4,67	4,7	0,09	2,78	0,001	2,78	1,01E-01						
30Si	3,1	4,58	0	2,64	0	2,64	1,07E-01						
P	100	5,13	0,2	3,307	0,005	3,312	1,72E-01	30,97	1,82E+00	3,54E+28	1,87E-06	1,23E-01	6,77E-02
S	---	2,847	---	1,0186	0,007	1,026	5,30E-01	32,07	2,07E+00	3,89E+28	1,14E-06	6,05E-02	2,92E-02
32S	95,02	2,804	0	0,988	0	0,988	5,40E-01						
33S	0,75	4,74	1,5	2,8	0,3	3,1	5,40E-01						
34S	4,21	3,48	0	1,52	0	1,52	2,27E-01						
36S	0,02	3	0	1,1	0	1,1	1,50E-01						
Cl	---	9,577	---	11,5257	5,3	16,8	3,35E+01	35,45	3,17E-03	5,38E+25	5,31E-09	2,71E-03	8,55E-01
35Cl	75,77	11,65	6,1	17,06	4,7	21,8	4,41E+01						
37Cl	24,23	3,08	0,1	1,19	0,001	1,19	4,33E-01						
Ar	---	1,909	---	0,458	0,225	0,683	6,75E-01	39,95	1,78E-03	2,68E+25	5,27E-10	3,64E-05	2,05E-02
36Ar	0,337	24,9	0	77,9	0	77,9	5,20E+00						
38Ar	0,063	3,5	0	1,5	0	1,5	8,00E-01						
40Ar	99,6	1,83	0	0,421	0	0,421	6,60E-01						
K	---	3,67	---	1,69	0,27	1,96	2,10E+00	39,10	8,60E-01	1,32E+28	5,00E-07	5,38E-02	6,25E-02
39K	93,258	3,74	1,4	1,76	0,25	2,01	2,10E+00						
40K	0,012	3	---	1,1	0,5	1,6	3,50E+01						
41K	6,73	2,69	1,5	0,91	0,3	1,2	1,46E+00						
Ca	---	4,7	---	2,78	0,05	2,83	4,30E-01	40,08	1,55E+00	2,33E+28	1,13E-06	7,59E-02	4,90E-02
40Ca	96,941	4,8	0	2,9	0	2,9	4,10E-01						
42Ca	0,647	3,36	0	1,42	0	1,42	6,80E-01						
43Ca	0,135	-1,56	---	0,31	0,5	0,8	6,20E+00						

	conc	Coh b	Inc b	Coh xs	Inc xs	Scatt xs	Abs xs	At. Wght	ρ	N	δ	μ	μ/ρ
	[%]	[fm]	[fm]	[barn]	[barn]	[barn]	[barn]	[amu]	[g/cm³]	[1/m³]	[1]	[1/cm]	[cm²/g]
44Ca	2,086	1,42	0	0,25	0	0,25	8,80E-01						
46Ca	0,004	3,6	0	1,6	0	1,6	7,40E-01						
48Ca	0,187	0,39	0	0,019	0	0,019	1,09E+00						
Sc	100	12,29	-6	19	4,5	23,5	2,75E+01	44,96	2,99E+00	4,00E+28	5,07E-06	2,04E+00	6,83E-01
Ti	---	-3,438	---	1,485	2,87	4,35	6,09E+00	47,87	4,54E+00	5,71E+28	-2,02E-06	5,96E-01	1,31E-01
46Ti	8,2	4,93	0	3,05	0	3,05	5,90E-01						
47Ti	7,4	3,63	-3,5	1,66	1,5	3,2	1,70E+00						
48Ti	73,8	-6,08	0	4,65	0	4,65	7,84E+00						
49Ti	5,4	1,04	5,1	0,14	3,3	3,4	2,20E+00						
50Ti	5,2	6,18	0	4,8	0	4,8	1,79E-01						
V	---	-0,3824	---	0,0184	5,08	5,1	5,08E+00	50,94	6,11E+00	7,22E+28	-2,84E-07	7,35E-01	1,20E-01
50V	0,25	7,6	---	7,3	0,5	7,8	6,00E+01						
51V	99,75	-0,402	6,35	0,0203	5,07	5,09	4,90E+00						
Cr	---	3,635	---	1,66	1,83	3,49	3,05E+00	52,00	7,19E+00	8,33E+28	3,11E-06	5,45E-01	7,58E-02
50Cr	4,35	-4,5	0	2,54	0	2,54	1,58E+01						
52Cr	83,79	4,92	0	3,042	0	3,042	7,60E-01						
53Cr	9,5	-4,2	6,87	2,22	5,93	8,15	1,81E+01						
54Cr	2,36	4,55	0	2,6	0	2,6	3,60E-01						
Mn	100	-3,73	1,79	1,75	0,4	2,15	1,33E+01	54,94	7,43E+00	8,14E+28	-3,13E-06	1,26E+00	1,69E-01
Fe	---	9,45	---	11,22	0,4	11,62	2,56E+00	55,85	7,87E+00	8,48E+28	8,25E-06	1,20E+00	1,53E-01
54Fe	5,8	4,2	0	2,2	0	2,2	2,25E+00						
56Fe	91,7	9,94	0	12,42	0	12,42	2,59E+00						
57Fe	2,2	2,3	---	0,66	0,3	1	2,48E+00						
58Fe	0,3	15	0	28	0	28	1,28E+00						
Co	100	2,49	-6,2	0,779	4,8	5,6	3,72E+01	58,93	8,90E+00	9,09E+28	2,33E-06	3,89E+00	4,37E-01
Ni	---	10,3	---	13,3	5,2	18,5	4,49E+00	58,69	8,90E+00	9,13E+28	9,68E-06	2,10E+00	2,36E-01
58Ni	68,27	14,4	0	26,1	0	26,1	4,60E+00						
60Ni	26,1	2,8	0	0,99	0	0,99	2,90E+00						
61Ni	1,13	7,6	3,9	7,26	1,9	9,2	2,50E+00						
62Ni	3,59	-8,7	0	9,5	0	9,5	1,45E+01						
64Ni	0,91	-0,37	0	0,017	0	0,017	1,52E+00						
Cu	---	7,718	---	7,485	0,55	8,03	3,78E+00	63,55	8,96E+00	8,49E+28	6,74E-06	1,00E+00	1,12E-01
63Cu	69,17	6,43	0,22	5,2	0,006	5,2	4,50E+00						
65Cu	30,83	10,61	1,79	14,1	0,4	14,5	2,17E+00						
Zn	---	5,68	---	4,054	0,077	4,131	1,11E+00	65,39	7,13E+00	6,56E+28	3,84E-06	3,44E-01	4,83E-02
64Zn	48,6	5,22	0	3,42	0	3,42	9,30E-01						
66Zn	27,9	5,97	0	4,48	0	4,48	6,20E-01						
67Zn	4,1	7,56	-1,5	7,18	0,28	7,46	6,80E+00						
68Zn	18,8	6,03	0	4,57	0	4,57	1,10E+00						
70Zn	0,6	6	0	4,5	0	4,5	9,20E-02						
Ga	---	7,288	---	6,675	0,16	6,83	2,75E+00	69,72	5,91E+00	5,10E+28	3,83E-06	4,89E-01	8,28E-02
69Ga	60,1	7,88	-0,85	7,8	0,091	7,89	2,18E+00						
71Ga	39,9	6,4	-0,82	5,15	0,084	5,23	3,61E+00						
Ge	---	8,185	---	8,42	0,18	8,6	2,20E+00	72,64	5,32E+00	4,41E+28	3,71E-06	4,76E-01	8,96E-02
70Ge	20,5	10	0	12,6	0	12,6	3,00E+00						
72Ge	27,4	8,51	0	9,1	0	9,1	8,00E-01						
73Ge	7,8	5,02	3,4	3,17	1,5	4,7	1,51E+01						
74Ge	36,5	7,58	0	7,2	0	7,2	4,00E-01						
76Ge	7,8	8,2	0	8	0	8	1,60E-01						
As	100	6,58	-0,69	5,44	0,06	5,5	4,50E+00	74,92	5,72E+00	4,60E+28	3,11E-06	4,60E-01	8,04E-02
Se	---	7,97	---	7,98	0,32	8,3	1,17E+01	78,96	4,79E+00	3,65E+28	3,00E-06	7,31E-01	1,53E-01
74Se	0,9	0,8	0	0,1	0	0,1	5,18E+01						
76Se	9	12,2	0	18,7	0	18,7	8,50E+01						
77Se	7,6	8,25	0,6	8,6	0,05	8,65	4,20E+01						
78Se	23,5	8,24	0	8,5	0	8,5	4,30E-01						
80Se	49,6	7,48	0	7,03	0	7,03	6,10E-01						
82Se	9,4	6,34	0	5,05	0	5,05	4,40E-02						
Br	---	6,795	---	5,8	0,1	5,9	6,90E+00	79,90	3,12E+00	2,35E+28	1,64E-06	3,01E-01	9,65E-02
79Br	50,69	6,8	-1,1	5,81	0,15	5,96	1,10E+01						
81Br	49,31	6,79	0,6	5,79	0,05	5,84	2,70E+00						
Kr	---	7,81	---	7,67	0,01	7,68	2,50E+01	83,80	3,68E-03	2,64E+25	2,13E-09	8,64E-04	2,35E-01
78Kr	0,35	---	0	---	0	---	6,40E+00						
80Kr	2,25	---	0	---	0	---	1,18E+01						
82Kr	11,6	---	0	---	0	---	2,90E+01						
83Kr	11,5	---	---	---	---	---	1,85E+02						
84Kr	57	---	0	---	0	6,6	1,13E-01						
86Kr	17,3	8,1	0	8,2	0	8,2	3,00E-03						
Rb	---	7,09	---	6,32	0,5	6,8	3,80E-01	85,47	1,63E+00	1,15E+28	8,38E-07	8,25E-02	5,06E-02
85Rb	72,17	7,03	---	6,2	0,5	6,7	4,80E-01						
87Rb	27,83	7,23	---	6,6	0,5	7,1	1,20E-01						
Sr	---	7,02	---	6,19	0,06	6,25	1,28E+00	87,62	2,54E+00	1,75E+28	1,26E-06	1,31E-01	5,18E-02
84Sr	0,56	7	0	6	0	6	8,70E-01						
86Sr	9,86	5,67	0	4,04	0	4,04	1,04E+00						
87Sr	7	7,4	---	6,88	0,5	7,4	1,60E+01						
88Sr	82,58	7,15	0	6,42	0	6,42	5,80E-02						
Y	100	7,75	1,1	7,55	0,15	7,7	1,28E+00	88,91	4,47E+00	3,03E+28	2,41E-06	2,72E-01	6,08E-02
Zr	---	7,16	---	6,44	0,02	6,46	1,85E-01	91,22	6,51E+00	4,30E+28	3,17E-06	2,86E-01	4,39E-02
90Zr	51,45	6,4	0	5,1	0	5,1	1,10E-02						
91Zr	11,32	8,7	-1,08	9,5	0,15	9,7	1,17E+00						
92Zr	17,19	7,4	0	6,9	0	6,9	2,20E-01						
94Zr	17,28	8,2	0	8,4	0	8,4	4,99E-02						
96Zr	2,76	5,5	0	3,8	0	3,8	2,29E-02						

	conc	Coh b	Inc b	Coh xs	Inc xs	Scatt xs	Abs xs	At. Wght	ρ	N	δ	μ	μ/ρ
	[%]	[fm]	[fm]	[barn]	[barn]	[barn]	[barn]	[amu]	[g/cm³]	[1/m³]	[1]	[1/cm]	[cm²/g]
Nb	100	7,054	-0,139	6,253	0,0024	6,255	1,15E+00	92,91	8,57E+00	5,55E+28	4,03E-06	4,11E-01	4,80E-02
Mo	---	6,715	---	5,67	0,04	5,71	2,48E+00	95,94	1,02E+01	6,41E+28	4,43E-06	5,25E-01	5,14E-02
92Mo	14,84	6,91	0	6	0	6	1,90E-02						
94Mo	9,25	6,8	0	5,81	0	5,81	1,50E-02						
95Mo	15,92	6,91	---	6	0,5	6,5	1,31E+01						
96Mo	16,68	6,2	0	4,83	0	4,83	5,00E-01						
97Mo	9,55	7,24	---	6,59	0,5	7,1	2,50E+00						
98Mo	24,13	6,58	0	5,44	0	5,44	1,27E-01						
100Mo	9,63	6,73	0	5,69	0	5,69	4,00E-01						
Tc	(2.3E5 a)	6,8	---	5,8	0,5	6,3	2,00E+01	98,00	1,15E+01	7,06E+28	4,94E-06	1,86E+00	1,62E-01
Ru	---	7,03	---	6,21	0,4	6,6	2,56E+00	101,07	1,24E+01	7,37E+28	5,33E-06	6,75E-01	5,46E-02
96Ru	5,5	---	0	---	0	---	2,80E-01						
98Ru	1,9	---	0	---	0	---	<8.						
99Ru	12,7	---	---	---	---	---	6,90E+00						
100Ru	12,6	---	0	---	0	---	4,80E+00						
101Ru	17	---	---	---	---	---	3,30E+00						
102Ru	31,6	---	0	---	0	144,8	1,17E+00						
104Ru	18,7	---	0	---	0	4,483	3,10E-01						
Rh	100	5,88	---	4,34	0,3	4,6	1,45E+02	102,91	1,24E+01	7,26E+28	4,39E-06	1,09E+01	8,74E-01
Pd	---	5,91	---	4,39	0,093	4,48	6,90E+00	106,42	1,20E+01	6,80E+28	4,14E-06	7,74E-01	6,44E-02
102Pd	1,02	7,7	0	7,5	0	7,5	3,40E+00						
104Pd	11,14	7,7	0	7,5	0	7,5	6,00E-01						
105Pd	22,33	5,5	-2,6	3,8	0,8	4,6	2,00E+01						
106Pd	27,33	6,4	0	5,1	0	5,1	3,04E-01						
108Pd	26,46	4,1	0	2,1	0	2,1	8,55E+00						
110Pd	11,72	7,7	0	7,5	0	7,5	2,26E-01						
Ag	---	5,922	---	4,407	0,58	4,99	6,33E+01	107,87	1,05E+01	5,86E+28	3,57E-06	4,00E+00	3,81E-01
107Ag	51,83	7,555	1	7,17	0,13	7,3	3,76E+01						
109Ag	48,17	4,165	-1,6	2,18	0,32	2,5	9,10E+01						
Cd	---	4,87-0,7i	---	3,04	3,46	6,5	2,52E+03	112,41	8,65E+00	4,63E+28	2,32E-06	1,17E+02	1,35E+01
106Cd	1,25	5	0	3,1	0	3,1	1,00E+00						
108Cd	0,89	5,4	0	3,7	0	3,7	1,10E+00						
110Cd	12,51	5,9	0	4,4	0	4,4	1,10E+01						
111Cd	12,81	6,5	---	5,3	0,3	5,6	2,40E+01						
112Cd	24,13	6,4	0	5,1	0	5,1	2,20E+00						
113Cd	12,22	-8,0-5,73i	---	12,1	0,3	12,4	2,06E+04						
114Cd	28,72	7,5	0	7,1	0	7,1	3,40E-01						
116Cd	7,47	6,3	0	5	0	5	7,50E-02						
In	---	4,1-0,054i	---	2,08	0,54	2,62	1,94E+02	114,82	7,31E+00	3,83E+28	1,62E-06	7,53E+00	1,03E+00
113In	4,3	5,39	0,017	3,65	0,000037	3,65	1,20E+01						
115In	95,7	4,0-0,056i	-2,1	2,02	0,55	2,57	2,02E+02						
Sn	---	6,225	---	4,871	0,022	4,892	6,26E-01	118,71	7,31E+00	3,71E+28	2,38E-06	2,05E-01	2,80E-02
112Sn	1	6	0	4,5	0	4,5	1,00E+00						
114Sn	0,7	6,2	0	4,8	0	4,8	1,14E-01						
115Sn	0,4	6	---	4,5	0,3	4,8	3,00E+01						
116Sn	14,7	5,93	0	4,42	0	4,42	1,40E-01						
117Sn	7,7	6,48	---	5,28	0,3	5,6	2,30E+00						
118Sn	24,3	6,07	0	4,63	0	4,63	2,20E-01						
119Sn	8,6	6,12	---	4,71	0,3	5	2,20E+00						
120Sn	32,4	6,49	0	5,29	0	5,29	1,40E-01						
122Sn	4,6	5,74	0	4,14	0	4,14	1,80E-01						
124Sn	5,6	5,97	0	4,48	0	4,48	1,33E-01						
Sb	---	5,57	---	3,9	0,007	3,9	4,91E+00	121,76	6,68E+00	3,30E+28	1,89E-06	2,91E-01	4,36E-02
121Sb	57,3	5,71	-0,05	4,1	0,0003	4,1	5,75E+00						
123Sb	42,7	5,38	-0,1	3,64	0,001	3,64	3,80E+00						
Te	---	5,8	---	4,23	0,09	4,32	4,70E+00	127,60	6,24E+00	2,94E+28	1,76E-06	2,66E-01	4,26E-02
120Te	0,096	5,3	0	3,5	0	3,5	2,30E+00						
122Te	2,6	3,8	0	1,8	0	1,8	3,40E+00						
123Te	0,908	-0,05-0,116i	-2,04	0,002	0,52	0,52	4,18E+02						
124Te	4,816	7,96	0	8	0	8	6,80E+00						
125Te	7,14	5,02	-0,26	3,17	0,008	3,18	1,55E+00						
126Te	18,95	5,56	0	3,88	0	3,88	1,04E+00						
128Te	31,69	5,89	0	4,36	0	4,36	2,15E-01						
130Te	33,8	6,02	0	4,55	0	4,55	2,90E-01						
I	100	5,28	1,58	3,5	0,31	3,81	6,15E+00	126,90	4,93E+00	2,34E+28	1,27E-06	2,33E-01	4,73E-02
Xe	---	4,92	3,04	2,96	0	0	2,39E+01	131,29	5,85E-03	2,68E+25	1,36E-09	6,41E-04	1,10E-01
124Xe	0,1	---	0	---	0	---	1,65E+02						
126Xe	0,09	---	0	---	0	---	3,50E+00						
128Xe	1,91	---	0	---	0	---	<8						
129Xe	26,4	---	---	---	---	---	2,10E+01						
130Xe	4,1	---	0	---	0	---	<26.						
131Xe	21,2	---	---	---	---	---	8,50E+01						
132Xe	26,9	---	0	---	0	---	4,50E-01						
134Xe	10,4	---	0	---	0	---	2,65E-01						
136Xe	8,9	---	0	---	0	---	2,60E-01						
Cs	100	5,42	1,29	3,69	0,21	3,9	2,90E+01	132,91	1,87E+00	8,47E+27	4,73E-07	2,79E-01	1,49E-01
Ba	---	5,07	---	3,23	0,15	3,38	1,10E+00	137,33	3,59E+00	1,57E+28	8,21E-07	7,05E-02	1,96E-02
130Ba	0,11	-3,6	0	1,6	0	1,6	3,00E+01						
132Ba	0,1	7,8	0	7,6	0	7,6	7,00E+00						
134Ba	2,42	5,7	0	4,08	0	4,08	2,00E+00						
135Ba	6,59	4,67	---	2,74	0,5	3,2	5,80E+00						
136Ba	7,85	4,91	0	3,03	0	3,03	6,80E-01						

	conc	Coh b	Inc b	Coh xs	Inc xs	Scatt xs	Abs xs	At. Wght	ρ	N	δ	μ	μ/ρ
	[%]	[fm]	[fm]	[barn]	[barn]	[barn]	[barn]	[amu]	[g/cm³]	[1/m³]	[1]	[1/cm]	[cm²/g]
137Ba	11,23	6,83	---	5,86	0,5	6,4	3,60E+00						
138Ba	71,7	4,84	0	2,94	0	2,94	2,70E-01						
La	---	8,24	---	8,53	1,13	9,66	8,97E+00	138,91	6,15E+00	2,67E+28	2,26E-06	4,97E-01	8,08E-02
138La	0,09	2	---	8	0,5	8,5	5,70E+01						
139La	99,91	8,24	3	8,53	1,13	9,66	8,93E+00						
Ce	---	4,84	---	2,94	0,001	2,94	6,30E-01	140,12	6,77E+00	2,91E+28	1,45E-06	1,04E-01	1,53E-02
136Ce	0,19	5,8	0	4,23	0	4,23	7,30E+00						
138Ce	0,25	6,7	0	5,64	0	5,64	1,10E+00						
140Ce	88,48	4,84	0	2,94	0	2,94	5,70E-01						
142Ce	11,08	4,75	0	2,84	0	2,84	9,50E-01						
Pr	100	4,58	-0,35	2,64	0,015	2,66	1,15E+01	140,91	6,77E+00	2,89E+28	1,36E-06	4,10E-01	6,05E-02
Nd	---	7,69	---	7,43	9,2	16,6	5,05E+01	144,24	7,01E+00	2,93E+28	2,32E-06	1,96E+00	2,80E-01
142Nd	27,16	7,7	0	7,5	0	7,5	1,87E+01						
143Nd	12,18	14	21	25	55	80	3,37E+02						
144Nd	23,8	2,8	0	1	0	1	3,60E+00						
145Nd	8,29	14	---	25	5	30	4,20E+01						
146Nd	17,19	8,7	0	9,5	0	9,5	1,40E+00						
148Nd	5,75	5,7	0	4,1	0	4,1	2,50E+00						
150Nd	5,63	5,3	0	3,5	0	3,5	1,20E+00						
Pm	(2.62 a)	12,6	3,2	20	1,3	21,3	1,68E+02	145,00	7,30E+00	3,03E+28	3,93E-06	5,75E+00	7,88E-01
Sm	---	0,8-1,65i	---	0,422	39	39	5,92E+03	150,36	7,52E+00	3,01E+28	2,48E-07	1,80E+02	2,39E+01
144Sm	3,1	-3	0	1	0	1	7,00E-01						
147Sm	15,1	14	11	25	143	39	5,70E+01						
148Sm	11,3	-3	0	1	0	1	2,40E+00						
149Sm	13,9	-19,2-11,7i	31,4-10,3i	63,5	137	200	4,21E+04						
150Sm	7,4	14	0	25	0	25	1,04E+02						
152Sm	26,6	-5	0	3,1	0	3,1	2,06E+02						
154Sm	22,6	9,3	0	11	0	11	8,40E+00						
Eu	---	7,22-1,26i	---	6,57	2,5	9,2	4,53E+03	151,96	5,24E+00	2,08E+28	1,54E-06	9,43E+01	1,80E+01
151Eu	47,8	6,13-2,53i	4,5-2,14i	5,5	3,1	8,6	9,10E+03						
153Eu	52,2	8,22	3,2	8,5	1,3	9,8	3,12E+02						
Gd	---	6,5-13,82i	---	29,3	151	180	4,97E+04	157,25	7,90E+00	3,02E+28	2,02E-06	1,51E+03	1,91E+02
152Gd	0,2	10	0	13	0	13	7,35E+02						
154Gd	2,1	10	0	13	0	13	8,50E+01						
155Gd	14,8	6,0-17,0i	5-13,16i	40,8	25	66	6,11E+04						
156Gd	20,6	6,3	0	5	0	5	1,50E+00						
157Gd	15,7	-1,14-71,9	5-55,8i	650	394	1044	2,59E+05						
158Gd	24,8	9	0	10	0	10	2,20E+00						
160Gd	21,8	9,15	0	10,52	0	10,52	7,70E-01						
Tb	100	7,38	-0,17	6,84	0,004	6,84	2,34E+01	158,93	8,23E+00	3,12E+28	2,37E-06	9,43E-01	1,15E-01
Dy	---	16,9-0,276i	---	35,9	54,4	90,3	9,94E+02	162,50	8,55E+00	3,17E+28	5,51E-06	3,44E+01	4,02E+00
156Dy	0,06	6,1	0	4,7	0	4,7	3,30E+01						
158Dy	0,1	6	0	5	0	5	4,30E+01						
160Dy	2,34	6,7	0	5,6	0	5,6	5,60E+01						
161Dy	19	10,3	4,9	13,3	3	16	6,00E+02						
162Dy	25,5	-1,4	0	0,25	0	0,25	1,94E+02						
163Dy	24,9	5	1,3	3,1	0,21	3,3	1,24E+02						
164Dy	28,1	49,4-0,79i	0	307	0	307	2,84E+03						
Ho	100	8,01	-1,7	8,06	0,36	8,42	6,47E+01	164,93	8,80E+00	3,21E+28	2,65E-06	2,35E+00	2,67E-01
Er	---	7,79	---	7,63	1,1	8,7	1,59E+02	167,26	9,07E+00	3,26E+28	2,62E-06	5,48E+00	6,04E-01
162Er	0,14	8,8	0	9,7	0	9,7	1,90E+01						
164Er	1,56	8,2	0	8,4	0	8,4	1,30E+01						
166Er	33,4	10,6	0	14,1	0	14,1	1,96E+01						
167Er	22,9	3	1	1,1	0,13	1,2	6,59E+02						
168Er	27,1	7,4	0	6,9	0	6,9	2,74E+00						
170Er	14,9	9,6	0	11,6	0	11.6(1.2)	5,80E+00						
Tm	100	7,07	0,9	6,28	0,1	6,38	1,00E+02	168,93	9,32E+00	3,32E+28	2,42E-06	3,53E+00	3,79E-01
Yb	---	12,43	---	19,42	4	23,4	3,48E+01	173,04	6,90E+00	2,40E+28	3,07E-06	1,40E+00	2,03E-01
168Yb	0,14	-4,07-0,62i	0	2,13	0	2,13	2,23E+03						
170Yb	3,06	6,77	0	5,8	0	5,8	1,14E+01						
171Yb	14,3	9,66	-5,59	11,7	3,9	15,6	4,86E+01						
172Yb	21,9	9,43	0	11,2	0	11,2	8,00E-01						
173Yb	16,1	9,56	-5,3	11,5	3,5	15	1,71E+01						
174Yb	31,8	19,3	0	46,8	0	46,8	6,94E+01						
176Yb	12,7	8,72	0	9,6	0	9,6	2,85E+00						
Lu	---	7,21	---	6,53	0,7	7,2	7,40E+01	174,97	9,84E+00	3,39E+28	2,51E-06	2,75E+00	2,80E-01
175Lu	97,39	7,24	2,2	6,59	0,6	7,2	2,10E+01						
176Lu	2,61	6,1-0,57i	3,0+0,61i	4,7	1,2	5,9	2,07E+03						
Hf	---	7,7	---	7,6	2,6	10,2	1,04E+02	178,49	1,33E+01	4,49E+28	3,56E-06	5,13E+00	3,86E-01
174Hf	0,2	10,9	0	15	0	15	5,61E+02						
176Hf	5,2	6,61	0	5,5	0	5,5	2,35E+01						
177Hf	18,6	0,8	0,9	0,1	0,1	0,2	3,73E+02						
178Hf	27,1	5,9	0	4,4	0	4,4	8,40E+01						
179Hf	13,7	7,46	1,06	7	0,14	7,1	4,10E+01						
180Hf	35,2	13,2	0	21,9	0	21,9	1,30E+01						
Ta	---	6,91	---	6	0,01	6,01	2,06E+01	180,95	1,67E+01	5,54E+28	3,94E-06	1,47E+00	8,86E-02
180Ta	0,012	7.(2.)	---	6,2	0,5	7	5,63E+02						
181Ta	99,988	6,91	-0,29	6	0,011	6,01	2,05E+01						
W	---	4,86	---	2,97	1,63	4,6	1,83E+01	183,84	1,94E+01	6,34E+28	3,17E-06	1,45E+00	7,50E-02
180W	0,1	5.(3.)	0	3	0	3	3,00E+01						
182W	26,3	6,97	0	6,1	0	6,1	2,07E+01						
183W	14,3	6,53	---	5,36	0,3	5,7	1,01E+01						

	conc	Coh b	Inc b	Coh xs	Inc xs	Scatt xs	Abs xs	At. Wght	ρ	N	δ	μ	μ/ρ
	[%]	[fm]	[fm]	[barn]	[barn]	[barn]	[barn]	[amu]	[g/cm³]	[1/m³]	[1]	[1/cm]	[cm²/g]
184W	30,7	7,48	0	7,03	0	7,03	1,70E+00						
186W	28,6	-0,72	0	0,065	0	0,065	3,79E+01						
Re	---	9,2	---	10,6	0,9	11,5	8,97E+01	186,21	2,10E+01	6,80E+28	6,44E-06	6,89E+00	3,27E-01
185Re	37,4	9	2	10,2	0,5	10,7	1,12E+02						
187Re	62,6	9,3	2,8	10,9	1	11,9	7,64E+01						
Os	---	10,7	---	14,4	0,3	14,7	1,60E+01	190,23	2,26E+01	7,15E+28	7,88E-06	2,20E+00	9,72E-02
184Os	0,02	10	0	13	0	13	3,00E+03						
186Os	1,58	11,6	0	17	0	17	8,00E+01						
187Os	1,6	10	---	13	0,3	13	3,20E+02						
188Os	13,3	7,6	0	7,3	0	7,3	4,70E+00						
189Os	16,1	10,7	---	14,4	0,5	14,9	2,50E+01						
190Os	26,4	11	0	15,2	0	15,2	1,31E+01						
192Os	41	11,5	0	16,6	0	16,6	2,00E+00						
Ir	---	10,6	---	14,1	0	14	4,25E+02	192,22	2,24E+01	7,02E+28	7,65E-06	3,08E+01	1,38E+00
191Ir	37,3	---	---	---	---	---	9,54E+02						
193Ir	62,7	---	---	---	---	---	1,11E+02						
Pt	---	9,6	---	11,58	0,13	11,71	1,03E+01	195,08	2,15E+01	6,62E+28	6,54E-06	1,46E+00	6,80E-02
190Pt	0,01	9	0	10	0	10	1,52E+02						
192Pt	0,79	9,9	0	12,3	0	12,3	1,00E+01						
194Pt	32,9	10,55	0	14	0	14	1,44E+00						
195Pt	33,8	8,83	-1	9,8	0,13	9,9	2,75E+01						
196Pt	25,3	9,89	0	12,3	0	12,3	7,20E-01						
198Pt	7,2	7,8	0	7,6	0	7,6	3,66E+00						
Au	100	7,63	-1,84	7,32	0,43	7,75	9,87E+01	196,97	1,93E+01	5,91E+28	4,64E-06	6,29E+00	3,25E-01
Hg	---	12,692	---	20,24	6,6	26,8	3,72E+02	200,59	1,36E+01	4,07E+28	5,31E-06	1,62E+01	1,20E+00
196Hg	0,2	30,3	0	115	0	115	3,08E+03						
198Hg	10,1	---	0	---	0	---	2,00E+00						
199Hg	17	16,9	15,5	36	30	66	2,15E+03						
200Hg	23,1	---	0	---	0	---	<60.						
201Hg	13,2	---	---	---	---	---	7,80E+00						
202Hg	29,6	---	0	---	0	9,828	4,89E+00						
204Hg	6,8	---	0	---	0	---	4,30E-01						
Tl	---	8,776	---	9,678	0,21	9,89	3,43E+00	204,38	1,19E+01	3,49E+28	3,15E-06	4,65E-01	3,93E-02
203Tl	29,524	6,99	1,06	6,14	0,14	6,28	1,14E+01						
205Tl	70,476	9,52	-0,242	11,39	0,007	11,4	1,04E-01						
Pb	---	9,405	---	11,115	0,003	11,118	1,71E-01	207,20	1,14E+01	3,30E+28	3,19E-06	3,72E-01	3,28E-02
204Pb	1,4	9,9	0	12,3	0	12,3	6,50E-01						
206Pb	24,1	9,22	0	10,68	0	10,68	3,00E-02						
207Pb	22,1	9,28	0,14	10,82	0,002	10,82	6,99E-01						
208Pb	52,4	9,5	0	11,34	0	11,34	4,80E-04						
Bi	100	8,532	---	9,148	0,0084	9,156	3,38E-02	208,98	9,75E+00	2,81E+28	2,47E-06	2,58E-01	2,65E-02

Table A.1: Neutron scattering lengths and the resulting refractive indices of isotopes under normal conditions [Neu92].

A.2 Overview of the neutron scattering lengths of the elements

	Z	Coh b	Inc b	Coh xs	Inc xs	Scatt xs	Abs xs	Weight	ρ	ρ	δ	μ	μ/ρ
		[fm]	[fm]	[barn]	[barn]	[barn]	[barn]	[amu]	[g/cm³]	[1/m³]	[1]	[1/cm]	[cm²/g]
H	1	-3,739	---	1,7568	80,26	82,02	0,3326	1,01	8,99E-05	5,37E+25	-2,07E-09	0,0044	49,2129
He	2	3,26	---	1,34	0	1,34	0,00747	4,00	1,79E-04	2,68E+25	9,01E-10	0,0000	0,2028
Li	3	-1,9	---	0,454	0,92	1,37	70,5	6,94	5,30E-01	4,60E+28	-8,99E-07	3,3054	6,2366
Be	4	7,79	0,12	7,63	0,0018	7,63	0,0076	9,01	1,85E+00	1,24E+29	9,91E-06	0,9443	0,5104
B	5	5,3-0,213i	---	3,54	1,7	5,24	767	10,81	2,34E+00	1,30E+29	7,11E-06	100,6750	43,0235
C	6	6,646	---	5,551	0,001	5,551	0,0035	12,01	2,26E+00	1,13E+29	7,75E-06	0,6295	0,2785
N	7	9,36	---	11,01	0,5	11,51	1,9	14,01	1,25E-03	5,37E+25	5,18E-09	0,0007	0,5767
O	8	5,803	---	4,232	0,0008	4,232	0,00019	16,00	1,43E-03	5,38E+25	3,21E-09	0,0002	0,1593
F	9	5,654	-0,082	4,017	0,0008	4,018	0,0096	19,00	1,70E-03	5,39E+25	3,14E-09	0,0002	0,1277
Ne	10	4,566	---	2,62	0,008	2,628	0,039	20,18	9,00E-04	2,69E+25	1,26E-09	0,0001	0,0796
Na	11	3,63	3,59	1,66	1,62	3,28	0,53	22,99	9,70E-01	2,54E+28	9,49E-07	0,0968	0,0998
Mg	12	5,375	---	3,631	0,08	3,71	0,063	24,31	1,74E+00	4,31E+28	2,38E-06	0,1627	0,0935
Al	13	3,449	0,256	1,495	0,0082	1,503	0,231	26,98	2,70E+00	6,02E+28	2,14E-06	0,1045	0,0387
Si	14	4,1491	---	2,163	0,004	2,167	0,171	28,09	2,33E+00	4,99E+28	2,13E-06	0,1168	0,0501
P	15	5,13	0,2	3,307	0,005	3,312	0,172	30,97	1,82E+00	3,54E+28	1,87E-06	0,1233	0,0677
S	16	2,847	---	1,0186	0,007	1,026	0,53	32,07	2,07E+00	3,89E+28	1,14E-06	0,0605	0,0292
Cl	17	9,577	---	11,5257	5,3	16,8	33,5	35,45	3,17E-03	5,38E+25	5,31E-09	0,0027	0,8545
Ar	18	1,909	---	0,458	0,225	0,683	0,675	39,95	1,78E-03	2,68E+25	5,27E-10	0,0000	0,0205
K	19	3,67	---	1,69	0,27	1,96	2,1	39,10	8,60E-01	1,32E+28	5,00E-07	0,0538	0,0625
Ca	20	4,7	---	2,78	0,05	2,83	0,43	40,08	1,55E+00	2,33E+28	1,13E-06	0,0759	0,0490
Sc	21	12,29	-6	19	4,5	23,5	27,5	44,96	2,99E+00	4,00E+28	5,07E-06	2,0430	0,6833
Ti	22	-3,438	---	1,485	2,87	4,35	6,09	47,87	4,54E+00	5,71E+28	-2,02E-06	0,5964	0,1314
V	23	-0,3824	---	0,0184	5,08	5,1	5,08	50,94	6,11E+00	7,22E+28	-2,84E-07	0,7354	0,1204
Cr	24	3,635	---	1,66	1,83	3,49	3,05	52,00	7,19E+00	8,33E+28	3,11E-06	0,5447	0,0758
Mn	25	-3,73	1,79	1,75	0,4	2,15	13,3	54,94	7,43E+00	8,14E+28	-3,13E-06	1,2585	0,1694
Fe	26	9,45	---	11,22	0,4	11,62	2,56	55,85	7,87E+00	8,48E+28	8,25E-06	1,2036	0,1529
Co	27	2,49	-6,2	0,779	4,8	5,6	37,18	58,93	8,90E+00	9,09E+28	2,33E-06	3,8913	0,4372
Ni	28	10,3	---	13,3	5,2	18,5	4,49	58,69	8,90E+00	9,13E+28	9,68E-06	2,0997	0,2359
Cu	29	7,718	---	7,485	0,55	8,03	3,78	63,55	8,96E+00	8,49E+28	6,74E-06	1,0030	0,1119
Zn	30	5,68	---	4,054	0,077	4,131	1,11	65,39	7,13E+00	6,56E+28	3,84E-06	0,3442	0,0483
Ga	31	7,288	---	6,675	0,16	6,83	2,75	69,72	5,91E+00	5,10E+28	3,83E-06	0,4891	0,0828
Ge	32	8,185	---	8,42	0,18	8,6	2,2	72,64	5,32E+00	4,41E+28	3,71E-06	0,4764	0,0896
As	33	6,58	-0,69	5,44	0,06	5,5	4,5	74,92	5,72E+00	4,60E+28	3,11E-06	0,4598	0,0804
Se	34	7,97	---	7,98	0,32	8,3	11,7	78,96	4,79E+00	3,65E+28	3,00E-06	0,7308	0,1526
Br	35	6,795	---	5,8	0,1	5,9	6,9	79,90	3,12E+00	2,35E+28	1,64E-06	0,3010	0,0965
Kr	36	7,81	---	7,67	0,01	7,68	25	83,80	3,68E-03	2,64E+25	2,13E-09	0,0009	0,2349
Rb	37	7,09	---	6,32	0,5	6,8	0,38	85,47	1,63E+00	1,15E+28	8,38E-07	0,0825	0,0506
Sr	38	7,02	---	6,19	0,06	6,25	1,28	87,62	2,54E+00	1,75E+28	1,26E-06	0,1315	0,0518
Y	39	7,75	1,1	7,55	0,15	7,7	1,28	88,91	4,47E+00	3,03E+28	2,41E-06	0,2719	0,0608
Zr	40	7,16	---	6,44	0,02	6,46	0,185	91,22	6,51E+00	4,30E+28	3,17E-06	0,2856	0,0439
Nb	41	7,054	-0,139	6,253	0,0024	6,255	1,15	92,91	8,57E+00	5,55E+28	4,03E-06	0,4114	0,0480
Mo	42	6,715	---	5,67	0,04	5,71	2,48	95,94	1,02E+01	6,41E+28	4,43E-06	0,5255	0,0514
Tc	43	6,8	---	5,8	0,5	6,3	20	98,00	1,15E+01	7,06E+28	4,94E-06	1,8589	0,1616
Ru	44	7,03	---	6,21	0,4	6,6	2,56	101,07	1,24E+01	7,37E+28	5,33E-06	0,6752	0,0546
Rh	45	5,88	---	4,34	0,3	4,6	144,8	102,91	1,24E+01	7,26E+28	4,39E-06	10,8518	0,8744
Pd	46	5,91	---	4,39	0,093	4,48	6,9	106,42	1,20E+01	6,80E+28	4,14E-06	0,7742	0,0644
Ag	47	5,922	---	4,407	0,58	4,99	63,3	107,87	1,05E+01	5,86E+28	3,57E-06	4,0038	0,3813
Cd	48	4,87-0,7i	---	3,04	3,46	6,5	2520	112,41	8,65E+00	4,63E+28	2,32E-06	117,0971	13,5372
In	49	4-0,054i	---	2,08	0,54	2,62	193,8	114,82	7,31E+00	3,83E+28	1,58E-06	7,5320	1,0304
Sn	50	6,225	---	4,871	0,022	4,892	0,626	118,71	7,31E+00	3,71E+28	2,38E-06	0,2047	0,0280
Sb	51	5,57	---	3,9	0,007	3,9	4,91	121,76	6,68E+00	3,30E+28	1,89E-06	0,2911	0,0436
Te	52	5,8	---	4,23	0,09	4,32	4,7	127,60	6,24E+00	2,94E+28	1,76E-06	0,2657	0,0426
I	53	5,28	1,58	3,5	0,31	3,81	6,15	126,90	4,93E+00	2,34E+28	1,27E-06	0,2330	0,0473
Xe	54	4,92	3,04	2,96	0	0	23,9	131,29	5,85E-03	2,68E+25	1,36E-09	0,0006	0,1096
Cs	55	5,42	1,29	3,69	0,21	3,9	29	132,91	1,87E+00	8,47E+27	4,73E-07	0,2788	0,1491
Ba	56	5,07	---	3,23	0,15	3,38	1,1	137,33	3,59E+00	1,57E+28	8,21E-07	0,0705	0,0196
La	57	8,24	---	8,53	1,13	9,66	8,97	138,91	6,15E+00	2,67E+28	2,26E-06	0,4968	0,0808
Ce	58	4,84	---	2,94	0,001	2,94	0,63	140,12	6,77E+00	2,91E+28	1,45E-06	0,1039	0,0153
Pr	59	4,58	-0,35	2,64	0,015	2,66	11,5	140,91	6,77E+00	2,89E+28	1,36E-06	0,4098	0,0605
Nd	60	7,69	---	7,43	9,2	16,6	50,5	144,24	7,01E+00	2,93E+28	2,32E-06	1,9641	0,2802
Pm	61	12,6	3,2	20	1,3	21,3	168,4	145,00	7,30E+00	3,03E+28	3,93E-06	5,7523	0,7880
Sm	62	0,8-1,65i	---	0,422	39	39	5922	150,36	7,52E+00	3,01E+28	2,48E-07	179,5660	23,8785
Eu	63	7,22-1,26i	---	6,57	2,5	9,2	4530	151,96	5,24E+00	2,08E+28	1,54E-06	94,2734	17,9911
Gd	64	6,5-13,82i	---	29,3	151	180	49700	157,25	7,90E+00	3,02E+28	2,02E-06	1509,3235	191,0536
Tb	65	7,38	-0,17	6,84	0,004	6,84	23,4	158,93	8,23E+00	3,12E+28	2,37E-06	0,9432	0,1146
Dy	66	16,9-0,276i	---	35,9	54,4	90,3	994	162,50	8,55E+00	3,17E+28	5,51E-06	34,3623	4,0190
Ho	67	8,01	-1,7	8,06	0,36	8,42	64,7	164,93	8,80E+00	3,21E+28	2,65E-06	2,3498	0,2670
Er	68	7,79	---	7,63	1,1	8,7	159	167,26	9,07E+00	3,26E+28	2,62E-06	5,4773	0,6039
Tm	69	7,07	0,9	6,28	0,1	6,38	100	168,93	9,32E+00	3,32E+28	2,42E-06	3,5349	0,3793
Yb	70	12,43	---	19,42	4	23,4	34,8	173,04	6,90E+00	2,40E+28	3,07E-06	1,3978	0,2026
Lu	71	7,21	---	6,53	0,7	7,2	74	174,97	9,84E+00	3,39E+28	2,51E-06	2,7505	0,2795
Hf	72	7,7	---	7,6	2,6	10,2	104,1	178,49	1,33E+01	4,49E+28	3,56E-06	5,1337	0,3857
Ta	73	6,91	---	6	0,01	6,01	20,6	180,95	1,67E+01	5,54E+28	3,94E-06	1,4748	0,0886
W	74	4,86	---	2,97	1,63	4,6	18,3	183,84	1,94E+01	6,34E+28	3,17E-06	1,4518	0,0750
Re	75	9,2	---	10,6	0,9	11,5	89,7	186,21	2,10E+01	6,80E+28	6,44E-06	6,8873	0,3273
Os	76	10,7	---	14,4	0,3	14,7	16	190,23	2,26E+01	7,15E+28	7,88E-06	2,1968	0,0972
Ir	77	10,6	---	14,1	0	14	425	192,22	2,24E+01	7,02E+28	7,65E-06	30,8134	1,3756
Pt	78	9,6	---	11,58	0,13	11,71	10,3	195,08	2,15E+01	6,62E+28	6,54E-06	1,4577	0,0680
Au	79	7,63	-1,84	7,32	0,43	7,75	98,65	196,97	1,93E+01	5,91E+28	4,64E-06	6,2860	0,3254
Hg	80	12,692	---	20,24	6,6	26,8	372,3	200,59	1,36E+01	4,07E+28	5,31E-06	16,2379	1,1984
Tl	81	8,776	---	9,678	0,21	9,89	3,43	204,38	1,19E+01	3,49E+28	3,15E-06	0,4652	0,0393
Pb	82	9,405	---	11,115	0,003	11,118	0,171	207,20	1,14E+01	3,30E+28	3,19E-06	0,3725	0,0328
Bi	83	8,532	---	9,148	0,0084	9,156	0,0338	208,98	9,75E+00	2,81E+28	2,47E-06	0,2582	0,0265

Table A.2: Neutron scattering lengths and the resulting refractive indices of the elements under normal conditions [Neu92].

Abbreviations

ANTARES	Advanced Neutron Tomography and Radiography Experimental System
CCD	Charged coupled device
DI	Dark current image
DQE	Detective quantum efficiency
ESF	Edge spread function
ESRF	European Synchrotron Radiation Facility, Grenoble, France
FFT	Fast Fourier Transform
FOV	Field of view
FRM-II	Forschungsreaktor München II
FWHM	Full width at half maximum
IDL	Interactive Data Language
ILL	Institute Laue Langevin, Grenoble, France
IP	Image Plate
JPEG/JPG	Image file format named after the Joint Photographic Experts Group
LD800	L/D-ratio 800
LUT	Look-up table
MCNP	Monte Carlo Nuclear Particle Code
MTF	Modular transfer function
NI	Neutron imaging
NPCI	Neutron phase contrast imaging
NPCR	Neutron phase contrast radiography
NPCT	Neutron phase contrast tomography
NR	Neutron radiography
NT	Neutron tomography
OB	Open beam image
PMV	Photo multiplier voltage
PSI	Paul Scherrer Institute, Villigen, Switzerland
PSF	Point spread function
ROI	Region of Interest
SNR	Signal-to-noise ratio
TEM	Transmission electron microscopy
TIFF/TIF	Tagged Image File Format
TUM	Technische Universität München
UTG	Lehrstuhl für Umformtechnik und Gießereiwesen der TUM

References

[Adi05] Adib M., Kilany M., Habib N., Fathallah M., Czech. Journal of Physics 55, pp. 563-578, 2005

[All00] Allman B. E., et al, *Phase Radiography with neutrons*, Nature, London, 408, pp. 158-159, 2000

[Bae02] Baechler S., Kardjilov N., Dierick M., Jolie J., Kühne G., Lehmann E., Materna T., *New features in cold neutron radiography and tomography part I: thinner scintillators and a velocity selector to improve the spatial resolution*, Nucl. Inst. and Meth. in Phys. Res. A 491, pp. 481-491, 2002

[Bor02] Born Max and Emil Wolf, Principles of Optics, Cambridge University Press, 2002

[Bor87] Born R. and Hohlwein D., Nucl. Instr. and Meth. A 262, 359-365, 1987

[Bon65] Bonse U. and Hart M., Appl. Phys. Lett. 6. p. 155, 1965

[Bro06] Brookhaven National Laboratory (BNL), ENDF Files from the National Nuclear Data Center, Version ENDF/B-VII.0 at 300K, December 15, 2006, website (http://www.nndc.bnl.gov/exfor7/endf00.htm)

[Büc93] Bücherl T. et al, Nucl. Inst. and Meth. in Phys. Res. A 333, pp. 502-506, 1993

[Can86] Canny J., *A computational approach to edge detection*, IEEE Trans. Pattern Analysis and Machine Intell. 8, pp. 679-698, 1986

[Cha32] Chadwick, J., *The Existence of a Neutron*, Proc. Roy. Soc., A, 136, p. 692-708, 1932

[Cow95] Cowley J. M., *Diffraction Physics*, North-Holland PL, 1995

[Der87] Deriche R., *Using Canny's criteria to derive a recursively implemented optimal edge detector,* Int. J. of Computer Vision 1, pp. 167-187, 1987.

[Dub02] Dubus F., Bonse U., Biermann T., Baron M., Beckmann F., Zawisky M., Proc SPIE Vol. 4502, pp. 359-370, 2002

[Dou05] Dougherty R.P., *Extensions of DAMAS and benefits and limitations of deconvolution in beamforming*, AIAA Paper 2005-2961, May, 2005

[Erd76] Erdtmann G., *Neutron Activation Tables*, Verlag Chemie, Weinheim, New York, 1976

[Fen73] Fenimore E. E., Cannon T. M., *Coded aperture imaging with uniformly redundant arrays*, Applied Optics, Vol. 17 No. 3, 1973

[Fuj04] Fujine S., et al., *Statistical image analysis of high-sensitivity neutron images obtained by cooled CCD systems*, Applied Radiation and Isotopes 61, Elsevier, 465-470, 2004

[Goe79] Goetz K., Foerster E., Zaumseil P., Kalashnikov M. P., Mikhailov Iu. A., Sklizkov G. V., Fedotov S. I., Soviet Journal of Quantum Electronics, vol. 9, pp. 607-610, 1979

[Gol47] Goldberger M. L., Seitz F., Phys. Rev. 71,1947

[Gol79] Golub R., Pendlebury J. M., Re. Progr. Phys. 42, 439, 1979

[Grü05] Grünauer F., *Design, optimization, and implementation of the new neutron radiography facility at FRM-II*, PhD thesis, Technische Universität München, 2005

[Gur95] Gureyev T. E., Roberts A., Nugent K., J. Opt. Soc. Am. A 12, pp.1942-1946, 1995

[Han90] Hangleiter T. et al, J. Phys.: Cond. Matter 2, 6837, 1990

[Har81] Von der Hardt P., Röttger H., *Neutron Radiography Handbook*, D. Reidel Publishing Company, Dordrecht Boston London, 1981

[Hec07] Hecht E., *Optik*, Addison-Wesley, Bonn München, 2007

[Her80] Herman Gabor T., *Image Reconstruction from Projections - The Fundamentals of Computerized Tomography*, Academic Press, New York 1980

[Hug58] Hughes D. J. and Schwartz R. B., *Neutron Cross Sections*, Brookhaven National Laboratory, Upton, New York, 1958

[Kak99] Kak A. C., Slaney M., *Principles of Computerized Tomographic Imaging*, IEEE Press, New York, 1999

[Kal48] Kallman H., *Neutron Radiography*, 1948

[Kam96] Kamali Moghadam K., Ziaie F., Nucl. Inst. Meth. A 377, pp. 45-47, 1996

[Kar99] Karasawa Haga Y., Kumazawa S., Niimura N., *Gamma-ray sensitivity and shielding of a neutron image plate*, J. Appl. Cryst. 32, pp. 878-882, 1999

[Kar03] Kardjilov N., *Further developments and applications of radiography and tomography with thermal and cold neutrons*, PhD thesis, Technische Universität München, 2005

[Kob96] Kobayashi H., Matsumoto T., Matsubayashi M., Brenizer J. S. Jr., Lindsay J. T., Nucl. Inst. Meth. A 377, pp. 37-40, 1996

[Kob90] Kobayashi H., Wakao H., *Accurate measurement of L, D and L/D for divergent collimators*, in: Fujine S., Kanda K., Matsumoto G., Barton J. P. (Eds.), Neutron Radiography, Vol. 3, Kluwer Academic Publishers, Dordrecht, pp. 889–892, 1990

[Kub99] Kuba A., Hermann G. T., *Discrete Tomography: Foundations, Algorithms and Applications*, Birkhäuser, Boston, 1999

[Lei62] Maier-Leibnitz H. and Springer T., Z. f. Phys. 167, p. 386, 1962

[Mar80] Marr D. and Hildreth E., *Theory of edge detection*, Proc. Royal Soc. London, 207, 187-217,1980

[McM03] McMahon P. J., Allman B. E., Jacobson D. L., Arif M., Werner S. A., Nugent K. A., Phys. Rev. Lett., vol. 91, nr. 14, 145502, 2003

[Mer61] Mertz L. & Young N., *Fresnel Transformations of Images*, Proc. Int'l Conf. on Optical Instruments and Techniques, Ed. K. J. Habell, p. 305, Chapman & Hall, London, 1961.

[Mez76] Mezei F., Novel polarized neutron devices: supermirror and spin component amplifier, Communications on Physics 1, pp. 81-85, 1976

[Miy86] Miyahara J., Takahashi K., Amemiya Y., Kamiya N., Satow Y., Nucl. Instrum. Methods A, pp. 246, 572, 1986

[Neu92] Neutron News, Vol. 3, No. 3, 1992, pp. 29-37

[Pap68] Papoulis A., *Systems and Transforms with Applications in Optics*, McGraw-Hill, New York, 1968.

[Pau78] Paul W., Trinks V., Fundamental Physics with reactor neutrons and neutrinos, p. 18, Inst. Phys. Conf. Ser. 42

[Pin69] Pingle K. K., *Visual perception by computer,* In A. Grasselli, *Automatic Interpretation and Classification of Images*, pp. 277-284, Academic Press, New York, 1969

[Pfe05] Pfeiffer F., Bunk O., Weitkamp T., van der Veen J. F. and Robinson I. K., Phys. Rev. Lett. 94, 164801, 2005

[Pfe06] Pfeiffer F., Grünzweig C., Bunk O., Frei G., Lehmann E. and David C., Phys. Rev. Lett. 96, 215505, 2006

[Pfe06a] Pfeiffer F., Weitkamp T., Bunk O. and David C., Nature Physics, Vol. 2, 2006

[Pre70] Prewitt J. M. S., *Object enhancement and extraction,* In A. Rosenfeld and B. S. Lipkin, Picture Processing and Psychophysics, pp. 75-149, Academic Press, New York, 1970

[Rad17] Radon J., Ber. Verh. Sächs. Akad. Wiss. Leipzig, Math.-Nat. 69, 262, 1917

[Rau74] Rauch H., Treimer W., Bonse U., Physics Letters 47A, p. 369-371, 1974

[Rau92] Rausch C., Bücherl T., Gähler R., Seggern v. H., Winnacker A., Recent developments in neutron detection, Neutrons, X-Rays, and Gamma Rays 1737, pp. 255-263, 1992

[Rau00] Rauch H. and Werner S. A., *Neutron Interferometry*, Clarendon Press, Oxford, 2000

[Rob65] Roberts L. G., *Machine perception of three-dimensional solids*, In J. T. Tippet et al., *Optical and Electro-Optical Information Processing*, pp. 159-197, MIT Press, Cambridge, 1965.

[Roe95] Röntgen, C. R., *On a New Kind of Rays*, Nature 53, 274, 1896

[Ros82] Rosenfeld A., Kak A. C., *Digital Picture Processing*, Second edition, Volume 1, Academic Press, New York London Paris San Francisco Sao Paulo Sydney Tokyo Tornto, 1982

[Rus95] Russ, J.C., *The image processing handbook*, CRC Press, Boca Raton Ann Arbor London Tokyo, 1995

[Schil99] Schillinger B., *Neue Entwicklungen zu Radiographie und Tomographie mit thermischen Neutronen*, PhD Thesis, Technische Universität München, Mensch & Buch Verlag, Berlin 1999.

[Schil99a] Schillinger B., *Estimation and measurement of L/D on a cold and thermal neutron guide*, Sixth World Conference on Neutron Radiography, Osaka, 1999

[Sea89] Sears V. F., *Neutron optics*, Oxford University Press, 1989

[Seg89] von Seggern H., Cryst. Latt. Def. Amorph. Mat. 18, p. 399, 1989

[Ski84] Skinner G. K., *Imaging with coded-aperture masks*, Nuclear Instruments and Methods in Physics Research 221, 33-40, 1984

[Sla90] Slaney

[Son83] Sonoda M., Takano M., Miyahara J., Kato H., *Computed Radiography utilizing scanning laser stimulated luminescence*, Radiology 148, pp. 833-838, 1983

[Sta00] Stamatelatos I. E. and Messoloras S., Rev. Sci. Instr. 71, pp. 70-73, 2000

[Str04] Strobl M., Treimer W., Hilger A., Feye-Treimer U., *Neutron tomography in double crystal diffractometers*, Physica B 350, pp. 155-158, 2004

[Tea83] Teague M. R., J. Opt. Soc. Am. 73, pp. 1434–1441, 1983

[Tho91] Thoms M., v. Seggern H., Winnacker A., Phys. Rev. B 44, 9240, 1991

[Tor80] Torre V. and Poggio T. A., *On edge detection,* IEEE Trans. Pattern Analysis and Machine Intell., 8, pp. 147-163, 1980

[Wea99] Weaire D., Hutzler S., *The Physics of Foams*, Clarendon Press, Oxford, 1999

[Web69] Webb F. J., Nucl. Instr. and Meth. 69, pp. 325-329, 1969

[Wie49] Wiener N. *Extrapolation, Interpolation, and Smoothing of Stationary Time Series*, Wiley, New York, 1949

[Wil96] Wilkins S. W., Gureyev T. E., Gao D., Pogany A., Stevenson A. W., *Phase contrast imaging using polychromatic hard X-rays*, Nature 384, pp. 335-338, 1996

[Wou73] Wouters A., *Direct Method of decoding Multiple Images*, Applied Optics, Vol. 12, No. 8, 1973

[XRT08] XRT, http://www.xrt.com.au, 2008

[Zer34] Zernike F., Physica 1, pp. 689, 1934; see also Proc. Phys. Soc. 61, pp. 158, 1948

[Zer42] Zernike F., *Phase-contrast, a new method for microscopic observation of transparent objects. Part I and II*, Physica 9, pp. 686-698 and 974-986 (1942)

Acknowledgements

At this point I want to thank all the people who have supported me over the last years and have contributed to the successful completion of this work.

First of all I want to thank Prof. Dr. Peter Böni who gave me the opportunity to work on this exciting scientific topic at his chair. I am very grateful for his constant support and the opportunities to participate at international conferences and collaborations.

Especially, I want to thank my supervisor Dr. Burkhard Schillinger, the leader of the ANTARES team without whom this work would not have been possible. His guidance helped me to overcome many obstacles and his leadership created the positive and creative atmosphere the ANTARES group has become famous for at FRM-II.

Many thanks to Elbio Calcada, the engineer of the ANTARES team who often made the impossible possible...and in the end even look elegant (see Fig. 2.17).

For the good cooperation and the great comradeship inside and outside the reactor building I want to thank Pegor Aynajian, Dr. Markus Bleuel, Dr. Johannes Brunner, Dr. Florian Grünauer, Dr. Wolfgang Häußler, Christian Hesse, Dr. Markus Hölzel, Wolfgang Kaltner, Dr. Nikolay Kardjilov, Martin Mühlbauer, Julia Repper, Michael Schulz, Dominik Streibl, Uwe Wasmuth and the other colleagues and friends at FRM-II, who made my time there an beautiful and unforgettable experience.

Many thanks to Anna Brunnbauer and Sören Schlimm for their good work as working students at ANTARES.

For the support during the TOF-measurements of the spectral neutron flux density with different crystal filters I want to thank Dr. Karl Zeitelhack.

For the financial support I want to thank the Deutsche Forschungsgemeinschaft (DFG).

The successful DFG project became possible by the good cooperation with the institute of metal forming and casting UTG with its head Prof. Dr.-Ing. Hartmut Hoffmann, who I want to thank for his support. Special thanks go to Sophie Hippmann and Andreas Mackensen whose dedication lead to the success of this joint project.

For the great support at measurements at PSI and many good discussions I want to thank Dr. Eberhard Lehmann, Gabriel Frei, Guido Kühne and Peter Vontobel.

Many thanks to Dr. Christian David, Christian Grünzweig and Prof. Dr. Franz Pfeiffer for the interesting discussions about grating based interferometry and their efforts to use this technique at FRM-II.

For introducing me to the tomography group at FRM-II and many helpful conversations I want to thank Dr. Joachim Baumann and Dr. Manfred Schuster.

In the same way I want to thank Prof. Dr. Jürgen Mollenhauer and Prof. Dr.-Ing. Jörg Wellnitz for the exciting discussions and for providing us with many interesting samples.

Many thanks to Christian Herzog and Uwe Stiegel the other members of the workshops at FRM-II. In the same way I want to thank Jörg Pulz and his network team for the good maintenance of the computer network and for the many times they helped quickly to overcome technical issues during measurements.

At this point I also want to thank all the “invisible” people who work hard at FRM-II to supply the scientists reliably with neutrons.

Last but not least I want to thank my family and friends, who supported me all the time. In particular I want to thank my fiancée Katrin for her trust in me and her patience with me.